INSTITUT DE FÍSICA
D'ALTES ENERGIES

UNIVERSITAT AUTÒNOMA
DE BARCELONA

Observation of the Crab pulsar wind nebula and microquasar candidates with MAGIC

PH.D. DISSERTATION
Universitat Autonoma de Barcelona
speciality: Astrophysics

Roberta Zanin
IFAE
Edifici Cn, UAB
08193 Bellaterra (Barcelona), Spain
roberta@ifae.es

supervised by:

Juan Cortina Blanco
IFAE
Edifici Cn, UAB
08193 Bellaterra (Barcelona), Spain
cortina@ifae.es

Enrique Fernández Sánchez
IFAE
IFAE & UAB
Edifici Cn, UAB
08193 Bellaterra (Barcelona), Spain
enrique.fernandez@ifae.es

To Florian Goebel

irreplaceable friend
and dearest collegue

Vorrei sapere a che cosa e servito
vivere, amare e soffrire
spendere tutti i tuoi giorni passati
se presto hai dovuto partire,
se presto hai dovuto partire
voglio pero ricordarti com eri
pensare che ancora vivi
voglio pensare che ancora mi ascolti
e che come allora sorridi,
e che come allora sorridi

Contents

Acronyms

asl above sea level

ADAF Advection Dominated Accretion Flow

ADC Analogical to Digital Converter

AGASA Akeno Giant Air Shower Array

AGILE Astro-rivelatore Gamma a Immagini LEggero

AGN Active Galactic Nucleus

AMANDA Antarctic Muon And Neutrino Detector Array

AMC Active Mirror Control

AMI Arcminute Microkelvin Imager

ANTARES Astronomy with a Neutrino Telescope and Abyss environmental RESarch

ARGO-YBJ Astrophysical Radiation with Ground-based Observatory at YangBaJing

ASCII American Standard Code for Information Interchange

ASM All-Sky Monitor

ATel Astronomical Telegram

BAT Burst Alert Telescope

BATSE Burst And Transient Source Experiment

BH Black Hole

CANGAROO Collaboration of Australia and Nippon for a GAmma-Ray Observatory in the Outback

CASA-MIA Chicago Air Shower Array-Michigan Muon Array

CAT Cherenkov Atmospheric Telescope

CC Central Control

CCD Charge-Coupled Device

CCNN Close Compact Next Neighbor

CD Color-color Diagram

CE Common Era

CGRO Compton Gamma-Ray Observatory

CGS Cm Gr Second

CH Counting House

CL Confidence Level

CMB Cosmic Microwave Background

CoG Center of Gravity

CPU Central Processing Unit

CR Cosmic Ray

CTA Cherenkov Telescope Array

DAQ Data AcQuisition

DC Direct Current

DoF Degree of Freedom

DRS2 Domino Ring Sampler 2

DT Discriminator Threshold

EAS Extensive Atmospheric Shower

EAS-TOP Extensive Atmospheric Shower-TOP

EGRET Energetic Gamma-Ray Experiment Telescope

EHE Extra High Energy

ESA European Space Agency

FB Flaring Branch

FADC Flash Analogical to Digital Converter

FIFO First In, First Out

FIR Far InfraRed

FoV Field of View

GBI Green Bank Interferometer

GCN Gamma-ray burst Coordinate Network

GLAST Gamma-ray Large Area Space Telescope

GBM GLAST Burst Monitor

GPS Global Positioning System

GRB Gamma Ray Burst

GUI Graphical User Interface

GZK Greisen-Zatsepin-Kuzmin

HB Horizontal Branch

HE High-Energy

HEGRA High Energy Gamma Ray Astronomy

HESS High Energy Stereoscopic System

HiRES High Resolution fly's eye

HMXB High-Mass X-ray Binaries

HST Hubble Space Telescope

HTML HyperText Markup Language

HV High Voltage

IACT Imaging Atmospheric Cherenkov Telescope

IC Inverse Compton

IFAE Institut de Física d'Altes Energies

IGM InterGalactic Magnetic

INAF Istituto Nazionale AstroFisica

INFN Istituto Nazionale Fisica Nucleare

IP Internet Protocol

IPR Individual Pixel Rate

IR InfraRed

ISM InterStellar Medium

KASCADE KArlsruhe Shower Core and Array DEtector

LAT Large Array Telescope

LED Light Emitting Diode

LMXB Low-Mass X-ray Binarie

LUT Look-Up Table

LVDS Low Voltage Differential Signal

LV Low Voltage

MAGIC Major Atmospheric Gamma-ray Imaging Cherenkov

MARS MAGIC Analysis and Reconstruction Software

MC Monte Carlo

MHD MagnetoHydro Dynamic

MIR MAGIC Integrated Readout

MJD Modified Julian Date

MPI Max-Planck Institute for physics

MQ MicroQuasar

MSP MilliSecond Pulsar

MUX Multiplexing readout system

NASA National Aeronautics and Space Administration

NB Normal Branch

NEMO NEutrino Mediterranean Observatory

NESTOR Neutrino Extended Submarine Telescope with Oceanographic Research

NIM Nuclear Instrumentation Module

NS Neutron Star

NSB Night Sky Background

NT-200 Neutrino Telescope-200

OA Online Analysis

OVRO Owens Valley Radio Observatory

PC Personal Computer

PCA Proportional Counter Array

PCI Peripheral Component Interconnect

PDF Probability Density Function

PI Principal Investigator

PLC Programmable Logical Controller

PULSAR PULSer And Recorder

PMT Photo Multiplier Tube

PSF Point Spread Function

PWN Pulsar Wind Nebula

PWNe Pulsar Wind Nebulae

QE Quantum Efficiency

RF Random Forest

RMS Root Mean Square

RXTE Rossi X-ray Timing Explorer

RT Ryle Telescope

SBIG Santa Barbara Instrument Group

SCCP Slow Control Cluster Processor

SDM Standard Disk Model

SED Spectral Energy Distribution

SI Systéme International d'unités, *i.e.* international system of units

SN SuperNova

SNe SuperNovae

SNR SuperNova Remnant

SSC Synchrotron Self Compton

ST Sum Trigger

TAC Time Allocation Committee

TCP/IP Transmission Control Protocol/Internet Protocol

ToO Target of Opportunity

UHE Ultra High Energy

US United States

UL Upper Limit

UTC Universal Time Coordinated

UV Ultra Violet

VCSEL Vertical-Cavity Surface-Emitting Laser

VERITAS Very Energetic Radiation Imaging Telescope Array System

VHE Very High Energy

VI Virtual Instrument

VME Virtual Mobile Engine

XRB X-Ray Binarie

ZA Zenith Angle

Unit definition

- **Electronvolt (eV)** is a unit of energy equal to $\equiv 1\,6 \times 10^{-19}$ J. It is the amount of energy gained by one unbound electron moving in an electric potential of 1 Volt.
- **Erg (erg)** is a unit of energy in the Cm Gr Second (CGS) unit system. It corresponds to 10^{-7} J which is about 1 TeV.
- **Jansky (Jy)** is a unit of spectral flux density often used in radio astronomy. 1 Jy corresponds to 10^{-26} $\frac{\mathrm{W}}{\mathrm{m^2Hz}}$ in the Systéme International d'unités, *i.e.* international system of units (SI).
- **Gauss (G)** is a unit of magetic field. In the SI 1 G = 10^{-4} T.
- **Light year (ly)** is a unit of distance which is common in astrophysics. 1 ly is the distance that light travels in a vacuum in one year. In the SI 1 ly = 9.4607×10^{15} m.
- **Parsec (pc)** unit of distance equal to 3.26 ly. A parsec is the distance from the Sun to an astrophysical object which has a parallax angle of one arcsecond.
- **Modified Julian Date (MJD)** consists in a dating method based on continuing day counts. The MJD provides the number of days which have ellapsed since midnight of Wedenesday November 17, 1858.

Introduction

The history of the γ-ray astronomy in the past twenty years is marked by the success of the Imaging Atmospheric Cherenkov Telescope (IACT) in the exploration of the Very High Energy (VHE) band. The last generation of IACTs, with the High Energy Stereoscopic System (HESS), Very Energetic Radiation Imaging Telescope Array System (VERITAS), and Major Atmospheric Gamma-ray Imaging Cherenkov (MAGIC) telescopes, have been capable to increase the total number of known VHE emitting sources from a few to almost one hundred in just seven years of operation. This population comprises galactic and extragalactic objects. IACTs have proved to be very effective in both the discovery of new emitters, as well as in the fine analysis of the physics properties of well established sources. Among them, the Crab Pulsar Wind Nebula is probably the best studied astrophysical object and the archetypal Pulsar Wind Nebula (PWN). Due to its brightness at almost all wavelenghts, it is considered as an astrophysical candle. Despite the Crab Nebula broad-band spectrum has been thoroughly studied across twenty orders of magnitudes, from radio frequencies to VHEs, further effort is needed to resolve the contradictions in the combination of all the multiwavelenght results. With the commissioning of the second MAGIC telescope in 2009 and the beginning of the operations in stereoscopic mode, the performance of the instrument improved dramatically, allowing MAGIC to reach the lowest ever energy threshold among all the existing IACTs, and describe the Crab Nebula spectrum with unprecedented precision down to 50 GeV. This achievement is of crucial importance for the VHE γ-ray astrophysics in the pre-CTA era, since it can cast new light on some of the unsolved mysteries of one of its most established sources.

On the other hand, MAGIC made a strong impact in the discovery of new VHE sources and, with the improved sensitivity of the stereoscopic mode, this will be even more so in the future. Among the galactic objects, MicroQuasars (MQs) constitute some of the best candidates for VHE emission, but despite several well accepted models predict such signal, it has not been detected. There are, in fact, evidences that the three binary systems which have been unambiguously detected at energies above few hundreds of GeV are binary pulsars rather than accreting microquasars. Nevertheless, the recent detection of the microquasar Cygnus X-3 above 100 MeV by both *Astro-rivelatore Gamma a Immagini LEggero (AGILE)* and *Fermi* satellites, and the claim of short one-day flares from Cygnus X-1 reported by *AGILE* confirmed that microquasars remain interesting targets for VHE telescopes. MAGIC made a strong effort in searching for VHE signals from microquasars, but found only a non-significant evidence of signal from Cygnus X-1 in 80 minutes of observation on September 24, 2006. MAGIC tried to detect similar flares in the following four years but the subsequent hundred more hours of observations were unsuccessful. Besides Cygnus X-1, MAGIC pointed at two other microquasar candidates, whose results are presented in this thesis: Cygnus X-3 and Scorpius X-1. The most constraining Upper Limits (ULs) to the integral flux of these sources at the energy above few hundred GeV are provided. Further investigations are being planned to discover these sources at VHE in the next years.

After short introduction to astroparticle physics and VHE astrophysics, this thesis is di-

vided in three parts.
The first part is dedicated to the MAGIC telescopes (Chapter 2) and the standard analysis chain (Chapter 3). It describes the technical contributions the author made during her thesis work. In particular, the chapter about the MAGIC provides a detail description of the instrument in the context of its control system and an overview of the observation strategies and the online procedures. The author was the main responsible for the extension of the central control program to the system of two telescopes and for the online analysis.

The second part is devoted to PWNe. After a short introduction to the topic (Chapter 4), it presents the main topic of this part of the thesis, the Crab Pulsar Wind Nebula. Chapter 5 describes the observations of the Crab Nebula with the MAGIC stereoscopic systems and the resulting high-precision measurements of its differential energy spectrum and light curve. The last part of the thesis is dedicated to microquasars. It starts with a short introduction on this class of astrophysical source from both a phenomenological and theoretical point of view (Chapter 6). Finally the analyses and corresponding results of the MAGIC observations of Cygnus X-3 (Chapter 7) and Scorpius X-1 (Chapter 8) are presented. Particular attention is drawn on trigger strategy used in the observational campaigns of these transient sources. This is an issue of key importance for planning future observations.

1

The non-thermal universe

Cosmic rays are energetic charged particles originating from outer space, both in our Galaxy and in some extragalactic objects. By interacting with radiation and magnetic fields at the site of their production, they emit non-thermal radiation which spans from radio frequencies up to ultra-high-energies. This chapter provides a short description of the non-thermal Universe and the techniques which can be used to observe it. Particular attention is paid to the γ-ray astronomy and its main observational targets.

Much of classical astronomy and astrophysics deals with thermal radiation emitted by hot and warm objects such as stars, planets, and dust. However, at the beginning of the 20^{th} century higher energy phenomena were observed suggesting the existence of non-thermal radiation from the Universe. In 1912, Victor Hess discovered the Cosmic Rays (CRs) and in 1938 Pierre Auger proved the existence of Extensive Atmospheric Showers (EASs), cascades of particles initiated by primary CRs with energies above 10^{15} eV. Modern instruments reveal that the CR spectrum extends up to 10^{20} eV and beyond (§ 1.1). Such high energies cannot be produced in thermal processes unless they trace back to the very early stage of the Big Bang. Their production must be explained through other mechanisms.
In mid 20^{th} century the detection of radio-waves from the galactic plane (Staelin, D. H. & Reifenstein, III, E. C., 1968) and X-ray radiation from outside the solar system (Giacconi, R. et al., 1962), led to the identification of non-thermal mechanisms producing synchrotron radiation. The latter is emitted when high-energy electrons are deflected in magnetic fields (§ A.4.1). Other common non-thermal mechanisms are the Inverse Compton (IC) scattering of energetic electrons on seed photons (§ A.2.1) and the interaction of VHE protons (CRs) with ambient matter to produce hadronic showers.

The interest on the non-thermal phenomena increased when their important role to understand the evolution of the Universe was recognized. Non-thermal and thermal radiations provide similar contributions to the total energy balance of the Universe. In addition, since CRs carry the highest known energies, they offer the possibility of exploring fundamental

physics beyond the reach of terrestrial accelerators.

Non-thermal radiation can thus be studied either by observing CRs or electromagnetic radiation over wide ranges of the electromagnetic spectrum (from radio to γ-rays). However, since the charged particles of the CRs are deflected by randomly oriented component of the galactic magnetic field, they lose their directional information and impinge upon the Earth nearly uniformly from all directions. Therefore, the information they provide is only related to their energy spectrum and chemical composition, except for the highest energies (above 10^{20} eV) for which the charged particles are no longer bended by the magnetic fields. Apart from these extreme energies, astronomy can be carried out only by looking at neutral particles, *i.e.* γ-rays and neutrinos, which travel on straight paths. The production of these neutral messengers is always associated to the presence of accelerated charged particles which interact with radiation and magnetic fields. Thus, they can be used to study the sources of the CRs.

1.1 Cosmic rays

CRs are mostly constituted by protons and helium nuclei (98%), with a smaller amount of heavier nuclei, electrons, neutrinos and γ-rays.

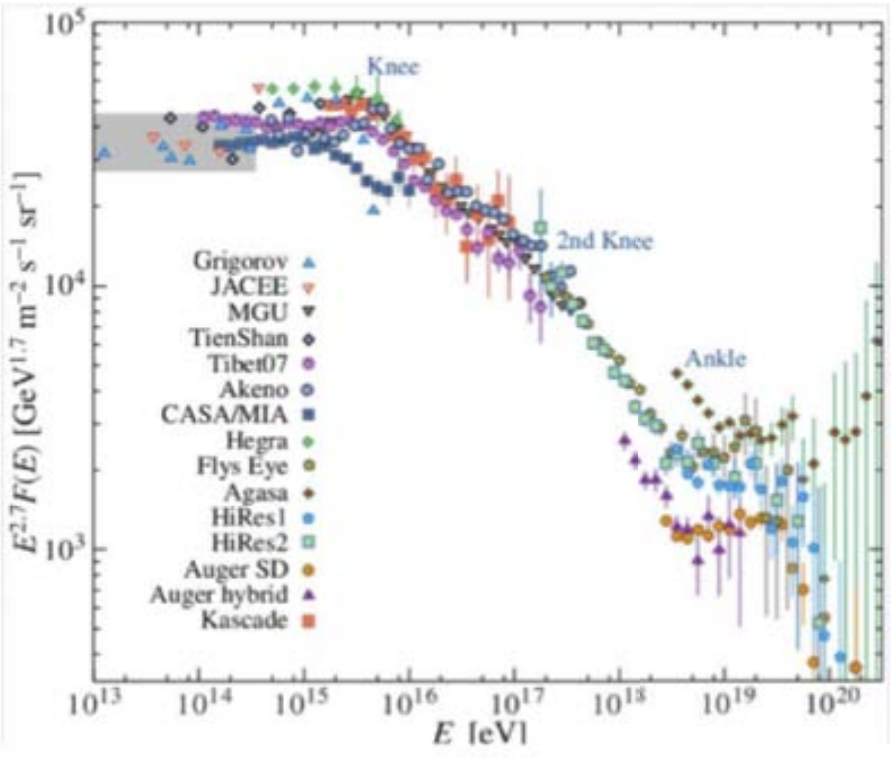

Figure 1.1: CR spectrum. following a broken power-law where the three power-laws are separated by the *knee* and the *ankle*. Note that the spectrum is multiplied by a power $E^{2\,7}$ in order to make the structures in the spectrum more visible. Taken from Halzen, F. (2010).

Figure 1.1 shows the CR spectrum. It covers 13 orders of magnitudes from 10^8 to 10^{21} eV. Particles with energy lower than 10^{10} eV come from the Sun, as the stellar wind prevents particles with that energy and coming from outside the solar system to reach the Earth. The

CR spectrum follows a broken power-law (dN/dE $E^{-\alpha}$ with α varying in sub-regions). The three power-laws are separated by two features known as the *knee* at $\equiv 3 \cdot 10^{15}$ eV (3 PeV) and the *ankle* at 10^{18} eV (1 EeV), respectively (Halzen, F., 2010). The spectral index changes from $\alpha = -2\,65$ to $\alpha = -3\,1$ and then it hardens back to $\alpha = -2\,7$. The changes in slope seem to be related to the different origin of the CRs: CRs below the *knee* are believed to be accelerated inside our Galaxy, whereas beyond the *ankle* they should have an extragalactic origin. This latter notion comes from the fact that protons with energies above 1 EeV have Larmor radii in the galactic magnetic field ($\approx$ 3–6 μG, Blumer, J. et al. 2009) which are too large to be contained, and so such particles must come from outside the Galaxy. On the other hand, the origin of the CRs in the intermediate region, between the *knee* and the *ankle*, still remains a mystery. There are different scenarios which try to explain the *knee* like changes of acceleration mechanisms (Stanev, T. et al., 1993) at the sources of CRs (supernova remnants or pulsar or unknown sources) or effects of due to propagation (Ptuskin, V. S., et al., 1993). All the models predict a change of the CR composition over the *knee*. As expected for acceleration proportional to the particle charge, the average mass of the particles increases after the *knee*. The KArlsruhe Shower Core and Array DEtector (KASCADE) collaboration reported that the *knee* might be due to the cut-off of light elements (Antoni, T., et al., 2005). Another important question about the CR spectrum concerns its natural end. The interaction between CRs and photons from the Cosmic Microwave Background (CMB)

$$p + \gamma_{CMB} \quad \Delta^* \quad p + \nu_0 \tag{1.1}$$
$$p + \gamma_{CMB} \quad \Delta^* \quad n + \nu^+ \tag{1.2}$$
$$\tag{1.3}$$

results in a cut-off of the spectrum at $4-6\times10^{19}$ eV. Its measurements by High Resolution fly's eye (HiRES) (Abbasi, R. U., et al., 2008) and Auger (Abraham, J., et al., 2008) experiments are in good agreement (Figure 1.2). Known as the Greisen-Zatsepin-Kuzmin (GZK) cut-off (Greisen, K., 1966), it limits the maximum distance that CRs of $E \equiv 10^{20}$ eV can travel to $\approx$ 50 pc.

The most direct information about CRs can be obtained by detectors above the atmosphere on stratospheric balloons or in outer space on satellites. They provided most of the known information about galactic CRs up to $10^{12} - 10^{14}$ eV. However, above those energies, other indirect techniques must be used to study CRs. They are all based on the fact that the showers of secondary particles, produced when primary particles interact with the Earth's atmosphere, are energetic enough to be detected from ground. Charge particles, like electrons and muons, can be observed with scintillator counters and water tanks, whereas hadrons can be registered in calorimeters. Alternatively, the Cherenkov light produced by the showers can be detected by imaging Cherenkov detectors. The exploration of the energies above 10^{16} requires detectors with areas larger than 1 km^2 (§ B). The real step forward was obtained at the highest energies by the Pierre Auger Observatory which, with its 3000 km^2 coverage in the Southern site allowed to measure the extragalactic CRs (§ **??**).

1.1.1 Galactic cosmic rays

Up to the *knee*, and possibly also between the *knee* and the *ankle* of the CR spectrum, the CRs are thought to have a galactic origin, *i.e.* to be accelerated within our Galaxy. Already in 1934 Baade, W. & Zwicky, F. (1934) suggested that SuperNovae (SNe) could be the source

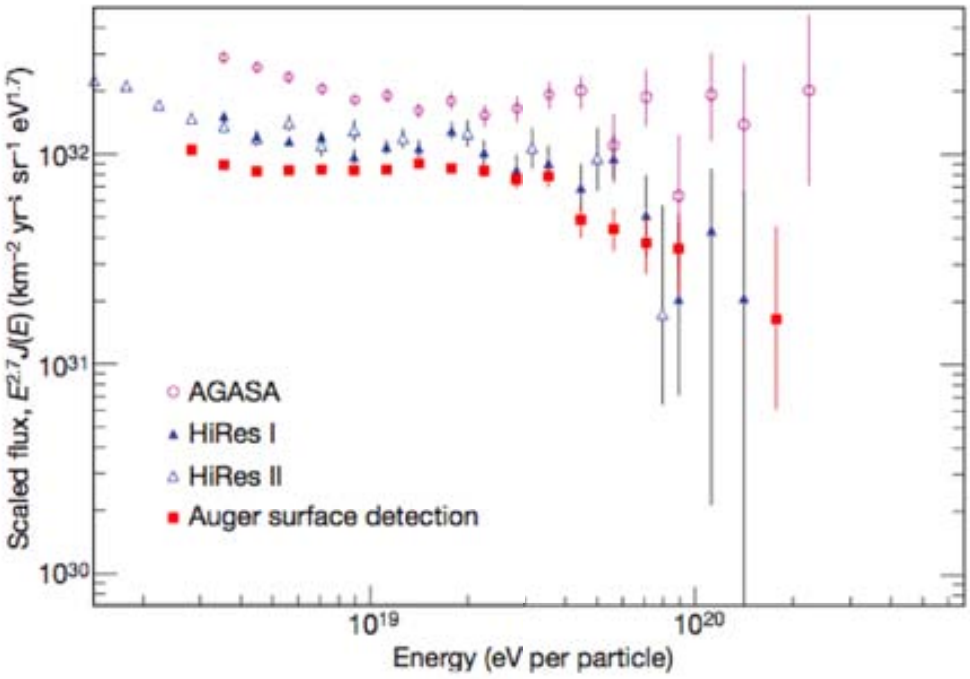

Figure 1.2: Measurements of the GZK cut-off. The results by HiRES and Auger experiments are in good agreement if one considers a 25% systematic error. The first measurement of the CR spectrum at such energies by AGASA shows a significant discrepancy. The CR spectrum is multiplied by the power $E^{-2\,7}$ to enhance the cut-off. Taken from Bauleo, P. M. & Rodríguez Martino (2009).

of galactic CRs provided that a substantial fraction of the energy released in the explosion is employed to accelerate relativistic particles. This notion was based on the assumption that particles can be accelerated in diffusive shocks occurring in SuperNova Remnants (SNRs) (§ 4.2) expanding into the InterStellar Medium (ISM).
Galactic CRs interacting with ambient material should generate γ-rays and neutrinos from the decay of secondary pions. These sources should be identifiable by a flat energy spectrum extending up to several hundreds of TeV. Referred to as Pevatrons, they have not been detected so far. Nevertheless, there are three sources detected by the Milagro experiment considered as possible PeVatron candidates: they show a power-law spectrum with a photon index of $\sim$ 2 and no cut-off up to few tens of TeV (Abdo, A. A., et al., 2007), in contrast with the spectra of the best-studied SNRs. In addition, up to now it has been impossible to identify γ-ray of pionic origin in the known SNRs. Detecting neutrino flux from any SNR would provide the definitive evidence that these are the sources of CRs. According to Gonzalez-Garcia, M. C. et al. (2009), if the Milagro sources are PeVatrons, IceCube will be able to reveal them as such at the 5 σ level in 5 years. The IceCube experiment showed an anisotropy at 5 σ level in the arrival time of CRs, mainly muons at a median energy of 20 TeV (Abbasi, R. U., et al., 2010). This anisotropy might either be associated to unknown structures of the galactic magnetic fields or diffusive particle flows from galactic sources. If this result will be confirmed, this might provide a new way to identify PeVatron sources.

1.1.2 Extra-galactic cosmic rays

There is no clear separation between the spectra of the galactic and extragalactic CRs, even though the *ankle* is considered as the partition marker. The mechanisms responsible for the acceleration of particles up to 10^{18} eV are still unknown. However, as CRs above these energies are no longer confined by the galactic magnetic field, it is natural to think that they are produced by extragalactic sources.

The scenario which is most generally credited with explaining such "extragalactic" component associate their origin to diffuse shocks in extragalactic astrophysical sources. For a given magnetic field, B, and size of the emission region, R, the maximum acceleration energy, E_{max}, is:

$$E_{max} \backsimeq 10^{18}\text{eV}\ Z\beta_s \left(\frac{R}{\text{kpc}}\right)\left(\frac{B}{\text{G}}\right) \tag{1.4}$$

where β_s is the shock velocity and Z the particle charge.

Given the above formula, the most plausible extragalactic astrophysical sources as sources of CR acceleration are (Figure 1.3):

- Active Galactic Nucleus (AGN) (§ 1.4) (Ahlers, M. et al., 2005)
- Gamma Ray Bursts (GRBs) (§ 1.4). Waxman, E. (1995) predicted that acceleration might take place during the formation of GRBs.
- Radio galaxy lobes (Figure 1.8)
- InterGalactic Magnetic (IGM) field

Alternatively, non-acceleration models have been proposed. They assume that the CRs of $E > 10^{18}$ eV are produced in decays of super-heavy particles as might be dark matter particles (Berezinsky, V. et al., 1997).

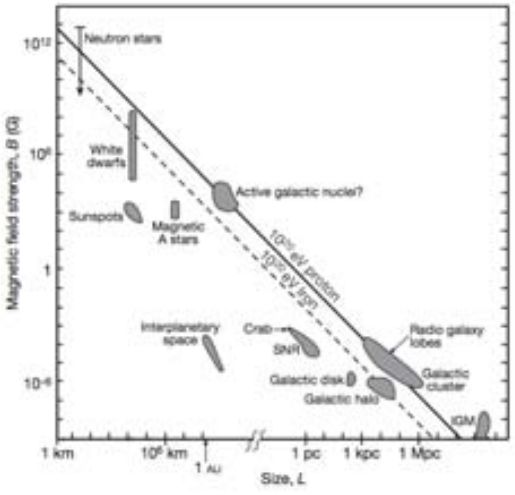

Figure 1.3: Hillas plot. It displays the magnetic field strenght, B, as a function of the size of the emitting region, L. The maximum acceleration energy $\propto L \cdot B$ is represented by the solid line. Only those sources above the solid line can accelerate particles in the GZK energy range. Taken from Bauleo, P. M. & Rodríguez Martino (2009).

1.2 γ-ray astrophysics

γ-ray astrophysics has proved very successful in the last century in studying the High-Energy (HE) particle of the non-thermal Universe. γ-ray astrophysics covers a large energy range: by convention its lower energy corresponds to the mass of the electron (0.5×10^6 eV), the minimum energy of γ-rays produced in electron-positron annihilation. γ-rays extend to the higher possible energies, which are effectively set by the observations of CRs (10^{20} eV), but theoretically there is no upper limit. Presently the energy region of γ-rays is explored rather inhomogeneously. So far primary γ-rays have been detected only in the *low* (MeV), *high*

(GeV) and *very* (TeV) HE domain. Nevertheless the existence of *ultra* (PeV) and *extra* (EeV), Ultra High Energy (UHE) and Extra High Energy (EHE) γ-rays is generally accepted. This classification in sub-bands of the γ-ray astrophysics is partially related to different acceleration mechanisms and distinct observational techniques (Table 1.1).

	energy range	**detector**	**detection mechanism**	**experiment**
low HE	$<$ 30 MeV	balloon	Compton Effect	
high HE	100 MeV – 50 GeV	satellites	Calorimeter	*EGRET, Fermi*
very HE (VHE)	50 GeV – 100 TeV	ground	Cherenkov	MAGIC,VERITAS, HESS Whipple, HEGRA, CANGAROO, Milagro
ultra HE (UHE)	100 TeV – 100 PeV	ground	Cherenkov	CASA-MIA
extra HE (EHE)	$>$ 100 PeV	ground	Cherenkov	HiRES, Auger

Table 1.1: Classification of the γ-ray astrophysics. From left to right: the energy range, the main type of detector, the detection mechanism and the principal experiments.

Since the Earth's atmosphere is not transparent to γ-rays, their direct detection is only possible through space-based experiments. However, the constraints on the maximum size and weight of the detector which can be hosted by a satellite result in relatively small effective areas (≤ 1 m^2). Therefore, space-based missions cannot observe astrophysical source at energies larger than some hundreds of GeV (depending on the mission lifetime). VHE primary γ-rays produce EASs which can reach the ground though; hence can be detected indirectly. The VHE band is explored by ground-based telescopes. Their huge detection ($-$ 1 m^2) areas can compensate the rapid decrease of the flux of astrophysical sources with the energies. However, given the high background induced by CR showers, the large detection areas alone cannot provide adequate sensitivity for effective study the CRs: ground-based detectors must have the capability of rejecting the CR induced showers.

γ-ray satellites use different detection techniques depending on the energy of the target γ-rays. Such an energy determines the dominant physical process:

- **0.1–0.3 MeV**: the dominant process is the photo-electric absorption. Detectors are instrumented with scintillator counters and solid state detectors.

- **0.5-30 MeV**: the dominant process becomes the Compton scattering, although the pair production cannot be considered as negligible. A typical Compton instrument consists of two separated detector layers where one of the two acts as *converter* and the other as *absorber*. The Compton scatter of the incoming γ-ray with an electron of the *converter* is followed by the photo-electric absorption of the scattered photon in the *absorber*. By measuring the position and the energy of the interactions, the event can be reconstructed and the direction of the primary γ-ray determined.

- **0.03–300 GeV**: the dominant process is electron-positron pair production. The detector consists of three parts: a *converter* where the primary γ-rays are converted to electron/positron pairs, a *tracker* which measures the lepton tracks, providing precise estimation of the primary γ-ray direction and of the energy loss, and finally a *calorimeter* which brings the leptons to rest in order to determine their remaining energy.

The γ-ray satellites usually have a very good background (CRs) rejection thanks to an *anti-coincidence* system which suppresses the charged particles which isotropically hit the detector.

The first γ-ray satellite, Explorer 11, was launched in 1961, but only the European Space Agency (ESA) mission COS-B (1975–1982) and the National Aeronautics and Space Administration (NASA) one SAS-2 provided the first detailed views of the γ-ray Universe (1972–1973). The first milestone of the γ-ray astrophysics was set by the Energetic Gamma-Ray Experiment Telescope (EGRET) experiment on board of the Compton Gamma-Ray Observatory (CGRO) (1991–2000). It revealed more than 270 galactic and extragalactic objects between 0.1 and 10 GeV. A step further in HE astrophysics was signed by the innovative *Fermi* satellite (formerly called GLAST), launched in June 2008. *Fermi* hosts two instruments: the Large Array Telescope (LAT) and the complementary GLAST Burst Monitor (GBM). *Fermi*/LAT is an imaging, wide Field of View (FoV), high-energy γ-ray telescope covering the energy range between 100 MeV to about 300 GeV (Atwood, W. B., et al., 2009), whereas the *Fermi*/GBM consists of 12 detectors sensitive to the range from 8 keV to 30 MeV. These 12 detectors are oriented in different positions of the sky providing nearly the full sky coverage. They are used to detect GRBs (§ 1.4).

There are two main types of VHE ground-based telescopes which have proved successful up to now. The principal ground-based γ-ray experiments are shortly presented in § B.1 and § B.2.

- **Air shower arrays**. They are arrays of detectors capable of detecting the particles in EASs. By measuring the arrival time of the shower front at the individual stations, the direction of the primary CRs can be estimated. In order to estimate the energy of the primary particle, the shower must be entirely contained within the complete detector. This leads to building big arrays in excess of 10^4 m^2. There are different techniques which allow for the EAS detection. The most direct one uses plastic scintillators coupled with muon detectors (*air shower particle arrays*). A more indirect technique is based on the detection of the Cherenkov light produced by the shower charged particles either travelling through the atmosphere (*atmospheric Cherenkov arrays*) or inside water tanks (*water Cherenkov arrays*). Other air shower arrays detect the air fluorescence produced by the EASs in the atmosphere (*air fluorescence arrays*).

  The first generation of air shower arrays mainly comprises *air shower particles arrays*. They are very inefficient detectors of γ-rays, as they can only sample the tail of the EAS at ground level and have hardly any handle to separate γ-rays from background CR. In addition, the sparse sampling leads to very high energy thresholds (> 50 TeV). None of this first generation of EAS arrays detected any γ-ray emitter. The substantial progress in lowering the energy threshold, achieved by the second generation, was obtained either by increasing the sensitive detector area or building the detector at much higher altitude. The first approach was followed by the Milagro collaboration, whereas the second by the Tibet AS$_\gamma$ array located at 4300 m above sea level (asl).

- **Atmospheric Cherenkov telescopes** (IACTs). An energetic γ-ray on hitting the Earth atmosphere, initiates an EAS, with a typical shower maximum around 8–12 km asl. The shower charged particles, mostly electrons and positrons, emit Cherenkov light when their speed exceeds that of the light in the atmosphere. This light, beamed along the direction of the incident γ-ray, illuminates nearly uniformly a dish of $\equiv 120$ m radius on the ground. If a telescope is located within the Cherenkov light pool, it can collect part of this light and focus it onto a $\equiv 3$–5° FoV camera composed of Photo Multiplier

Tubes (PMTs). These photon detectors are capable of resolving the images of the showers which have a typical angular extension of $\sim 0.5°$. An image reconstruction algorithm allows the determination of the main parameters of the primary particles, such as energy and incoming direction.
The exploration of this technique occurred in the 90s, when the pioneering Whipple telescope, with a 10 m diameter reflector, reported the detection of the Crab Nebula as the first VHE astrophysical source (Weekes, T. C., et al., 1989). In the following years, other experiments, High Energy Gamma Ray Astronomy (HEGRA) (Aharonian, F. A., et al., 2000), Collaboration of Australia and Nippon for a GAmma-Ray Observatory in the Outback (CANGAROO) (Tanimori, T., et al., 1998) and Cherenkov Atmospheric Telescope (CAT) (Barrau, A., et al., 1997), confirmed the success of the technique discovering a ten of VHE sources, mainly nearby AGNs. The second generation of IACTs offered an order of magnitude improvement in flux sensitivity and a significant reduction of the energy threshold down to some tens of GeV. In the last seven years, with the HESS, MAGIC and VERITAS telescopes in operation, the number of VHE sources reached 100, and they represent different galactic and extragalactic source populations (§ 1.4).

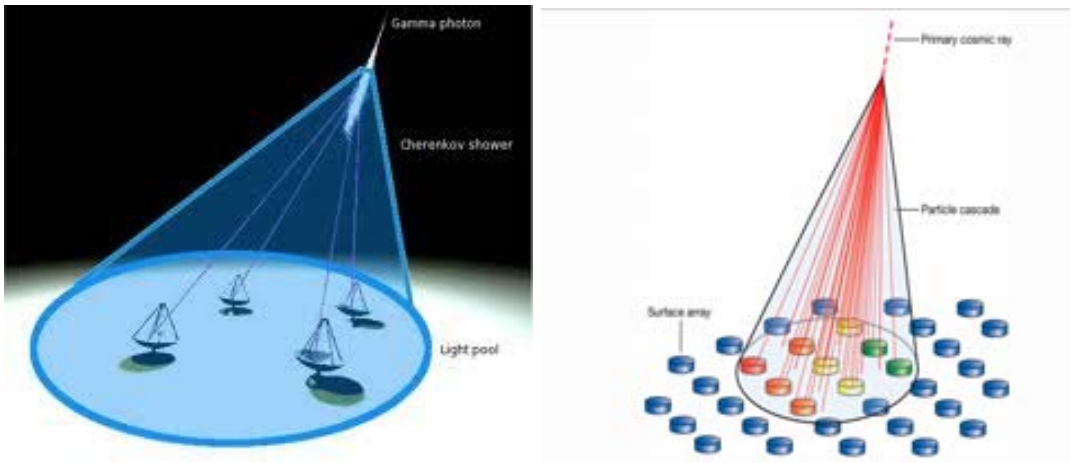

Figure 1.4: Sketch of detection techniques in VHE γ-ray astrophysics. *On the left:* the atmospheric Cherenkov technique; *On the right:* the scheme of the EAS arrays.

Each of the above-mentioned types of ground-based telescopes has advantages and disadvantages. IACTs have better angular and energy resolutions than air shower arrays. On the other hand, they are optical instruments which operate only during dark time or under moderate moonlight conditions and have a small FoV, whereas air shower arrays continuously scan the "entire" sky. These complementary features define different roles for the two category of detectors. IACTs are perfect instruments for morphological and spectral studies of TeV sources with a limited extension. While air shower arrays can monitor the whole sky for strong transients.

Despite the results obtained by the current instruments are already impressive, an order of magnitude improvement in the entire VHE domain can lead to the discovery of many other TeV-emitter, and above all to deeper studies of spectra and morphologies of the known sources. This is the goal for the next generation ground-based γ-ray detectors and it yielded the construction design of the world-wide project, Cherenkov Telescope Array (CTA): an array

of tens of telescopes. The design scenario foresees three types of telescopes with different mirror sizes in order to cover the entire energy range from 10 GeV up to 100 TeV (CTA Consortium, 2010). Figure 1.5 shows the sensitivity for the current IACTs compared with the one expected for CTA.

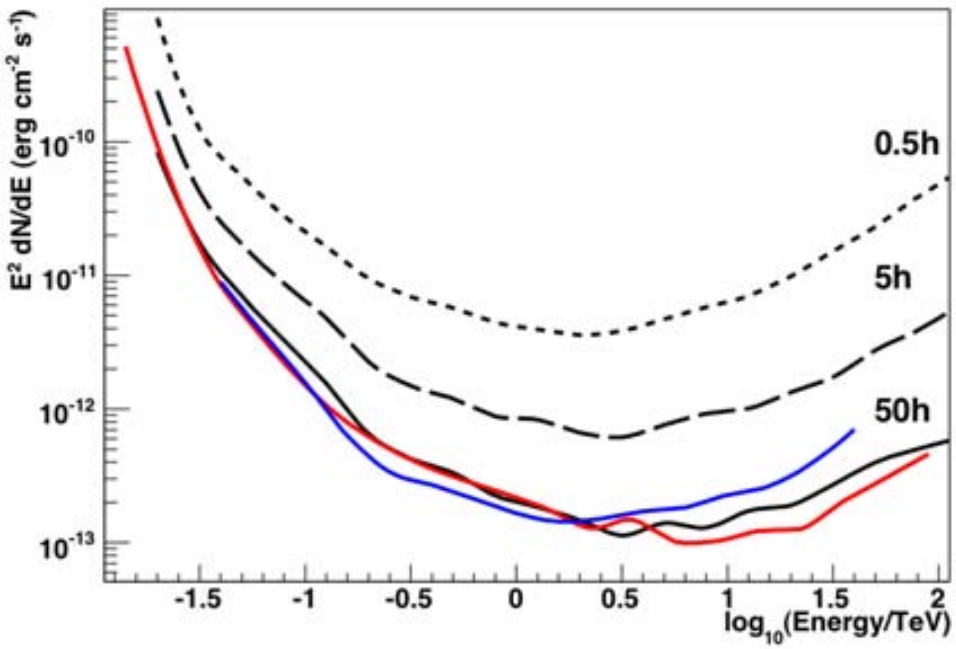

Figure 1.5: The differential sensitivity expected for CTA. The black lines show the sensitivity of the design concept for different observation times. Colorful lines illustrate the sensitivity obtained with different analysis methods. Taken from CTA Consortium (2010).

1.3 Neutrino astrophysics

Neutrino astrophysics in the energy range of MeV is well established. It has led to the observation of solar neutrinos and neutrinos from the supernova SN1987A (Hirata, K. et al., 1987). On the other hand, higher-energy neutrinos, GeV-neutrinos, have not been detected so far. Given their very weak signals, the sources of background, mainly muons and neutrinos produced by CRs in the Earth's atmosphere, must be reduced as much as possible. For this reason, neutrino detectors are built deep underground or underwater. However, since underground detectors have turned to be too small to detect the expected neutrino fluxes, the new frontier of the high-energy neutrino astrophysics is led by much larger arrays built in open water and ice. These instruments consist of PMTs detecting the Cherenkov light from charged particles produced by neutrino interactions (Figure 1.6).

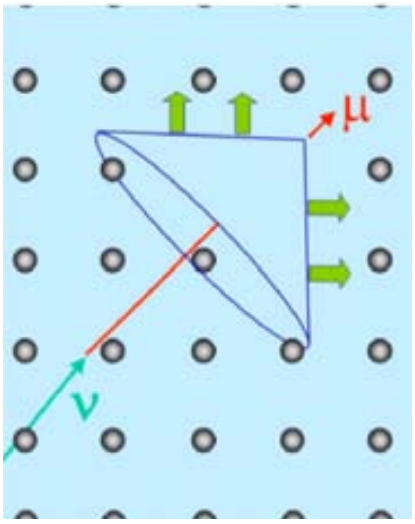

Figure 1.6: Sketch of neutrino telescopes.

Since the Cherenkov radiation produces a strong signal in water and ice, the energy threshold of these detectors is as low as some tens of GeV. This low energy threshold and the fact that the Sun and nearby SNe produce very high fluxes of neutrinos lead to the detection of a large amount of atmospheric neutrinos. These atmospheric neutrinos constitute an important source of background, but, on the other hand, they allow for signal calibrations. The new generation of neutrino telescopes can reach energies as high as $10^{13} - 10^{14}$ eV. With the inaugurations of the 1 km^3 IceCube array in the South Pole on April 28, 2011, a new era for the neutrino astrophysics has begun (§ B.3).

1.4 Astrophysical sources

Established TeV γ-ray emitters are:

- **Pulsars**, rapidly rotating and highly magnetized Neutron Stars (NSs). The accelerated particles near the pulsar are beamed out the magnetosphere along the magnetic axis. Since the rotation and magnetic axes of the pulsar are not aligned, the observer see the pulsar's emission only when the beam crosses his line of sight. Pulsars can produce γ-ray emission. Many of them have been detected below few GeV (Abdo, A. A., et al., 2010b). The mechanisms of such radiation are still poorly understood. Only recently VHE radiation from the Crab Pulsar has been detected (Aliu, E., et al., 2008; Otte, N., 2011) establishing the pulsar as another class of VHE source population. They will be discussed in detail in § 4.1.

- **SNRs**. A SNR is the leftover of a SuperNova (SN) explosion. The remnant consists of the material ejected by the explosion and the ISM it sweeps up along the way. In interactions with the lower density ISM, the remnant creates shock waves. Particles are accelerated in these shocks through the Fermi acceleration mechanism (§ A.1). The ultra-relativistic particles produced in the shock emit synchrotron radiation up to several

hundreds of MeV, and higher-energy emission by IC scattering. Prominent detected SNRs emitting VHE are: Cas A (Aharonian, F. A., et al., 2001; Albert, J., et al., 2007b), IC 433 (Albert, J., et al., 2007a), RX J1713.7–3946 (Aharonian, F. A., et al., 2006c), Vela X (Aharonian, F. A., et al., 2006d).

- **Pulsar Wind Nebulae (PWNe)**. A PWN is a bubble of relativistic particles and magnetic fields created when the relativistic pulsar wind interacts with the ambient medium, either the SNR or the ISM. In this interaction particles are accelerated up to ultra-relativistic energies. These particles, mainly electrons, are an efficient source of VHE γ-rays by IC scattering with ambient photons. The archetypal PWN is the Crab Nebula, which is the brightest VHE steady VHE source in the Northern sky. PWNe are the main topic of Chapter 4.

- **γ-ray binary systems**. They are galactic binary systems whose dominant emission is in the γ-ray energy band. They consist of a compact object, either a NS or a Black Hole (BH) orbiting around a massive star. Two main scenarios can explain the observed VHE emission: either wind/wind interactions in the pulsar binary scenario or accretion in the microquasar scenario. In a pulsar binary system, the compact object is a rotating NS and the pulsar winds interacting with the stellar wind can originate shocks where particles are accelerated. These ultra-relativistic particles IC scattering with the stellar photons produce the observed VHE radiation. In the microquasar scenario, the compact object accretes matter from the companion star creating an accretion disk. The latter ejects relativistic jets containing ultra-relativistic particles which can produce VHE γ-rays. These systems will be discussed in detail in Chapter 6.

- **Galactic center**. The center of our Galaxy was established as a steady VHE photon emitter (Aharonian, F. A., et al., 2006a; Albert, J., et al., 2006a). It is a very crowed region, possibly containing SNRs, PWNe and/or BHs (like Sgr A*). The origin of the VHE emission might be related to one or more of these source populations.

- **AGNs**. An AGN is a galaxy hosting a super-massive BH ($\leq 10^6$ $M_\odot$) in its center.

  According to the *unified AGN model* (Urry, C. M. & Padovani, P., 1995) the BH is surrounded by an accretion disk and fast moving clouds which emit Doppler-broadened lines. In around 10% of the AGNs, the in-falling matter turns into powerful collimated relativistic jets orthogonal to the galaxy plane. Figure 1.7 shows a sketch of an AGN.
  The observed properties of the AGNs mainly depend on the viewing angle of the observer, the accretion rate and the mass of the BH. AGNs are classified using optical and radio observations (Figure 1.8). AGNs which have low optical luminosity are called *Seyfert galaxies* and *radio galaxies*. The more powerful AGNs in the optical and are the *radio quasars* and *BL Lac*. When the jet of this loud optical AGNs is aligned with the line of sight of the observer, they are called *blazars*. A more detailed classification can be found in Figure 1.8.

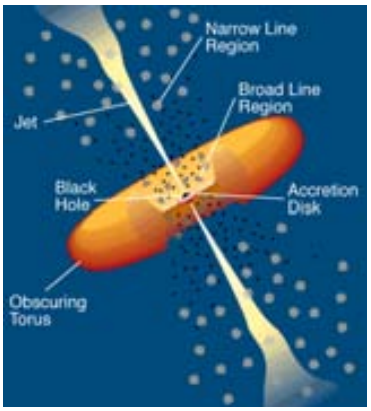

Figure 1.7: Sketch of an AGN.

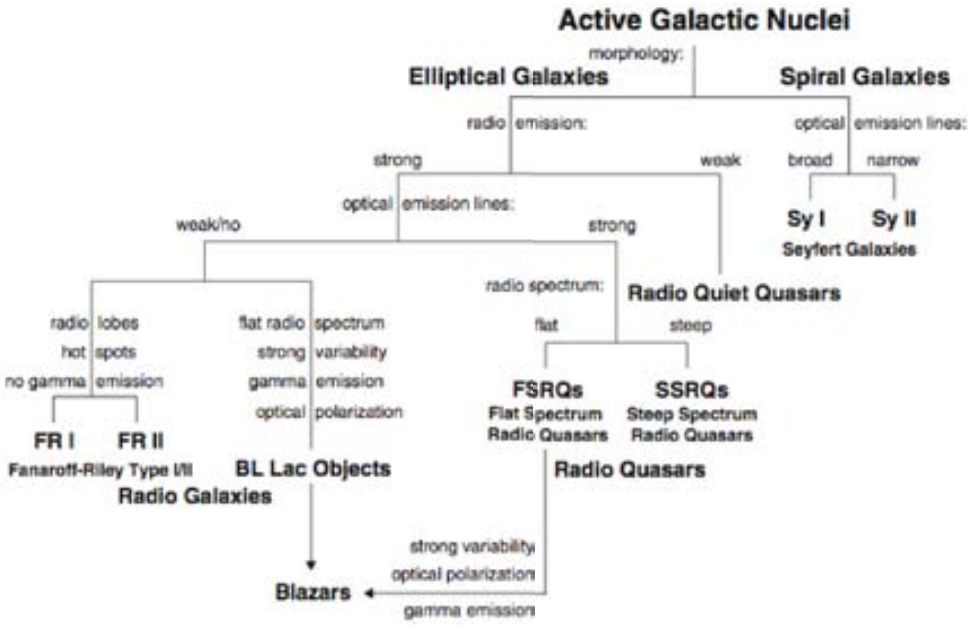

Figure 1.8: Classification scheme for AGNs. Taken from Mazin, D. (2007).

- **starburst galaxies**. A starburst galaxy is a galaxy with an exceptionally high rate of star formation. As a result, the rate of SN explosions in these galaxies is much higher than usual: ~ 1/year. This guarantees both the mechanism of acceleration of particles at SNR shocks and a large amount of seed photons for IC scattering and consequent production of VHE γ-rays. The prototypes of the starburst galaxies are M82 which has been detected by VERITAS above 700 GeV (Acciari, V. A., et al., 2009), and NGC 253 discovered by HESS (Acero, F., et al., 2009a).

- **GRBs**. A GRB is a sudden very short and intense γ-ray outburst of extragalactic origin (average $z = 2.3$–2.7). GRBs, observed at a typical rate of one per day, are isotropically distributed in the sky (Figure 1.9). Up to now the origin of GRBs is still unknown and they are believed to be originated from two possible different progenitors:

  – the sudden catastrophic collapse of rapidly rotating very massive stars ($M > 100$ $M_\odot$)

  – the merger of two compact objects

  Two different origins are considered because there are two distinct families of GRBs: a long duration (> 2 s) one, possibly related to the first class of progenitors with lower energies, and a short duration (< 2 s) one, related to the latter class. A GRB is typically characterized by a prompt emission mainly emitting in the soft γ-rays followed by a so-called afterglow emission. The latter is observed at all wavelengths from X-rays to radio frequencies and it can last from hours to weeks. The prompt emission is usually so intense that almost over-shine the entire sky in γ-rays. It is interpreted as the result of the growth of huge relativistic jets. No GRBs have been detected in the VHE band so far. Nevertheless, they are still considered as interesting targets for this branch of astrophysics because many models predict VHE emission during the prompt and the

afterglow phases.

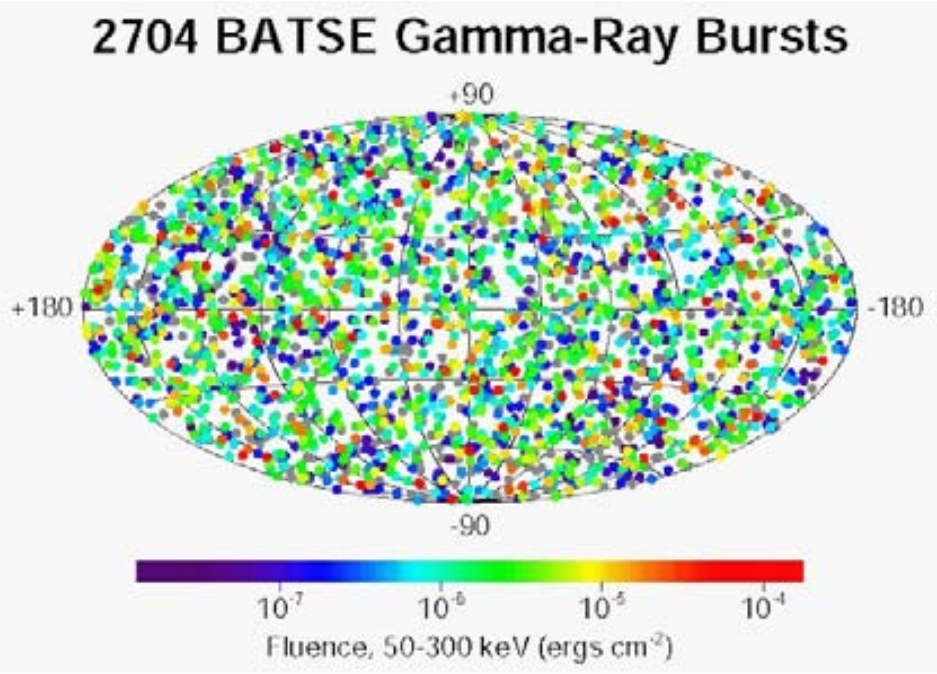

Figure 1.9: GRB sky as seen by BATSE. In 1991–2000, BATSE detected 2074 GRBs, much more than ever previously recorded.

PART ONE

THE MAGIC DETECTOR
and
DATA ANALYSIS

.

2

The MAGIC Telescopes

The two MAGIC imaging atmospheric Cherenkov telescopes, designed for the detection of very high energy γ-rays, are operating in stereoscopic mode since Autumn 2009 after the commissioning of the second telescope. Located in the Canary island of La Palma, they both consist of a 17 $\oslash$ parabolic reflector dish focusing the collected Cherenkov light onto a pixelized camera. The very large reflective surface permits to lower the detector energy threshold, as well as the use of an ultra-fast 2GSample/s readout system. The main technical characteristics of the MAGIC telescopes are described in this chapter with a particular stress on the upgraded version of the MAGIC I clone, called MAGIC II. The chapter follows the logic of the control system which breaks the telescopes up in autonomous functional units, called subsystems. It ends with the description of the central control program, which allows to control and monitor all the subsystems, and a short description of the main online procedures.

The author has been responsible for the central control program since the end of 2007. She followed the commissioning of the second telescope in Summer 2008 during which she was in charge of adapting the existing control program to the stereoscopic system (Zanin, R. & Cortina, J., 2009; Cortina, J., et al., 2010). The stereo data taking is detailed described in the *data operation manual* (Cortina, J. & Zanin, R., 2011). The author has been responsible also for the online analysis of MAGIC I mono data (Zanin, R. et al., 2008).

2.1 Introduction

The MAGIC telescopes are two 17 m diameter imaging atmospheric Cherenkov telescopes (IACTs). They are located in the Canary island of La Palma (28° 45' N, 17° 54' W, 2225 m above sea level) at the Roque de los Muchachos observatory. The first telescope MAGIC I started operations in stand-alone mode in 2004. MAGIC became a stereoscopic system in Autumn 2009 when the second telescope, MAGIC II, completed the commissioning phase.

The MAGIC telescopes make use of the imaging Cherenkov technique (§ 1.2) to detect VHE γ-rays. They were designed to decrease the energy threshold of the previous generation of IACTs allowing the exploration of the lowest region of the VHE band between 30 and 100 GeV. In the three years of operation before the advent of the *Fermi* satellite, in June 2008, MAGIC I was the only instrument capable of studying such energy range (Albert, J.,

Figure 2.1: The MAGIC stereoscopic system of telescopes. On the left MAGIC I , operating since 2004. On the right, MAGIC II ended its commissioning phase in Autumn 2009. On the back ground , the Gran Telescopio Canarias, a 10.4 m ⊘ optical telescope also located the Roque de los Muchachos observatory.

et al., 2008d,e; Aliu, E., et al., 2008). The optimization of the energy threshold required to improve and often pioneer key technological aspects of the IACT technique. The low density of Cherenkov light at ground for low energy showers makes their detection more difficult. Since less light is available, a low energy shower can easily be confused with fluctuations of the Night Sky Background (NSB) light. Thus, its detection depends on the signal-to-noise ratio of the telescope. Following Aharonian, F. A. et al. (2008), this latter quantity is proportional to the square root of the reflective area, A, times the light detection efficiency (including the mirror reflectivity and the PMT efficiency), ϵ, and inversely proportional to the square root of the signal integration time, θ, and the solid angle of the pixels, Ω. Therefore, the energy threshold, E_{th}, can be expressed by the following equation:

$$E_{th} \equiv \overline{\frac{\Omega\,\theta}{A\epsilon}} \tag{2.1}$$

This equation explains why the MAGIC telescopes were designed to have the largest reflector in the world (even though, at the time of writing this thesis, HESS II, a 28 m diameter IACT is under construction), high efficiency PMTs, and a fast readout electronics to minimize the NSB light integration time. The specific technical advances will be discussed in the following sections as the main parts of the detector are described.
A 17 m diameter reflector allows the reconstruction of primary γ-rays above 70 GeV (zenith angle dependent) (Albert, J., et al., 2008d), and the construction of the second telescope provided a further improvement of the instrument energy threshold down to 50 GeV (Aleksić J., et al., 2011b). However this is mainly due to the enhancement of the sensitivity as a result of the stereoscopic approach.

Moreover, the exploration of the lowest region of VHE paved the way for the ground-

based detection of γ-ray sources at large cosmological distances. This is because the pair attenuation of γ-rays, which can inhibit their propagation, is less efficient in this energy range. Subsequently the improved prospects of detecting GRB, extremely energetic and short lived explosions occurring mostly at large redshifts, made this search one of key MAGIC science goals. Since the life time of a GRB is estimated to span between 10 s and 100 s (Paciesas, W. S., et al., 1999) following-up GRB alerts, coming from satellites, implies that the telescope should be repositioned within some tens of seconds. Therefore, a powerful drive system together with a light structure became important requirements in the telescope design, which led to the use of an innovative light-weight, high-rigidity material for the telescope frame construction.

MAGIC II, thought of as a clone of the first telescope, was constructed to improve the instrument's sensitivity. The stereoscopic approach permits to reconstruct more precisely the image parameters which disentangle a gamma shower from a background one, enhancing the background suppression. Being built when MAGIC I operation was already well understood, the design of MAGIC II was modified in many aspects in order to improve its performance.

2.2 Telescope subsystems

Each telescope can be broken up in different functional units, called **subsystems**. The list below shows all the possible *tasks* of an IACT with the involved hardware/mechanical elements and the corresponding subsystems (according to MAGIC naming).

- The *telescope movements* are handled by the **drive system** operating the telescope frame.
- The *light collection* requires a reflective surface (reflector) made up of mirror tiles which, in the particular case of MAGIC, can be re-oriented depending on the telescope's elevation angle. This mirror adjustment is performed by the **active mirror control** subsystem.
- *Cherenkov photons* are *detected* using PMTs which are hosted inside the **camera**.
- The *calibration* of the instrument which allows the computation of the conversion factor between digital signals and physical quantities. The **calibration system** makes use of a set of Light Emitting Diodes (LEDs).
- The *data* are *digitized* in a set of electronic boards which convert the PMT analog signals into digital ones and prepare them for the final data storage. This is the function of the **readout subsystem**.
- The *on-line event selection* is electronically performed by the **trigger system** which discriminates between events from EAS and NSB light. Thus, it indicates if it is worth or not to record a detected event.
- The *data storage* is done by the **data acquisition system** which records the acquired data to disk in order to be analyzed o ine.

Moreover, there are the so-called **common subsystems** which do not constitute any functional part of the telescope, but simply collect information useful for the data taking, such as weather conditions (by the **weather station**, and the **pyrometer**), GRB alerts (by the **GRB alert program**), etc.

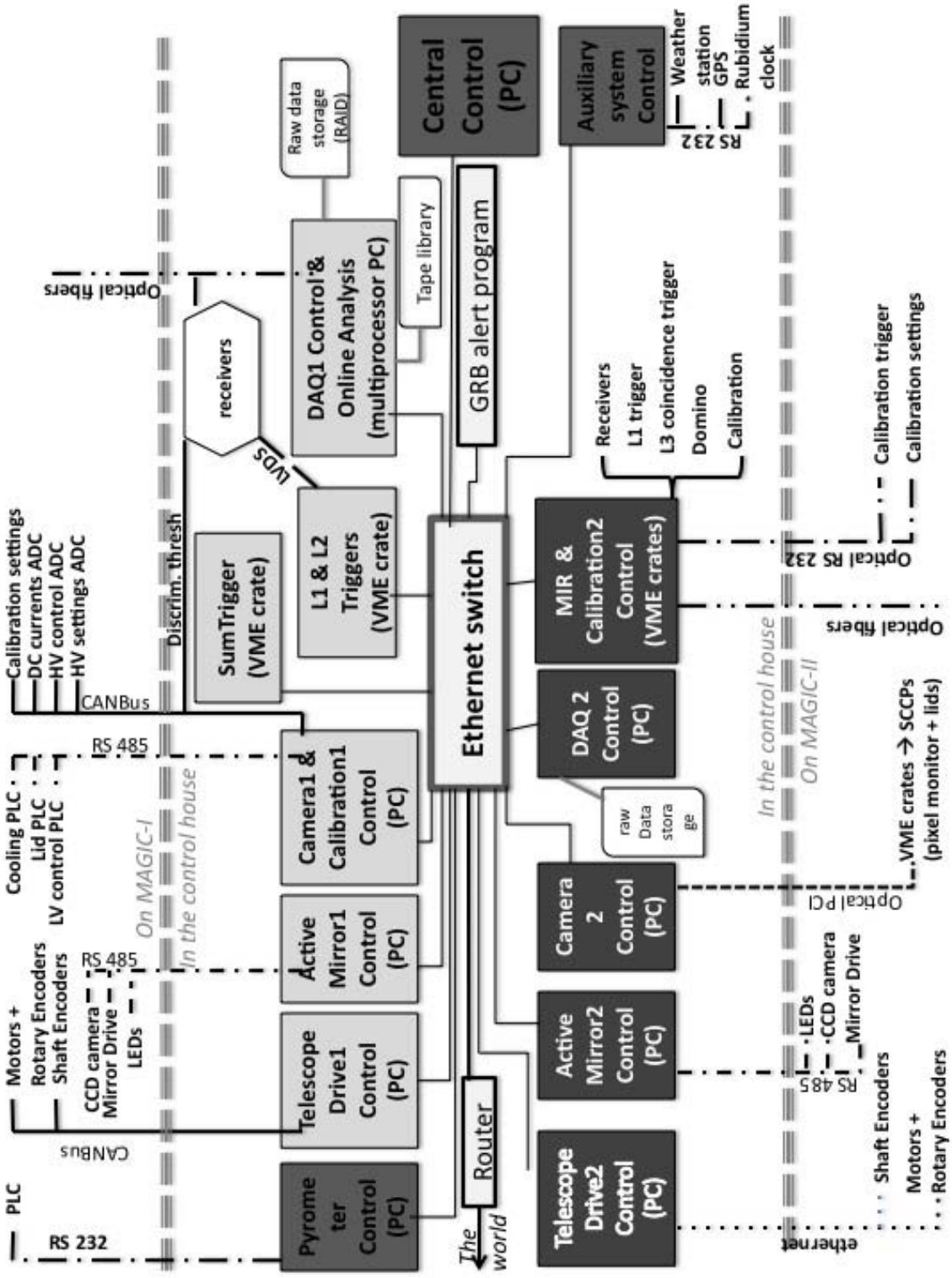

Figure 2.2: Outline of the central control scheme. The CC program interacts with each subsystem control program coordinating the data taking and providing the user a friendly interface to operate the telescopes.

Each subsystem is controlled via software by a control program installed in a Personal Computer (PC) in the counting house. Each control program can be run by the operator in stand-alone mode, or remotely by the CC program. The latter, communicating via Ethernet with all the subsystem programs, can coordinate their actions, thus automatizing the data taking procedure and providing the user with a graphical interface for instrument operation. Figure 2.2 shows the outline of the MAGIC control system.

In the following, the different subsystems will be described in detail, emphasizing, for each of them, the differences between MAGIC I and MAGIC II .

2.2.1 Frame and drive system

The telescope frame satisfies three main requirements: 1) it is large, 2) it is light-weight, 3) it is stiff. The first requirement is meant to guarantee a low energy threshold, the second one a fast repositioning, and the third a good image quality since it avoids deformations of the reflector. The space frame is a three-layer structure made of low-weight carbon fiber-epoxy tubes joined by aluminium knots (Figure 2.3), with a total weight of 5.5 tons (less than a third of an equivalent steel structure). According to the specifications the maximum deformation of the structure, for any orientation of the telescope, is below 3.5 mm, confirming the high rigidity of the chosen material (Bretz, T. et al., 2009). The carbon fiber-epoxy is also especially resistant to the harsh atmospheric conditions of the MAGIC site[1].
The camera PMTs, located at the focal distance of ≡17 m, is carried by a single tubular arch (Figure 2.3), and stabilized by thin steel cables anchored to the main dish structure. Nevertheless, small bendings of the structure, due the weight of the camera (≡ half a ton), are unavoidable during the telescope tracking, but can be corrected by an automatic system of mirror re-orientation (§ 2.2.3).

The telescope mount makes use of the alt-azimuth drive to track sources during large exposures, like most of the optical telescopes. The allowed motion in azimuth spans from -90° to +318° and the range in elevation spans from -70° to +90°. The drive mechanism has two drive chains controlled by synchronous motors with gears which are linked to the chain sprocket wheels (Figure 2.4). The azimuthal drive chain is fixed on a circular railway rail of 20 m diameter, and it is moved by two motors. The elevation drive chain with just one motor is mounted on a slightly oval ring below the mirror dish which forms integral part of the camera support must structure. For safety reasons this chain is equipped with an extra brake, operating as holding brake. The azimuth and elevational movements are regulated by individual programmable micro controllers dedicated to analog motion control, called MACS.

The pointing of the system is constantly cross-checked by a feedback pointing system which consists in three shaft-encoders (one on the azimuth axis and two at the opposite sides of the elevation axis) evaluating the angular telescope position with a 14-bit precision/360°. These measurements compared with the positions readout by the motors themselves can be used to estimate the intrinsic mechanical accuracy of the pointing system. Bretz, T. et al. (2009) showed that this accuracy for the 80% of the time is much better than 1' on the sky (a fifth of a pixel diameter).

In MAGIC I , the control program of the drive system communicates with both the encoders

[1]Temperatures below 0° C are typical at the MAGIC site in Winter, whereas the frame su ers under strong solar irradiation in Summer.

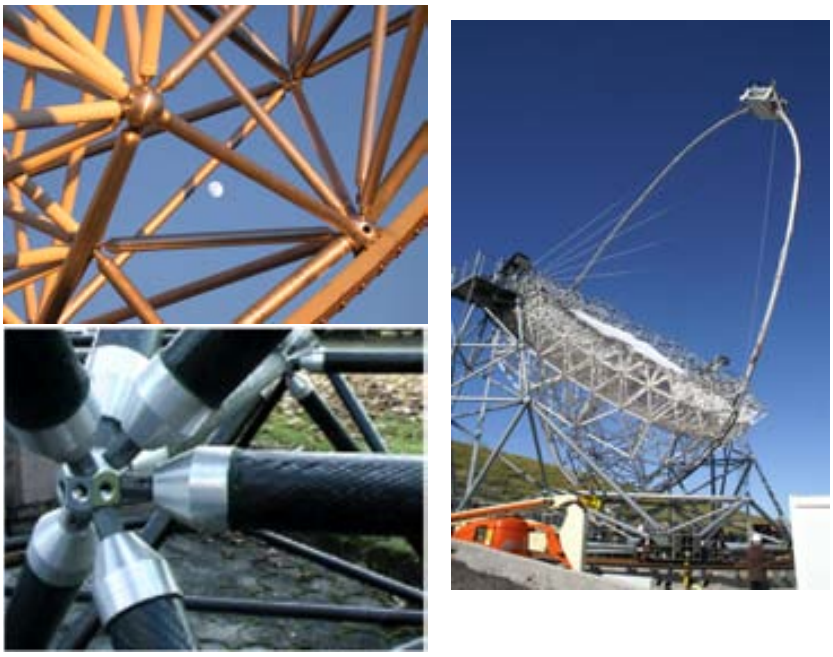

Figure 2.3: The telescope mount. *On the left:* two pictures of the carbon fiber-epoxy tubes and an Aluminium knot junction. *On the right:* a picture of MAGIC II where the frame structure and the mast holding the camera are visible (before the complete mirror installation).

and the MACS through a CANbus protocol. During MAGIC II construction many mechanical parts of the drive system were replaced by better performing ones, especially for what regards the communication protocols. The main upgrades are:

- The two MACS were replaced by a single professional Programmable Logical Controller (PLC) which communicates with the software control program via Ethernet.
- Absolute 13-bit shaft-encoders with a better resolution were installed. They are read out by an Ethernet interface.

The use of the PLCs, instead of MACS makes the hardware and software maintenance much easier. This was the main reason for which MAGIC I drive system was also upgraded in May 2009. Now the two drive systems are exactly two clones.

Pointing models

In order to account for the constant deformations of the mechanical structures, the tracking software employs analytical pointing models, which are updated every few months. These models, also called *bending models*, are based on the *TPoint*™ telescope modeling software[2]:

[2] *http://www.tpsoft.demon.co.uk/* by Wallace, P. M.

a) A detail of the azimuth drive chain and the azimuth rail

b) Azimuth motor sitting on a 2-wheel bogey

c) Elevation motor

d) Telescope support central axis

Figure 2.4: The drive system. a) the azimuth drive chain where the azimuth circular rail is visible. b) one of the two azimuth motors. c) the elevation motor mounted on its rail. The orange dish on the motor is the brake. d) the telescope support central axis.

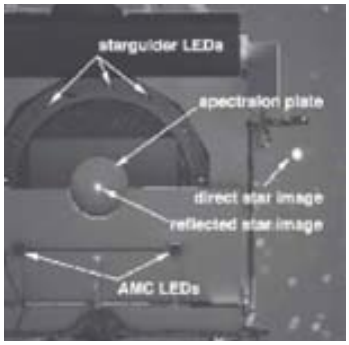

Figure 2.5: *TPoint* picture taken with the SBIG camera. Taken from Garczarczyk, M. (2007).

each possible source of mechanical deformation is described by a separate term in the model analytical function, and the corresponding coefficient is determined from the positions of at least 50 bright stars. These positional measurements are carried out by taking *TPoints* pictures of the star images reflected on the inferior camera lid, as shown in Figure 2.5. The superior lid is open to keep in the figure the reference LEDs of the starguider system (§ 2.2.1). This position of the lids is known as *TPoint mode*. The picture is taken with the Santa Barbara Instrument Group (SBIG) camera, a high sensitivity Charge-Coupled Device (CCD) camera integrated in the Active Mirror Control (AMC) (§ 2.2.3).
The definition of a good bending model needs many *TPoints* and uniformly distributed over the sky.

2.2.2 Starguider system

The starguider system is powerful tool for the determination of the relative mispointing. Its concept relies on the observations of bright stars in the FoV used as "guide stars". Possible offsets are obtained by comparing the observed star positions with the catalogue ones. However, the quality of such mispointing measurement depends on the sky visibility, hence atmospheric conditions. Thus, the starguider reliability is defined by the ratio between the number of observed stars and the number of expected stars.

The starguider system uses a high sensitivity CCD camera equipped with a Schneider-Kreuznach Xenoplan 1.9/35mm wide-field lens (more information in Wagner, R. (2006)). This camera is read out at a rate of 25 frames per second using a frame grabber connected to the PC of the drive system. Since the drawback for the high sensitivity is the high noise level, good quality images can be obtained only by averaging many (typically 125) single shots (Figure 2.6). The software in charge of the picture managing is implemented into the drive system control program.

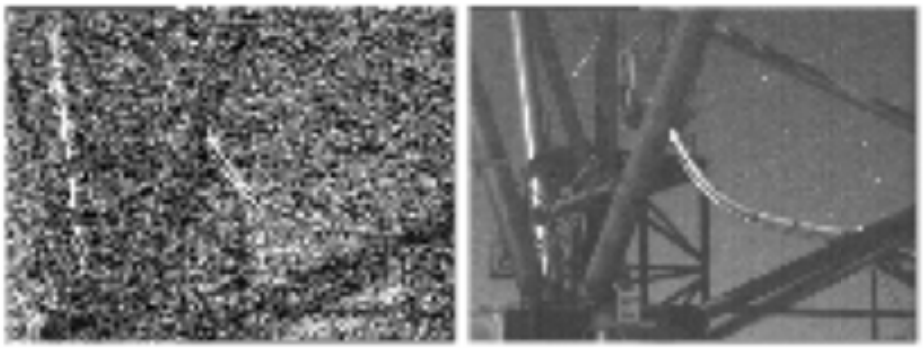

Figure 2.6: Pictures taken with the starguider CCD camera. *On the left:* a single shot picture showing the high noise level; *On the right:* picture obtained averaging 125 single shots.

The CCD camera is mounted in the center of the reflector dish. Given its 6.2° FoV, it simultaneously observes part of the PMT camera and the sky position the telescope is pointing at (Figure 2.7). In addition the starguider system includes a set of dim LEDs installed on the PMT camera. They provide a reference frame which is necessary for the mispointing determination.

2.2.3 Reflector

The 17 m diameter reflector follows a parabolic profile which allows to preserve the temporal structure of the shower light flashes. This information is important to reduce the number of accidental triggers due to NSB light, and thus to improve the signal to noise ratio, as demonstrated in Aliu, E., et al. (2009). For such a large reflector, the time spread between photons hitting the center and photons hitting the edges of the mirror surface is non-negligible. Therefore, the solutions used by the other IACTs, such as a Davies and Cotton mounting spherical reflector (Davies & Cotton, 1957), which performs even better than a parabolic reflector for small size telescopes (Lewis, 1990), would never work for a large diameter telescope like MAGIC. For example, a spherical reflector of 17 m diameter would introduce a time delay of tens of ns which is much more than the duration of a Cherenkov pulse would spoil the shower time structure.

The parabolic reflectors of both MAGIC telescopes are tessellated in 247 individually movable 1 m^2 mirror panels covering a total surface of 234 m^2[3]. These panels can be re-

[3]The mirror panels at the edges of the surface are smaller than 1 m^2.

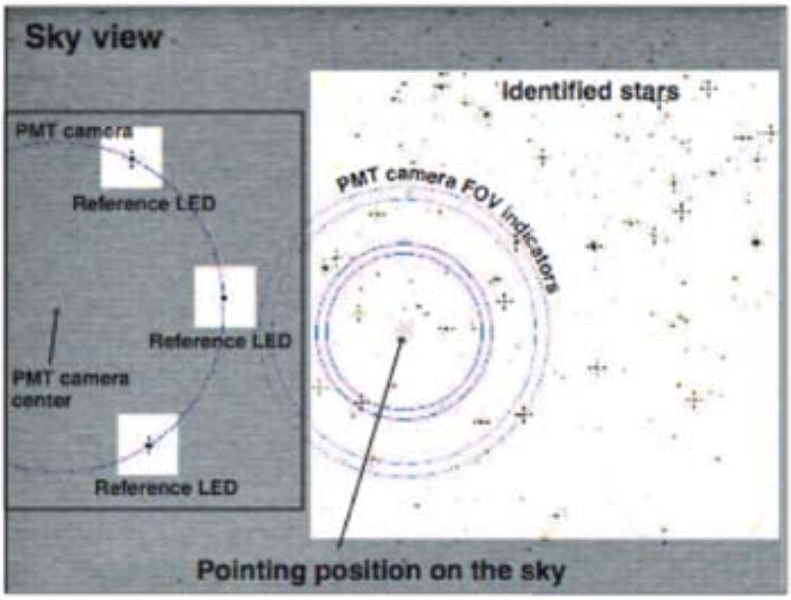

Figure 2.7: The FoV of the starguider CCD camera. Taken from Wagner, R. (2006).

oriented by the AMC depending on the telescope elevation.

While in MAGIC I each mirror panel comprises four spherical mirrors of 0.5 x 0.5 m^2 each, in MAGIC II each panel consists of just 1 m^2 spherical mirror. The decision of increasing the mirror size for MAGIC II was a compromise between costs and needed manpower for the installation (the four mirror tiles require an inter-alignment before the installation), and the necessity of keeping the size of the spherical mirror as small as possible: the smaller the spherical sections, the better the whole reflector follows a parabolic shape. The reason for going to 1 m^2 and not other sizes is related to the existing telescope frame which is a grid of tubes with 1 m step (Figure 2.8). This modification was shown not to worsen the overall performance Doro, M. (2009).

Figure 2.8: MAGIC space frame structure.

The MAGIC telescopes are equipped with three different types of mirrors, basically because every group which took the responsibility of the mirror construction chose a different design. For a detailed review of all the used technologies the reader can refer to Doro, M., et al. (2011), the main characteristics being summarized below.

- **0.25 m^2 aluminium mirrors**. The 0.25 m^2 aluminium mirrors have an innovative design with respect to conventional glass mirrors. They are composed of two thin layers of aluminium inter-placed by a 20.7 mm thick honeycomb structure which ensures high

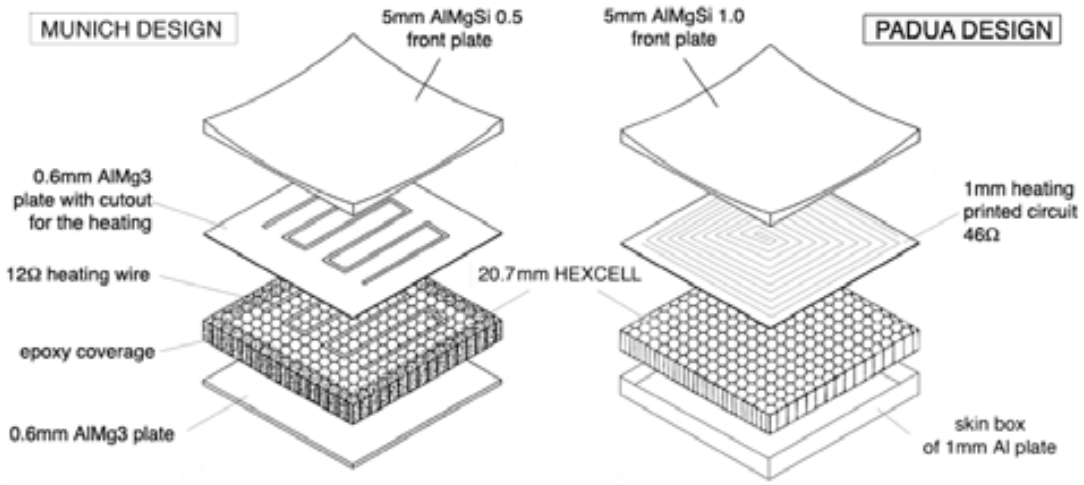

Figure 2.9: The two designs of MAGIC I mirrors. *On the left:* MPI design. *On the right:* INFN-Padova design.

rigidity and low weight at the same time. The reflective layer is not made by pure aluminium, which would be the best-suited reflective material for the Cherenkov spectral range, because of its rapid aging and low stiffness and an AlMgSi more resistant alloy is employed instead. Just above the hexcell structure, a heater board is placed whose aim is eventually to heat the mirror in order to avoid ice formation. All these layers are glued together with an epoxy structural weld in autoclave creating the so called "sandwich". At this stage the tiles, called *raw-blanks* are pre-milled to give them a rough radii of curvature of 35 m. To reach then the exact curvature which will fit the overall parabolic shape and increase the reflectivity, the upper side of the sandwich is finally milled with high precision by using a diamond-milling machine. In addition, a 100 nm layer of quarzum is vacuum-deposited on the surface of the mirror in order to protect it against corrosion and acid rain. There are two slightly different models of this kind of mirrors which are sketched in Figure 2.9: one produced by the MPI Munich, Germany and the other one by the INFN in Padova, Italy. The differences consist in the thickness of the materials, the contamination of the used aluminium and the fact that the bottom layer in the Italian mirrors is shaped as a box more than as a plate. MAGIC I is almost entirely equipped with these mirrors except for some 1 m^2 mirrors (described in the next point) which were installed for testing purposes. The average reflectivity of these mirrors is around 85% (Doro, M., et al., 2008).

Figure 2.10: MAGIC I mirror staggering.

The design of the 0.25 m^2 aluminium mirrors was aimed to minimize the gap between the four mirrors within a panel in order to reduce the overall light loss. Unfortunately this spacing was too small and the panels touched each other during the observations. Monte Carlo (MC) simulations showed that staggering the mirrors by less than 10 cm did not degenerate the shower images due the introduction of a time delay. Therefore, the mirrors were shifted 20 mm backward or 60 mm forward with respect to their initial position (Figure 2.10).

- **1 m^2 aluminium mirrors**. The 1 m^2 aluminium mirrors, entirely produced by INFN-Padova, Italy, are the second generation of the mirrors described above. Basically, they are a scaled-up version of the same mirror, since the structure is pretty similar to 0.25 m^2 sandwich tile, without the heater board which was found to be useless. Nevertheless, there is one main difference in the production of these new mirrors. It was introduced to solve a degradation effect appearing in some MAGIC I mirrors in form of "bubbles" at the edges of the tile. These "bubbles" are due to the humidity entering the sealing which, when converted to ice, deforms the surface. The new design introduces a sealing of the mirror box which is favoured by a small increase in size of the upper aluminium plate with respect to the layers below. The aluminium layer is then made thinner enough to be roughly curved through the use of molds. This avoids the pre-milling procedure. In addition, since each panel consists of just one tile, it is no longer necessary to build a back-panel to hold the mirror tiles and the AMC motors. Therefore, the back of the 1 m^2 mirrors has a central hole hosting the AMC motor and three more smaller holes for the mirror installation on the telescope frame. Out of the 247 mirror tiles of MAGIC II, 143 are 1 m^2 aluminium mirrors. Their reflectivity is around 87% (Doro, M., 2009).

- **1 m^2 glass-Al mirrors**. The remaining 104 mirror tiles of MAGIC II were produced with a totally different technology, called *cold slumping* technique. They were designed by the Istituto Nazionale AstroFisica (INAF) together with the Brera astronomical observatory, Italy. According to this technique, a thin 1.7 mm sheet of glass is elastically deformed to be molded into the desired spherical shape. The mold is diamond-milled through the same technique used for the aluminium mirrors. This deformed glass sheet is just the upper surface of the usual "sandwich" tile consisting of a honeycomb structure which provides the necessary rigidity and another sheet of glass on the bottom. This sandwich is then aluminized and quartz-coated to protect the reflective surface.
  The optical quality of these mirrors is worse, than that of the aluminium mirrors. Their Point Spread Function (PSF) of $\equiv$ 6 mm doubles that of the aluminium mirrors, but is still well inside the size of a camera pixel. This draw-back is compensated by a better reflectivity, around 88%, and a lower production cost.

Active mirror control

For the first time in IACTs, MAGIC makes use of an Active Mirror Control to counteract small deformations of the mirror support dish during repositioning or tracking.

Each mirror unit is fixed to the carbon fiber frame at three points, two of which are equipped with actuators with one/two lateral freedom(s) (Figure 2.11). Each actuator contains a motor which allows to move the panel with a precision smaller than 20 τm, corresponding to a displacement at the camera plane of the light spot of less than 1 mm (Biland, A., et al., 2008). The electronics handling the actuators is housed in 62 boxes attached to telescope frame, and it is controlled from a computer via a RS-485 serial connection. Each mirror panel hosts a guidance laser used to monitor the panel orientation. Four LEDs are placed on the camera lids (Figure 2.12), and they are used as reference points. The AMC system needs a CCD camera to monitor the laser spot position on the lids of the MAGIC camera. It has 3.5° FoV and 2 Mpixel resolution. The AMC system, however, includes also a high sensitivity and dynamic range CCD-camera which allows for PSF and reflectivity measurements. This second camera is known as SBIG camera: it is a STL-1001E from the company Santa Barbara Instrument Group. Both the cameras are mounted in the center of the reflector dish.

Figure 2.11: AMC motors. *On the left:* Picture of a mirror box from the back. The three mounting points, two of which with attenuators, are visible. *On the right:* Picture of an actuator fixed on the telescope frame.

The mirrors are adjusted every time that the telescope zenith angle changes by 5° by using Look-Up Tables (LUTs)[4], but, at the very beginning of MAGIC I, it was done through laser adjustment. The latter procedure computes the position of each panel so that the light emitted by the laser, placed at the panel center, is correctly positioned on the camera plane (Garczarczyk, M., et al., 2003).

The AMC is also used to monitor the single mirror reflectivity after the mirror installation. While tracking a bright star with all mirrors de-focused, but one, the comparison of the star image reflected on the camera plane with the star image itself (taken with the SBIG camera) provides an estimation of the absolute reflectivity. The same procedure with all the mirrors focused properly allows the measurement of the overall reflectivity, defined by the point spread function of the reflector (optical PSF). The PSF is the photon distribution of an optical point-like source at the focal plane, and is usually well fitted to a 2-dimensional Gaussian function. This is an important measurement from the analysis point of view, since the optical PSF affects significantly the telescope point spread function (gamma PSF). The latter is defined as the standard deviation of the 2-dimensional Gaussian fit of a γ-ray point-like source image on sky. It is a way to describe the *angular resolution* of the instrument (§ 3.8).

This monitoring procedure, called mirror re-alignment or AMC calibration, is performed al-

[4]LUTs are tables containing the position of each mirror unit per zenith angle bin.

Figure 2.12: Guidance lasers. MAGIC I with all the guidance lasers switched on.

most every two years. Interested readers can refer to Garczarczyk, M. (2007) for more information.

2.2.4 Camera

The sensitivity of the telescope depends strongly on the quality of the shower images. Hence, it depends on the performance of the camera, which hosts the photo-sensors converting the Cherenkov photons produced by EASs into electrical signals. Some key features of the photo-sensors are: high Quantum Efficiency (QE), fast response, and fine pixelization.

Each telescope is instrumented with a different camera, which will be described separately in the following subsections. Not only components of improved performance, such as the PMTs themselves, were used for the MAGIC II camera, but the structure of the camera itself is different. Nevertheless, in both cameras the pixels are double-protected by a transparent Plexiglas window and by two lids which open during the observations. In addition, both of them are equipped with air cooling and heating systems preventing the camera from getting too hot or reaching the dew point. Since the second camera represents a significant improvement with respect to the first one, the MAGIC collaboration decided to also upgrade the MAGIC I camera with an exact clone of the MAGIC II camera. This upgrade began in Summer 2011.

MAGIC I camera

The MAGIC I camera has hexagonal shape, and 3.6° FoV. It is equipped with 576 PMTs of two different kinds. 396 of them have 0.1° FoV (1 inch ⌀), and cover the inner section of the camera up to 1.2° radius (inner pixels). The remaining 180 PMTs for the outer part of the camera (outer pixels) have 0.2° FoV. Figure 2.13 shows a photo of the MAGIC I camera from both front and back side. The use of two different PMT sizes is a compromise between cost and performance: the trigger region is, in fact, entirely covered by the more expensive and better performing 1 inch ⌀ pixels.

The PMT photocatode, of hemispherical shape, is enhanced in QE up to 28% with a diffuse lacquer coating doped with P-Terphenyl which shifts the short wavelength Ultra Violet (UV) component of the Cherenkov light into the spectral range of larger sensitivity (Paneque, D. et al., 2004). This treatment was used for the first time in the MAGIC PMTs. In order to

minimize the losses into the dead space between the round PMTs, hex-to-round light guides were used. The light concentrators, consisting of a thin aluminium tube, channel the incoming light into the PMT with an incident angle of approximately 40°. The total QE of the entire system (mirrors, effective PMT QE, light guides) is ≡ 15% between 300 and 600 nm.

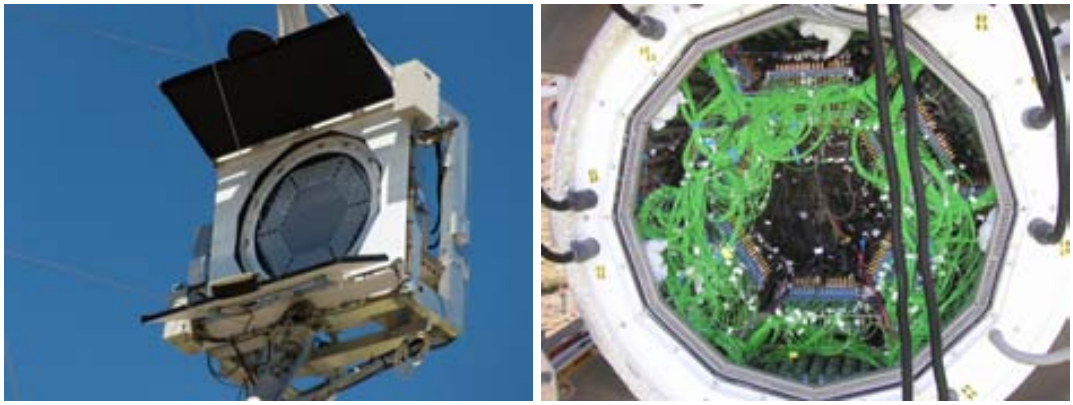

Figure 2.13: MAGIC I camera. *On the left:* photo of the front of the camera where the two type of PMTs are visible. *On the right:* picture of rear of the camera.

The PMTs have only 6-dynodes and run at a relatively low gain of 20000–40000 to prevent high anode currents during moonlight observation from damaging the devices. This needs to be compensated with fast, high gain amplifiers at the base of the PMTs. Each pixel is connected to a High Voltage (HV) regulator. The applied HV can be monitored with a 12-bit Analogical to Digital Converter (ADC).

The control program of this subsystem is developed into two different layers: one involves the communication with the hardware and is written in C/C++ programming languages, and a second layer for the operation is written in the visual programming language of LabVIEW (Cortina, J., et al., 2003). The communication with the hardware is mainly performed through two CANbus lines of 200 m length to control and monitor the PMT HV. CANbus is also used to control devices with a serial port access by using CANbus to RS-232 converter. In addition, the camera cooling, and the power of the camera electronics are controlled by two PLCs which are accessible using Modbus protocol via RS-485 lines.

MAGIC II camera

The camera of MAGIC II is instead of circular shape with a FoV of 3.5° similar to the MAGIC I camera. It has a modular design (Figure 2.15) which simplifies the access to the photo-sensors, making either the maintenance of the actual system or a possible upgrade with improved photo-sensors easier. The camera is uniformly equipped with 1039 0.1° FoV PMTs grouped into 169 clusters (Borla Tridon, D., et al., 2009). The trigger region comprises only 91 clusters covering a circle of 2.5° diameter (≡ 5% larger than trigger region of MAGIC I).

All pixels are Hamamatsu R10408 6-dynode photo-tubes with hemispherical photocatode, an enhanced QE of around 32%, and an integrated control power unit (Figure 2.14). The latter includes a Crockroft-Walton voltage supply, which provides the high voltages for the PMTs, and a round-circuit board for the front-end analog signal processing, entirely designed at MPI-Munich, Germany. This hand-made circuit amplifies the PMT signal to compensate for the PMTs low gain, and then back-converts the analog to optical signal by Vertical-Cavity Surface-Emitting Lasers (VCSELs). The amplifier can receive as input also test pulses with an amplitude adjustable between 0-1.6 V. This allows for linearity tests of the entire readout chain. In addition, the round board hosts monitoring circuits which provide readout of the average PMT currents, the PMT voltages, the VCSEL temperatures, etc..
On the front side, the pixels are equipped with Winston cones to minimize the light losses due to the dead area between pixels. The pixel modules together with the light guides are encapsulated into aluminium tubes.

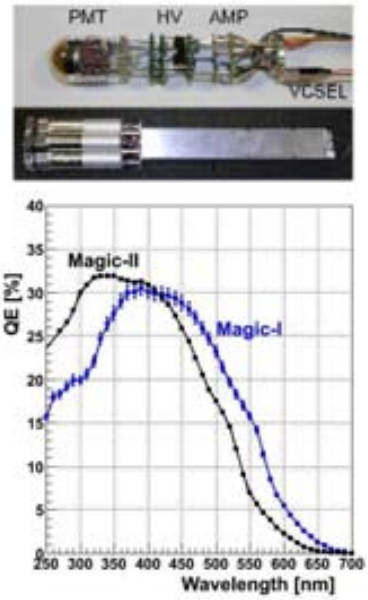

Figure 2.14: MAGIC II PMT. *On top:* photo of a pixel and a cluster module. *On bottom:* plot of the pixel QE as function of the wavelength.

Every group of seven pixels constitutes a cluster. A Slow Control Cluster Processor (SCCP) controls the pixel electronics (readout and setting), the power distribution, and the test pulse generator. Each SCCP is connected via Ethernet cables to a Virtual Mobile Engine (VME) board inside one of the two VME crate on the back of the camera. These VME crates communicate with the camera control PC in the counting house via an opticalPeripheral Component Interconnect (PCI) to VME link. The camera control program, written in LabVIEW visual programming language, is fully described in Steinke, B., et al. (2009).

Figure 2.15: MAGIC II camera. *On the left:* photo of the camera from the front side. *On the right:* picture of the rear of the camera.

2.2.5 Calibration system

The calibration system has mainly two aims:

- it allows to adjust the HV of the PMTs so that their gain is uniform throughout the camera (flat-fielding procedure). This guarantees that most pulses fall within the dynamic range of the readout, and makes the trigger adjustment and the whole analysis easier. This process takes a long time (1–2 hrs), but it needs to be rarely done (1–2 times a year).
- it permits to monitor online the gains of the channels in time scales of tens of seconds. This is essential because the gain of the electronic chain is not stable, mainly because of gain variations in the VCSELs, which may be as large as 10–20% in $\equiv$ 1 minute.

The MAGIC calibration system provides fast light pulses at different wavelength and different intensities in order to calibrate the whole dynamic range of the camera photo-sensors and their readout. The MAGIC I system consists of a box located at the center of the reflector dish which houses 64 LEDs emitting at three wavelengths: 370 nm (UV LEDs), 460 nm (blue LEDs), and 520 nm (green LEDs). The light pulses have 3-4 ns duration, a good approximation of the Cherenkov pulses. The MAGIC II system consists of frequency tripled passively Q-switched Nd-YAG laser, operating at 355 nm with a pulse width of 700 ps. In order to obtain a dynamic range two rotating filter wheels are used. They allow to illuminate the camera with intensities within 100 steps between 1 and 1000 ph.e.. This system is placed at the center of MAGIC II reflector.

2.2.6 Readout and data acquisition systems

The electric pulses at the base of the PMT are converted into optical pulses using VCSELs, which are coupled to optical fibers. The latter transmits the signal to the Counting House (CH), 80 m away. Such analog optical transmission has never been used in IACTs before. Its purpose is to protect the signal from the ambient electromagnetic noise in the line, reduce the weight on the telescope and decrease the signal losses from the camera to the CH.

In the counting house, the optical signals are split into two branches and back-converted into electronic signals in the *receiver boards*. One branch goes to the trigger system, while the other, after being delayed to wait for the trigger response, goes to the Data AcQuisition (DAQ). The DAQ, consisting of a Flash Analogical to Digital Converter (FADC), digitizes the electronic signals and records them into raw data files. Both MAGIC I and MAGIC II readout systems sample the pulses at a speed of 2 GSample/s, even though with completely different electronics, which will be described in detail in the following subsections.

MAGIC I readout system

When MAGIC I was inaugurated, it was equipped with a readout system sampling the signal at 300 MSample/s. A sketch of this system is shown in figure 2.16. The digital signals produced in the receiver boards and going to the DAQ were amplified, stretched to $\equiv$ 6-7 ns and further split into a high and a low gain channel in order to increase the dynamic range. The high gain branch was amplified by a factor 10, while the low gain was delayed by 55 ns. The switch from high- to low-gain was activated only if the high-gain signal exceeded a certain threshold ($\equiv$ 50 photo-electrons). The delay in the low-gain channel allowed the system to connect the low-gain signal into the output and to block the high-gain one. The

output was sent to long ring buffers where it waited for the trigger decision. If passed, it was readout with FADC modules and stored in First In, First Out (FIFO) buffers. The dead time was around 1 μs. A multi-thread readout program, written in the C++ environment, read the data from the FIFO buffer and wrote to the raw files (Goebel, F., et al., 2003).

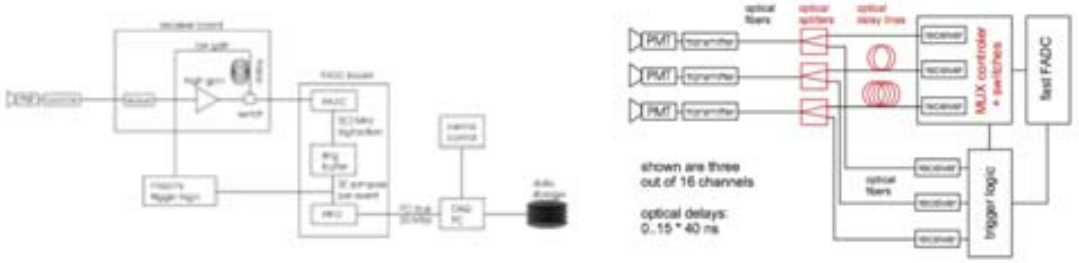

Figure 2.16: Sketches of the two MAGIC I readout systems. *On the left:* 300 MSample/s readout system in operation between 2003 and February 2007. *On the right:* the current MAGIC I readout system sampling at 2 GSample/s and making use of the multiplexing technique.

The system was upgraded to an ultra fast FADC of 2 GHz sampling rate which makes use of a novel fiber-optic multiplexing technique[5]. Multiplexing is possible as the signal duration (few ns) and the trigger frequency ($\sim$ 1 kHz) result in a low duty cycle for the digitizers. The fiber-optic Multiplexing readout system (MUX) uses commercial FADC modules (produced by the company *Acqiris*) to digitize 16 channels consecutively. The concept is shown in figure 2.16.

In preparation for the MUX installation, fiber optic splitters were installed already in April 2006. Afterwards, half of the split signal is sent directly to the receiver boards, so digitized and sent to the trigger system, and the other half is delayed by using optical fibers before back-converting it into digital signal. Within group of 16 channels, each channel is delayed of 40 ns with respect to the previous one. The maximum delay is of 1160 ns to account for the 40 ns for the 16 channels and 560 ns needed to wait for the trigger decision. On the multiplexer boards the optical signals are converted back to electronic signals by using PIN diodes. Fast high bandwidth MOSFET-switched open for 40 ns channel by channel. Finally the signals are summed in two active summation stages and digitized by the Acqiris boards. The reader interested on this commercial device can refer to Goebel, F., et al. (2008). These digitized data are stored on five on-boards with a dead time (before the next event can be recorded) of 2.5 μs. Each on-board is subdivided into three segments, with a capacity of 50 events each, which is read out asynchronously by a rank-mounted PC controlled by the MUX control program. The MuxDaq program combines the data coming from the five PCs and transmitted via Ethernet, and stores them in a buffer ring. Once the data integrity is checked, it performs a quick signal reconstruction for the on-line data quality monitor and consequently stores the data into raw files. All these tasks are performed in parallel as independent threads of the MuxDaq program. Figure 2.17 shows a scheme of this program.

[5]The multiplexing technique combined multiple analog signals in one optical fiber.

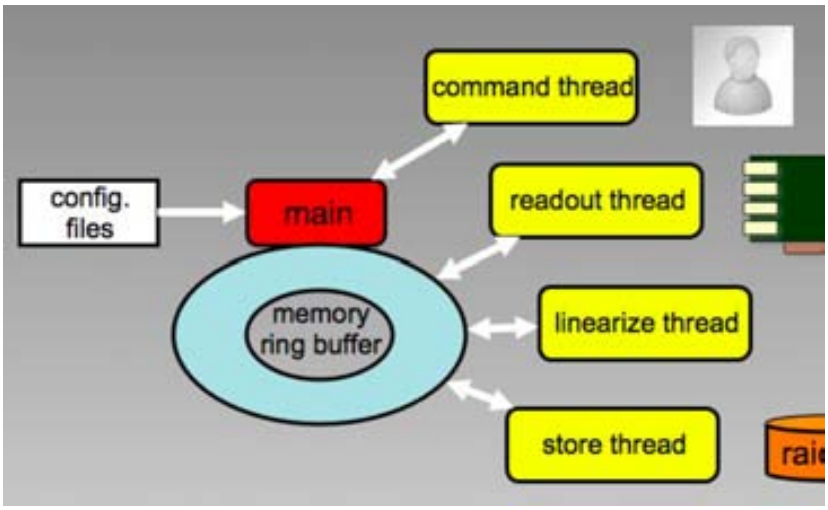

Figure 2.17: Scheme of the DAQ multi-thread C-program.

The upgraded readout system allows to sample the pulse more accurately: the high sampling rate leads to a finer signal reconstruction which permits to obtain more reliable values of the signal arrival time. The time resolution is around 0.4 ns (for the previous readout it was 1 ns). In addition, since the signal stretching is no longer needed, the signal integration window is much smaller including much less noise, as shown in figure 2.18. This technical advancement results in a considerable reduction of the background, thus in a consistent improvement of the instrument sensitivity (Aliu, E., et al., 2009).

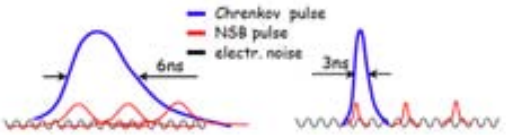

Figure 2.18: MUX. Scheme of a PMT pulse, created by Cherenkov photons, with a 300 MSample/s (left) and 2 GSample/s (right) system.

Between the installation of fiber optic splitters and the one of the MUXs, signal were split before being converted to digital signals into the receivers boards, but, except for this detail, the two branches of signal followed the same scheme as the first readout system.

MAGIC II readout system

The readout system of MAGIC II differs significantly from that of the first telescope. New receivers boards and a new digitization system were designed, while the data acquisition program was adapted to the new features. MAGIC II readout is a complex system which has to handle more than thousand channels, a factor two larger with respect to MAGIC I , and to store a data flow of the order of 100 MByte/s.

The new receivers boards, called MONSTER, represent a major advance respect to MAGIC I (Tescaro, D., et al., 2009). These boards are more compact: each of them processes 24 pixels, instead of the 8 pixels of the MAGIC I boards. Besides they monitor the individual pixel rates, and the discriminator thresholds, trigger delays and trigger widths, they can be set from remote in few ns. The boards follow the VME standard.

The digitization of the signal is performed through the so-called Domino Ring Sampler 2 (DRS2)[6] chip.

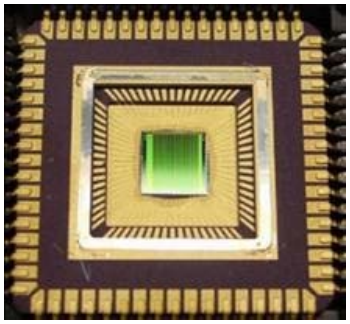

Figure 2.19: The DRS2 chip.

Each DRS2 chip hosts 10 input analog channels, each associated with a pixel in the camera. Each DRS2 channel is equipped with 1024 capacitors organized as a ring buffer. In this capacitors, signal is continuously recorded, such that, once the last cell is written, the first one gets overwritten. The DRS2 chip is a highly non-linear and temperature sensitive device (complete characterization in Bitossi, M. (2009)). Therefore, it is necessary to perform a calibration (domino calibration) of the chip on a regular basis. This domino calibration has to produce the calibration curve for each capacitor of the DRS2 chip (1024 capacitors x 1039 pixels $\equiv 10^6$).

The operation of the DRS2 required the development of a set of new boards. The PULSer And Recorder (PULSAR) boards are used as motherboards that host the mezzanines carrying the DRS2 chip. A PULSAR is a general purpose VME interface board for high energy physics developed by the University of Chicago. The philosophy of its design is to use one type of motherboard to interface any user data with any industrial standard link through the use of custom mezzanine cards. Each PULSAR board hosts 4 customized mezzanines, carrying two DRS2 chips each, for a total of 80 channels each. A special PULSAR board, called *digital*, is especially programmed to sample the trigger signal and to measure its arrival time. This information is transmitted to the other PULSAR boards, called *analog*, for reading out the region of interest only. Another special PULSAR board, called *busy*, provides the busy signal which inhibits the trigger while the system is processing a given event. External digital information like the time stamp or the trigger tag are introduced in the data flow via two front panel connectors.

All these hardware components, plus MAGIC II trigger and calibration systems, and stereo trigger are steered by one single multi-thread C-program through the VMEbus. This program is called MAGIC Integrated Readout (MIR) (Tescaro, D., et al., 2009). The fact that MIR integrates all components of the readout, allows for a close interaction between individual components needed during the data taking, as well as for the domino calibration procedure. This procedure takes into account the non-linear response of the DRS2 chip. Therefore, the signals of each channel are corrected by using previously computed calibration curves.

The digitized data are readout by the DAQ program. It interfaces with the PULSAR boards through FILAR cards[7], which are PCI cards installed in the DAQ PC, and HOLA boards, which are mezzanines installed on the PULSAR boards. A shared memory buffer between HOLA and FILAR the DAQ program to process the data, without stopping their digitization. The DAQ program then follows the same scheme as the MuxDAQ program (Figure 2.17) with three main threads: reading, analyzing and storing. Further information about this program can be found in Tescaro, D., et al. (2009), Aleksić, J. (2009), and Tescaro, D. (2010).

[6] *http://drs.web.psi.ch*
[7] *http://hsi.web.cern.ch/hsi/s-link/devices/ lar/*

2.2.7 Trigger

The trigger system discriminates the Cherenkov showers from NSB light. It does so by selecting only fast pulses (< 5ns) which are detected simultaneously in a compact region of the camera. In fact, since the light from EASs is more intense than the NSB one, it involves several neighbor pixels at the same time. MAGIC II trigger system is basically a copy of the one of the first telescope. Nevertheless, the uniform MAGIC II camera design allows an increasing in trigger area from 1.2° up to 2.5° diameter FoV.

The *level zero* (L0) trigger is already hosted in the receiver boards: they generate digital signals only for those channels with an input signal above a certain Discriminator Threshold (DT). These DTs are programmable providing the possibility to keep a stable rate even under variable light conditions. Thanks to dedicated channel rate counter the individual pixel rate is available on-line.

The digital signals are then sent to the *level one* (L1) trigger unit which is active in 19 overlapping hexagonal macrocells (Figure 2.20). Its task is to determine if there are channels with spatial and temporal correlation (topological reconstruction). Different topologies can be used to evaluate the spatial correlation, but all of them are based on the Close Compact Next Neighbor (CCNN) logic. The latter accepts those events for which N adjacent pixels in a compact configuration have passed the L0 trigger.

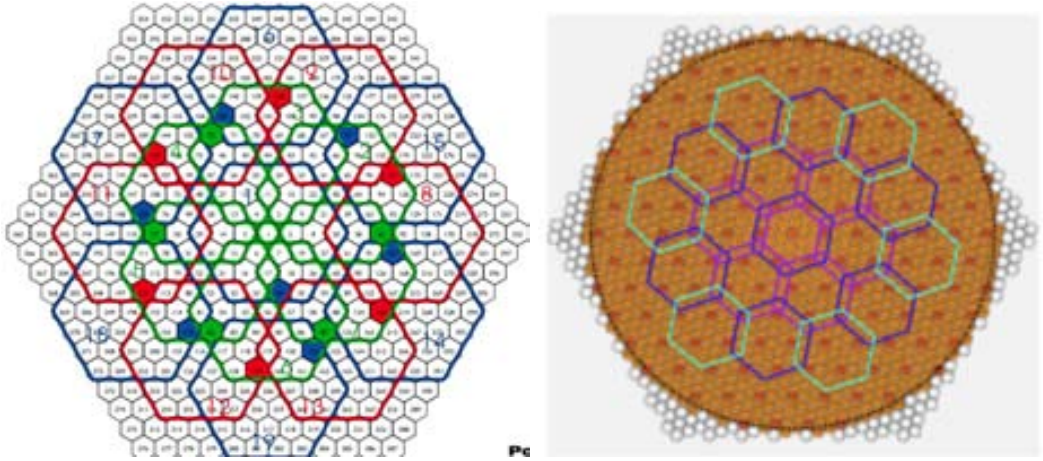

Figure 2.20: Camera layout with overlaid the 19 trigger macrocells defining the trigger area. *On the left:* MAGIC I ; *On the right:* MAGIC II

Once a global trigger signal is produced, it is sent to the *level two* (L2) trigger (Paoletti, R., et al., 2007). At the moment, this unit has no decisional power: it monitors the trigger rate, applies a scaling factor[8] to the final rate which triggers the readout system, and merges L1 triggers with triggers generated by the calibration system and the stereo trigger.
When the two telescopes operate in stereoscopic mode there is a further *level three* (L3) trigger, also called *stereo trigger*. It rejects all those events which have been triggered by just one telescope. In order to minimize the L3 coincidence gate, the signals triggered by the individual telescopes are delayed by a time depending on the pointing direction of the corresponding telescope.

All triggered signals are sent via Low Voltage Differential Signal (LVDS) to a VME crate,

[8]The scaling factors are known in MAGIC as prescalers

connected via VMEbus to the control PC running a program, which monitors and sets all the trigger parameters.

2.2.8 Sumtrigger

The Sum Trigger (ST) is a new trigger concept developed to lower the trigger threshold of the first MAGIC telescope by a factor of two, down to 25 GeV. At the moment of writing this thesis, it is implemented in MAGIC I only, and it operates in parallel to the standard trigger. An upgraded ST is foreseen to be installed also in MAGIC II in the near future.
The main idea is that trigger decision is taken on the sum of several analog signals, minimizing the signal to noise ratio of low energy showers ($\equiv$ 25 GeV) over the NSB light (Rissi et al., 2009). The camera is subdivided into 24 overlapping patches, each of which consists of 18 pixels. In each patch the analog signals of all the pixels are clipped and then summed up. The clipping of the individual analog signals, before summing, rejects accidental triggers due to large after-pulses of the PMT signals. Only pixels in one patch contribute to the trigger decision. The ST was successfully used to detect pulsed γ-ray emission from the Crab pulsar with the MAGIC telescope (Aliu, E., et al., 2008).

The ST was implemented using Nuclear Instrumentation Module (NIM) electronics connected to a VME crate which allows for a software control of the ST monitoring and setting functionality. Due to the different electronics employed, the ST is considered at the moment as a separate subsystem, but its upgraded version will be implemented within the framework of the standard trigger.

2.2.9 Pyrometer

The pyrometer is a device installed on the left side of the MAGIC I reflector (Figure 2.21). It measures the sky temperature [K] from the integral thermal flux of infrared radiation between 8–14 τm-wavelengths. The pyrometer has Germanium lenses with a FoV of 2° and an optical axis aligned with the MAGIC optical axis. These lenses focus the radiation into a thermoelectric sensor. The integral flux is then calculated according to the Planck's law under the hypothesis of a perfect black body (emission coefficient = 1).

The sky temperature is used to evaluate a *cloudiness* parameter which provides a rough estimate of the sky quality, defined as:

$$\frac{\mathrm{T_{meas}} - \mathrm{T_{low}}}{\mathrm{T_{up}} - \mathrm{T_{low}}} \tag{2.2}$$

when $\mathrm{T_{meas}}$ is the measured sky temperature, and $\mathrm{T_{low}} = 250$ K, $\mathrm{T_{up}} = 200$, two values which indicate the best and the worst weather conditions respectively.

The pyrometer device is controlled by a PLC which communicates with its control program, written in LabVIEW environment, using the RS-232 protocol.

2.2.10 GRB monitoring alert system

The GRB alert program is a daemon which monitors the Gamma-ray burst Coordinate Network (GCN)[9] for any alert on GRBs. The GCN information is sent directly over a Transmission Control Protocol/Internet Protocol (TCP/IP) Internet socket to the GRB alert

[9] *http://gcn.gsfc.nasa.gov*

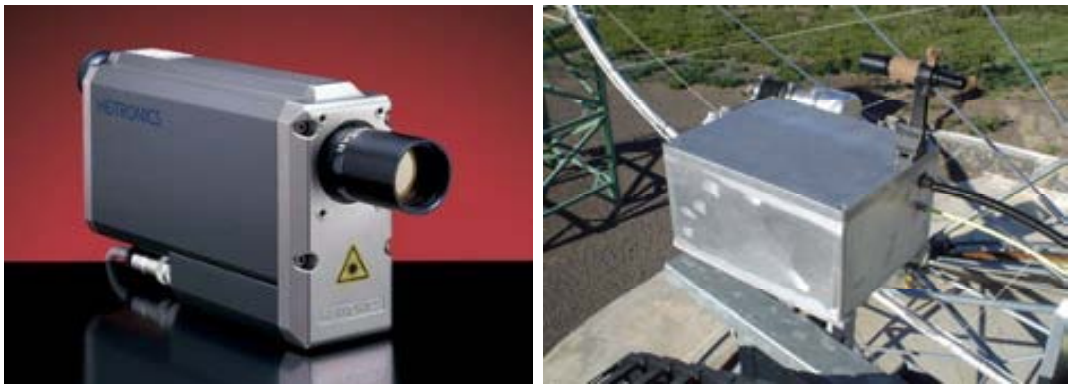

Figure 2.21: Pyrometer.

program. The program validates the alert with predefined observability criteria, such as distance of the GRB to the Sun or the Moon, zenith angle of the candidate GRB and uncertainty on the given position. If the alert fulfills all these criteria, then it is sent to the central control program which takes the control over this observation.

2.2.11 Clocks

There are two official clocks installed at the MAGIC site: a Global Positioning System (GPS) receiver and an atomic Rubidium clock. They provide the time stamp for the DAQ systems. The difference between both devices is monitored through a NIM module and reported to an auxiliary PC through a serial RS-232 connection. The program which reads out this information writes an American Standard Code for Information Interchange (ASCII) file.

2.2.12 Weather station

The weather station is a microprocessor weather station MWS 5MV high quality steel with data-logger and forced ventilation by fan made by Reinhardt GmbH. The information collected by this device is read out over a serial connection, by a program which writes the weather values onto a file. The readout occurs every minute.

2.3 Operation of the telescopes

All subsystems of the two MAGIC telescopes can be controlled and monitored from the CC program through its Graphical User Interface (GUI). The central control is the key program for the operation of the two telescopes, as it defines all the standard procedures for data taking and occasional calibrations. This section provides an overview of the observation strategies ad the online procedures, whereas the CC is described in the next section.

2.3.1 Scheduling of sources

MAGIC observations are grouped in one-year long cycles. Cycle I started in May 2005. At the moment of writing this thesis, the telescopes are about to complete cycle VI. Every year the Time Allocation Committee (TAC) evaluates the proposals for the next cycle of observations. Proposals are ranked A (the highest) to C (the lowest). The rank defines the observation priority. It is then the task of the scheduler to arrange the observations according to their

obtained grade. A "tentative" observation schedule is produced every sidereal month. The schedule defines the observation time slot for every object, along with the observation mode, the moonlight conditions, and the zenith angle. The schedule can be modified if, in the meanwhile, any observation trigger activates (§ 2.3.2).

2.3.2 Regular and ToO observations

MAGIC observations can be carried out either as Target of Opportunity (ToO) observations, or regular observations.

Regular observations are arranged whenever the source is visible in La Palma, for a number of hours which depend on the expected/known brightness of the source. These campaigns are meant for the study of objects with a stable and constant flux.

ToO observations instead, are activated by trigger alerts which makes use of multi-wavelength, and multi-experiment information. Most of their targets are variable sources showing sudden flux enhancements, called "flares", which are to a large extent unpredictable. Nevertheless, since the VHE radiation is often correlated to the emission in other energy bands, a flux enhancement in another wavelength can be used to trigger MAGIC. Trigger strategies which rely on the status of the X-ray emission take advantage from public data released by monitoring detectors, such as All-Sky Monitor (ASM) or Burst Alert Telescope (BAT), on board of the *RXTE* and *Swift* satellites respectively. Since August 2009, new soft γ-ray data recorded by *Fermi*/LAT are made publicly available every six hours. Trigger alerts based on optical, infrared or radio frequencies generally require previous agreements with the corresponding experiments. Although they can be replaced by the use of Astronomical Telegrams (ATels)[10] which provide an internationally recognized, but not refereed, system for the notification of transient astronomical phenomena. ATels are released almost on real time to allow for multi-wavelength observation coverage of the objects.
Trigger alerts for MAGIC can come also from other IACTs. Such alerts normally relate to sources which are well known VHE emitters for which there is no more competition between experiments. All of them organize monitoring programs and observe variable sources constantly along their period of visibility, hoping to catch some flares. For this reason, an Online Analysis (OA) tool which provides results in real time is necessary (§ 2.5). On the other hand, the VERITAS collaboration still operates the Whipple telescope with this purpose.

2.3.3 Source pointing modes

MAGIC observations are carried out either in *tracking* or in *wobble* mode. The observation mode determines the background estimation procedure.

In the *tracking*, or *on/off*, mode the telescope tracks directly the source, and, therefore, the source position is always located at the camera center. These observations are called *on* pointings. In this observation mode, additional data are needed for the background estimation. *Off* pointings are carried out observing a region of the sky with no known γ-ray source in the FoV, and in the same observational conditions (background light, presence of stars, and zenith angle) as *on* pointings.

Most of the MAGIC observations are carried out in *wobble* mode, or more properly *false-source tracking* mode, (Fomin, V. P., et al., 1994). The telescope tracks alternatively two opposite directions in the sky located at a defined offset (default 0.4°) from the source position. The wobble position is swapped, generally, every 20 minutes. This is the favoured observation

[10] *http://www.astronomerstelegram.org/*. It is responsibility of the International Astronomic Union.

mode because it does not require any additional *off* data. Since the source position does not coincide with the camera center, there are regions of the camera where γ-ray events are not expected, and can be used to define the *off* data sample (§ 3.9). In this way no observation time is lost pointing at dark regions of the sky. Moreover, the background estimation is much more reliable, as it is derived from the same data sample of the source observation. However, this observation mode has two main drawbacks: a loss in γ-ray efficiency, estimated of the order of 15-20%, due to the smaller effective trigger region around the source, and a possible bias introduced by the off-center source position which mainly depends on the camera inhomogeneities. The wobbling of the observation positions is meant to take into account this effect: for every source pointing, the background is estimated from the same physical region of the camera taken from the symmetric wobble position.

2.3.4 Calibration and data runs

The expression *data taking* includes the entire online procedure of observing the scheduled sources, from the source pointing to the data storage. It can be completely performed through the CC program, subject of the next section. In fact, by communicating with all the subsystems (§ 2.2), the CC program can coordinate every single operation of the telescopes.

MAGIC data are classified according to the kind of events they record. Mainly there are:

- **calibration runs** contain trigger generated by the calibration system. They are used for the data calibration (§ 3.3).
- **pedestal runs** contain random triggers with a null probability of recording atmospheric shower events. They are used to define the electronic noise of the electronic chain.
- **data runs** all the cosmic events which trigger the telescopes. These runs can include also pedestal and calibration events, interleaved with cosmic events at a rate of 25 Hz respectively (hereafter *interleaved events*). These additional calibration events allows for a constant update of the calibration factors (§ 3.3) in the recorded data.

Each source observation requires at least one pedestal and one calibration run, usually taken before the data runs.

Each telescope records stereo events independently. The event correspondence is done (§ 3.5.1), later on, o ine, by using the trigger number which is delivered by the L3 trigger (§ 2.2.7). In order to ease up the file management in the o ine analysis, data runs are grouped into data sequences with a *run number* which is common for both telescopes (given by the CC program). Files in the data sequence (whose number is different from telescope to telescope) have a second number, called *subrun number* which is given by the corresponding DAQ system. In standard data taking, a data sequence lasts for 20 minutes. Whereas, each data subrun usually contains a couple of minutes of observations, even though this depends on the trigger rate.

2.4 Central control

The central control program allows an operator to configure all subsystems of the telescopes and take data. It also permits to monitor the most relevant parameters of the subsystems through a graphical user interface. The program is called *SuperArehucas*.

The implementation of the standard procedures for stereo data taking inside the CC leads to a level of automatization which permits to avoid oversights, and possible misuse of the instrument. Nevertheless, the CC confers the full control over the telescope to the operators. For example, they can configure the various components of the detector, according to the observational conditions. They can also stop any automatic procedure in case of extraordinary problems during data taking.

The CC program is written in LabVIEW 8.5 in order to take advantage of the built-in control utilities and the graphical capabilities of this platform. SuperArehucas includes 756 subroutines, which in LabVIEW are called Virtual Instruments (VIs).

2.4.1 Communication with telescope subsystems

Communication between CC and every subsystem is performed through C-coded TCP/IP sockets. Sockets are endpoints of inter-process communication based on a combination of Internet Protocol (IP) addresses and port numbers. When two of these endpoints, setup by two unrelated processes (also residing in two different machines) connect, they create a reliable byte stream which can be read or written. Thus, in the general socket communication scheme, a server program listens in a socket connected to a port number. A client program can connect its own socket to the server's socket which it writes to. In the meanwhile, the server socket reads the data sent in.

The control system of the MAGIC telescopes expects each subsystem to open both a server and a client socket: one is used to receive instructions/data from the CC, and the other one to send to the CC all its relevant information. Analogously, SuperArehucas has two sockets for each subsystem.

In order to establish a connection with each subsystem, at start up, the CC starts polling subsystem by subsystem for availability, and this fact is displayed to the user. Every subsystem sends a ASCII report to the CC every second describing its state, time stamp, and all relevant operational parameters. The state variable is used to define the action of the subsystem. If the CC does not receive any report from a subsystem for more than 10 s, it defines the corresponding subsystem state as "unavailable". The central control sends a CC-report every 10 s to each subsystem which, in this way, can know when the CC is available. Moreover, reading the CC-report is the only mean a subsystem has to be aware of the running parameters of the other subsystems. Commands from CC are sent through the same thread of the CC-report. They are executed by the subsystem as if the user had input them directly at the corresponding console.

2.4.2 Program structure

The logic of the central control program is based on several decisional loops implemented as individual threads (Figure 2.22), and an extensive use of global variables:

- The **report thread** takes care of the *report* system: it sends every 10 s the CC-report to all subsystems, and reads out every second the *reports* that the subsystems send it. The information contained in the received *reports* is then processed and saved into a set of global variables ("subsystems global variables").
- The **GUI control thread** monitors controls, *i.e.* buttons and menus. Whenever one of them is clicked, the loop activates the global variable which identifies the function ("function global variables") the operator requests.

- The **action thread** starts the functions requested by means of the controls: it constantly checks if one the "function global variables" has been activated, and acts consequently by calling the corresponding VI.
- The **subsystem panel thread** displays on the GUI (§ 2.4.3) all the information received from the subsystems *reports*. It makes use of the "subsystem global variables".
- The **camera display thread** displays the status of all relevant parameters in all individual pixels (§ 2.4.3).
- The **GRB thread** activates the GRB automatic procedure whenever a GRB alert is received through the report sent by the GRB monitor program (§ 2.2.10).

The fact that the procedures the CC performs are executed in subroutines which run in background, guarantees the operator a full control over them. In fact, the operator can always intervene by means of the controls in the GUI. Nevertheless, there is the exception given by the automatic GRB procedure.

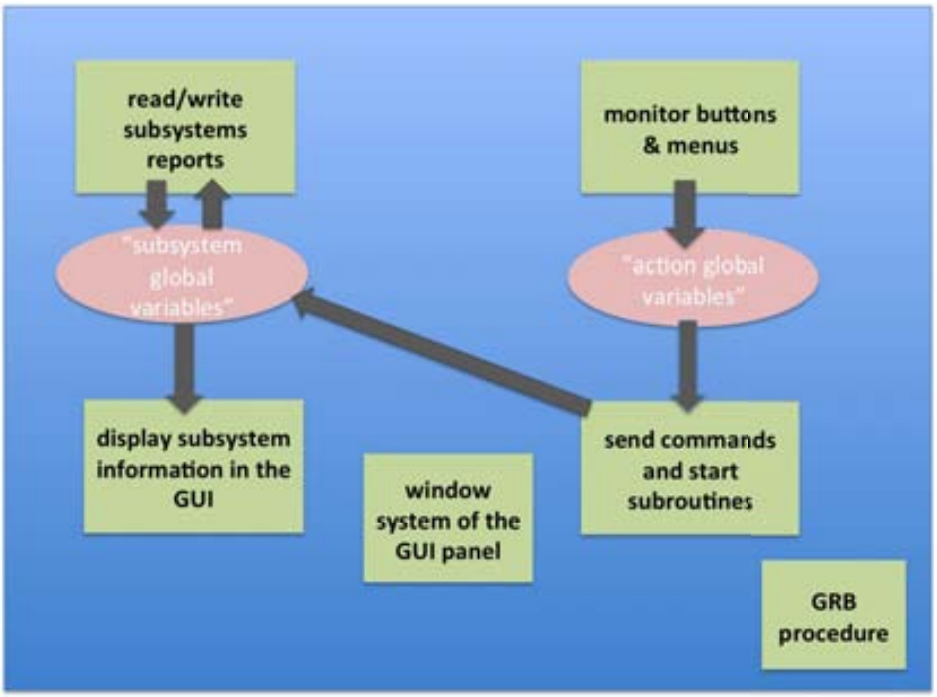

Figure 2.22: Scheme of the main loop of the central control program. Rectangles identify threads.

Safety checks

All the specific actions are executed by sending fixed commands, in the ASCII format, to the involved subsystems (§ 2.4.1). However, before sending the commands the CC program performs additional decisional loops to check if the addressee is correctly configured to be able to execute the required action. These checks prevent possible mistakes which can deteriorate the data quality and avoid that the command will be unsuccessful.

Moreover, the subsystem parameters are constantly compared to safety limits or standard values and warning or safety reactions result when the parameters seem to show problematic states. For example, if the external humidity measured by the weather station, exceeds a certain value, the electronic inside the camera can be damaged. Therefore, the CC program immediately closes the lids which protect the camera. If the sun is still present, the system does not allow the operator to rump the HVs up in order not to ruin the PMTs. If the wind speed is too high, this can destroy the telescope frame or the lids if opened: in this case the CC closes the lids and parks the telescope. If, for any reason, the drive system changes action unexpectedly during data taking, the CC automatically stops the data acquisition and informs the shifters. Warning messages are issued through colorful pop-up windows and sounds.

2.4.3 Status of the subsystems: graphical user interface

SuperArehucas graphical user interface is shown in Figure 2.23. It contains all the information which are needed to monitor the data taking procedure and determine the overall performance of the detector.

Status of individual pixels: pixel displays

On the left side of the GUI, there are three pixel displays for each telescope (in Figure 2.23 MAGIC I above and MAGIC II below). Each of these displays can show the following information for each of the pixels:

- **charge of the last event processed by the DAQ system** in FADC counts. This information comes from the rough signal extraction performed online by the DAQ system (§ 2.2.6). The charge is pedestal-subtracted only if the DAQ has taken at least a pedestal run before.

- **PMT anode Direct Currents (DCs)** in μA allow to monitor the intensity of the light background. During normal operation they must be under 7 μA. Stars in the FoV are visible through a DC increase.

- **PMT HV readout** in Volt. This display is useful to identify dead pixels.

- **PMT HV settings** in Volt. They should be equal to the HV readout values within a 10% . If they are systematically different for all the pixels, it means that the HV ramping up procedure has failed. If they differ only for some pixels, it is due to a checking routine of the camera program which reduces the HV of those pixels with too high DCs.

- **Individual Pixel Rate** in Hz monitors accidental triggers in individual pixels due to noise. During stereo data taking it should be around 500 kHz.

- **DTs** in arbitrary units (higher DT indicates a more restrictive trigger level). They are adjusted in real time during data taking by the so-called "Individual Pixel Rate (IPR) control" routine.

- **trigger delay times** in arbitrary units. They should be fixed to their optimal values and hardly modified.

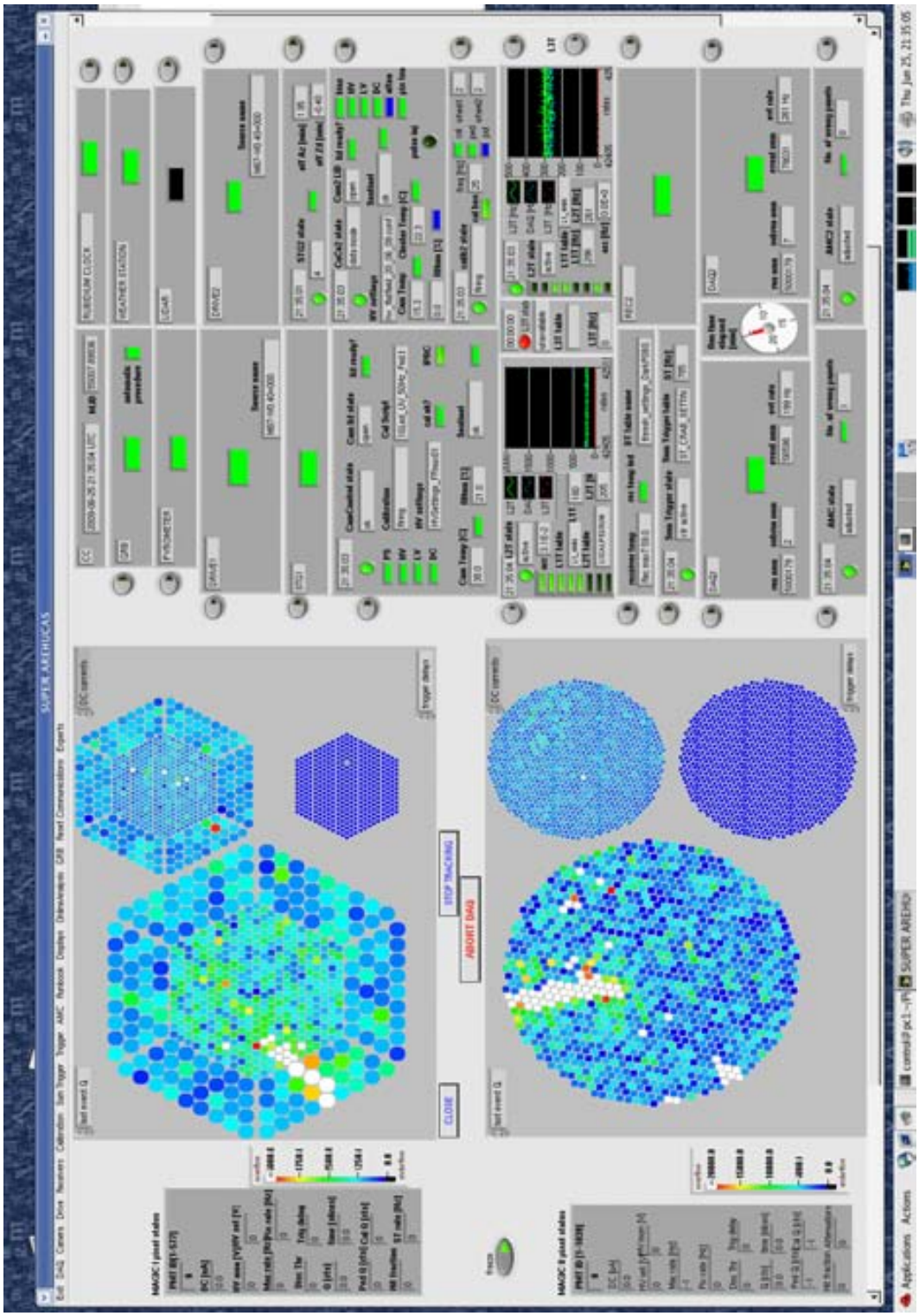

Figure 2.23: The graphical user interface of the central control program.

- **average pixel charge in the last pedestal run** in FADC counts. This display is updated every new pedestal run.

- **average pixel charge in the last calibration run** in FADC counts. This display is updated every new calibration run.
- **trigger rate in the 19 macro-cells** in Hz. This is the only display which does not include pixel information. It shows only 19 values. Each of which corresponds to one trigger macro-cell (§ 2.2.7).

The color scale of all the displays goes from blue (lowest) to red (highest). Black indicates underflow, and white overflow. The color scale can be changed by the operator through the corresponding function in the menu. Running the mouse over the largest displays, the operator can check the values of all the above described parameters, and the pixel numbers. The latter are shown in the two panels on the left side of the camera displays.

Status of the subsystem elements: subsystem panel

The right side of the GUI shows a panel built-up of 23 windows, one for each subsystem (§ 2.2). These windows are grouped in such a way that they form three sub-panels: the top central one for the "common subsystems", the bottom left for MAGIC I , and the bottom right for MAGIC II subsystems. Each window contains the main information that the corresponding subsystem sends to the CC every second through its reports (§ 2.4.1). As a result, the variables inside the window are updated with the same frequency. Nevertheless, each window has two possible states: one which includes all the subsystem information needed to identify a problem ("full state"), and a more compact one which shows a LED, whose color indicates the subsystem behavior (green: everything is fine, yellow: alarm state, red: there is a problem), and just information indispensable for data taking ("LED state"). In case of green light, the operator can choose which state of the window to visualize by using the button on the external side of the window. If any problem appears, the window will immediately switch on the "full state", and it cannot be changed until the problem is solved. The "full state" windows always contain: a round LED indicating the status of the TCP communication between the CC and the corresponding subsystem, the state of the subsystem, and a clock showing the time of the last report received by the CC (large time differences with respect to the time of the CC computer, shown in the first top left window, indicate that the communication is malfunctioning). The additional information for each subsystem is listed below.

- **pyrometer**:

  cloudiness (2.2.9)

  status of the sky quality

- **GRB monitor**:

  status of the automatic GRB procedure

  status of the GRB observations

  GRB coordinates (only if any)

- **weather station**:

  external temperature

  external humidity

  wind speed [km/h]

wind direction

- **clocks**:

  time difference between the GPS receiver and the rubidium clock (2.2.11) [μs]

- **lidar**: not yet available.

- **MAGIC I and MAGIC II drive**:

  name of observed source
  requested position [RA, DEC]
  requested position [az, zd]
  observed position [RA, Dec]
  observed position [az, zd]

- **MAGIC I and MAGIC II starguider**:

  azimuth mispointing [°]
  zenith mispointing [°]
  status of the mispointing

- **MAGIC I camera**:

  status of the electronic power Low Voltages (LVs)
  status of the pixel HVs
  status of the electronics power supplies
  status of the DCs
  state of the lids
  HV settings file-name
  temperature inside the camera [°C]
  humidity inside the camera [%]
  status of the IPR control
  state of the *sentinel*. The *sentinel* indicates the response of the safety routines of the camera control program.
  MAGIC I calibration state. The calibration system for MAGIC I is setup through a script launched by the MAGIC I camera control program. That is the reason for which this subsystem has been merged with the MAGIC I camera program.
  name of the calibration script

- **MAGIC II camera**:

  status of the HVs, LVs, biases, DCs, attenuators, pixel temperature
  lid state
  HV settings file-name
  temperature inside the camera [°C]
  humidity inside the camera [%]
  mean temperature of the clusters [°C]
  sentinel state
  status of the pulse injector

- **MAGIC II calibration**:

  interleaved ped/cal frequency [Hz]

  status of the calibration box

  filter wheel settings

  status of the calibration switches

- **MAGIC I and MAGIC II trigger**

  L1T rate [Hz]

  L2T rate [Hz]

  L1T table name

  L2T table name

  accidental events rate [Hz]

  status of the prescaling factors

  graph showing the rate behavior as function of time. Both DAQ and trigger rates are displayed.

- **MAGIC I sum trigger**:

  sum trigger table name

  sum trigger rate

- **MAGIC I receivers**:

  receiver temperature [°C]

  DT table name

  the **MAGIC II receiver**:

  state of the PULSAR boards

  temperature of the electronics racks [°C]

  DT table name

  status of the IPR control

  state of the cooling system for the electronics racks

  communication status of the cooling system control program

- **MAGIC I and MAGIC II DAQ**

  run number

  run sub-number

  event number

  event rate [Hz]

  free available disk space [MBytes]

  elapsed time since last wobbling

- **MAGIC I and MAGIC II AMC**:

  number of de-focused mirror panels

  status of de-focused mirror problem

2.4.4 Central control functions

The functions available in the CC program can be called through either buttons in the GUI or menus.

Buttons control the functions which are used more often during the operation of the telescopes. They are related to the telescopes positioning, the camera lids, and the data taking (Figure 2.23). The buttons are visible only when the relevant subsystems are available. They usually start pop-up menus which guide the operator through the operation he/she wants to perform. The following buttons are available:

- **POSITION** . When the telescope is stopped and the drive system is available, the button "POSITION" allows the operator to move the telescope. When it is clicked, a pop-up window offers three possibilities:
  - "positioning and tracking" which allows the operator either to select the source from any of the available catalogues[11] or to type in the desired coordinates. The first option guarantees the definition of the correct source name. After having selected the position, the operator is asked about the observation mode (§ 2.3.3). In case of *wobble* observations, the CC takes care of computing the wobbling positions depending on the requested offset, and rotation angle. Only at this point the telescope starts slewing, and, when reached the position, tracking.
  - "park position" will move the telescope to the park position
  - "special fixed position" where the operator can input a fixed position in azimuth and zenith coordinates.
- **STOP TRACKING** . It stops the telescope.
- **OPEN LIDS** and **CLOSE LIDS** control the movements of the camera lids.
- **START DAQ** . It starts the data taking procedure. It is visible only when the main subsystems involved in the data taking procedure (readout systems, DAQs, triggers, and cameras) are available. When pressed, the CC warns the operator about possible problems with any of the subsystems. In such a case, the operator decides if keeping on and starting the data taking. A pop-up window gives the operator the possibility to select the calibration and pedestal setup (both for pedestal/calibration runs and *interleaved events*), and the prescaling factors. The data taking procedure comprises two loops: the external one which scans the data sequences, and an internal one which records the data sequence. The first loop takes care of:
  - setting the correct *run number* for the data sequence
  - taking calibration and pedestal runs (usually they are taken just once per source observation, before first corresponding data sequence).
  - computing and changing wobble position every data sequence
  - performing mirror adjustment (§ 2.2.3) every data sequence
  - notifying the operator through a loud sound the end of the data sequence

[11] *SuperArehucas* uses catalogues in Xephem format. Xephem is a free astronomical software package.

The internal loop, which is in charge of recording the data, saves also the subsystems reports, received during data run, into specific files called *report files* (".rep"). Later on, the content of these *report files* is added to data in the o ine analysis (§ 3.2).

- **ABORT DAQ** . It stops the data sequence main loop.

All the other functions which the CC can perform are accessible through the menus on top of the GUI. These functions include the settings of the various subsystems, occasional procedures and some basic operations. The latter are usually performed within more complex subroutines which define complex procedures. Below, the reader can find the list of all the available functions, with a short description. In general, the setting functions of pixel-related parameters always gives the possibility to set the values pixel-by-pixel or for the whole camera together by uploading a file containing the predefined settings. Whereas, the "save to file" function saves the current settings in a file with the appropriate format so that it can be used by the setting function.

- **Exit**
  - **quit *SuperArehucas***
- **DAQ**
  - **go to daq test** :"daq test" defines a state of the DAQ systems in which data are recorded, but not stored to disk. This state allows the operator to monitor the rate and get a feeling of how events look like.
  - **go to standby** : "standby" defines another state of the DAQ systems are stopped (no data recording).
  - **pedestal run**
  - **calibration run**
  - **linearity run**: it takes a linearity run which contains pedestal and calibration events in bunches of different intensities. They are meant to check the linearity of the electronic chain during the observation night.
  - **dominocalibration run [only MAGIC II]**: it performs the domino calibration (§ 2.2.6). It feeds the channels of the DRS2 chip with known increasing charge levels for a fixed number of events. For each level the response is determined.
  - **abort dominocalibration run**: it allows to interrupt the the dominocalibration run which takes more than 5 minutes to finish.
  - **input source name**: it allows to change the default source name which is given by the CC itself.
  - **power on/off MAGIC II readout + trigger electronics**: it can be done from remote only for the more modern MAGIC II electronics.
  - **data with pulse injector [only MAGIC II]**: it starts the data taking procedure using the pulse injector as pulse generator. These data are important to study the response of the electronic chain after the PMTs.
  - **enable/disable drive check**: this check controls that the state of the drive system does not change unexpectedly. It is an important check since it allows to find out if one telescope stops during the data taking because of some mechanical or software failures.

  - **enable/disable humidity check**: this check controls that the humidity does not exceed the safety limits. In such a case, the CC activates automatically the safety procedure to prevent possible damages to the electronics.

- **Camera**
  - **switch on/off LV [only MAGIC II]**: the LVs of the camera can be switched on from remote only for the MAGIC II telescope camera.
  - **set HVs** the HV settings can be done either pixel by pixel or for the full camera by uploading a file with the predefined settings.
  - **save HVs to file**: it saves the current HV settings in a file with the appropriate format so that it can be used by the above function.
  - **set biases [only MAGIC II]**: the bias settings can be done either pixel by pixel or for the full camera by uploading a file with the predefined settings.
  - **set attenuators [only MAGIC II]**
  - **enable/disable pulse injector [only MAGIC II]** (§ 2.2.4)
  - **starguider LEDs on/off**: it activates the dim references LEDs of the starguider system. (§ 2.2.2)
  - **open TPoint lid** (§ 2.2.1)

- **Drive**
  - **arm/disarm cosy** it activates a safety procedure which foresees that if someone enters one of the two fences around the telescopes, the corresponding drive system immediately stops the telescope movements. Cosy is the name of the drive system control program.
  - **enable/disable starguider mode**: it actives/disactivates the starguider control.
  - **choose the star**: it is the only subroutine written in C++ language within the MARS environment (Chapter 3). It select the convenient star for the next TPoint, taking into account the sky distribution of the already taken TPoints (§ 2.2.1).
  - **take a TPoint** (§ 2.2.1)

- **Receivers**
  - **enable/disable IPR control**: the IPR control keeps the IPR below a reference value. Thus, it increases or decreases the DTs of a given pixels if its IPR is respectively too high or too low[12].
  - **set DTs**
  - **save DTs to file**

[12] In more detail, the IPR control operates as follows:

* when enabled, it saves the current DTs as the minimum possible DT.
* if a pixel has a too high IPR, it increases the DT by one step, and it iterates until the pixel IPR is low enough.
* if a pixel has a too low IPR, and its DT has been increased with respect to the initial minimum value, it tries to reset the DT to its minimum value. After resetting it, it checks if the IPR is low enough, otherwise it increases it again.

  - **set trigger delays**
  - **save trigger delays to file**
  - **set pulse width**
  - **MAGIC I IPRC setup**: it allows to set up the parameters used by the IPR control algorithm. For MAGIC I the IPR control is implemented in *SuperArehucas*. In fact, the receivers of MAGIC I communicate directly with the CC via serial port, without any control program.
  - **MAGIC II IPRC setup**: it allows to set the parameters of the MAGIC II IPR control which is implemented into the MIR program (§ 2.2.6). This is much faster (no communication between subsystem in between) than the MAGIC I one.
  - **rec2 full/reduced report**: the report of the MAGIC II receiver subsystem is so long (it contains many information for each pixel, for a total amount of 1039 pixels), that the CC needs more than 1 sec to read it out, and this can cause a loss of information from overlapping with subsequent reports. For this reason, by default, the MAGIC II receiver report does not send pixel-by-pixel information about the trigger delays and pulse widths (these setting should never change during the data taking).
  - **set one receiver channel**
  - **read all trigger delays [only MAGIC I]**: this function kind of substitutes the monitoring tasks of the report system.
  - **read all DTs [only MAGIC I]**: see above

- **Calibration**
  - **start calib. script [only MAGIC I]**
  - **stop calibration**: it stops the calibration triggers.
  - **switch on/off calibration box [only MAGIC II]**
  - **calibration laser on/off [only MAGIC II]**
  - **check laser**: it is a procedure to check the status of the laser, which, for hardware reasons, cannot be monitored other than trying to fire.
  - **setup calibration [only MAGIC II]**: it allows to set the filter wheels of the MAGIC II calibration system (§ 2.2.5).

- **Sum Trigger**
  - **enable/disable ST control**
  - **change ST control parameters**
  - **set ST DTs**: ST DTs are the discriminator thresholds of the sum trigger. They are expressed in mVolt. They can be set patch-by-patch or for all the patches by uploading a predefined file (§ 2.2.8).
  - **modify ST DTs**: it allows to monitor the rates o the single sum trigger patches, and in case they are not constant, to change the ST thresholds of the necessary patches.
  - **save ST DTs to file**

- **Trigger**
  - **load trigger table**
  - **define prescaling factors** (§ 2.2.6).
  - **start/stop triggers**
  - **rate report on/off**: it activate/disactivate the sending of the trigger reports to the CC. It is used only for testing purposes.
- **AMC**
  - **laser adjust** (§ 2.2.3)
  - **enable/disable TPoint mode [only MAGIC II]**
  - **take SBIG picture [only MAGIC II]**: at the moment, pictures with the AMC CCD camera (§ 2.2.3) can be taken from the CC only for MAGIC II . The MAGIC I SBIG camera control program is not integrated in the AMC program. Therefore it does not communicate with the CC.
- **GRB**
  - **enable/disable automatic procedure**
  - **testing GRB procedure from *SuperArehucas***: a special subroutine sends a GRB alert. Thus, only the GRB data taking procedure can be tested.
  - **activate/disactivate telescopes movements for test**
- **Runbook**
  - **add comment to runbook** (§ 2.4.5)
- **Online analysis**
  - **start OA**: it is only needed in special cases when the automatic launch of the OA fails (§ 2.5).
- **Display**
  - **set colors**: it set the color scale of the camera displays described in § 2.4.3.
- **Reset communications**. This menu provides a "reset communication function" for every opened socket (§ 2.4.1). Generally the CC program opens two sockets for each subsystem (the server and the client). In all these cases the "reset communication function" resets both of them. Nevertheless, there is the exception of the subsystems controlled by the MIR program (§ 2.2.6): for them *SuperArehucas* uses a unique client socket, and different server sockets. For this reason, in the case of the MIR subsystems, the "reset communication function" specifies the socket it resets. The socket resetting is performed through shell-BASH scripts.

  reset camera1

  reset DAQ1

  reset drive1[13]

[13]Since the starguider subsystem is controlled by the drive control program, the starguider1 reports are sent/read through the same sockets as the drive.

reset AMC1

reset trigger1

reset sum trigger1

reset receivers1

reset pyrometer

reset GRB

reset camera2

reset drive2

reset AMC2

reset DAQ2

reset cooling

reset read from trigger2

reset read from receivers2

reset read from calibration2

reset read from stereo trigger

reset read from pulsars

reset write to calib2/L3/pulsar/rec2/trigger2

- **Experts** These functions should be used by observers.
  - **send command**: it allows the operator to send arbitrary commands to the desired subsystem.
  - **atfield** (§ 2.2.5).
  - **ADA** stands for automatic delay adjustment. It calls a subroutine whose algorithm looks for the optimal trigger delays and save the results in a file.

2.4.5 Error/event logging

SuperArehucas keeps errors and general event information in a number of ASCII files:

- the **debug file** (".dbg") contains detailed debug information of the program operation.
- the **runbook file** (".rbk") logs the operator names and all their comments.
- the **run summary file** (".run" in plain ASCII and ".run.html" in HyperText Markup Language (HTML)) contains information about each subrun. There is one file for each telescope. These "run files" are used to fill the MAGIC database.
- the **CC report files** (".rep"), one for each telescope, contain the *reports* of the corresponding subsystems, plus the common ones. These files can be converted into the ROOT format (§ 3.2) to study the evolution of the subsystems during the session.

2.5 Online analysis

The OA is a program which performs a simplified data analysis during data taking. It is written in C++ programming language within the standard MAGIC software environment, MARS, (Chapter 3).

The main purpose of the OA is to extend observations in case a flare is detected in real time. It generates *alpha plots* (§ 3.9), which allow to estimate the level of the source activity. The sensitivity (§ 3.9.1) of the online analysis is rather worse than that of the standard o ine analysis: it is sensitive to flares at the level of 40% of the Crab Nebula flux in 20 minutes of observation (typical observation time for monitoring purposes). This reduced sensitivity is due to the fast processing time needed for the analysis: it has to be at least as fast as the data taking. Nevertheless, the performance of the OA can still be improved, also because it has not been adapted to the stereo analysis yet. In addition, the OA can help the operators to monitor the quality of the observations since it allows to monitor the camera inhomogeneities and the relative gain of the pixels.

The OA consists of four main steps. First, it reconstructs and calibrates the signals digitized by the 2 GSample/s FADC of MAGIC I . Afterwards, an image cleaning algorithm rejects all those signals which are the result of fluctuations of the NSB light. The remaining pixels make up the shower image which is then parametrized. The third analysis step separates γ-ray candidate events from cosmic-ray events among the recorded images. Finally, it performs the search for a γ-ray signal from the observed source by statistically evaluating the number of γ-ray candidate events over the estimated background events (those which survived to the gamma/hadron separation).

From the image parametrization on, the OA makes use of the MAGIC standard analysis tools, which are described in detail in Chapter 3, the first steps of the analysis are performed by simplified algorithms:

- Recorded signals are sampled by MAGIC I MUX DAQ in 80 FADC slices, out of which only 50 are stored to disk (from 16 to 64, the others contain only "switching noise"). For each pixel, the **signal reconstruction** procedure looks for the FADC slice with the highest value, the signal peak. The average baseline is calculated in ten slices far from the peak. The integral of the signal calculated over 15 slices around the peak, after the pedestal subtraction, provides the signal charge in FADC counts. Figure 2.24 illustrates the procedure.

- The goal of the **calibration** is converting the integrated signal from FADC counts to number of ph.e. in the PMTs. First, it performs a flat-field of the camera in order to guarantee that all the pixels have an equal response to light (relative calibration). Then the signal is multiplied by a fixed factor to convert the FADC counts into units defined as the average number of ph.e. in an inner pixel (absolute calibration). In particular, the OA calibration procedure, for each new data file, loops over the first 300 interleaved calibration events whose signal is extracted as described above. Afterwards, it obtains the relative conversion factors by comparing the average signal of each pixel to the average charge of all the pixels. The absolute conversion factor is fixed at 0.018 ph.e. per FADC count and it is applied to both inner and outer pixels (§ 2.2.4).

- The OA **image cleaning** algorithm selects only those pixels with a signal charge larger than 8 ph.e., as long as they have at least one neighbor pixel with at least 8 ph.e..

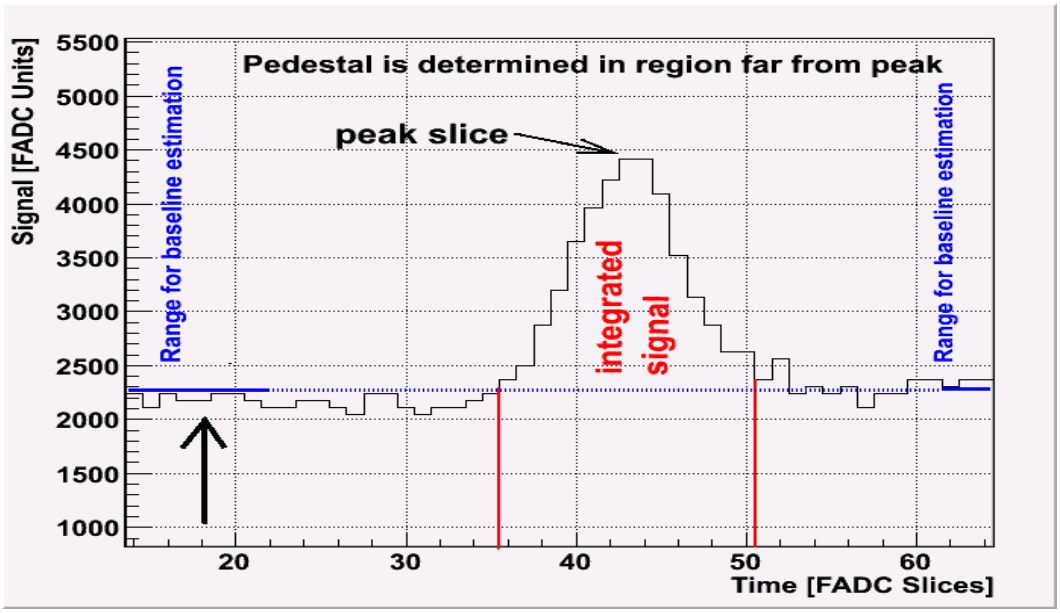

Figure 2.24: Example of a signal reconstruction of the online analysis. In the FADC range 16–64, the peak is found at slice 43. Moving 25 slices away to the left, slice 18 is reached. Therefore, the pedestal values should be estimated from slice 13 to 23. However, since the first three slices are not included in the considered range, three slices at the upper edge (62–65) are included in the baseline calculation. The signal is integrated over 15 slices around the peak position, between the slice 36 and the slice 50.

The OA γ/hadron separation is based on a fixed estimation of the *hadronness* global variable which gives a sort of probability that an event is hadron-like (§ 3.7). Finally, the distribution of the *alpha* parameter provides the number of γ-ray candidates which survive the fixed selection cuts: $hadronness < 0.1$ and $alpha < 8°$ (§ 3.9).

The OA has been very successful in several instances, mainly in the context of the AGN monitoring program. An example of a detected flare is the one from Mrk 421 in January 2010; the corresponding *alpha* distribution is shown in Figure 2.25.

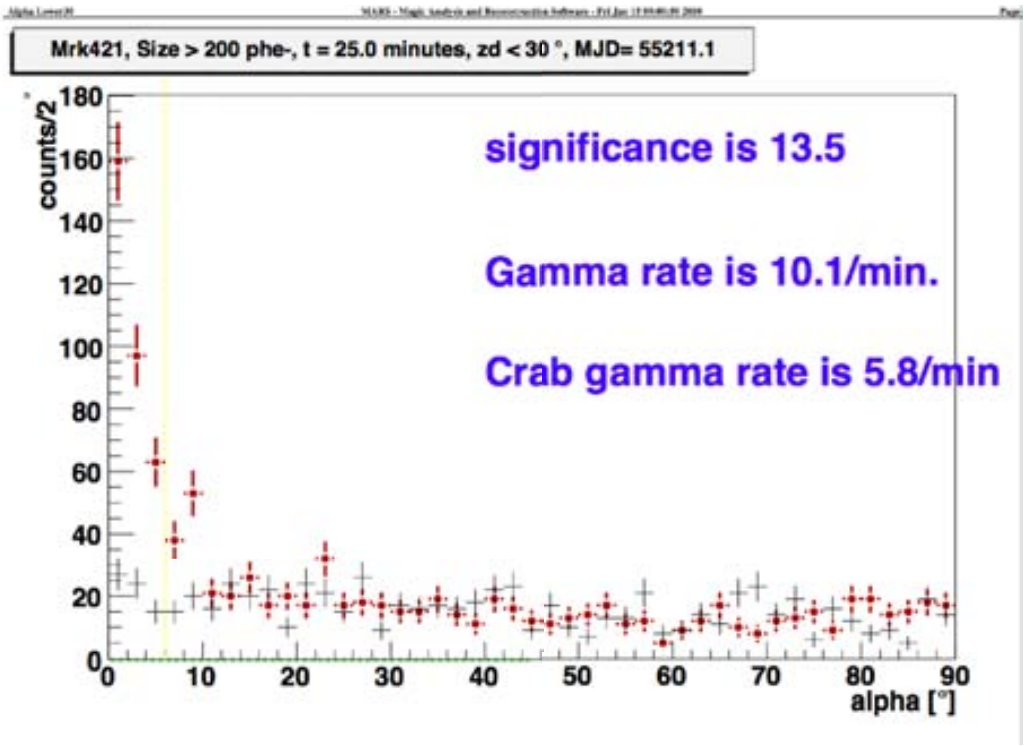

Figure 2.25: Example of an *alpha* distribution produced by the online analysis. It shows a flare of the AGN Mrk 421 occurred in January 2010.

3

The MAGIC standard analysis chain

The software for the standard MAGIC data analysis, MARS, is programmed in the ROOT environment. Several executables take care for the various analysis steps, from signal reconstruction and calibration to identification, and the spatial, spectral and temporal characterization of γ-ray sources. This chapter will describe the standard analysis chain for the analysis of both mono and stereo data with a special emphasis on their differences.
The author contributed in the development of the software for the stereoscopic analysis. Part of this work is described in Carmona, E., et al. 2011.

The software of the MAGIC collaboration is named MARS, acronym of MAGIC Analysis and Reconstruction Software (Moralejo, A., et al., 2009). It is a collection of object-oriented programs written in C++ programming language. They make use of classes and libraries of the ROOT[1] software framework.

Several consecutive steps form the standard analysis chain. They are represented in the flow diagram shown in Figure 3.1:

- **Reconstruction of the Cherenkov pulses** in each PMT of the camera, and their **calibration** into number of photo-electrons (ph.e.). The corresponding program is called *callisto*.
- **Image cleaning** removing pixels which contain noise, and **calculation of image parameters**. The corresponding program is called *star*.
- Merging the data streams from two telescopes and **calculation of the stereo parameters**. The corresponding program is called *superstar*.
- **Training for γ/hadron separation, and energy estimation**, and production of the corresponding matrices. The program, called *coach*, needs a sample of simulated MC γ-ray events and a sample of background events taken from real data.

[1] ROOT is a software framework developed at CERN and originally designed for particle physics analysis. It is available at http://root.cern.ch.

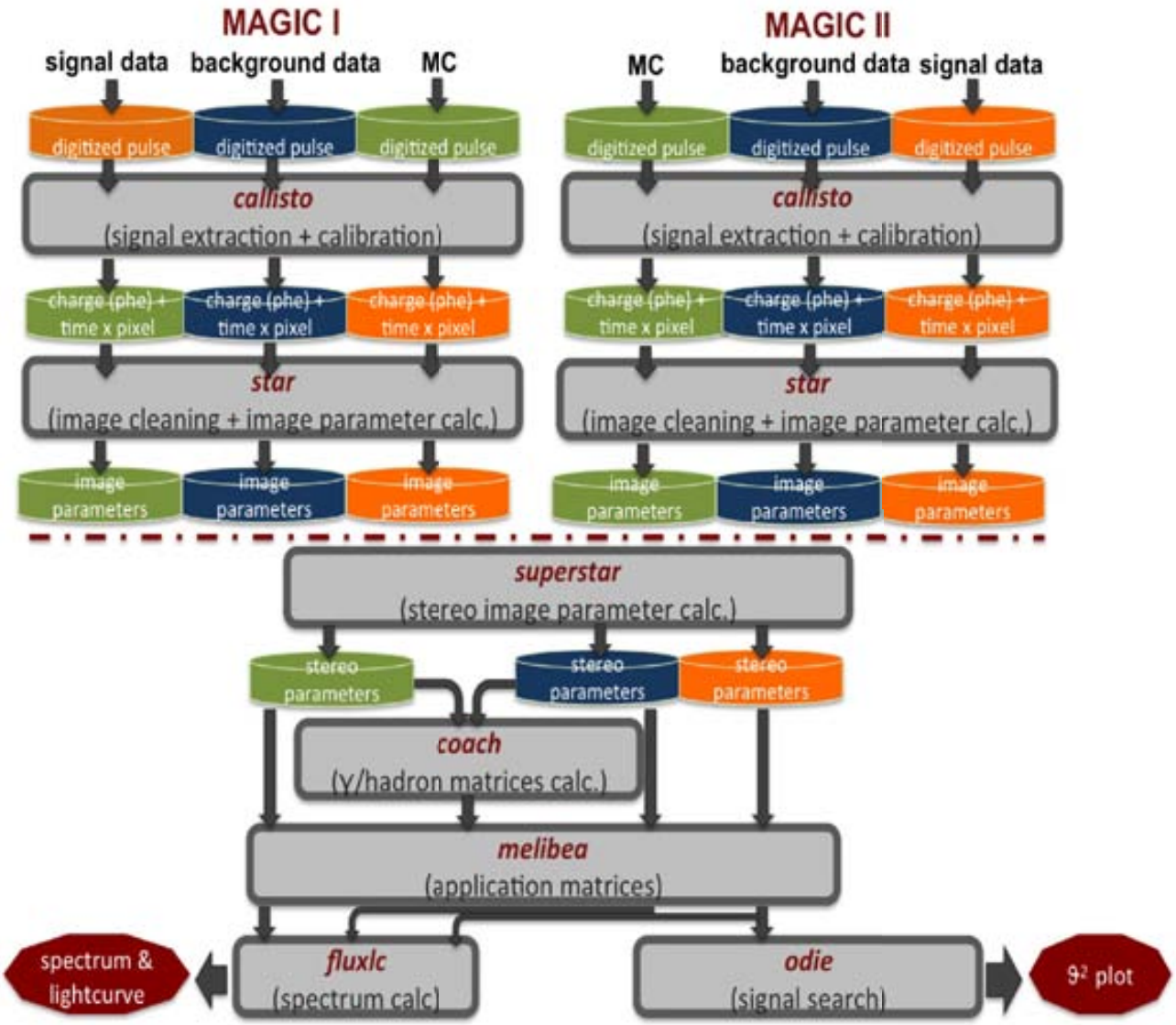

Figure 3.1: Flow diagram of the MAGIC standard analysis chain.

- **Application of the γ/hadron separation and energy estimation matrices** to signal data, background data and a test sample of simulated MC γ-ray events. The corresponding program is called *melibea*.

- **Determination of the statistical significance of the γ-ray signal**. The corresponding program is called *odie*.

- **Computation of the differential energy spectrum and light curve**. The corresponding program is called *fluxlc*.

- **Unfolding of the energy spectrum** in order to correct for the finite energy resolution of the instrument. The program is called *unfolding*.

3.1 Monte Carlo simulations

The MAGIC analysis chain relies on MC simulation of γ-ray events. Since the background rate in real data is 10^4 times larger than the γ-ray rate in a typical TeV source, real data are essentially made up of background events. Simulated γ-ray images are compared to images produced by real cosmic rays in order to discriminate among them which ones are γ-ray candidates. Nevertheless, also protons and He^{++} ions events can be simulated, and are used for specific purposes, such as performance studies (Aleksić J., et al., 2011b).

The MC software used in MAGIC is divided into three stages:

- **Shower simulation**. The CORSIKA 6.019 program (Heck, D. et al., 1998) simulates EAS initiated by VHE γ-rays or hadrons. In particular, it uses the EGS4 code for electromagnetic shower generation and QGSJET-II and FLUKA for respectively high- and low-energy hadronic shower generation. The Cherenkov photons produced in the simulated showers and reaching the ground in the vicinity of the telescope are saved into disk. The CORSIKA program models the atmosphere using the so-called United States (US) standard atmosphere.

- **Simulation of photon absorption and re ection in the telescope re ecting surface**. This stage accounts for the Cherenkov light absorption and scattering in the atmosphere. The standard US atmospheric model is considered to account for the Rayleigh scattering. The effect of Mie scattering losses is calculated using the Elterman model (Elterman, 1964) for the distribution of aerosols and ozone. This second stage also simulates the reflection of the Cherenkov photons on the reflector dish to obtain their arrival directions and times on the camera plane. One of the input of the program is the mirror reflectivity discussed in § 2.2.3.

- **Simulation of the telescope photo-detectors and electronics**. The incoming directions of the Cherenkov photons are smeared out according to the optical PSF (§ 2.2.3). This task clearly belongs to the previous stage, but it is performed here to make the simulation more flexible. Finally the simulation of the response of the PMTs, trigger and data acquisition electronics allows to produce the final Cherenkov images. It considers noise levels (electronic noise and night sky background light) as measured in real data.

Further details about MC simulations can be found in Majumdar, P. et al. (2005).The output files have the same format of the raw data files. Thus, they can be analyzed according to the standard analysis chain in the MARS framework.

The standard MC production simulates γ-ray events coming from a point-like source with a power-law spectrum. Nevertheless, there are specific MC productions for diffuse γ-ray emission. The latter is necessary for the study of extended sources.

In this thesis work, different MC samples for point-like sources are used. They account for the varying performance of the instrument over the years (due both to hardware upgrades and aging effects), and the different observation modes (§ 2.3.3).

3.2 Conversion into ROOT format and merging of control data stream

The first step of the analysis chain converts raw data files to ROOT files which can be treated within the MARS and ROOT frameworks. At the same time, the report files (2.4) are synchronized and merged with the data events. From this point on, all the information that the subsystems send to the CC program during data-taking (§ 2.2) can be easily accessed from the data files.

3.3 Signal reconstruction and calibration

Data contain the sampling of the triggered pulses which are digitized by ultra-fast 2GSample/s FADC. The recorded signals are sampled in 80 FADC time slices, but MAGIC I MUX DAQ stores only 50 samples, since the others contain only "switching noise". The analysis of these samples, called *signal extraction*, provides the signal arrival time, its amplitude and intensity in FADC counts. Afterwards, a *calibration* procedure converts the arbitrary units, FADC counts, to equivalent ph.e. which are proportional to the Cherenkov photons. MAGIC II data are first corrected for the non-linear response of the DRS2 chip (§ 2.2.6).

Several algorithms were studied within the MAGIC collaboration to optimize the signal extraction (Albert, J., et al., 2008b), but only the standard ones are used in this thesis work: the "digital filter" for MAGIC I pre-MUX data (digitized by FADC at 300 MSample/s, refer to § 2.2.6 for more detailed information), the "cubic spline extractor" for MAGIC I MUX data, and the "sliding window" for MAGIC II data (digitized at 2 GSample/s).

- **Digital filter**: it performs a fit of the Cherenkov digitized pulse to a standard predefined pulse form. This procedure outputs a signal amplitude, a signal integral, and a signal arrival time. This method works properly only if the signal shape is constant. This explains why this algorithm was dropped after the upgrade of MAGIC I readout to the MUX system, which no longer requires artificial shaping and stretching of digital signals (§ 2.2.6).

- **Cubic spline extractor**: it interpolates the pedestal subtracted samples with a cubic-spline curve. Afterwards, it looks for the maximum of the interpolation function representing the signal amplitude. The signal intensity in FADC counts is obtained as the spline integral in a window of fixed size with variable integration limits which depend on the maximum position. The signal arrival time is defined as the position of the half maximum at the rising edge of the pulse.

- **Sliding window extractor**: it searches for the maximum integral content of a number of consecutive FADC slices inside a defined time range (global window). The signal arrival time is the average of the FADC slices time, weighted over the FADC slice contents.

Once the signal is reconstructed, the charge, in FADC counts, is converted into the number of ph.e. arriving at the first dynode of the PMT. This conversion is performed through the *F-factor* method (Mirzoyan, R., 1997) which uses calibration events to estimate the proportional relation between ph.e. and FADC counts. Calibration events are generated by short light pulses ($\equiv$ 2 ns) with an intensity which is comparable to real Cherenkov pulses. The *F-factor* method assumes that the number of ph.e. per calibration event in every pixel follows

a Poissonian distribution with mean N. However, the measured charge in FADC counts has a mean value, Q , and a Root Mean Square (RMS), η, which is wider than pure Poissonian expectation due to the multiplication process of electrons in the PMT dynodes. The relative widths of the two distributions can be written as:

$$F \cdot \frac{1}{\overline{N}} = \frac{\eta}{Q} \tag{3.1}$$

where F, called F-factor, is an intrinsic parameter of each PMT measurable in the laboratory. In principle, also the electronic chain can contribute to the broadening of the measured charge distribution, but its effect can be neglected with respect to that due to the PMT itself. The spread of the F-factor distributions for both MAGIC I and MAGIC II PMTs is small enough to allow one single value of F for each telescope.
Since Q and η are measured in calibrated events and the F is known, Equation 3.1 can be used to compute the mean number of ph.e. in calibration events. The conversion factor from number of FADC counts to ph.e., C is hence:

$$C = \frac{N}{Q} = F^2 \frac{Q}{\eta^2} \tag{3.2}$$

The conversion factors change during the night mainly due to variations in the response of the analog to optical converters, which are very sensitive to temperature changes. Therefore, the conversion factors have to be constantly updated. This is done through the interleaved calibration events which are recorded with a rate of 25 Hz during the data taking of cosmic ray events (§ 2.3.4). A complete description of the calibration procedure can be found in Gaug, M. (2008).

During MAGIC observations, typically around 10–15 pixels cannot be calibrated, because of hardware problems. Instead of excluding those pixels from the analysis, their signals are interpolated by averaging the value of the signal in the neighboring pixels.

3.4 Image cleaning

At this stage of the analysis, the data files contain the charge (in ph.e.), and the arrival time of the signal extracted in every pixel and event. The image reconstruction is performed by a so-called image cleaning algorithm. This algorithm identifies those pixels containing information about the showers, hence rejects those ones whose "signal" is just the result of fluctuations of the NSB light (Figure 3.2). The efficiency of such an algorithm is crucial for the detection of low energy γ-ray showers (below 100 GeV), where the Cherenkov light can be easily confused with the background light. Several algorithms were developed to yield the analysis energy threshold closer and closer to the trigger energy threshold (Shayduk, M. et al., 2005; Gaug, M., 2008; Rissi, M., 2009; Aliu, E., et al., 2009), but only the ones used in this thesis work are described below.

3.4.1 Standard timing image cleaning

The standard image cleaning defines two absolute charge thresholds to discriminate between *core* and *boundaries* pixels. The threshold q_{core} is larger than $q_{boundary}$. In addition, a core pixel is required to have at least another neighbor pixel fulfilling the same conditions. This

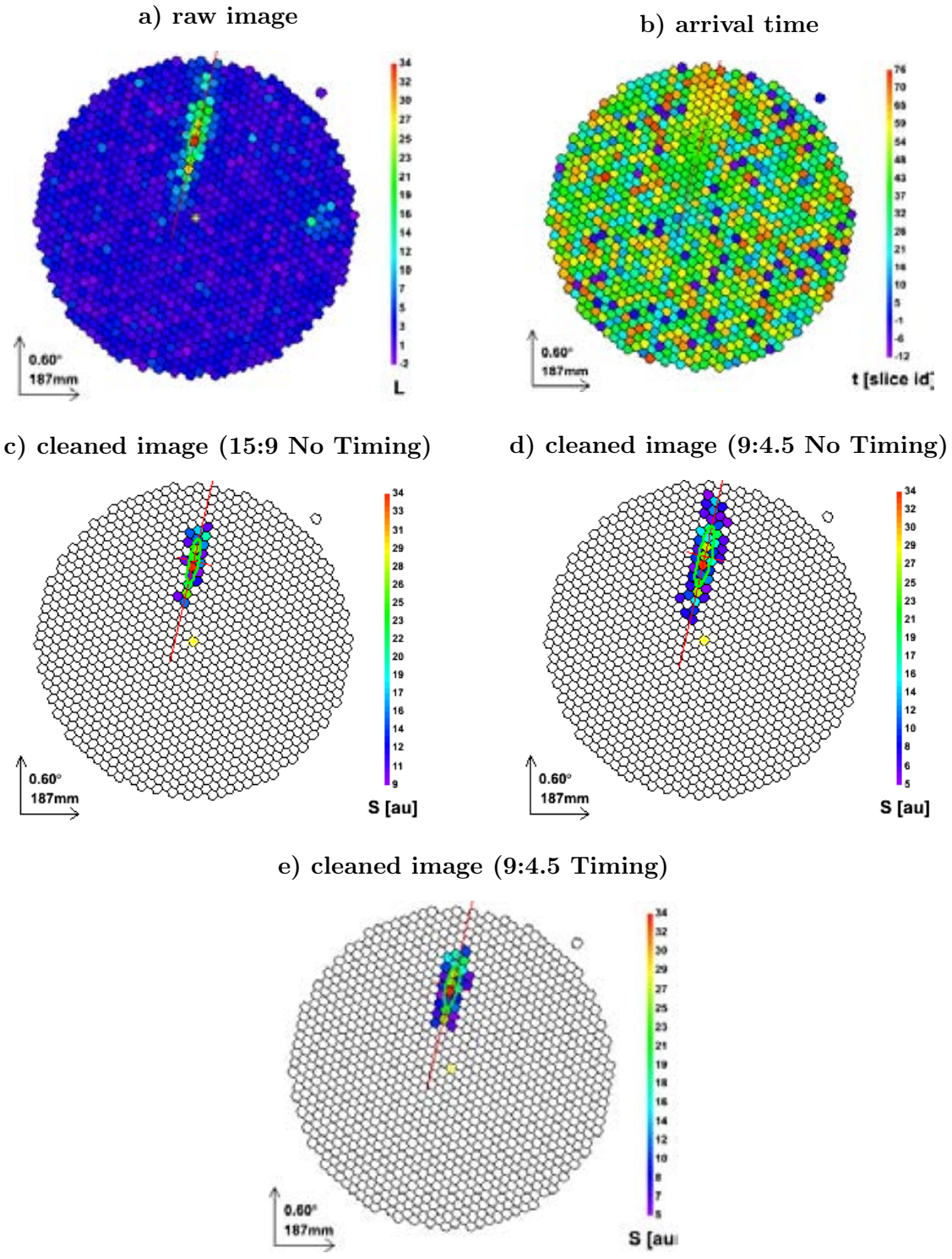

Figure 3.2: Real event recorded with MAGIC II . a) event charge and b) arrival time before image cleaning. The following panels show the reconstructed image c) with a high threshold image cleaning 15:9 without timing constraints, d) with standard image cleaning levels 9:4.5 without timing information, and e) with standard thresholds and timing constraints.

second requirement avoids that pixels unrelated to the image, but with large charge due to

PMT afterpulses, survive the image cleaning procedure. Boundary pixels must have at least one core neighbor. An optimal choice of the two charge thresholds is crucial to the analysis performance. Relaxing these values results in an increase of the number of survived pixels and favours the detection of the lowest γ-ray showers. On the other hand, the lower the energy, the higher the probability to include noise in the reconstructed image is, and this degrades the image parameters.

In addition, the current standard image cleaning algorithm makes use of the signal arrival time to improve its performance. This allows to lower the charge thresholds limiting the impact of the noise in the shower parameters. Since Cherenkov flashes are very short and asynchronous with respect to NSB light, arrival times of shower-produced signals must fall into a time window of few ns. The implementation of these timing constraints requires:

- the arrival time of the single core pixel does not differ from the average of the arrival times of all the core pixels by more than a fixed offset, *TimeOffset*
- the difference between the arrival time of the boundary pixel and that of its core neighbor does not exceed a fixed *TimeDifference*.

Further details can be found in Aliu, E., et al. (2009).

Since both the cameras and the readout systems of the two telescopes are different, the image cleaning settings have to be optimized for each telescope separately. The charge thresholds are higher for MAGIC II. The timing constraints remained unchanged, as both the instruments sample at the same frequency of 2 GHz. Table 3.1 shows the standard levels of the standard timing image cleaning.

	q_{core} [ph.e.]	$q_{boundary}$ [ph.e.]	*TimeOffset* [ns]	*TimeDifference* [ns]
MAGIC I dark	6	3	4.5	1.5
MAGIC II dark	9	4.5	4.5	1.5
MAGIC I moderate moon	8	4	4.5	1.5

Table 3.1: Settings for the standard timing image cleaning.

Timing image cleaning under moonlight

The standard timing image cleaning provides a stable analysis. Moreover, the possibility to modify the standard settings accounts for different light conditions during observations, making the algorithm more robust. For example, the charge thresholds must be increased for data taken under moonlight, as they are characterized by larger NSB fluctuations.
Britzger, D., et al. (2009) performed a detailed study of MAGIC I mono data taken with MUX readout system (§ 2.2.6) under different moonlight conditions. Moonlight causes an increase of the NSB level which can be monitored through the PMT anode DCs. They took the NSB level during completely dark observations as a reference. It is 0.18 ph.e./ns for an inner pixel (0.1° ⌀), corresponding to an anode DC of $\equiv$ 1 μA, for a Galactic region of the sky. They concluded that data taken under low moonlight conditions with an average DC below 2.5 μA can be treated as dark observations. In addition, as long as the average DCs

does not exceed 4 μA, the standard timing image cleaning, with higher charge thresholds for core and boundary pixels, allows to use the standard MC, and no correction in the MC is needed. The charge thresholds they suggested for this moderate moonlight conditions are 8 and 4 for core and boundary pixels respectively.

A similar study on stereoscopic observations is ongoing at the moment of writing this thesis. The description of these preliminary results goes, however, beyond the purpose of this section, since none of the stereo analyses presented in this thesis work is characterized by moon light conditions.

3.4.2 Sum image cleaning

The sum image cleaning is based on the definition of core and boundary pixels depending on their charge levels ($q_{core} > q_{boundary}$) as the standard timing image cleaning does. However, it introduces more constraints taking advantage from the compactness in time and extension of the Cherenkov images. These additional constraints allow to lower the charge thresholds. A core pixel has to lie within a compact group of x next neighbor (x-NN) pixels, where x is equal to 2, 3 or 4, and the total clipped charge of the x-NN group of pixels has to exceed the threshold of the corresponding group, $Q_{th}^{x\mathrm{NN}}$. This so-called "clipping" procedure[2] is applied in order to prevent large accidental signals (essentially PMT afterpulses) to dominate the charge in an x-NN group. Both clipping levels and summed thresholds are defined in terms of q_{core}:

$$Q_{th}^{x-\mathrm{NN}} = S_{th}^{x\mathrm{NN}} \cdot x \cdot q_{core} \tag{3.3}$$

$$Q_{x-\mathrm{NN}}^{clip} = C^{x\mathrm{NN}} \cdot \frac{Q_{th}^{x\mathrm{NN}}}{x} \tag{3.4}$$

In this way the optimization of the setting parameters $S_{th}^{x\mathrm{NN}}$ and $C^{x\mathrm{NN}}$ is independent from the noise level (both electronic and NSB light), hence it is independent from the telescope. In addition, the arrival time of a core pixel has to fall within a time window, $\Delta t_{x\mathrm{NN}}$ (different for each multiplicity), from the mean arrival time of the corresponding x-NN group. Boundary pixels are defined like in the standard timing image cleaning. Table 3.2 shows the values of the parameters used in this thesis work.

	xNN	q_{core} [ph.e.]	$q_{boundary}$ [ph.e.]	$C^{x\mathrm{NN}}$	$S_{th}^{x\mathrm{NN}}$	$\Delta t_{x\mathrm{NN}}$ [ns]	$\Delta t_{boundary}$ [ns]
MAGIC I	2NN	4	3	2.20	1.8	0.9	1.5
	3NN			1.05	1.3	1.2	
	4NN			1.05	0.7	1.9	
MAGIC II	2NN	7	4	2.20	1.8	0.9	1.5
	3NN			1.05	1.3	1.2	
	3NN			1.05	0.7	1.9	

Table 3.2: Settings for the sum image cleaning.

Generally the sum image cleaning recovers more pixels than the standard one. This is an important aspect in the reconstruction of low energy γ-ray images which contain only few pixels. In fact, this algorithm below 100 GeV is more efficient than the standard timing image cleaning (§ 5.2.1).

[2]Signal clipping means limiting the signal amplitude below a certain level.

3.5 Parameter reconstruction

The pixels which survived to the image cleaning procedure form the reconstructed shower image, *i.e.* the Cherenkov light distribution on the camera plane. For further analysis, every image is now parametrized by a set of parameters describing its shape, orientation and also timing properties. Image parameters are classified according to their function:

- *Hillas parameters*, computed as image moments up to the second order (Hillas, A. M., 1985) are strictly related to physics of EASs. Figure 3.3 gives a graphical idea of some parameters described below.
  - **Size**: total charge, in ph.e., contained in the image. It is related to the energy of the primary γ-ray initiating the shower (Figure 3.4).
  - **Width**: the RMS spread of the light along the minor axis of the ellipse image. It related to the lateral distribution of the shower.
  - **Length**: the RMS spread of the light along the major axis of the ellipse image. It related to the projection of the shower longitudinal development.

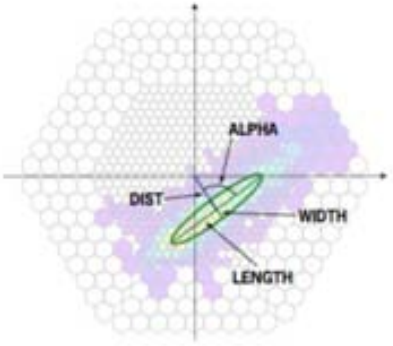

Figure 3.3: Sketch showing the definition of some image parameters. Taken from Albert, J., et al. 2008d.

  - **Conc(N)**: fraction of the image charge which is contained in the N brightest pixels. The image compactness which tends to be larger for γ-induced showers. From now on, *conc* will stand for *conc(2)*, which is the one generally used.

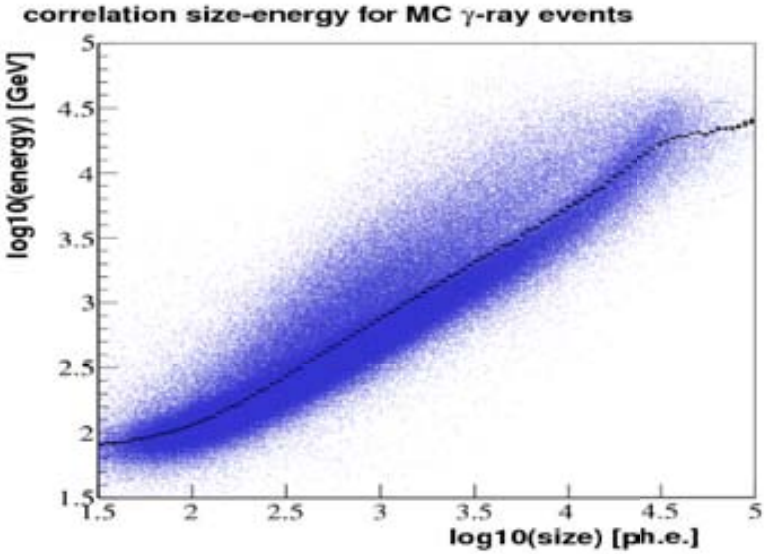

Figure 3.4: Correlation between the *size* and the energy image parameters.

- *Source dependent parameters* still have a physical interpretation, but they are separated from the previous class because of their dependence from the expected source position.

They are computed with respect to a reference point in the camera plane. Source dependent parameters are mainly used in the analysis of data taken with a telescope operating in stand-alone mode (mono data), as explained in § 3.9.

  - **Dist**: the angular distance between the Center of Gravity (CoG) of the image and the expected source position in the camera plane. It allows to estimate the shower impact parameter.
  - **Alpha**: the absolute value of the angle between the major axis of the image and the line connecting the image CoG and the camera center. Since γ-ray-induced showers always point towards the source position on the camera plane, they are characterized by small values of *alpha*. On the other hand, hadronic showers, being isotropically distributed on the camera plane, have a flat *alpha* distribution.

- *Time-related parameters* exploit shower time properties. Their use in the γ/hadron separation (§ 3.7) of the mono data analysis was proved to reduce the background level by a factor 2 (Aliu, E., et al., 2009), hence to increase MAGIC I sensitivity for point-like sources by a factor 1.4 (1.2) in data recorded with the new ultra fast (old 300 MHz) readout system (§ 2.2.6).

  - **Time RMS**: the RMS spread of the arrival time of the Cherenkov photons over the pixels belonging to the "cleaned" image.
  - **Time gradient**: the linear coefficient of the fitted arrival time projection along the major axis of the ellipse. It measures the event time profile. The sign of this parameter depends on the expected source position in the camera plane: it is positive if the arrival time increases moving away from the source location, negative otherwise. For γ-ray induced showers with a precise direction, this parameter is correlated to the impact parameter, and, as result, to the *dist* parameter, whereas no such correlation exists for hadronic events (Figure 3.5).

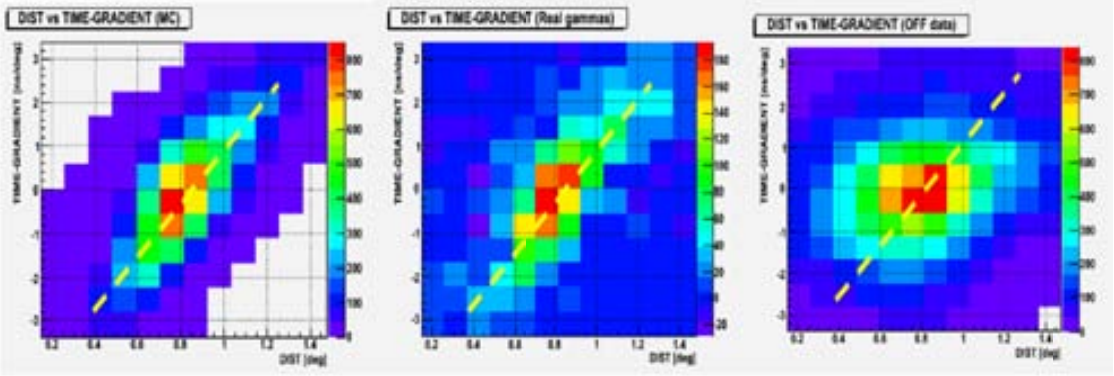

Figure 3.5: Correlation between the *Time gradient* and *dist* parameter. *On the left:* for simulated MC γ-ray events; *At center:* for real γ-ray-induced showers; *On the right:* for hadronic events taken from real data. Taken from Tescaro, D. (2010).

- *Ghost-busting parameters* discriminate between head and tail of Cherenkov showers in reconstructed images taking advantage from the asymmetries of the charge distribution. The shower head identifies the upper part of the shower. This fact creates a narrower section of the image with a higher photon density. On the other hand, the shower tail

generates a broader and sparser image section which follows the increase of the shower lateral development.

  - **Asymmetry**: the signed distance between the image CoG and the pixel with the highest content. It is positive when the shower head is closer to the camera center than the cascade tail.
  - **M3Long**: the third moment of the image along its major axis. The sign of this parameter follows the same convention as the *asymmetry* one.

- *Image quality parameters* allow an estimation of the image reconstruction accuracy.
  - **Leakage**N: the fraction of the shower light contained in the N outermost rings of pixels in the camera. Unless explicitly specified, only *leakage1* will be considered. Images with large *leakage* are likely to be truncated, and this fact has to be taken into account during the estimation of the energy of the primary γ-ray.
  - **Number of islands**: the number of separated groups of pixels which survive the image cleaning procedure (Figure 3.6).

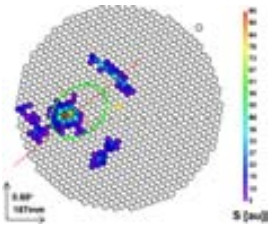

Figure 3.6: Example of a three islands event.

3.5.1 Stereo parameter reconstruction

Up to this section the described analysis code runs over the data of each telescope separately. At this point, there are two sets of data containing the same events from two different points of view. The task of the next analysis step consists of combining in one data set the matching pairs of events. At the same time, stereoscopic parameters, giving a 3-dimensional event description, are computed. Refer to Kohnle, A., et al. (1996) for a detailed description of these parameters.

- **Shower axis**: a shower axis is characterized by a direction and an impact point on the ground. The direction, θ, is defined as the intersection of the major axes of the two images, once superimposed on a camera plane (hereafter *crossing method*). The impact point on the ground is determined by the intersection of the major axes of the two elliptical images starting from the telescope positions (taking into account the distance between the two telescopes). Refer to Figure 3.7 for a graphical explanation. The accuracy of shower axis determination depends on the relative positions of the telescopes and the shower: the more parallel the two images on camera planes are, the larger the uncertainty in the reconstructed parameters.

- **Impact parameter with respect to each telescope**: the perpendicular distance between the shower axis and the telescope pointing axis.

- **Shower maximum height**, *Hmax*: once the shower direction is known, the height of the shower maximum is obtained by using the angle at which the image CoG is viewed from each telescope. The height of the shower maximum depends on the cascade energy: higher energy showers penetrate deeper into the atmosphere, hence their maxima are closer to the ground (smaller values). This parameter has a high discriminating power mainly at low energies. In fact, while the shower maximum height distribution has a single Gaussian shape for γ-ray events, it shows a second peak at the height of 2–3 km above the telescopes for low energy ($size < 300$ ph.e.) background events (for high energy background events the distribution has a single peak, but broader than the one for γ-ray events). This second peak is produced by single muon events. Figure 3.8 shows the distribution of the height of shower maximum in different *size* bins for data and MC simulated γ-ray and proton events (Aleksić J., et al., 2011b).

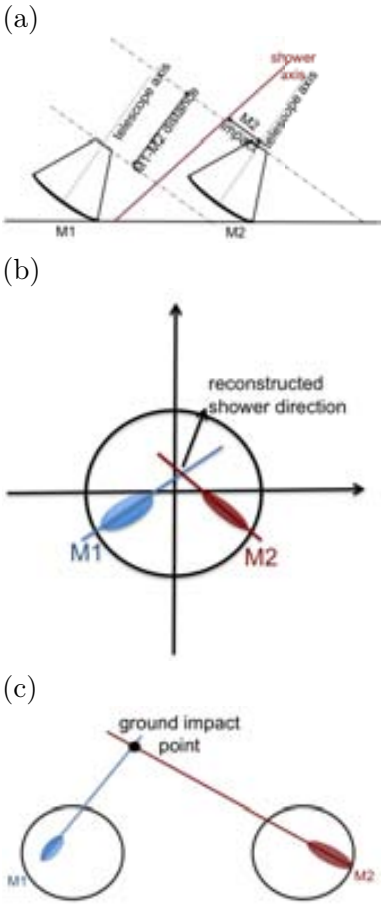

Figure 3.7: Shower axis reconstruction in a stereoscopic view. (a) Geometry definition. (b) Reconstruction of the shower direction as the intersection of the image major axes, once superimposed the two images. (c) Reconstruction of the shower impact point at ground. It is determined from the intersection of image major axes starting from the telescope positions.

- **Cherenkov radius**: the radius of the Cherenkov light pool on the ground. It is computed by assuming the Cherenkov light produced by a single electron of the shower at the height of the shower maximum and with an energy which is equivalent to the critical energy, 86 MeV.

- **Cherenkov photon density**: the photon density on the ground. It is evaluated under the same assumptions done for the previous parameter.

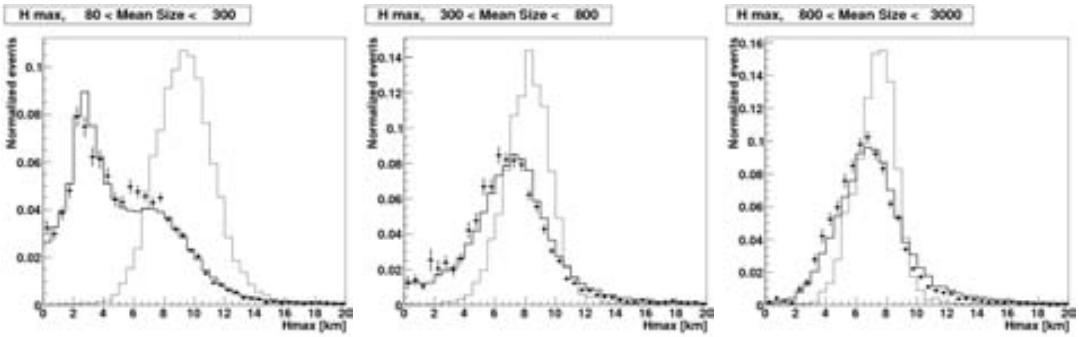

Figure 3.8: Shower maximum height distributions for different *size* bins for MC γ rays (dotted line), MC protons (full circles), and real data (solid line). *size* is expressed in ph.e.. Taken from Aleksić J., et al. (2011b).

3.6 Data quality checks

At this stage, the data files contain all the image parameters needed for the following analysis steps which lead to the signal detection and flux estimation. In order to guarantee stable and solid results, it is important to perform some checks on the data quality, and eventually reject "bad" data. The data quality can be affected by weather, hardware failures, and cars passing at the MAGIC site (car lights produce a rapid increase of the trigger rate for few seconds).

Most of the bad quality data are due to the atmospheric conditions during data taking. In fact, the transparency of the atmosphere to Cherenkov light is inversely proportional to the quantity of aerosols and aqueous vapors in the sky depending on the presence of clouds or calima[3]: the higher the density, the lower the rate of cosmic-ray events detected at ground.

Despite the fact that, for safety reasons, γ-ray ground-based telescopes do not observe when the weather is bad, the range of allowed atmospheric conditions is wide. This obliges us to define o ine data selection criteria which guarantee a data sample with good and constant quality. These criteria are mainly based on *Cloudiness* (§ 2.2.9) and rate of analyzed events ("analysis rate", after the image cleaning) scaled with the Zenith Angle (ZA). These two variables are not directly correlated because the automatic IPR control (§ 2.4.4) changes the DT levels in order to keep the trigger rate as much constant as possible (§ 2.4.4), and this affects the telescope's trigger threshold. In order to compute the correct data quality cuts, it is important to scale the rate dependence on the ZA. The trigger rate, and the analysis rate, decrease with increasing ZA for the following reason. The larger the ZA, the thicker the atmosphere along the path of the shower so the shower develops further away from the telescope and the area illuminated on the ground is larger. On one hand, this implies a larger detection area; on the other hand, it means that the density of the light which reaches the telescope reflector is lower. The empirical rate-ZA relation follows (Figure 3.9):

$$\text{rate} = \text{rate}_0 \cdot \quad \overline{\cos \text{ZA}} \tag{3.5}$$

[3]Calima is the high-altitude, ultra-thin Saharan dust transported by the wind from Africa.

where rate_0 is the rate at zenith.
Generally, the data selection criteria are:

- *cloudiness* $< 50\%$
- analysis rate within 20% of the mean value. This condition is first applied to data belonging to the same observation night in order to discard sporadic rate changes, due to cars or fast moving clouds. Later it is used for night-by-night observations in order to keep the rate of the entire data sample constant.

The range of the allowed parameters may depend on the goal of the analysis. For instance, a study of the flux variability of a new discovered source requires more stringent data selection cuts in order to prevent changing atmospheric conditions to induce fake variations of the source flux.

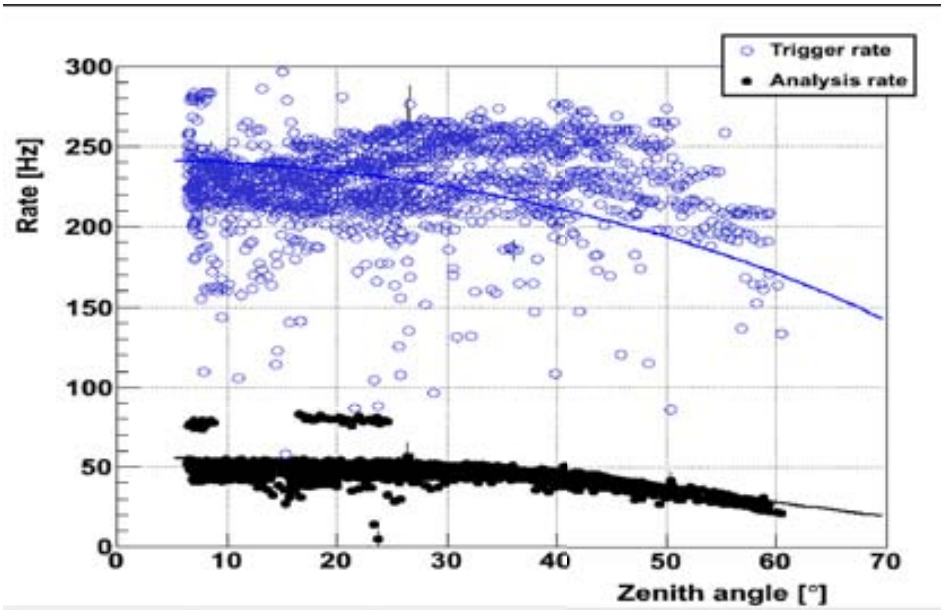

Figure 3.9: Empirical relation between rate and zenith angle.

The use of meteorological instruments (pyrometers, lidars...) during the γ-ray observations may help to quantify the effect of the atmospheric conditions on the data, and, as a result, to correct for it. At the moment, the only instrument available for the controlling of the atmosphere is a pyrometer. It provides a rough estimation of the sky quality evaluating the *cloudiness* parameter. While this information is sufficient to perform a data quality check, it cannot be used for the data correction and, for this reason, an elastic lidar is currently being commissioned at the MAGIC site.

3.7 γ/hadron separation

An IACT triggers on three different kinds of events:

- *accidental triggers*, mainly fluctuations of the signal due to background light, such as the NSB light, Moon light, or cars driving near the telescopes.

- *muons* with ultra-relativistic velocities hitting near the telescopes generate rings or sections of rings on the camera.
- *Extensive Atmospheric Showers* induced by hadrons or gamma rays.

Figure 3.10 illustrates the images formed on the camera of MAGIC II by each of these types of events.
In stand-alone telescope operation mode, the muon trigger rate is five times smaller than the hadron rate, and the accidental rate is lower than 1 Hz. In stereoscopic mode, it is at level of few Hz. Despite the coincidence trigger (§ 2.2.7) which exclude most of them, the trigger threshold of the two telescopes is much lower than the one of MAGIC I in stand-alone mode. The remaining and most important background contribution is due to the cascades of hadronic origin. This is why the selection of γ-ray events is often referred as γ/hadron separation.

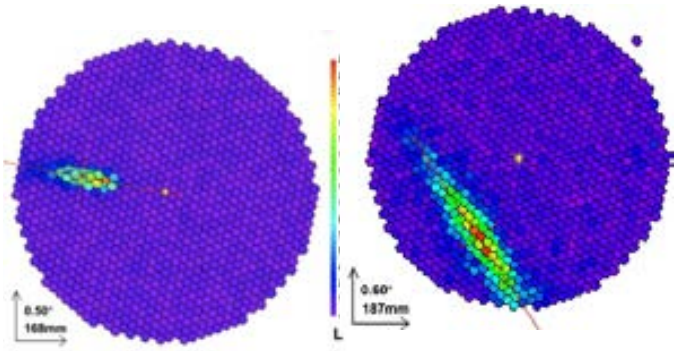

a) γ-ray candidate b) hadron candidate

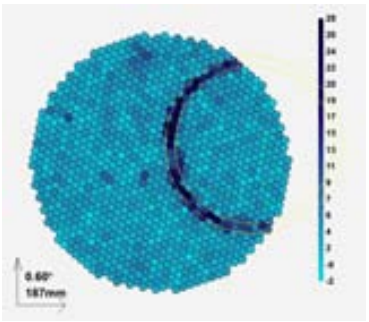

c) muon event

Figure 3.10: Example of Cherenkov images on MAGIC II camera.

γ/hadron separation is based on the image parameter distributions which reflect the varying development features of the hadronic cascades with respect to γ-induced ones. Once a set of parameters with high discriminating power is selected, the optimization of the cuts separating γ-ray from hadron candidates is performed and this leads to the definition of a global parameter, called *hadronness*. Images produced by γ-rays tend to produce a *hadronness* close to zero, whereas hadrons have a *hadronness* spread in the whole range from 0 to 1. *Hadronness* is estimated by means of a **Random Forest (RF)** algorithm (Albert, J., et

al., 2008c), a multi-dimensional classification system based on the construction of decisional trees. This is the most commonly used procedure for γ/hadron separation within the MAGIC collaboration, and also the most effective one according to Bock, R. K., et al. (2004).

The RF is first trained with events of known nature, *i.e.* MC simulated γ-ray events and hadron events extracted randomly from *off* data (§ 2.3.3). In order to avoid artifacts in the training, events in the hadron sample are selected in such a way that the shape of their *size* and ZA distributions matches that of the MC sample. RF uses a set of N high discriminating parameters to construct a large number (default 100) of decisional trees. If every parameter is considered as 1-dimensional vector, all the events are contained in an N-dimensional hypercube. A decisional tree grows as follows: once a starting point in the hypercube, and a starting parameter are selected at random, RF finds out the cut of the parameter which better separates both samples. The N-dimensional space is divided into two parts, called branches. The procedure is then repeated iteratively (another parameter is chosen, the corresponding optimized cut is selected, and the subsample split) so that the number of branches increases. The algorithm stops when a subsample composed only by one of the two initial categories of events (gammas or hadrons) is found; thus, the ending leaf of the tree is reached and it is labeled as 0 or 1 depending if it contains gamma or hadron events. The cut optimization is obtained by minimizing the *Gini index* (Gini, C., 1921). This index is expressed in terms of number of gammas, N_γ, number of hadronic events, N_{bg}, and total number of events, N, in the tree:

$$Q_{Gini} = 4 \cdot \frac{N_\gamma}{N} \cdot \frac{N_{bg}}{N} \tag{3.6}$$

Minimizing the *Gini index* corresponds to minimize the variance of the populations of γ-ray and hadronic events.

The application of the RF trees to the data sample to be analyzed constitutes the effective γ/hadron separation. Each real event has to pass through all the separating trees. For each tree the event is assigned with a value, 0 or 1, according to its characteristic parameter values and subsequently to the reached ending leaf. The average of all the obtained values over the N trained trees defines the *hadronness*. A *hadronness* distribution for background, and simulated MC γ-ray events is illustrated in Figure 3.11.

This γ-ray efficiency, ϵ_γ, is defined as the fraction of simulated MC γ-ray events between the number of events surviving all the analysis cuts, $N_{\gamma_{aftercuts}}$, and the total number of produced events, $N_{\gamma_{total}}$:

$$\epsilon_\gamma = \frac{N_{\gamma_{aftercuts}}}{N_{\gamma_{total}}} \tag{3.7}$$

The harder the cut, the better the background rejection, and the lower the gamma efficiency. Hard cuts are used for the search for signals where the gamma efficiency is not important.

3.8 Determination of the arrival direction: the Disp method

The arrival direction of the primary gamma ray can be determined in a rather straight-forward way in case of arrays of IACTs (§ 3.5.1), but requires a complex method based on MC simulations in case of stand-alone IACTs. It is the so-called *Disp method*, proposed by Fomin, V. P.,

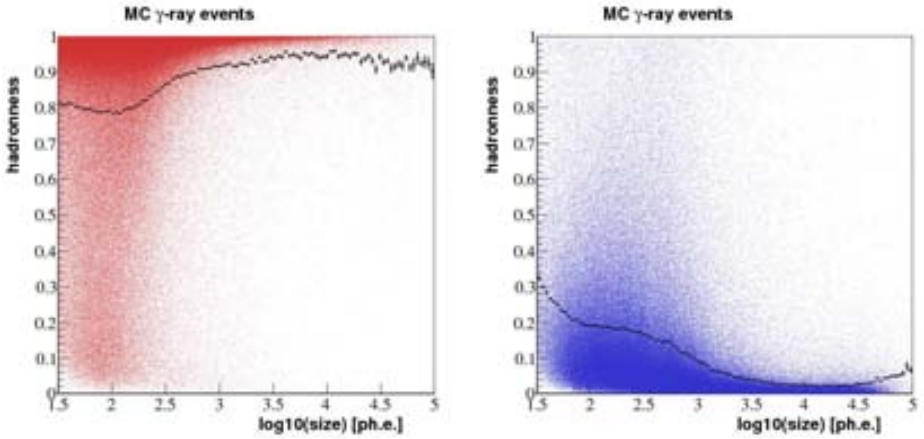

Figure 3.11: *hadronness* distribution as function of *size* . *On the left:* for a data sample; *On the right:* for a sample of simulated MC γ-ray events.

et al. (1994), and revised by Lessard, R. W. et al. (2001) within the Whipple collaboration. It was then applied in the data analysis of the HEGRA CT1 and MAGIC stand-alone telescopes (Kranich, D. & Stark, L. S., 2003; Domingo-Santamaria, E. et al., 2005).

Since the major axis of the image ellipse is the projection of the shower incoming direction on the camera plane, the source position lies on this axis at a certain distance from the image CoG. This distance, *disp*, can be estimated from the shower elongation ($width/length$) as follows:

$$disp = \mathrm{A}(size) + \mathrm{B}(size) \cdot \frac{width}{length + \eta(size) \cdot leakage2} \tag{3.8}$$

The correction term added to *length* accounts for the truncation of large images at the edge of the camera (expressed in terms of the *leakage* parameter, § 3.5). Also a second order polynomial dependence of the parameters on the logarithm of the image *size* is included. The optimization of the coefficients A, B, and η with MC data permits to estimate the *disp* parameter for each event. However, once the *disp* is known, the reconstructed source position is not univocally determined. As shown in Figure 3.12 there are two possible solutions along the major axis of the ellipse which can only be disentangled thanks to the ghost-busting parameters described in § 3.5.

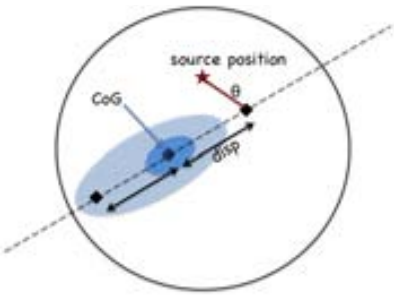

Figure 3.12: Schematic view of two possible solutions determined by the *Disp* method.

This *Disp method* based on the parametrization is not very efficient at high energies, where image truncation affects a large fraction of events. This means that the implementation of the correction factor is not accurate. Since the shower elongation-*disp* correlation invokes a multi-parameters space, a new method based on the RF algorithm has been implemented in the standard MAGIC analysis chain for mono data (hereafter *Disp RF*). The *Disp RF* is trained over a sample of simulated γ-ray events for which the correct source position, as result the *disp* parameter, is known. It grows a large number of decisional trees (§ 3.7) to estimate the correlation between disp and a set of given parameters. The optimal cut in each node

of the tree is decided minimizing the variance of the *disp* of the events of the split samples. Besides those parameters used in the above-described parametrization, and the ghost-busting ones (§ 3.5), new variables showing strong correlation with disp, can be used. These additional variables need to be source independent though, in order to avoid biases in the estimation of the source reconstruction. Since the *dist-time gradient* correlation, explained in § 3.5, can be interpreted as *disp-time gradient* correlation and, in this latter case, no assumption on the source position is necessary, the *time gradient* has been added to the RF set of parameters. It yields an improvement in the angular resolution, hence in the sensitivity by 20-30% (Aleksić, J., et al., 2010b).

The *Disp RF* method is also applied in the analysis of stereo observations. First, the *disp* parameter is calculated for all the events in each telescope separately. For each of two images, there are two possible reconstructed source positions along their major axis.

Figure 3.13 shows the situation once the two images on a camera plane are superimposed. The head/tail discriminators suggest the correct solution for each image (green point in the figure). If they coincide, the source position is easily reconstructed. At low energies, however, the performance of the ghost-busting parameters is so poor that many events would be discarded. Thus, a more efficient algorithm was implemented in the standard analysis chain. It determines the correct pair of positions without using the ghost-busting parameters. In fact, it evaluates the distance between all the four possible combinations of positions pairs, and chooses the closest pair only if its distance is smaller than a certain value (the only parameter of this algorithm). If none of the pair combinations satisfies this condition, the event is then rejected. This algorithm does not depend on the crossing position (§ 3.5.1), and therefore it works for all the image angles (also for parallel images).

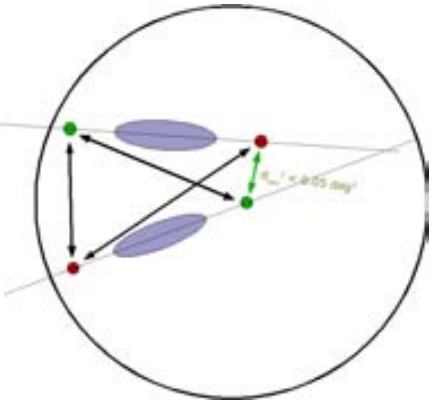

Figure 3.13: Sketch of the stereo *disp* algorithm. Once superimposed the two images, each of them has two possible reconstructed source positions, the favored one is drawn in green. Figure by S. Klepser.

The stereo reconstructed position is determined as the weighed average of the chosen pair of positions. From now on this procedure will be referred as *stereo Disp method*.

The *Disp method* provides an unbiased way to estimate the source position on the camera plane, since it does not require any assumption on the source position (source-independent analysis). In addition, it leads to the definition of a new image parameter: θ, defined as the angular distance between the reconstructed and the expected position of the source on the camera plane. The square of this parameter, θ^2, is more common. It is used because, while the θ^2 distribution is peaking at small values for γ-ray events, which point towards the source position, it is flat for hadronic events. This is due to simple geometrical reasons: the number of background events, which is independent of the arrival direction, is proportional to θ^2.

3.9 Signal detection

The distributions of the image parameters *alpha* and θ^2 (called *alpha plot*, § 3.5, and θ^2 *plot*, § 3.8, respectively) peak at small values for the γ-ray events, and flatten up for hadrons. For this reason, they define the geometrical space where to search for a γ-ray signal, defining the so-called signal region.

Choosing *alpha* rather than θ^2 depends on the kind of analysis that one wants to perform. A source-independent analysis is normally based on the θ^2 distribution, and employs image parameters whose definition does not depend on an a priori known source position. The θ^2 is reconstructed through the unbiased *Disp method* (§ 3.8). Also the RF for the γ/hadron separation is trained only with source-independent parameters. A source-dependent analysis, also known as *alpha analysis*, relies on an a priori assumption on the source position on the camera plane, which is needed for the calculation of the *alpha* parameter itself. This assumption permits to exploit source-dependent parameters, mainly *dist*, as additional discriminating variables in the RF for the γ/hadron separation. In addition, the introduction of the time parameters, such as the *time gradient* which is so strongly correlated with *dist* (§ 3.5), yields to a significant improvement of the analysis performance (Aliu, E., et al., 2009). Therefore, the *alpha analysis* is more performing than the θ^2 one in case of point-like sources with known positions and observed with a stand-alone telescope (mono data analysis). This does not apply to the stereo data analysis, which takes advantage from the powerful discriminating, source-independent stereoscopic parameters.

In searching for a γ-ray signal in a data sample (*on* data), the gamma selection cuts (mainly the *hadronness* cut) are applied, and the number of events within the signal region, N_{on}, counted. Among these γ-ray candidate events there some with a hadronic origin. In order to estimate the amount of these hadrons which survive all the selection cuts, an independent data sample with no expected signal (*off* sample) is used. The same analysis chain and same selection cuts as for the *on* data are applied to the *off* sample. In this way the number of background events, N_{off}, in the signal region is obtained. The number of γ-ray events, "excess events" N_{ex}, is defined as the difference between N_{on} and the scaled N_{off}:

$$N_{ex} = N_{on} - \alpha \cdot N_{off} \tag{3.9}$$

where α is the normalization factor between the *on* and the *off* samples. α is defined as the fraction of *on* events over *off* events in a region far away from the signal region and the distribution tails[4]. To test the null hypothesis (*i.e.* that all the observed excess events, N_{ex}, are compatible with background fluctuations) the Equation number 7 in Li, T.P. & Ma, Y.Q. (1983) is used. It defines the significance N_σ:

$$N_\sigma = \overline{2}\left(N_{on} \cdot ln\left[\frac{1+\alpha}{\alpha}\left(\frac{N_{on}}{N_{on}-N_{off}}\right)\right] + N_{off} \cdot ln\left[(1+\alpha)\left(\frac{N_{off}}{N_{on}-N_{off}}\right)\right]\right)^{1\ 2} \tag{3.10}$$

Figure 3.14 shows an example of the strong signal coming from the Crab Nebula (detected with two different data samples) by using the *alpha* distribution and the θ^2 distribution.

The *off* data sample depends on the observation mode (§ 2.3.3). If the *on* data are taken in *tracking* mode, the *off* sample consists of a completely independent data sample which

[4]The normalization region in the *alpha plot* spans from 20° 80° , whereas in the θ^2 *plot* from 0.1° 0.3° .

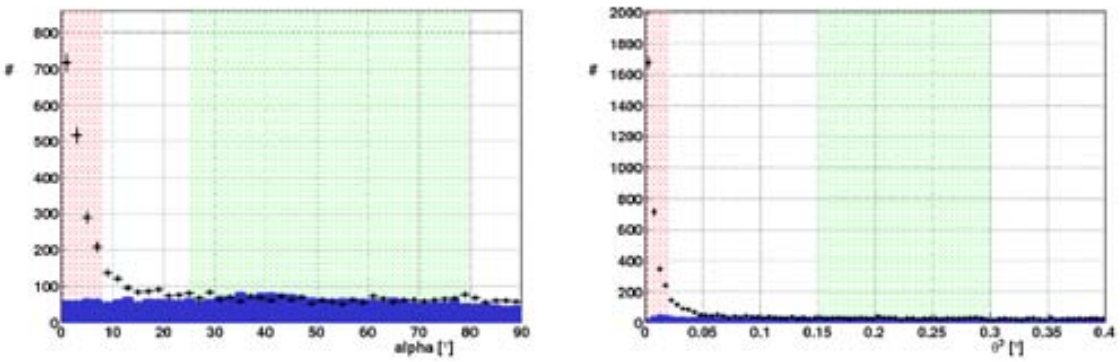

Figure 3.14: Example of detection of a signal from the Crab Nebula *On the left:* with an *alpha plot*; *On the right:* a θ^2 *plot.* The green shadow areas identify the normalization regions, whereas, the red ones the signal regions.

contains no γ-ray signal. This *off* sample has to be recorded under the same conditions (moonlight, telescope performance, zenith angle) as the *on* data sample. Finding an *off* sample perfectly compatible with the *on* one, and large enough to have at least the same statistics as the *on* one is, however, complicated, and it constitutes the main draw-back of such an observation mode.

For *wobble* observations, *on* and *off* samples are extracted from the same data. The *on* region corresponds to the source position on the camera plane, while the *off* region is centered at a position which is opposite to the source one with respect to the camera center. Within the telescope's angular resolution, the *off* region is defined far enough from the the *on* region so that no γ-ray events from the putative source contribute the *off* data sample. It is also possible to have two additional *off* regions corresponding to the rotation by $\pm 90°$ of source position with respect to the camera center. The geometrical distribution of the *on* and the *off* regions on the camera plane is shown in Figure 3.15. There are two main cases in which the use of just one *off* region is preferred despite its larger statistical error:

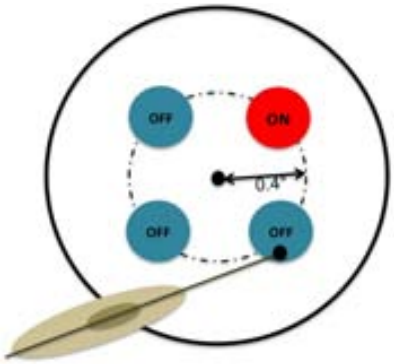

Figure 3.15: Sketch of the definition of the *on* and *off* regions in *wobble* observations.

- in case of strong sources where signal events can contaminate the *off* distribution. This effect is clearly seen in the *alpha plot* of Figure 3.14 where the *off* distribution shows a bump at angles 30°–40° .

- in case of low energy signals where the camera asymmetries can create a significant mismatch between the two additional *off* positions and give rise to false signals.

In the particular case of *wobble* observations, the normalization factor is geometrically defined as 1/number-of-*off*-regions.

3.9.1 Sensitivity

The performance of the analysis can be quantified also in terms of sensitivity. The sensitivity of ground-based γ-ray telescopes is usually defined as the γ-ray flux that will detected with a significance of 5η after 50 hrs of observation. It is, however, not common to use Equation 3.10 to compute the sensitivity, but instead a Gaussian approximation of it. The resulting number of standard deviations for a given observation time t is:

$$N_\sigma(t) = \frac{\overline{t}}{\mathrm{T}} \cdot \frac{\mathrm{N_{ex}}}{\overline{\mathrm{N_{off}}}} \tag{3.11}$$

where T is time in which N_{ex} and N_{off} were measured. If one considers t = 50 hrs and 5η detection as required by the standard definition, the sensitivity is expressed in terms of percentage of the Crab Nebula flux as $5\eta/N_\sigma(50\mathrm{hrs})$.

Since the performance of the telescope is variable on time scales of 6/months-1/year, the sensitivity is usually estimated using a reference Crab Nebula sample taken under observation conditions which are similar to the ones of the analyzed data sample (ZA, weather conditions, observation epoch to guarantee same telescope performance). The Crab Nebula is a well-known γ-ray source considered as the standard candle of the VHE γ-ray astrophysics due to its strong and stable emission in this energy band. This reference sample is used to estimate the sensitivity of the performed analysis.

3.9.2 Cut optimization

The selection of γ-ray candidates is performed through a cut on the *hadronness* parameter and a cut which defines the signal region (either an *alpha* or a θ^2 cut). These gamma selection cuts are optimized by maximizing the signal significance of the Crab Nebula reference data sample in the 2-dimensional parameter space. However, if the analyzed source is expected to have a much lower flux than the reference source, the number of excess events is scaled down to a value close to the expected flux level. In this way, the different signal-to-noise ratio is taken into account.

In addition to the gamma selection cuts, a minimum cut in the *size* parameter is applied throughout the whole analysis chain. The *size* cut rejects the small images for which the γ /hadron separation does not work. In addition, it reduces the effect of the camera inhomogeneities (§ 2.2.7) which mainly affect low *size* events. Therefore, the *size* cut guarantees a better performance of the analysis with the important trade-off of increasing the energy threshold of the analysis (§ 3.11): most of low energy events are, in fact, excluded by this cut.

3.10 Sky maps

Sky maps are histograms containing the arrival directions, in sky coordinates, of all γ-candidate events (events which survive the gamma selection cuts) after the subtraction of the expected background. Sky maps are produced by using the *Disp method* which reconstructs the shower arrival direction in an unbiased way (§ 3.8).

A special attention must be paid to the background subtraction because of the non-homogeneous camera acceptance, and the different star fields. This effect is simplified in case of *wobble* observations (§ 2.3.3), where the background is estimated from the same data set. The camera is divided into two halves: the source lies in one of the camera halves in the first *wobble* pointing, and in the other half in the second *wobble* position. Thus, only those events whose arrival directions lie in the half of the camera that does not contain the source are used for the background estimation (Errando, M., 2009). The obtained sky map of excess events is finally smoothed using a Gaussian function with σ equal to the angular resolution (§ 2.2.3). An example of a sky map obtained from a Crab Nebula data sample is shown in Figure 3.16.

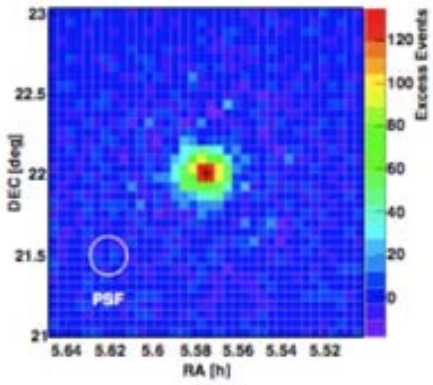

Figure 3.16: Example of sky map obtained from a Crab Nebula data sample, taken from Albert, J., et al. 2008d.

Sky maps of well known point-like sources are also used to check the instrument mispointing. The mispointing can be corrected by using the pointing information from the starguider system (§ 2.2.2).

3.10.1 Angular resolution

A point-like γ-ray source yields a sky distribution well fitted by a 2-dimensional Gaussian, whose standard deviation defines the instrument angular resolution, also known as γ-ray PSF. This PSF corresponds to radius containing 39% of γ-ray events from a point-like source. Figure 3.17 shows the stereo angular resolution, and, for completeness, it includes also the 68% containment radius. The stereo angular resolution is as good as 0.07° at 300 GeV, and even better at higher energies.

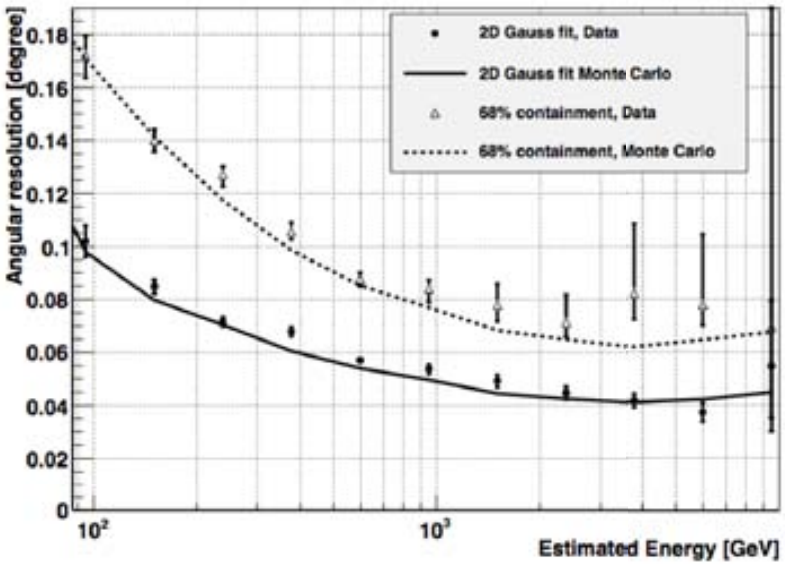

Figure 3.17: Angular resolution. for stereo analysis. Taken from Aleksić J., et al. (2011b).

3.11 Energy estimation

The energy estimation in the standard MAGIC analysis chain can be performed either by means of a RF or by using LUTs. The second method was introduced for the stereoscopic analysis and it became the standard option for such an analysis thanks to its faster processing time. The RF, however, can still be applied and provides a useful cross-checking tool. In the following, both methods will be described, since the first one was used for the analyses of mono data and the latter for stereo analyses.

The RF for the energy estimation is trained over a sample of MC γ-ray events whose energy, E_{true}, is known. The parameters considered in the RF are mainly *size*, *zenith angle*, and *conc*. *Shower maximum height* and *impact parameter* can be added in case of stereo observations. Also *leakage* is included to account for the image truncation at high energies. The decisional trees of the RF algorithm are built as described in § 3.7 with the only difference on how the optimal cut in each tree node is chosen. It is the cut which minimizes the variance of the E_{true} of the events in the split samples.

The energy LUTs are based on a simple model describing the distribution of the Cherenkov photons on the ground. This model relies on the *Cherenkov radius*, r_C, and *Cherenkov density*, α_C, (refer to § 3.5.1 for the parameter definition). The LUTs are built, independently for each telescope, by dividing a sample of simulated MC gammas, with known E_{true}, in bins of *size*, and $impact/r_C$. Since the energy of the primary γ-ray is proportional to $size/\alpha_C$, each of the table bins contains the mean value of the distribution of $E_{true} \cdot \alpha_C/size$ with an error which is given by the RMS of the distribution. The final energy estimation, E_{est}, is the weighted average value obtained from both telescopes, where the weight is given by the uncertainty associated to the corresponding bin. E_{est} is then corrected for the ZA: the empirical correction factor is $0.4 \cdot \cos(ZA)$.

3.11.1 Energy resolution

The *energy resolution* is defined as the η of a Gaussian fit to the peak of $(E_{est}\text{-}E_{true})/E_{true}$ distribution. This value provides an estimation of the goodness of the energy reconstruction for the bulk of events excluding all the outliers. The difference from zero of the peak of the $(E_{est}\text{-}E_{true})/E_{true}$ distribution gives the mean *energy bias*. The energy reconstruction is as good as it is close to the zero value. MAGIC I mono analysis has a resolution around 25% between 200 GeV and 1 TeV. On the other hand, for stereo analysis it is as good as 15% in the same energy range. The estimated energy of low-energy primary gammas is typically overestimated (positive *energy bias*) at low energies (below 200 GeV), and at very high energies (above some TeV). Figure 3.18 illustrates the *energy resolution and bias* as function of E_{true} for the stereo analysis.

The *energy threshold* of the analysis is defined as the peak of the E_{true} distribution either before or after applying the gamma selection cuts (§ 3.9).

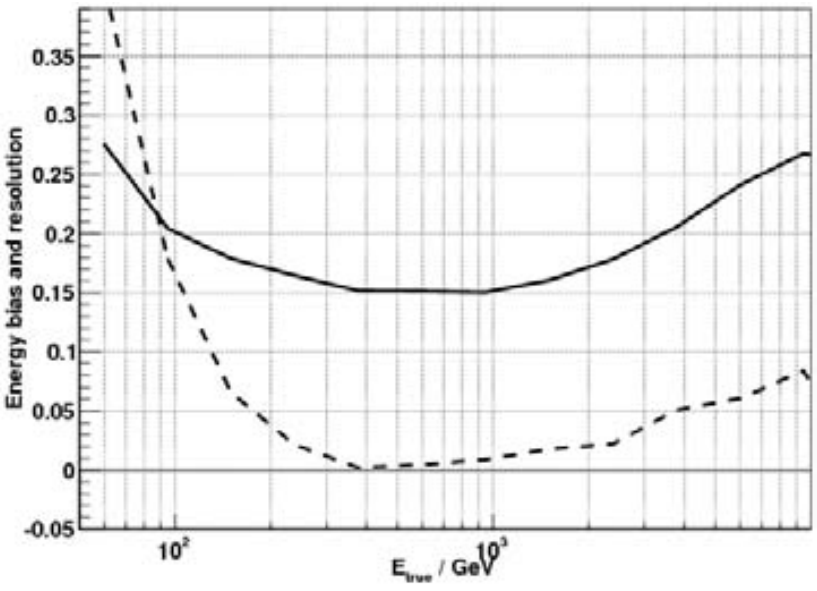

Figure 3.18: Energy resolution and bias. for stereo analysis.

3.12 Spectrum calculation

The differential γ-ray energy spectrum is defined as:

$$\sigma(\mathrm{E}) = \frac{\mathrm{dN}_\gamma}{\mathrm{dE} \cdot \mathrm{dA}_{\mathrm{eff}} \cdot \mathrm{dt}_{\mathrm{eff}}} \qquad [\text{photons TeV}^{-1}\ \text{cm}^{-2}\ \text{s}^{-1}] \tag{3.12}$$

where N_γ is the number of detected γ rays, t_{eff} is the effective observation time, and A_{eff} is the effective collection area.

- **Effective observation time**: it is the time in which the telescope was effectively recording events. Due to the dead time of the detector (§ 2.2.6), the effective observation time does not coincide with the real observation time.

  As the distribution of cosmic events in time follows a Poissonian distribution, the distribution of time differences, t, between successive events has an exponential behaviour:

  $$\frac{\mathrm{dN}}{\mathrm{d(t)}} \quad e^{-\lambda t} \tag{3.13}$$

  where ϕ is the ideal average event rate (no dead time). By fitting the measured time difference distribution with the function 3.13 for t larger than the maximum dead time, the ϕ parameter can be estimated, hence $\mathrm{T}_{\mathrm{eff}} = \mathrm{N}^{\mathrm{meas}}/\phi$ with $\mathrm{N}^{\mathrm{meas}}$ total number of measured events. More details about the calculation of the effective observation time can be found in Wittek W. (2002).

- **Effective collection area**: it is the geometrical area around the telescope where a γ-ray shower produces a trigger, $\mathrm{A}_{\mathrm{sim}}$, folded with the analysis efficiency in detecting γ-ray events, ϵ_γ (refer to § 3.7 for its definition). It mainly depends on the γ-ray energy and the zenith angle of the observation, whose effect has been already discussed in § 3.6.

The effective collection area A_{eff}, defined as:

$$A_{\rm eff}(E\ ZA) = A_{\rm sim} \cdot \epsilon_\gamma = A_{\rm sim} \cdot \frac{N_{\gamma aftercuts}}{N_{\gamma total}} \qquad [m^2] \tag{3.14}$$

is computed by using MC γ-ray events and their original energy, E_{true}. In Figure 3.19 the typical effective collection area for MAGIC stereoscopic observations is displayed. The trigger probability increases very fast at low energies until all showers within the light pool generate enough light to trigger the telescope, and then the effective collection area remains almost constant.

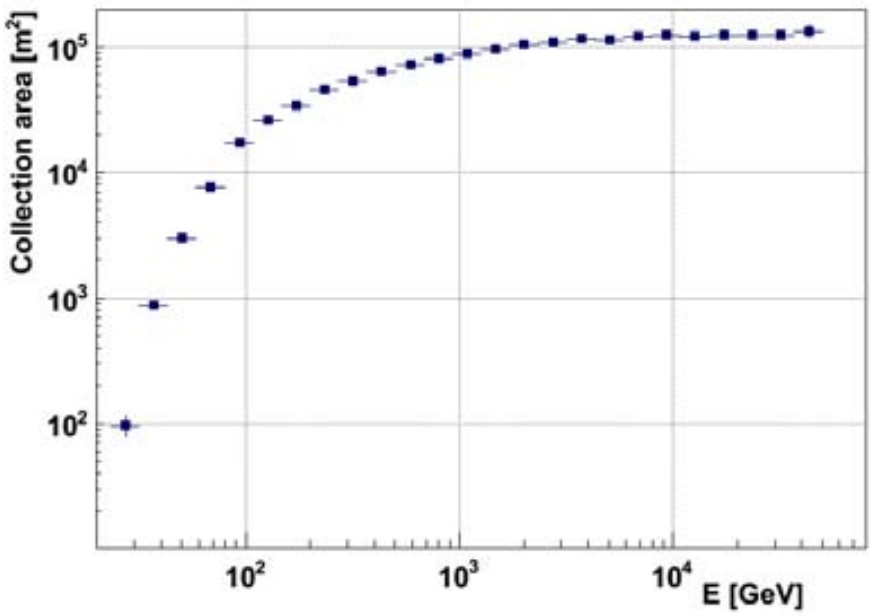

Figure 3.19: Typical effective collection area for stereoscopic observations at low zenith angles (ZA $< 30°$).

- **Number of excess events**: it is computed, for each energy bin, through either the *alpha* or the θ^2 distribution according to the kind of performed analysis (§ 3.9). The γ/hadron separation cuts, mainly *hadronness*, and *alpha*/θ^2 cuts, are determined separately bin-by-bin in order to obtain a constant cut efficiency around 70-80%. Such a large cut efficiency leads to the definition of much looser cuts with respect to the ones optimized for the signal extraction (§ 3.9). The main reason for this choice is that it guarantees a better agreement between MC and data, hence provides a correct estimation of the effective area.

The maximum number of energy bins used to determine a spectrum depends on the energy resolution which defines the minimum size bin, but also on the flux strenght of the source which determines the number of excess events for each energy bin. When fitting the spectrum, in fact, the significance of each spectral point is required to be at least 1.5η. Therefore, while for strong sources, like the Crab Nebula , the first condition on the energy resolution is the most constraining one, it is exactly the opposite for weak sources (10% of the Crab Nebula flux).

3.13 Spectral unfolding

The unfolding procedure permits to estimate a real/true observable by correcting the measured one from its natural distortions due to the finite resolution of the detector. In the particular case of an IACT, the image size (the sum of the charge, in ph.e., of all involved pixels contained in the shower image) is measured, the estimated energy (E_{est}) is then computed by means of statistical algorithms, but the event true energy (E_{true}) remains undetermined. Nevertheless, since the detector response can be described by the function $M(x\ y)$, the measured distribution, $g(y)$, can be written in terms of the true distribution, $f(x)$:

$$g(y) = \quad M(x\ y)f(x)dx + b(y) \tag{3.15}$$

where y indicates the estimated energy and x the true energy. Therefore, the aim of the unfolding procedure is to determine f given M and g. Being not analytically solvable, the problem is discretized:

$$y_i = M_{i\,j}x_j + b_i \qquad y = M \cdot x + b \tag{3.16}$$

The M matrix, also called *migration matrix*, is computed from a 2-dimensional plot of the number of γ-ray MC simulated events in the E_{true} –E_{est} plane. $M_{i\,j}$ indicates a sort of probability that events with true energy in bin j are measured in bin i of estimated energy due to the finite energy resolution of the detector. Figure 3.20 shows an example of migration matrix calculated with the standard MAGIC software which normalizes in bins of E_{true}. Generally M is not a squared matrix, because the binning in E_{est} might be different from the one in E_{true}.

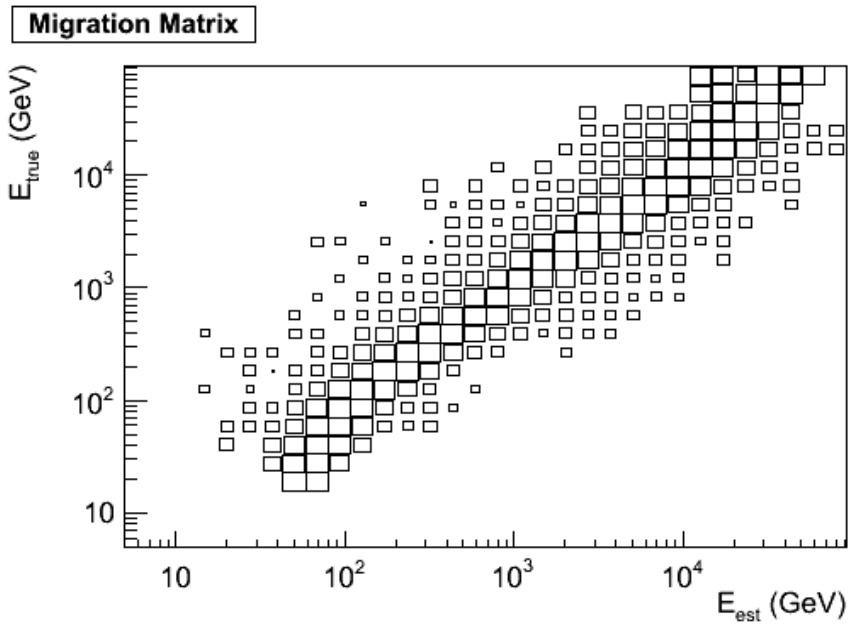

Figure 3.20: Example of migration matrix.

The unfolding does not take into account event losses due to the limited acceptance of the detector, or to trigger conditions. These losses, also estimated using MC γ-ray events, are included in the effective area.

There are different approaches to find the solution for x (Albert, J., et al., 2007c):

- **Unfolding with regularization**. It is based on the inversion of the migration matrix, which, however, is often not invertible. In this latter case, minimization methods, *i.e.* least square method, can provide the wanted solutions, as those x which, after folding with M, are most compatible with y. Although technically correct, the solution usually leads to large fluctuations making the distribution of the E_{true} differ from the physical one, hence useless. The remedy to this problem is regularization: adding a regularization term to the least square expression (γ_0^2) allows to smoothly suppress those insignificant coefficients[5] of the solution which are the cause of the large fluctuations (Anykeyev et al., 1991).
$$\gamma^2 = \gamma_0^2 + \frac{\theta}{2} Reg \tag{3.17}$$
Large values of θ, corresponding to no regularization, often produce noisy spectra which perfectly fit the data. On the other hand, small values of θ, indicating high level of regularization, yield to smooth unfolded distribution which can strongly deviate from the data. Thus, selecting the appropriate value for θ is very important.
In MAGIC, there are several unfolding methods which differ for the way the regularization is implemented. The most used ones are Tikonov, A.N. & Arsenin, V.J. (1979), Schmelling, M. (1998), and Bertero, M. (1989). The agreement within these methods is required to be confident on the results.

- **Forward unfolding**. It consists of parametrizing x as an analytic function which is a priori assumed (the assumed energy spectrum, in the treated particular case) and minimizing γ_0^2 with respect to these parameters. The minimization is generally solved analytically forcing the solution to be continuous. The parametrization can be interpreted as a regularization, leading to a suppression of the noise component of x, but no explicit regularization is done. It is not a real unfolding because its result is just the best fit, with corresponding errors, obtained using a priori assumed parametrization. Thus, the forward unfolding should only be used to check the results obtained with other unfolding methods.

3.14 Light curves

Light curves show integral γ-ray fluxes, in a considered energy range [E_0 E_1], as a function of time. The integral fluxes in the time intervals [T_i T_j] are computed from Eq. 3.12:

$$\Phi(E) = \int_{T_j}^{T_i} \int_{E_0}^{E_1} \sigma(E)\, dE\, dt \qquad [\text{photons cm}^{-2}\ \text{s}^{-1}] \tag{3.18}$$

and they can be negative in case of a negative statistical fluctuation of the number of excess events. In this case ULs to the integral flux are provided instead of flux points (§ 3.15).

The number of time bins is mainly determined by the statistics of the signal. Once the time bins are defined, the light curve is obtained by calculating, for each time bin, the number of excess events in the considered energy range. The effective collection area is computed for each time bin separately by using MC γ-ray events having a zenith angle distribution which resembles the one of the data in the considered time bin.

[5] Mainly the eigenvalues of the covariance matrix of $\vec{y}$ (after having been transformed to a diagonal matrix).

Since no real unfolding is applied to light curves, the effect of the finite energy resolution of the detector (*i.e.* the mismatch between the estimated energy, E_{est}, and the true one, E_{true}) are taken into account by expressing the effective collection area in terms of E_{est}. Using the same notation as for Eq. 3.19, it is calculated as follows. The geometrical area, A_{sim}, remains expressed in terms of E_{true}, as well as the total number of simulated γ-ray events, $N_{\gamma total}$, in the considered energy range. The number of γ-ray events surviving the gamma selection cuts in the given energy range is computed by using the estimated energy and it has to be weighted with the spectral shape.

$$A_{eff}(E_{est}) = A_{sim}(E_{true}) \cdot \frac{N_{\gamma aftercuts}(E_{est})}{N_{\gamma total}(E_{true})} \tag{3.19}$$

The choice of the lower energy limit is fundamental. On one hand, the effective collection area is very sensitive to small fluctuations in the energy reconstruction (mismatches between true and reconstructed energy) at low energies. On the other hand, due to the falling power-law spectra, the low energy events dominate the emission in the considered energy range. A lower energy limit at the beginning of the collection area plateau is normally safe.

3.15 Upper limits

Whenever no significant signal is found, ULs to the integral or differential flux of the source can be derived with a certain Confidence Level (CL).

From the measured quantities: number of excess events, N_{ex}, which, in this case, can be also negative, and number of background events, N_{bg}, one can estimate the UL on the number of excess event, N_{ex}^{UL}. This calculation is performed in two steps. First, under the hypothesis on the mean number of excess events μ_{ex} and background events μ_{bg}, the Probability Density Function (PDF) for N_{ex} is constructed: $P(N_{ex} \mid \mu_{Ex};\ \mu_{bg})$. The confidence interval $[N_{ex}^{low},\ N_{ex}^{up}]$ is defined as the range out of which would lie the result N_{ex} of only a percentage α of measurements (carried out under the same conditions):

$$P(N_{ex} \in [N_{ex}^{low};\ N_{ex}^{up}] \quad | \quad \mu_{ex};\ \mu_{bg}) = 1 - \alpha \tag{3.20}$$

The limit μ_{Ex}^{up} can be directly interpreted as upper limit on N_{Ex} at the CL=100(1-α). In fact Later, this PDF has to inverted in order to find the PDF for μ_{Ex} given N_{Ex} and N_{bg}: $P(\mu_{Ex} \mid N_{ex};\ N_{bg})$. The letter problem can be solved either through a Bayesian (Helene, O., 1983) or a frequentist approach which is the one adopted within the MAGIC collaboration. It is based on Feldman, G. J. & Cousins, R. D. (1998) which proposes the construction of a confidence belt: for each μ_{Ex} a confidence interval is derived, (Figure 3.21). Given a value of N_{Ex}, the confidence interval can then be inverted to obtain limits $[\mu_{Ex}^{low},\ \mu_{Ex}^{up}]$ satisfying:

$$P(\mu_{Ex} \in [\mu_{Ex}^{low}, \mu_{Ex}^{up}] \quad | \quad N_{Ex};\ N_{bg}) = \alpha \tag{3.21}$$

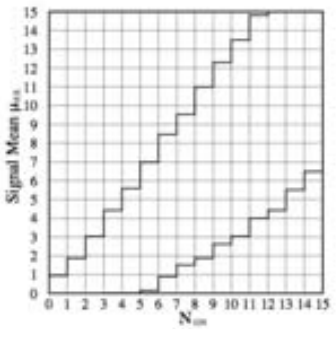

Figure 3.21: Confidence belt. Taken from Neyman, J (1937).

in (1-α) of the cases the μ_{Ex} will fall within the found range.
Rolke et al. generalized Feldman's method including a probability model for the background (Rolke, W. A. & López, A. M., 2001) and for the overall efficiency (Rolke, W. A. et al., 2005).

The latter work is used as reference in MAGIC for the UL calculation.

The chosen CL is 95% and the assumed systematic uncertainty is 30% . The latter includes also systematic errors on the analysis methods, such as changes in the efficiency. Therefore, the efficiency is assumed to be constant and equal to 1. Any deviation from these settings are explicitly stated in this thesis work.

The estimation of the ULs to the differential flux at the mean energy E_0 requires some assumptions. In fact, if no signal is detected, nothing else is known about the source itself. Therefore,

- the energy differential spectrum is assumed as $\sigma(E) = K \cdot S(E)$. Usually it is given by a power-law spectrum with a photon index α=2.6 (Crab-like spectrum):

$$\sigma(E) = K \cdot \left(\frac{E}{E_0}\right)^{-\alpha} \tag{3.22}$$

- the time evolution of the possible emission is assumed to be constant over the period of observation.

Under the above-mentioned assumptions, the integral flux can be expressed as:

$$K \int_{E_0} S(E)\, dE = \frac{\int_{E_0} dN_\gamma}{\int_{E_0} \int_0^{T_{obs}} A(E)\, dE\, dt} \tag{3.23}$$

where T_{obs} is the effective observation time. Thus, the UL to integral flux is given by:

$$K^{UL} < \frac{N_{Ex}^{UL}}{T_{obs} \cdot \int_{E_0} S(E)\, A(E)\, dE} \quad [\text{photons TeV}^{-1}\ \text{cm}^{-2}\ \text{s}^{-1}] \tag{3.24}$$

The integral over the effective area is the weigthed effective area average $< A_{eff} >$.

3.16 Systematic uncertainties

In addition to the statistical errors, the measurements of γ-ray differential energy spectra, and light curves are affected by systematic errors. The systematic uncertainties can be depending on which observable they affect: the energy scale, the flux normalization or the spectral slope. All the uncertainty estimations provided in the following were taken from Aleksić J., et al. (2011b), unless differently stated. They are summarized in Table 3.3.

- **Sources of systematic uncertainty on the energy scale:**
  - **MC atmospheric simulations**. MC simulations use a fixed atmosphere model (§ 3.1) which does not match the atmosphere at the Roque de los Muchachos Observatory perfectly. This can produce an effect as large as 3% (Albert, J., et al., 2008d). In addition, the model does not take into account seasonal variations. The average atmospheric values between Summer and Winter change by about 15% the transmission of the atmosphere though (Bernlohr, K., 2000).
  - **Atmospheric transmission losses**. Changes in the atmospheric transmission due to Mie scattering introduce an additional uncertainty in the energy scale.

After tight data quality (§ 3.6) cuts, this uncertainty is estimated of the order of 5%.

- **Light losses**. Light losses can be due to a worsening of the mirror reflectivity, or a degradation of the camera entrance window and the Winston cone light guides. Both of them can be caused by dust deposit. Light losses can be adjusted in the MC simulations. Nevertheless, due to malfunctioning of the AMC (§ 2.2.3), the light losses can vary from one night to another, and this introduces a systematic uncertainty on the energy scale of about 8%. This value was estimated by using reflected star images and the analysis of the muon images.
- **Signal extraction**. The method used for the signal extraction (§ 3.3) both in MAGIC I and MAGIC II produces an uncertainty in the number of ph.e. lower than 3%. This number was estimated by varying different windows of the signal extractor.
- **F-factor**. The F-factor method (§ 3.3) used for the signal calibration introduces a 10% effect on the energy scale.
- **Temperature dependence of the gain**. This produces a 2% effect on the energy scale.
- **PMT performance**. There are calibration uncertainties in the QE measurements of the PMTs ($\equiv$ 4%), in the estimation of the electron collection efficiency of the first dynode ($\equiv$ 5%) and in the evaluation of the light collected in the Winston cone (4%).
- **Flat-fielding of the camera**. The fact that the flat-fielding (§ 2.2.5) is done only at one wavelength and that it can be influenced by temperature drifts produces a 6–8% systematic effect on the energy scale at low energies and a smaller 2% effect at high energies (above $\equiv$ 300 GeV).

• **Sources of systematic uncertainty on the absolute ux**:

- **Background subtraction**. Dead pixels, stars in the FoV, as well as trigger inefficiencies make the camera highly inhomogeneous. On top of it, the stereo trigger produces a natural inhomogeneity. The stereo FoV can be treated as the overlapping region between two cones (not a circular area) originating from both telescopes. This results in an enhanced amount of triggered events in the direction given by the position of the second telescope and can lead to a 10–15% variation on the background estimation. However, this effect is reduced down to 1% uncertainty by wobbling the source position (§ 2.3.3) and estimating the background from the corresponding anti-source position (§ 3.9). This uncertainty depends on the ratio between excess and background. Therefore, it plays a different role depending either on strenght of the source flux or on the energy: the lower the energy, the higher this systematic error.
- **MC-data agreement**. Differences between simulated and real γ-ray showers may lead to an error in the calculation of the gamma efficiency (§ 3.7), and, subsequently, in the estimation of the effective collection area. The overall uncertainty, estimated by applying different cuts in the analysis, is about 10%.
- **Mispointing**. Relative pointing differences between MAGIC I and MAGIC II spoil the reconstruction of the stereo parameters (§ 3.8). The typical mispointing

systematic effect	class	uncertainty	night-to-night
MC atmospheric simulations	ES	3%	0%
atmospheric transmission losses	ES	5%	5%
light losses	ES	8%	8%
signal extraction	ES	3%	0
F-factor	ES	10%	0
temperature dependence of the gain	ES	2%	2%
PMT QE	ES	4%	0
PMT electron collection efficiency	ES	5%	0
light collection in Winston cone	ES	5%	0
flat-fielding	ES	2–8%	2%
background subtraction	FN	1–8%	1%
MC-data disagreement	FN	$\leq$ 10%	8%
mispointing	FN	1–4%	1–4%
NSB	FN	1–4%	0
non-linearity readout	SS	0.04	0
analysis	SS	0.1	0

Table 3.3: Uncertainty of the main sources of systematic effects. From left to right: the systematic effect, the class of the effect defines if it affect the energy scale (ES), the flux normalization (FN) or the spectral slope (SS), the overall value of the uncertainty and the value of uncertainty which can vary from night-to-night at energies above 300 GeV.

is smaller than 0.02° (Aleksić, J., et al., 2010b), and it causes a systematic error on the gamma efficiency $\leq$ 4%.

- **Different NSB levels**. Each FoV is characterized by its own NSB level. The latter can vary significantly in Galactic FoVs or in presence of star/moon light. Higher NSB means higher fluctuations which might spoil the image parameter calculation, hence decrease the efficiency in detecting γ-ray events. Dedicated MC studies estimated this effect to be 1–4%.

- **Sources of systematic uncertainty on the spectral slope**:

  - **Non-linearity of the readout chain**. Non-linearities in the analog signal chain and the small residual non-linearities of the DRS2 (§ 2.2.6) produce a systematic uncertainty of about 0.04 in the slope of a power-law differential energy spectrum.

  - **Analysis**. This uncertainty takes into account the effect of different unfolding methods (§ 3.13), different efficiencies of the gamma selection cuts (§ **??**), and different zenith angle ranges. This systematic error produces for a typical power-law spectrum a spread in photon index of 0.1. An independent estimation of this systematic uncertainty will be treated in detail in § 5.3.2.

The overall systematic uncertainty depends on the energy. The error on the flux normalization is estimated to be 11% at medium energies, above 300 GeV, and up to 19% at low energies (below 100 GeV). The energy scale of the MAGIC telescopes can be determined with a precision of 17% at low energies and of 15% at higher energies. The slope of the differential energy spectra is affected by a systematic uncertainty around 0.015.

Just some of the considered sources of systematic effect can produce variations in the flux from night-to-night. An estimation of the values for the night-to-night systematic uncertainties is given in Table 3.3.

PART TWO

CRAB PULSAR WIND NEBULA

Van Gogh - “Crab on its back”

4

Introduction to Pulsar Wind Nebulae

PWNe are bubbles of relativistic particles and magnetized fields created when the ultra-relativistic wind from a pulsar interacts with the ambient medium. They produce a broad-band spectrum of non thermal radiation from radio frequencies to TeV energies. The radiation is of synchrotron origin up to hard X-rays/soft γ-rays, while, at higher energies it results from Inverse Compton scattering on background radiation. PWNe can be used to improve our understanding of relativistic shocks and particle acceleration because they are nearby (hundreds to thousands of pc), their spectrum expands over many decades of energy, and many models for the radiation production have been developed. This chapter provides a short review on the state of the art of the current knowledge of the PWNe, and, in particular, of the Crab Nebula, the archetypal of the PWNe.

It is a summary extracted from literature.

PWNe are a class of cosmic sources which contain magnetized relativistic wind radiating non-thermal (synchrotron and IC) emission across the electromagnetic spectrum. These winds are constantly powered by rotating NSs, the so-called pulsars, usually located at their center. Pulsars release a third of their total rotational energy ($\equiv 10^{49}$ erg) into their surrounding nebulae. Since pulsars, as well as their nebulae, originate in SN explosions, they are contained within the shell of the SNRs. The SNRs are the leftover of the material ejected in the explosion an interacting with the ISM.

The best studied PWN is the Crab Nebula , considered as prototype of this class of object. Over the past decades 40–50 PWNe have been identified either in our own Galaxy or in the Magellanic Clouds. Because PWNe have a well-defined central energy source and are close enough to be spatially resolved, they act as a testing ground for studying both relativistic flows and shocks resulting from the interaction of relativistic winds with the ambient medium.

In the following, a summary of the current understanding of pulsars and PWNe is presented. The chapter includes a short description of the SNRs. The latter does not pretend to be exhaustive, but rather to introduce the concepts used in the other sections.

4.1 Pulsars

Pulsars are rapidly rotating, highly-magnetized NSs formed during the SN explosions of massive ($\leq$ 5–10 $M_\odot$) stars (§ 4.1.1).

In 1967 Pacini suggested that a rotating magnetized NS could be a possible energy source of the continuum emission from the Crab Nebula (Pacini, F., 1967). Around the same time, a source of pulsed radio emission with a period of 1.337 s was detected by chance in another portion of the sky (Hewish et al., 1968). This was the first instance of a new class of objects called pulsars, whose name derives from "pulsating stars". Their association with the rotating magnetized NSs was soon proposed by Gold, T. (1968) and Pacini, F. (1968) in the context of the magnetic dipole model. The latter foresaw losses of rotational energy through magnetic dipole radiation causing a gradual slowdown of the pulsar, hence, an increase of the pulse period, P. These predictions could be confirmed with the detection of a pulsar with a period $P = 33$ ms in the Crab Nebula (Staelin, D. H. & Reifenstein, III, E. C., 1968; Comella, J. M. et al., 1969), and the observation that its period increases of 36.5 ns per day (Richards, D. W. & Comella, J. M., 1969).

Pulsars can be classified through the measurements of its period, and its period derivative $\dot{P}$. The P-$\dot{P}$ diagram in Figure 4.1 shows two main populations of pulsars: "normal" pulsars with a period of ~ 0.5 s which increases at rates $\dot{P} \sim 10^{-15}$ s/s, and MilliSecond Pulsars (MSPs) with a period which spans from 1.5 ms to 30 ms, and a time derivative of 10^{-19} s/s. These two measured quantities permit to infer the pulsar age, the surface magnetic field, and

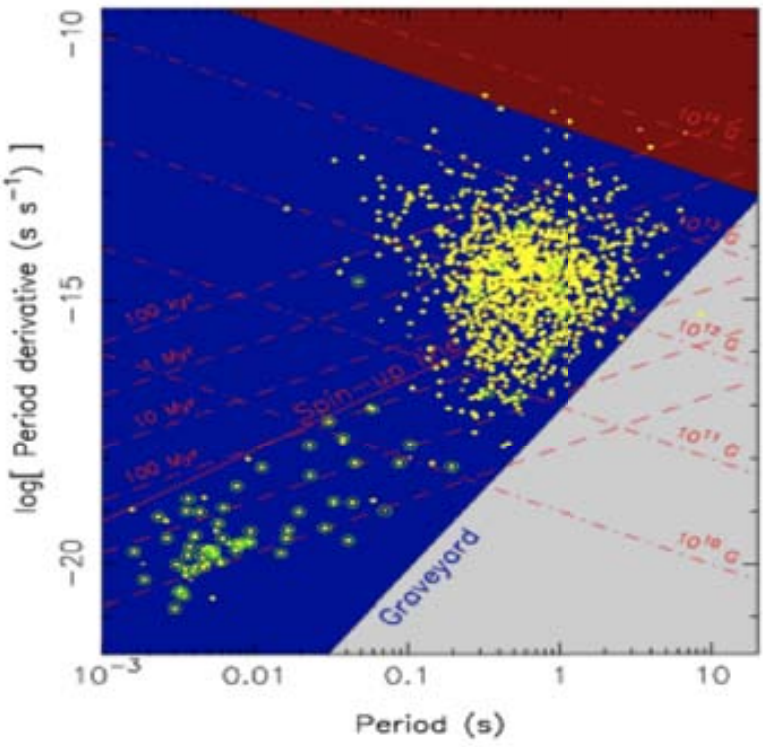

Figure 4.1: Pulsars P-$\dot{P}$ diagram. Taken from Lorimer, D. R. (2005).

the rate at which the pulsar rotational energy is dissipated. The latter, known as *spin-down*

luminosity, E, is defined as:

$$\mathrm{E} = -\frac{\mathrm{dE_{rot}}}{\mathrm{dt}} = I\Omega\Omega = 4\nu^2 I\frac{P}{P^3} \tag{4.1}$$

where I is the NS's moment of inertia ($\equiv 10^{45}$ g cm^{-2}), and $\Omega \equiv 2\nu$ P is the angular frequency of the star. The observed pulsars have *spin-down luminosities* which span from 10^{31} to 10^{38} erg/s. If a pulsar, with an initial period of P_0, loses the majority of its angular momentum through magneto-dipole radiation, the angular velocity obeys the differential equation $\Omega = -k\Omega^n$. The index n is the so-called "braking index" which can assume values in the range $2 < n < 3$, as determined from experimental measurements. n=3 corresponds to spin-down completely caused by losses of magnetic dipole radiation. By assuming that k is constant, the age, θ, of the pulsar can be derived:

$$\theta = \frac{P}{(n-1)P} \quad 1 - \left(\frac{P_0}{P}\right)^{n-1} \tag{4.2}$$

The quantity $\theta_C \equiv P\ (2P)$ (obtained assuming $n = 3$ and $P_0 \in P$) is known as the *characteristic age* of the pulsar. It provides an estimation of the pulsar age with an order-of-magnitude accuracy. The surface dipole magnetic field, $\mathrm{B_s}$, is roughly τR^3 with τ the magnetic dipole moment of the NS and R (10^{16} cm) the radius of the NS. Following the prescriptions for the τ estimation in Ostriker, J. P. & Gunn, J. E. (1969), $\mathrm{B_s}$ is given by:

$$\mathrm{B_s} \equiv 3\ 2 \times 10^{19}\ (PP)^{1\ 2}\ \mathrm{Gauss} \tag{4.3}$$

When substituting with reasonable values of P and P, B_s is of the order of 10^{10}–10^{14} G (Pacini, F., 1967). Figure 4.1 displays also the lines of constant magnetic fields and of constant characteristic time: MSPs are generally older than "normal" pulsars (10^8–10^9 years old compared to 10^3–10^4), and their surface magnetic fields are a factor 10^4 lower ($\equiv 10^{10}$ G).

Basically all the known pulsars lie within the Galactic plane at a distance smaller than $\equiv$1 kpc. Lorimer (2010) presents a study on the pulsar space distribution based on a uniformed sample of 1000 pulsars: the Galactocentric radius, R, and the dispersion from the Galactic plane, z, are shown in Figure 4.2. The vast majority of the nearly 2000 known pulsars are detected at radio frequencies. In the γ-ray band, the number of known pulsars has drastically increased in the last three years after the launch of the *Fermi* satellite. It passed from 6–7 to more than 60, among which, at present, 21 are radio quiet, despite deep radio follow-up observations. In addition, MSPs have been recently confirmed as a class of γ-ray emitters (Abdo, A. A., et al., 2009a).

4.1.1 Neutron stars

When massive stars approach their end, the radiation pressure does not balance the gravitational force any more. Therefore, the outer layers of the star are ejected and the core collapses producing a SN explosion (if the mass of the star is $\leq$ 5–10 $\mathrm{M_\odot}$). If the mass of the core is larger than 1.44 $\mathrm{M_\odot}$(Chandrasekhar, S., 1931), the gravitational pressure overcomes the pressure of the degenerated gas. β reactions take place, and transform most of the nuclei and electrons in neutrons: the star turns into a NS. If the mass of the NS does not exceed the critical value of about 2.9 $\mathrm{M_\odot}$ (Kalogera, V. & Baym, G., 1996), a stable equilibrium can be

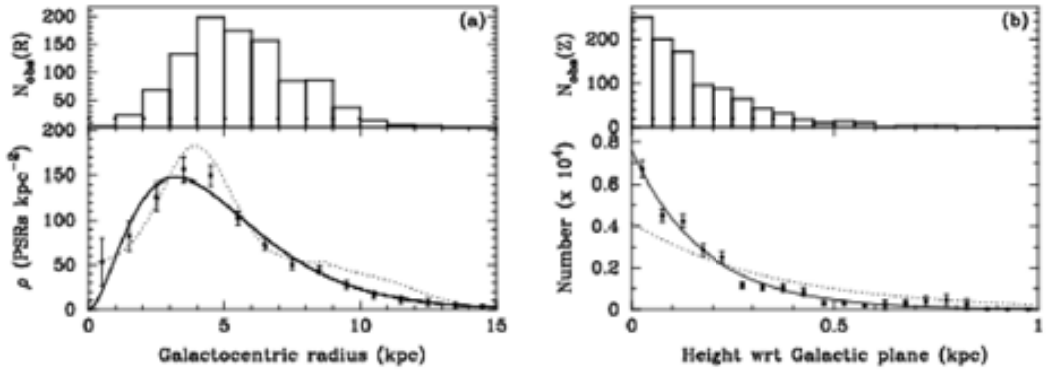

Figure 4.2: Pulsars space distribution. Observed number distribution (*top panels*) and model-derived distribution (*bottom panel*). *On the left:* for the Galactocentric radius; *On the right:* for the dispersion from the Galactic plane. Taken from Lorimer (2010).

reached: the gravitational pressure is balanced by the neutron degeneracy pressure. Since the NS retains most of the angular momentum of its progenitor star, and has a tiny fraction of the parent's radius, it is created with very high rotational speed. In addition, the conservation of the magnetic field, and the fact that the flux density scales like the square of the stellar radius explain the existence of strong magnetic fields in the NS. Thus, this newly formed compact object is converted into a strong rotating magnetic dipole, a pulsar. It emits electromagnetic radiation observed as pulses produced as the magnetic axis (and hence the radiation beam) crosses the observer's line of sight at each rotation: the so-called lighthouse effect.

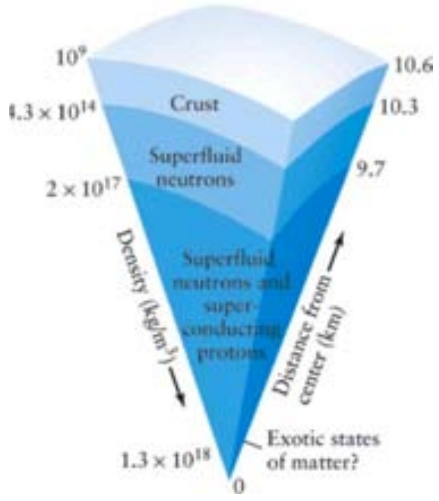

Figure 4.3: Structure of a NS.

A NS is typically about 10–20 km across with a density of 10^{14} g/cm^3. In its structure, a NS resembles more a planet than an ordinary star (Figure 4.3). Its core consists of densely-packed neutrons, with a bunch of electrons and protons, in a liquid state known as neutronium. A complete review about possible models of the inner structure of a NS can be found in Weber, F. (2005). The core is surrounded by a stiff crust, 1 km thick, of heavy nuclei through which electrons flow. At the surface, with a temperature of 10^6 K, electrons and heavy nuclei evaporate creating an atmosphere. The cooling processes at the surface can create a sort of starquakes which might be responsible for the glitches in the steady periods of the pulsars.

4.1.2 Neutron star magnetosphere

Considering the NS as a perfect conductor, a surface charge has to build up. In the following the highest electric potential is assumed to be at the star equator. The surface charges induce an electric field with a component parallel to the magnetic field, $E_{\parallel}$, thus perpendicular to the star surface. This component of the electric field is intense enough to pull the charges

out against the gravitational forces. If the charges are not trapped in the surface by binding forces (meaning the surface is not solid), they move perpendicularly to the surface as to short out the E component. The space surrounding the NS, called magnetosphere, is therefore populated with free-force plasma and electromagnetic fields.

The only available analytical description of the NS magnetosphere is that of Goldreich, P. & Julian, W. H. (1969). These authors assumed the simplest case where the magnetic field is that of a dipole aligned with the rotation axis (aligned rotator). In the realistic case, instead, magnetic dipoles are arbitrarily tilted with respect to the rotation axis (oblique rotators). In fact, even if the two axes coincided in the pre-supernova star, the mass loss during the explosion is unlikely to be symmetric especially in the presence of strong magnetic field. In the last decade, this realistic case has been treated using numerical methods: Contopoulos, I. et al. (1999) proposed solutions for a time-independent magnetosphere. Whereas, only recently, Spitkovsky, A. (2006) used new numerical methods to account for the time evolution.

A plausible picture of the pulsar magnetosphere distinguishes two separate zones: the inner magnetosphere where the pulsed emission comes from, and the wind zone populated by a relativistic magnetized wind.

- The **inner magnetosphere** is contained within the *light cylinder*. This is the cylinder around the NS where the velocity of the magnetosphere reaches the speed of light, c. Its radius, $\mathrm{R_{LC}}$, is defined as:

$$\mathrm{R_{LC}} \equiv \frac{c}{\Omega} \tag{4.4}$$

  and it has typical value of ≡100 km. The charged particles extracted from the star surface by the strong electric field move along the closed, and electric equipotential lines of the magnetic field. Therefore, they corotate with the NS, and their charge density is given by:

$$\alpha_{\mathrm{GJ}} \equiv \overline{\Omega} \cdot \overline{B} \quad (2\nu c) \tag{4.5}$$

  which is known as the Goldreich-Julian charged density. The corotation breaks down at large distances, at some point close to the *light cylinder*. Therefore, those particles bound to the lines closing outside the *light cylinder* can escape the rigid corotation. In particular, if the *critical line* is the magnetic field line with the same electric potential as the interstellar medium, electrons stream out along higher-latitude lines, whereas protons along lower-latitude lines (Figure 4.4). The corotation defines two separate zones within the inner magnetosphere: the *closed magnetosphere*, a region limited by the last field line that closes within the *light cylinder*, and the complementary *open magnetosphere*. In the *open magnetosphere*, the outflowing of charges reduce the charge density, thus a strong E develops. Consequently, particle acceleration can occur along the open magnetic lines. In presence of the strong magnetic field, the accelerated particles lose their energy via synchrotron radiation. The resulting photons create electron-positron pairs which start an electromagnetic cascade. These pairs short-out the parallel component of the electric field, self-limiting the acceleration. The produced primary and secondary photons constitute the observable pulsed emission from radio frequencies up to γ-rays. The energy contained in the pulsed emission makes up only a 10% of the spin-down luminosity. Most of it, in fact, leaves the magnetosphere in form of magnetized wind.

In the inner magnetosphere, only a small fraction (10^{-4}–10^{-5}) of the NS spin-down

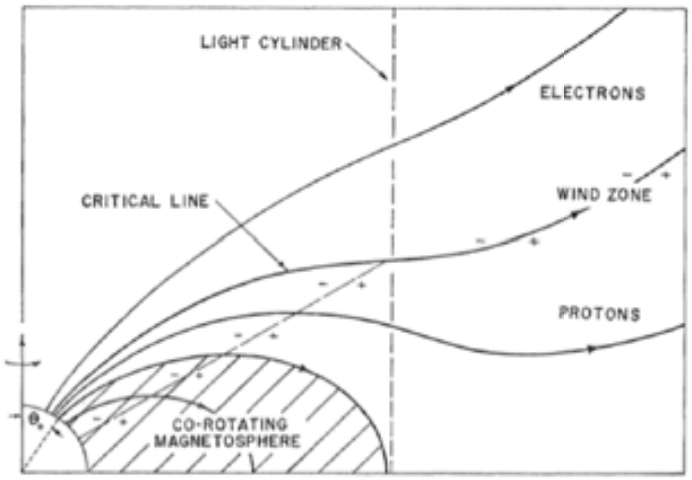

Figure 4.4: Sketch of the inner magnetosphere and wind zone in the particular case of an aligned rotator. The NS is bottom left. Taken from Goldreich, P. & Julian, W. H. (1969).

luminosity is converted into kinetic particle energy (Arons, J., 1979; Michel, F. C., 1982). In other words, all the energy flux is most likely Poynting flux dominated. This is quantified by the ratio of the Poynting flux, $L_P = \nu B^2/4\pi$, to particle kinetic energy flux, $L_E = n\nu\Gamma mc^2$, the so-called magnetization parameter σ (Kennel, C. F. & Coroniti, F. V., 1984a):

$$\sigma = \frac{B^2}{4\pi n\Gamma mc^2} \tag{4.6}$$

At the *light cylinder*, $\sigma \sim 10^4$ (Arons, J., 1979).

- The **wind zone** is the region included between the *light cylinder*, and the *termination shock*, at a distance r_s. The particles which have escaped the inner magnetosphere form a highly relativistic, and magnetized wind with a Lorentz factor as large as $\Gamma \sim 10^6$ (*unshocked pulsar wind*). This wind carries most of the spin-down energy of the NS in the form of electromagnetic, and particle energy density. The energy flux, which is Poynting dominating at the *light cylinder*, becomes a kinetic dominated flux before the *termination shock*, *i.e.* $\sigma < 1$. This energy transfer is a matter of debate (known as the σ problem). A dissipative transition cannot be the responsible process, as no intense X-ray radiation from this region has been observed: it is underluminous instead. Contopoulos, I. & Kazanas, D. (2002) derived a possible solution by using the conservation laws of the associated MagnetoHydro Dynamic (MHD) flow. The X-ray underluminosity is due to the fact the relativistic unshocked winds move with the magnetic field; thus, they do not emit synchrotron radiation. This statement does not exclude that this wind can be directly observed through its IC radiation (Bogovalov, S. V. & Aharonian, F. A., 2000).

The relativistic wind slows down to match the boundary condition imposed by the more-slowly-expanding material at the nebula radius. Thus, when the ram pressure of the wind is balanced by the pressure of the PWN, a *termination shock* forms. Its distance

from the pulsar has the following dependence:

$$r_s \propto \sqrt{\frac{\dot{\mathrm{E}}}{P_{PWN}}}. \tag{4.7}$$

where P_{PWN} is the total pressure in the shocked pulsar nebula (Gaensler, B. M. & Slane, P. O., 2006). Reasonable values of the nebula pression and $\dot{\mathrm{E}}$ yield *termination shock* radii in the order of 0.1 pc.

4.1.3 γ-ray emission from pulsars

In all models about the high-energy pulsar emission, charged particles are accelerated in the open magnetosphere (§ 4.1.2) by the component of the induced electric field which is parallel to the magnetic field. These accelerated particles emit curvature emission up to γ-rays. Moreover, the resulting photons create electron-positron pairs in the strong magnetic field. These pairs radiate synchrotron photons (their momenta have a component perpendicular to the magnetic field), many of which are able to produce a second generation of pairs. This electromagnetic cascade process stops when the synchrotron photons are no longer energetic enough to pair-produce. Finally, γ-rays can be emitted also by IC scattering of low energy synchrotron photons (SSC).

The open magnetosphere includes two presumable acceleration sites: above the magnetic poles of the NS, and in the vacuum gaps of the the open magnetosphere (Figure 4.5). Different assumptions on the acceleration site leads to different models for the γ-ray emission. The most popular ones are:

- the **polar cap** model (Sturrock, P. A., 1971; Arons, J. & Scharlemann, E. T., 1979; Daugherty, J. K. & Harding, A. K., 1982). It predicts that particle acceleration takes place near the NS surface close to its magnetic poles. This region extends for 0.5–1 stellar radii. The γ-rays are emitted by curvature radiation and IC upscattering A distinct feature of the polar cap model is a sharp "super-exponential" cut-off in the energy spectrum which is caused by the efficient pair production attenuation at the pair escape energy (Harding, A. K. et al., 1997), where the pair escape energy is the highest energy for which the photon can escape the magnetosphere without being subject to pair production. This cut-off shows an energy dependence which is inversely proportional to the surface of the magnetic field strength. The trade-off of this model is the fact that it predicts too small beam size to produce the observed wide pulse profiles.

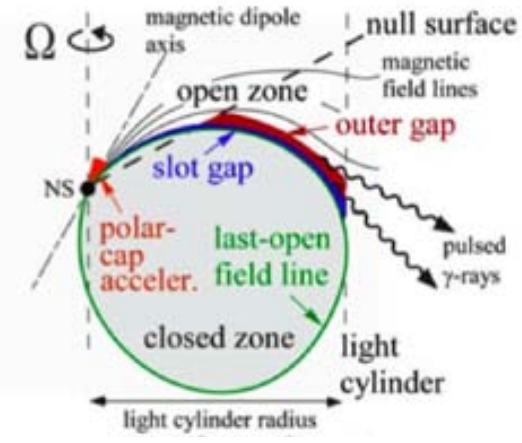

Figure 4.5: Sketch of the pulsar inner magnetosphere cross-section. It indicates the possible sites of particle acceleration. Taken from Hirotani (2008).

- the **slot gap** model. Scharlemann, E. T. et al. (1978) found that in the polar cap scenario the potential gap above the pole increases when approaching the last closed

field line. Based on these findings, Arons, J. (1983) pointed out the possibility of a low-latitude acceleration region, the "slot gap": a narrow bundle of field lines bordering the closed magnetosphere (Figure 4.5). The electromagnetic cascades in this region have higher pair multiplicity than in the polar cap because the primary electrons accelerate and produce over a larger distance. The radiation from the slot gap model naturally produces a wider cone of emission, solving the problem of the too narrow predicted bin sizes (Harding, A. & Muslimov, A., 2005).

- the **outer gap** model. Cheng, K. S. et al. (1986b,a) showed that a charge depleted volume (due to the charges streaming out along the field open lines) can form in the magnetosphere also at low-latitude. This gap is contained within the last closed field line, the null surface (defined as $\overrightarrow{\Omega} \cdot \overrightarrow{B} = 0$), the light cylinder, and an open magnetic field line which is limited by pair creation (Figure 4.5). The high-energy photons produced in the outer gaps are affected by a much less efficient pair production than in the polar caps because of orders of magnitude lower magnetic fields. The maximum γ-ray energy is determined by the maximum energy of the accelerated electrons, which is limited by radiation reaction losses. Therefore, the shape of the cut-off is expected to fall more gradually than in the polar cap models (exponential cut-off). Some outer gap models predict VHE pulsed emission due to IC scattering (Hirotani, K., 2006).

4.2 Supernova Remnants

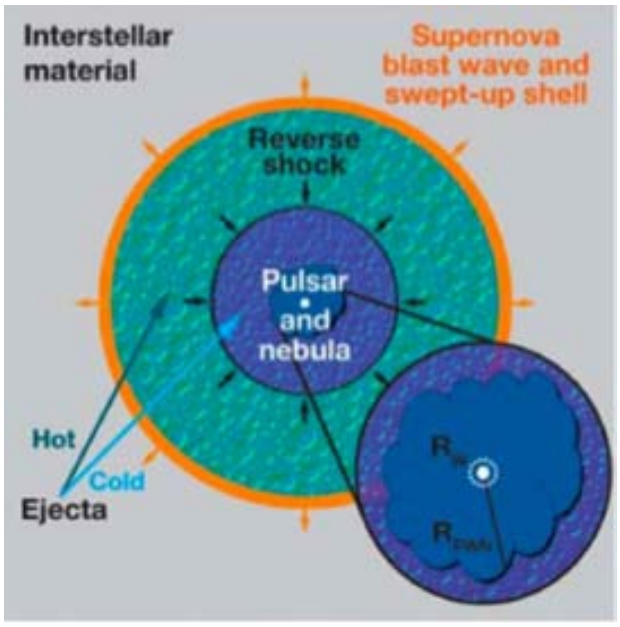

Figure 4.6: Sketch of a composed pulsar-PWN-SNR system. Taken from Gaensler, B. M. & Slane, P. O. (2006).

The material ejected during the SN interacts with the surrounding ISM, and it forms a SNR. The resulting shock (*forward shock*) wave have an initial speed of 10^3 km s^{-1}, and it constantly slows down as it sweeps up the surrounding material. The expansion can occur over tens of thousands of years until the shock speed falls below a few 10^2 km s^{-1}. At the *forward shock* the ambient gas is compressed and heated. After having swept up roughly its own mass from the surrounding ambient, the hot plasma starts to decelerate, and a *reverse shock* forms. It moves inward towards the pulsars, and the PWN. With the formation of this second shock the SNR enters into the so-called *Sedov phase* which is strongly affected by the ISM. Figure 4.6 shows a sketch of a composite pulsar-PWN-SNR system.

For a detailed review on SNRs, the reader is referred to Reynolds, S. P. (2008).

4.3 Pulsar wind nebulae

At the *termination shock*, the magnetic field is compressed, the *unshocked pulsar wind* (§ 4.1.2) is heated: the resulting energy distribution of the particles follows a power-law up to 10^{15} eV energies, and their pitching angles are randomized. The outflow is called *shocked pulsar wind*. When it interacts with the surrounding environment, it creates a PWN, also known as *plerion* (term coined by Weiler, K. W. & Panagia, N. (1978)). As the particles accelerated at the *termination shock* move through the magnetic field that comprises the PWN, they produce synchrotron radiation extending from radio wavelengths to beyond the X-ray band. Figure 4.7 sketches the different regions of a PWN.

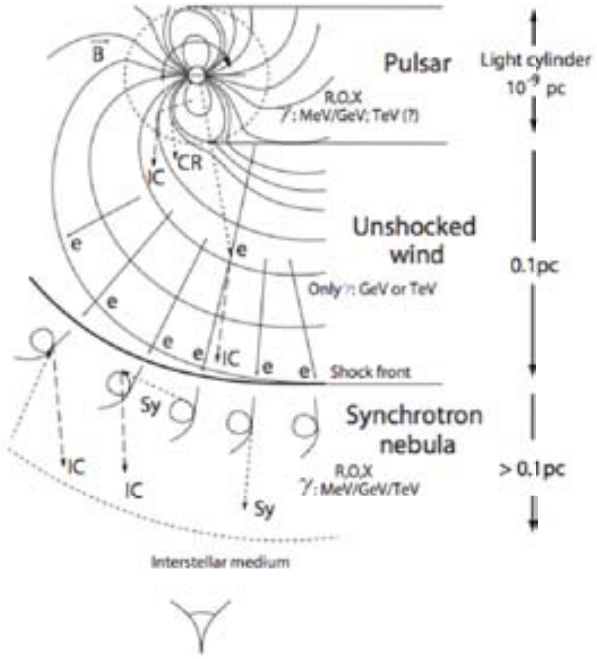

Figure 4.7: Sketch of how PWNe work. Taken from Aharonian, F. A. (2004a).

The most accepted theoretical models of PWNe are based on a relativistic MHD description of the pulsar winds before and after the *termination shock*. This approach was first presented by Rees, M. J. & Gunn, J. E. (1974) and further developed by Kennel, C. F. & Coroniti, F. V. (1984b), under the assumption of a spherical symmetry of the pulsar wind distributions (derived from an aligned rotator, § 4.1.2). Despite its simplicity, the model shows a good agreement with the observed synchrotron emission. Moreover, it can explain many of the observed properties of the PWNe.

- High-energy X rays emitting particles have a short lifetime for synchrotron losses, and they are present only in vicinity of the *termination shock*. Therefore, the size of the nebula decreases with increasing frequency, as it is clearly observed in the Crab Nebula.
- As the nebula expands, Rayleigh-Taylor instabilities form at its edges where the fast moving relativistic fluid meets the slower-moving supernova ejecta. They are believed to be the origin of the finger-like filamentary structures seen in the Crab Nebula in

the optical, and UV bands. Simulations indicate that 60–75% of the swept up mass is concentrated into these filaments (Bucciantini, N. et al., 2004).

- The higher the synchrotron losses, the steeper the resulting spectrum. This explains why the spectrum flattens out when the distance to the pulsar increases.

4.3.1 Inner structure

Recent observations showed that the inner region of PWNe is characterized by complex structures, generally referred as *jet-torus structures*. A main emission torus corresponding to the pulsar equatorial plane, and two jets of material that flow along the toroidal axis are clearly visible (Figure 4.8). Usually one of the two jets is fainter than the other as result of the Doppler beaming of the material whereby the intensity varies with the viewing angle (Pelling, R. M., et al., 1987). In addition, multiple arcs and rings are present together with a central knot, and the luminosity around the torus is not constant.

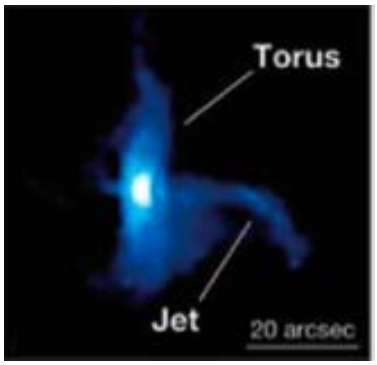

Figure 4.8: X-ray image of the PWN 3C 58. where the jet-torus structure is visible.

Such structure cannot be explained under the assumption of an isotropic energy flux of the *unshocked pulsar winds* proposed by Kennel, C. F. & Coroniti, F. V. (1984b). On the other hand, an equatorial flux, with a strong latitude dependence ($\propto \sin\psi$, with ψ the angle from the rotation axis), can describe it, as recently confirmed by numerical simulations (Bucciantini, N. et al., 2006). An equatorial flux, in fact, naturally produces an oblate *termination shock*. Subsequently, the speed of the outflow is not constant over the pulsar latitude (larger at higher latitudes). This explains the difference in the luminosity of distinct torus positions. Moreover, given a magnetic field distribution dependent on the pulsar latitude ($\propto \sin\psi$), this framework can also derive the jet collimation (Khangoulian, D. V. & Bogovalov, S. V., 2003). The modification of the *unshocked pulsar wind* energy flux distribution can be associated with the numerical solution found for the pulsar magnetosphere in case of oblique rotator (§ 4.1.2). These are the so-called *stripped wind models* (Spitkovsky, A., 2006).

4.3.2 Evolution of pulsar wind nebulae

Pulsars and PWNe are, at least initially, surrounded by a SNR. They constitute *composite systems*, and the SNR provides boundary conditions for the pulsar winds. Since the energy in the SNR ($\sim 10^{51}$ erg) is much larger than the total energy ejected by the pulsar during its lifetime ($\sim 10^{49}$ erg), the PWN cannot significantly affect the SNR. On the other hand, the evolution of the SNR has an important influence on the PWN morphology and its emission properties. Recent studies of the PWN-SNR system distinguish three main phases in the PWN evolution (Bucciantini, N., 2008):

- the initial phase is called **free expansion phase**, and lasts for about 1000–3000 yrs. The Crab Nebula is in this phase. The PWN is expanding in a cold freely expanding SNR, and this causes the formation of a thin shell of compressed material at the nebula edges. During this phase, the pulsar luminosity is high and almost constant.
  Both the expansion velocities of the PWN ($\sim 10^3$ km s^{-1}) and the SNR (($\sim$ 50–300 km s^{-1}) are much higher than the kick-off pulsar velocities ($\sim$ 10 km s^{-1}). Therefore the pulsar velocity does not play any role and the pulsar is located almost at the center of the PWN and of the SNR (Figure 4.9).

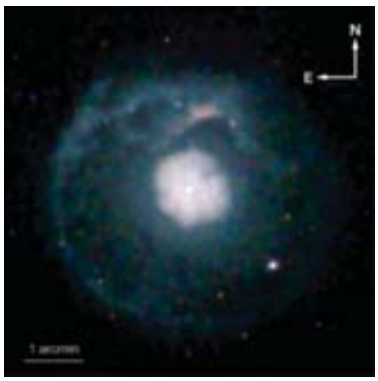

Figure 4.9: X-ray image of the G21.5-0.9 remnant. Taken from Gaensler, B. M. & Slane, P. O. (2006).

- the **reverberation phase** lasting about 10^4–10^5 yrs. This phase begins when the expanding PWN reaches the *reverse shock* (§ 4.2) of the SNR, and starts to be compressed. As a result the PWN responds with an increase in pressure and a sudden expansion. The system reverberates several times in this way. The PWN edges become subject of strong Rayleigh-Taylor instabilities which can cause efficient mixing of the pulsar wind with the SNR material.
  At this stage the injection from the pulsar decreases till to be negligible, and the evolution of the PWN depends mainly on the SNR *reverse shock*. Thus, the nebula can be displaced with respect to the location of the pulsar, leading to a variety of morphological structures. This results into a system where the pulsar is not located at the center of the non-thermal emission, as seen in Vela. As the system evolves, a relic nebula is created. The PWN G24.5 shows this kind of morphology. Figure 4.10 shows the two above-mentioned examples.

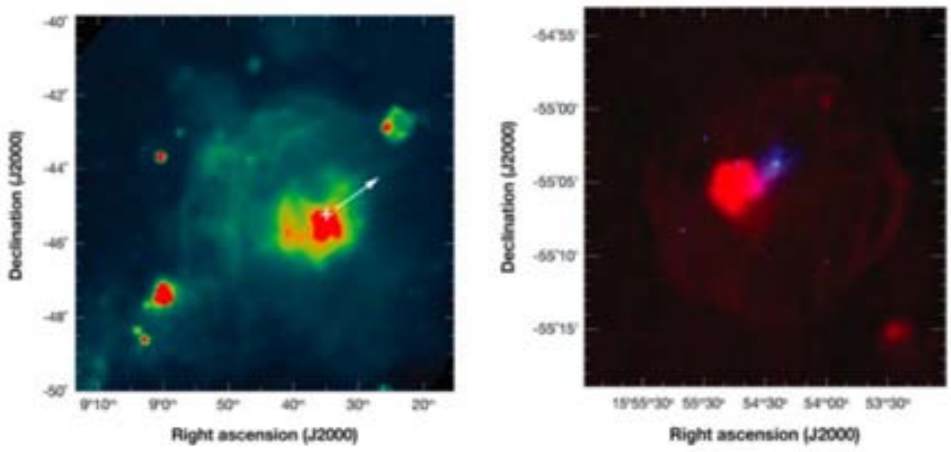

Figure 4.10: *On the left:* **Radio image of the Vela SNR**. *On the right:* **Image of the SNR G 317.1** in radio (red) and X-rays (blue). Taken from Gaensler, B. M. & Slane, P. O. (2006).

- After 10^7–10^8 yrs, the PWN enters its last phase where there is no more energy injection from the pulsar, and the SNR is already in its Sedov phase (§ 4.2). This phase depends on the pulsar kick. For slow moving pulsars, the PWN keeps on expanding adiabatically inside the SNR. Given the absence of injection, the PWN can be observed only as a faint extended radio source. Fast moving pulsars can escape from the SNR. They form bow-shock nebulae due to the interaction with the ISM. An example of a bow-shock nebula is given by W44 (Figure 4.11).

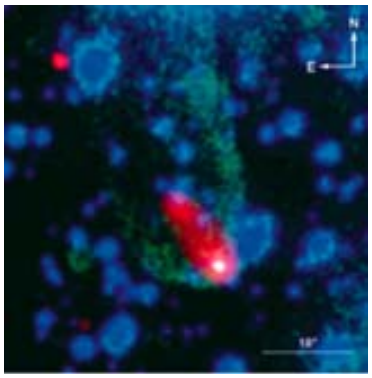

Figure 4.11: Image of the bow-shock nebula W44, with its Hα emission lines (green), and in the X-ray band (red). The background star emission is shown in blue. Taken from Gaensler, B. M. & Slane, P. O. (2006).

4.3.3 Pulsar wind nebula spectra

PWNe are characterized by broad-band spectra which can extend from radio frequencies up to VHEs. This emission is dominated by two major mechanisms based on the interactions of electrons and magnetic fields with photon fields in the nebula. The synchrotron component is responsible for the emission up to X-rays and soft γ-rays, whereas the second component derives from the IC scattering on background radiation. Figure 4.12 shows the broad-band spectrum of the Crab Nebula.

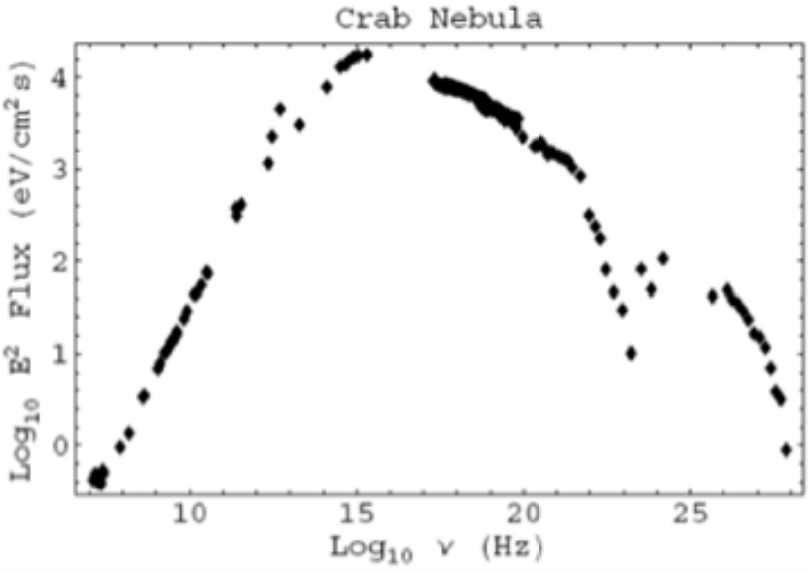

Figure 4.12: Broad-band spectrum of the Crab Nebula. The two main emission component are visible: the synchrotron at lower energies, and the IC one above some GeV.

From equation A.12 the typical energies for the production of the synchrotron photons in different energy bands can be derived. As shown in Figure 4.13, the detection of synchrotron radiation at 10^{13} eV is a clear evidence of effective acceleration of particles beyond

10^{14} eV. This emission presents specific spectral characteristics in the different energy bands, as described in the following.

- **Radio** synchrotron emission is characterized by a power-law distribution of flux, such that $S_\nu \propto \nu^\alpha$, where S_ν is the observed flux density at the frequency ν, and α the *spectral index* of the source. α has typical values of -0.3 $\lesssim \alpha \lesssim$ 0. The radio luminosity, usually calculated between 100 MHz and 100 GHz, is of the order of $L_R \approx 10^{34}$ erg s^{-1}. The efficiency of conversion of spin-down luminosity into synchrotron emission is defined as $\eta_R \equiv L_R/\dot{E} \approx 10^{-4}$ (Frail, D. A. & Scharringhausen, B. R., 1997).

- The synchrotron **InfraRed (IR)** radiation shows a power-law flux distribution with a spectral index $\alpha \approx$ -0.8. Its luminosity can however be dominated by a component associated with the Galactic dust, as in the case of the Crab Nebula (Marsden, P. L., et al., 1984).

- In the **optical** energy band, the synchrotron radiation is well-represented by a power-law distribution of flux with spectral indices which span from -1 to -0.5. The optical luminosity is $L_O \approx 10^{33}$ erg s^{-1}, and the corresponding conversion efficiency is $\eta_O \approx 10^{-5}$ (Shibanov, Y. A. et al., 2008).

- At **X-ray** energies, the emission is described by a power-law distribution of photons, such that $N_\gamma \propto E^{-\Gamma}$, where N_γ is the number of photons, and Γ the *photon index*. Typical indices are $\Gamma \approx 2$. The X-ray luminosity is $L_X \approx 10^{35}$ erg s^{-1} when integrated in the range 0.5–10 keV, and the efficiency conversion of spin-down luminosity into synchrotron emission is $\eta_X \approx 10^{-3}$ (Becker, W. & Truemper, J., 1997).

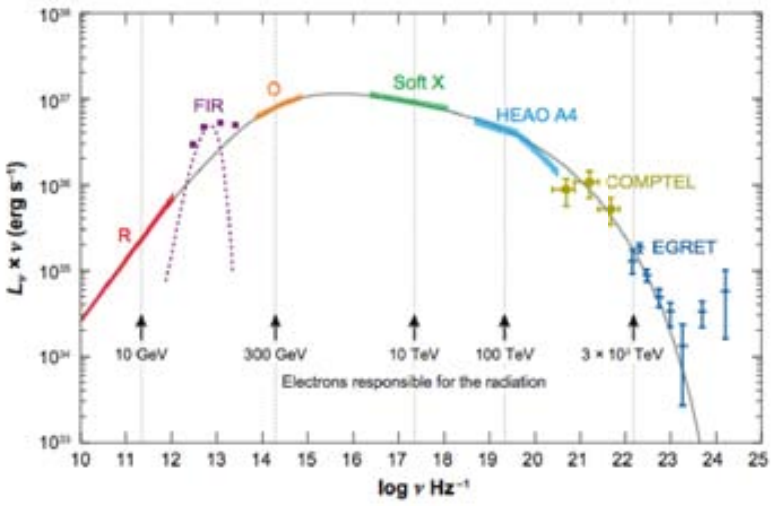

Figure 4.13: The synchrotron radiation from the Crab Nebula. The vertical lines indicate the energies of the electrons which produce the corresponding synchrotron photons. Taken from Atoyan, A. M. & Aharonian, F. A. (1996).

γ-ray emission from pulsar wind nebulae

The existence of ultra-relativistic electrons in the nebula leads to the production of detectable TeV γ-ray fluxes through IC scattering. This idea was first proposed by Gould, R. J. (1965), and then revised and applied to the Crab Nebula in the 90s (de Jager & Harding, 1992; de Jager, O. C., et al., 1996; Atoyan, A. M. & Aharonian, F. A., 1996; Hillas, A. M., et al., 1998; Bednarek, W. & Bartosik, M., 2003), after its detection above 700 GeV by the Whipple telescope (Weekes, T. C., et al., 1989).

The IC component can be estimated with good accuracy, as the target photon fields which play a role in the production of gamma rays are well known:

- the **synchrotron radiation**. It dominates till X-rays, except for the Far InfraRed (FIR). This photon field leads to application of the so-called Synchrotron Self Compton (SSC) model. According to this model, the relativistic electrons produce γ-rays through IC scattering on synchrotron photons produced by the same population of electrons.

- the 2.7 K **CMB radiation**. The IC scattering on this black-body radiation field leads to a significant increase of the fluxes at energies around 100 TeV. It is the only target photon field which is uniformly distributed over the nebula.

- the **FIR photons** from galactic dust. The IR photometry shows an "excess" at $\equiv 50$ τm which is attributed to the dust emission (Marsden, P. L., et al., 1984). de Jager & Harding (1992) showed that this photon field can contribute up to 50% to the total γ-ray flux.

- the **optical line emission from the nebula s filaments**. It has been only recently considered in the modelization of the Crab Nebula γ-ray spectrum, even though its role is still marginal with respect to the other ones.

The synchrotron radiation is the main target photon field for young PWNe, though. The number of synchrotron photons strongly depends on the strength of the magnetic field. For this reason the TeV γ-ray fluxes in young pulsars, such as the Crab Nebula , are very sensitive to the average magnetic field. Thus the comparison of the predicted and the observed VHE fluxes allows the determination of the magnetic field. The shape of the IC component does not depend much on the basic parameter of the nebula, resulting in an almost model-independent prediction of VHE fluxes.

4.4 The Crab Nebula

The Crab Nebula is almost certainly associated with a SN explosion observed in 1054 CE (Lundmark, K., 1921; Stephenson, F. R. & Green, D. A., 2002). The explosion of a 8–10 $M_\odot$ star (Kitaura, F. S. et al., 2006) was noted by the court astronomers of the Song emperor as a powerful transient phenomenon: the "guest star" remained visible during the daytime for three weeks, and was visible at night for 22 months. The Crab Nebula was discovered in 1731 by the English astronomer John Bevis. Few years later it was observed by Charles Messier and became the first object in his famous catalog of nebulous non-cometary objects. In fact, the Crab Nebula is also known as *M1*. In 1844, Lord Rosse named the nebula "the Crab" because of its resemblance to a crab which lives in rivers, as seen by a 72-inch reflecting telescope in the 19^{th} century (Figure 4.14).
The Crab Nebula is located in the Taurus constellation, close to ζ-Tauri. It is mainly observable from the northern hemisphere, but, being placed in the galactic plane, it is accessible also from the southern hemisphere at high zenith angles. The Crab Nebula lies at a distance of $\equiv 2$ kpc (Trimble, V., 1968).

Figure 4.14: Lord Rosse s drawing of the Crab Nebula . This work gave the name to the nebula because of its resemblance to a crab's claw.

The Crab Nebula is one of the best nonstellar objects in the sky ever studied. Due to its bright glow at almost all wavelengths, its observations exhibits a spatial and temporal resolution which allow to constrain relevant physics. The importance of the Crab Nebula to astrophysics does come from the high quality of its observations: a more complete and detailed comparison between theory and observations than it is possible with any other nonstellar astrophysical object.

Because of its apparent overall flux steadiness, the Crab Nebula has been considered as standard candle at almost all the wavelengths. It has been used to cross-calibrate X-ray and γ-ray telescopes, to check the instrument performance over time, and to provide units for the emission of other astrophysical objects. This notion changed dramatically in September 2010, when Tavani, M., et al. (2011) observed a strong γ-ray flare in which the radiation of the Crab Nebula above 100 MeV almost doubled within just few days. This surprising observation was immediately confirmed by the *Fermi*/LAT team (Abdo, A. A., et al., 2011). Such unexpected discovery raised a new interest of the astrophysical community on the Crab Nebula . It offers, in fact, a unique opportunity to test the mechanism of particle acceleration and high-energy emission in shocks (§ 4.4.6).

4.4.1 The Crab Pulsar

At the center of the Crab Nebula lies the Crab Pulsar, also known as PSR B0531+21. It is one of the most energetic pulsars in our Galaxy, with a spin-down luminosity of $\equiv 5 \times 10^{38}$ erg s^{-1}. With a period of 33 ms, its characteristic age has been estimated to 1240 yrs which is close to the observational value. The main characteristics of the Crab Pulsar are summarized

in Table 4.1. The PSR B0531+21 was first discovered at radio frequencies by the Arecibo

Parameter		Value
period	P	33 ms
period derivative	$\dot{P}$	4.21×10^{-13}
spin-down luminosity	L_{spin}	4.6×10^{38} erg s^{-1}
characteristic age	τ	1240 yr

Table 4.1: Parameters of the PSR B0531+21.

Observatory in Puerto Rico (Staelin, D. H. & Reifenstein, III, E. C., 1968), and it was the first pulsar to be detected at visible wavelengths (Cocke, W. J. et al., 1969). The EGRET experiment on board of the CGRO satellite reported the high-energy detection of the Crab Pulsar (Nolan, P. L., et al., 1993; Fierro, J. M. et al., 1998). The pulsation above 100 MeV was later confirmed by the *AGILE* and the *Fermi* collaborations (Pellizzoni, A., et al., 2009; Abdo, A. A., et al., 2010a). The latter performed also a spectral analysis which shows a spectrum better fitted by a power-law with an exponential cut-off at 5.8 ± 0.5 ± 1.2 GeV. Nevertheless, the ground-based telescopes detected the Crab Pulsar at higher energies. The stand-alone MAGIC telescope by using an innovative trigger (§ 2.2.8) managed to lower the energy threshold down to 25 GeV and reported a clear detection of the Crab Pulsar at 6σ level (Aliu, E., et al., 2008). At the moment of writing this thesis, the VERITAS collaboration showed pulsations above 150 GeV (Otte, N., 2011). This last result rules out the exponential cut-off claimed by the *Fermi* team at 5.6 σ CL. These observations of the Crab Pulsar in high energy γ-rays (Figure 4.15) can provide strong constraints on the location of the γ-ray emitting region: polar caps, slot gaps, or outer gaps (§ 4.1.3).

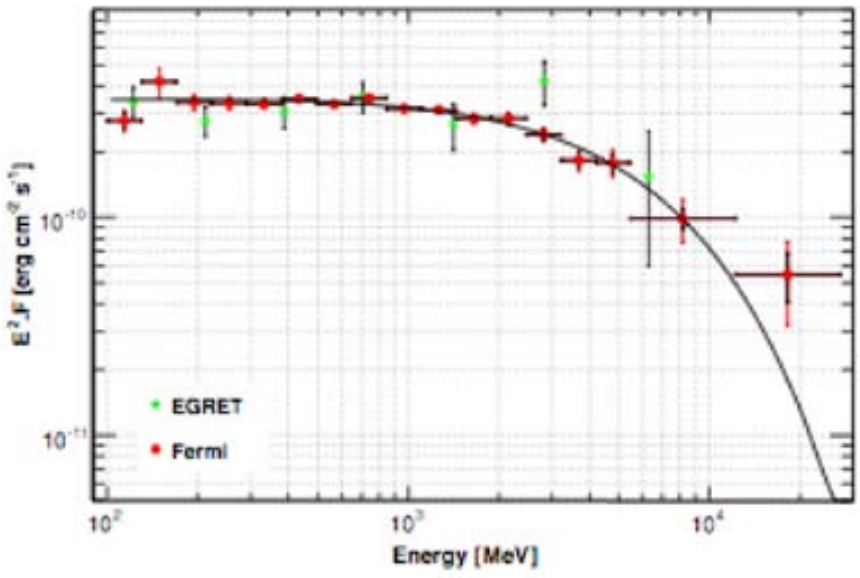

Figure 4.15: SED of the Crab Pulsar in the high energy γ-rays.

4.4.2 The Crab Pulsar Wind Nebula

The visible Crab Nebula is a PWN evolving within a much larger freely expanding SNR (Figure 4.16). Such a remnant, first predicted by Chevalier, R.A. (1977), remained unobserved for

long time. Only recently observations have provided direct evidence of its existence (Sollerman, J., et al., 2000). Nevertheless, the outer shock, driven into ambient stellar material by the expanding ejecta, persists undetected. It is estimated to have a radius of as much as 10 pc, seven times larger than the observed radius of the Crab Nebula.

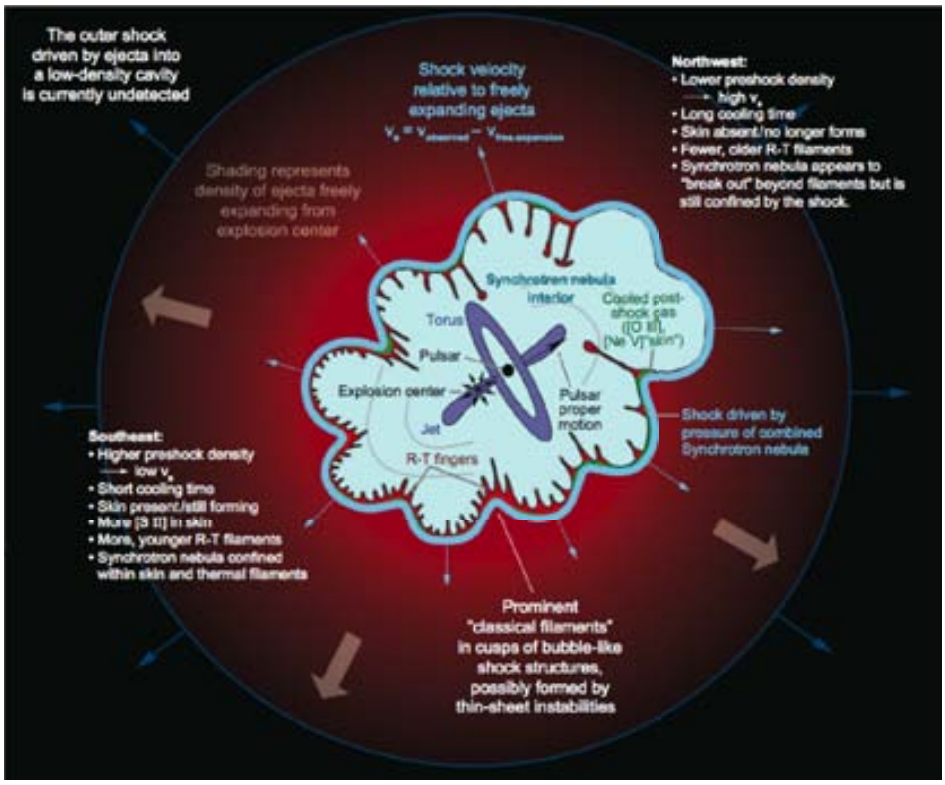

Figure 4.16: Sketch of the Crab Nebula structure. Taken from Hester, J. J. (2008).

The PWN is visible at all wavelenghts, and its size decreases with increasing the frequency (§ 4.3). At radio frequencies, the nebula has roughly elliptical shape ∼2.9 pc × 4 pc with the major axis aligned with the spin axis of the pulsar, and it is inclined by ∼30° into the plane of the sky. This major axis lies in the North-West/South-East direction which coincides with the axis of symmetry of the inner structure (§ 4.3.1). The latter consists of a X-ray emitting torus (0.4 pc of radius) with two bipolar beamed jets along the axis of the torus (Aschenbach, B. & Brinkmann, W., 1975; Brinkmann, W. et al., 1985; Weisskopf, M. C., et al., 2000). The surface brightness of the torus varies considerably with the azimuth angle as a result of the Doppler beam effect. High-resolution X-ray images of the Crab Nebula obtained with the *Chandra* satellite (Figure 4.17) allowed to identify small-scale structures, such as the *inner ring* (radius ∼ 0.1 pc) lying between the pulsar and the torus. It has a uniform brightness along the azimuth angle (less significant beaming effect), and is thought to represent the *termination shock* (§ 4.1.2). Several *knots* with diameter of 0.01 pc are detected close to the *inner ring*. The most famous *knot*, known as the *anvil*, lies along the projected inward extension of the jet. However, the surface brightness of the latter is too high to be explained as the superimposition of the ring and the jet surfaces. In addition, there are elliptical ripples, usually refereed as *wisps*. Observed at radio, optical, and X-ray wavelenghts, these features are extremely dynamical and variable on timescales of days (Scargle, J. D., 1969). The exact

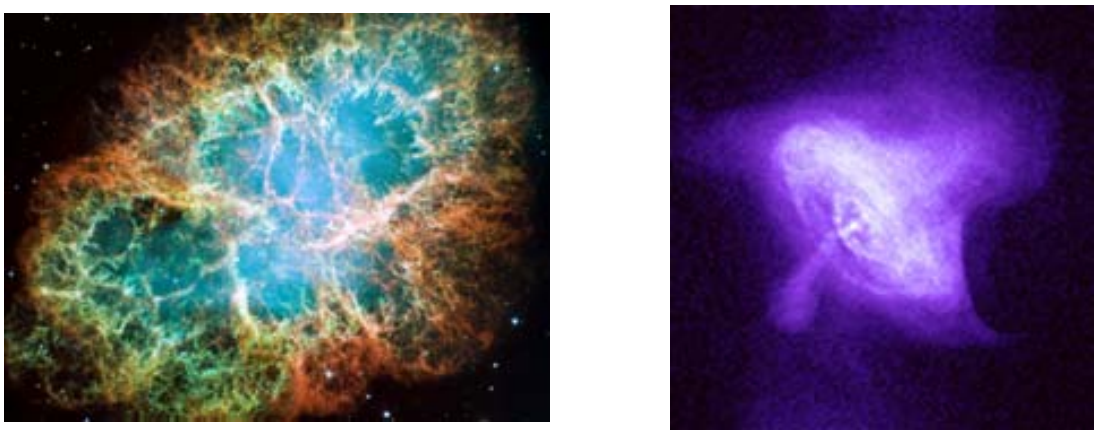

Figure 4.17: Images of the Crab Nebula . *On the left:* optical image obtained with the HST. In red the "skin" of high-ionization emission. *On the right:* X-ray image obtained with *Chandra* where the *jet-torus* structure and the inner ring are visible.

nature of the *wisps* is not known, but they are thought to be associated with a shock in the pulsar winds (§ 4.1.2).

The synchrotron nebula is confined by a faint "skin" of high-ionization emission from thermal gas. With a thickness of about 0.3–0.7 pc, it can interpreted as the cooling region behind the synchrotron-driven shock (Sankrit, R. & Hester, J. J., 1997). This skin contains a complex structure of thermal filaments which break up into many smaller structures (Figure 4.17). Filaments often resemble finger-shape pointing inward towards the center of the nebula, and are usually attached to the neighbors through arc-like bridges of emission. They have been interpreted as the results of Rayleigh-Taylor instabilities occurring when the thermal ejecta interact with the synchrotron nebula (Hester, J. J., et al., 1996). Further explanation on the origin and morphology of the filaments can be found in the review Hester, J. J. (2008).

Despite the apparent symmetry of the Crab structure, there is a large asymmetry in the North-West region of the nebula with respect to the South-East one:

- no skin is visible
- the synchrotron nebula extends beyond the edge of the visible filaments.
- there are fewer filaments, but they are longer and more prominent.

This asymmetry can be explained in terms of variations in the density of the ejecta into which the nebula is expanding (Sankrit, R. & Hester, J. J., 1997). The lower the density, the higher the shock velocities, and the longer the post-shock cooling time. If the cooling time behind the shock is less than the age of the Crab, the thermal emission produces the visible skin. The latter reaches sufficient density that Rayleigh-Taylor instabilities can grow producing the filaments. On the other hand, if the post-shock cooling time exceeds the age of the Crab, no thermal emission is created, thus neither skin nor filaments are visible. The overall observed features of the nebula suggest that the density of the ejecta is higher in the South-East region than in the North-West one. A plausible explanation for this density asymmetry can be derived from the pulsar proper motion (Ng, C.-Y. & Romani, R. W., 2006).

4.4.3 The broad-band spectrum of the Crab Nebula

The overall spectrum of the Crab Nebula extends over 20 orders of magnitudes in energy from radio frequencies up to VHEs. It is composed of two non-thermal broad components:

- a low-energy component dominates the overall output and extends from radio to γ-ray frequencies. This emission is thought to be synchrotron radiation, associated with the emission from electrons between a few GeV up to a few tens of TeV (Figure 4.7). It is confirmed through polarization measurements (Dean, A. J., et al., 2008). The Crab Nebula is remarkably efficient at converting the energy of the pulsar wind into synchrotron radiation, almost 26% of the entire energy injected by the pulsar in the nebula.
  The synchrotron emission peaks between optical and soft X-ray frequencies and comes primarily from the *torus*. The bump in the FIR is the result of the thermal emission from dust in the nebula. This dust is condensated from material ejected in the SN explosion.
  Assuming an average magnetic field of 2–3 $\times 10^{-4}$ G (Marsden, P. L., et al., 1984), the synchrotron losses in 1000 yrs (almost the age of the nebula) can account for the cooling of relativistic electrons only down to $E_{cr} \equiv 200$ GeV (Equation A.13). This simple consideration implies that two different populations of relativistic electrons should be distinguished in the Crab Nebula: the wind electrons freshly accelerated at the shock with energies $E \leq E_{cr}$ (E_{cr} corresponds to synchrotron radiation in the near-IR/optical band), and the radio electrons at lower energies responsible for the radio emission. This second population of electrons is considered a leftover from an early phase of evolution of the pulsar, during which it was injected in different parts of the nebula (Atoyan, A. M., 1999). An experimental proof for this argument of the two electron populations is given by the fact that the single power-law synchrotron spectrum steepens significantly in the near-IR/optical band (Marsden, P. L., et al., 1984) becoming inconsistent with the wind shock acceleration model for the Crab Nebula.

- the high-energy component dominates above 426 ± 35 MeV (Abdo, A. A., et al., 2011) and derives from IC scattering of high-energy electrons from the pulsars on mainly synchrotron photons (SSC, § 4.3.3). It peaks between some tens and some hundreds of GeV, but its position has not been clearly determined yet. The models for this high-energy component will be discussed in detail in § 4.4.5.

In the Crab Nebula the synchrotron emission reaches the soft γ-rays up to 1 GeV. This is a clear indication that electrons are accelerated at UHEs in the *termination shock*. Since such energetic electrons have short radiative lifetimes, they necessarily radiate close to the acceleration zone, hence identifying the site of the injection.

The soft γ-ray emission was first detected by the γ-ray satellites. In particular, the COS-B satellite showed a differential energy spectrum from 70 MeV up to 1 GeV which is well-fitted by a single power-law with photon index 2.7 ± 0.3 (Clear, J., et al., 1987). The EGRET experiment on board of the CGRO satellite extended the Crab Nebula spectrum up to 5 GeV, and the fitted single power-law had a photon index of 2.93 ± 0.15 (Nolan, P. L., et al., 1993). However, above 1 GeV the observed data points appeared to be significantly above the fitted model. A broken power-law, in fact, seemed to better fit the data, but not conclusively, due to the lack of statistics at the highest energies. This claimed hardening of the Crab Nebula spectrum provided the first indication of the transition energy where the

IC component becomes dominant with respect to the synchrotron one. It was just after the launch of the *Fermi* satellite in June 2008 that this claim found a clear confirmation. The *Fermi*/LAT collaboration published the Crab Nebula spectrum between 100 MeV and 300 GeV (Abdo, A. A., et al., 2010a). The latter is well described by the sum of two power-law spectra: the first one decreases (the falling edge of the synchrotron component), while the second increases with energy (the rising edge of the IC component):

$$\frac{\mathrm{dN}}{\mathrm{dEdtdA}} = (9\,1 \pm 2\,1) \times 10^{-13} E^{(-3\,99 \pm 0\,12 \pm 0\,08)} \tag{4.8}$$

$$+ \quad (6\,4 \pm 0\,7) \times 10^{-12} E^{(1\,64 \pm 0\,05 \pm 0\,07)} \quad \frac{\mathrm{photons}}{\mathrm{MeV\ cm^2\ s}} \tag{4.9}$$

4.4.4 The Crab Nebula at very high energies

The Crab Nebula was the first object to be well-established as γ-ray source at TeV energies. In 1989, the pioneering imaging Cherenkov Whipple telescope detected a clear signal (at 9 η CL) above 700 GeV coming from the position of the Crab Nebula (Weekes, T. C., et al., 1989). This detection was confirmed independently by the air shower telescopes at the Sandia Laboratory in New Mexico (Akerlof, C., et al., 1989). In the following decades, the imaging Cherenkov technique was successfully used for further observations of the Crab Nebula in the 0.06–100 TeV energy range (Vacanti, G., et al., 1991; Baillon, P., et al., 1993a; Barrau, A., et al., 1997; Tanimori, T., et al., 1998; Hillas, A. M., et al., 1998; Piron, F., et al., 2003; Aharonian, F. A., et al., 2004). Table 4.2 shows a summary of these historical results. The MILAGRO water-Cherenkov air shower detector observed the Crab Nebula at 15η and the flux derived from MILAGRO data at a median energy of 20 TeV is consistent with the flux obtained by the HEGRA collaboration (Abdo, A. A., et al., 2007).

Lately, the new generation of IACTs measured the first deviations of the Crab Nebula

experiment	**energy range** [TeV]	**norm. factor** [$\mathrm{TeV^{-1}cm^{-2}s^{-1}}$]	**photon index**	**norm. energy** [TeV]
Whipple (1991)	0.4–4	2.5×10^{-10}	2.4 ± 0.3	0.4
THEMISTOCLE (1993)	3–15	$(3.70 \pm 0.50)\times10^{-12}$	1.50 ± 0.20	5
CAT (1997)	0.4–5	$(2.46 \pm 0.22)\times10^{-11}$	2.55 ± 0.09	0.2
CANGAROO (1998)	7–50	$(2.01 \pm 0.36)\times10^{-13}$	2.53 ± 0.18	7
Whipple (1998)	0.4–5	$(3.20 \pm 0.17)\times10^{-11}$	2.49 ± 0.06	1
CELESTE (2002)	0.06–0.2	$(2.33 \pm 0.61)\times10^{-12}$	1.78 ± 0.43	0.1
HEGRA (2004)	0.3–100	$(2.83 \pm 0.04)\times10^{-11}$	2.62 ± 0.02	1
HESS (2006)	0.4-40	$(3.76 \pm 0.07)\times10^{-11}$	2.39 ± 0.03	1
MILAGRO (2007)	20	$(2.28 \pm 0.42)\times10^{-11}$	2.59[1]	1

Table 4.2: Summary of the results of the Crab Nebula spectrum fit obtained by different experiments. Only statistical errors are quoted.

differential energy spectrum from the single power-law model. The spectral points observed by HESS above 400 GeV follow a power-law with an exponential cut-off at 14.3 ± 2.1 TeV (Aharonian, F. A., et al., 2006b). This outcome is in contradiction with all previous results above 10 TeV. On the other hand, the stand-alone MAGIC telescope provided a spectrum extending from 0.8 up to 8 TeV which is better fit by a variable power-law (Albert, J., et al.,

2008d):

$$\frac{\mathrm{dN}}{\mathrm{dEdAdt}} = (6.0 \pm 0.2) \times 10^{-10} \tag{4.10}$$

$$\cdot \left(\frac{E}{300\mathrm{GeV}}\right)^{(-2.31\pm0.06)-(0.26\pm0.07)log10\left(\frac{E}{300\mathrm{GeV}}\right)} \frac{\mathrm{photons}}{\mathrm{TeV\ cm^2\ s}} \tag{4.11}$$

The hardening of the spectrum at energies below few hundreds of GeV indicates that the peak of the IC component is approaching. The fit to the MAGIC data points allowed an estimation of the peak at 77 ± 35 GeV.

Figure 4.18 illustrates the Spectral Energy Distribution (SED) of the Crab Nebula in the γ-ray energy domain. It includes the main experimental results obtained up to now. The overlap between satellites and ground-based telescopes measurements has become possible only in the last few years. If at low γ-ray energies, the innovative *Fermi* satellite filled the gap between few and a hundred of GeV, the construction of IACTs with larger reflectors allowed to lower the energy threshold of the ground-based telescopes down to 50 GeV.

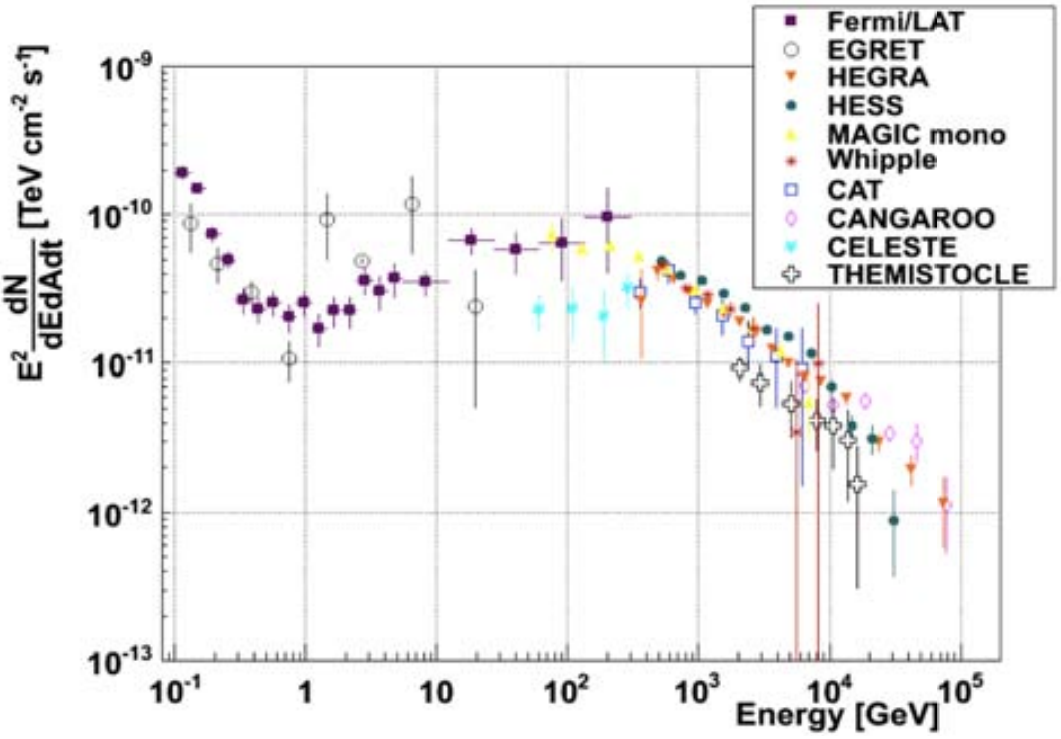

Figure 4.18: The SED of the Crab Nebula in the γ-ray energy domain.

At UHEs, above 100 TeV, the Crab Nebula has never been detected. The only available measurements at these energies are the ULs to the integral flux provided by the Chicago Air Shower Array-Michigan Muon Array (CASA-MIA) and the Extensive Atmospheric Shower-TOP (EAS-TOP) experiments (Ghia, P. L. & Navarra, G., 2005; Borione, A., et al., 1997). Figure 4.19 shows how these flux ULs do not constrain the the model (de Jager, O. C., et al., 1996). Such a check would require a factor 5 of improvement in sensitivity. Considering that the rate of γ-ray events at these energies is too low to be able to increase the observation time, the gaining factor can come just from the collection area (factor 25 larger). This fact explains why no further progress in understanding the UHEs was carried out since then.

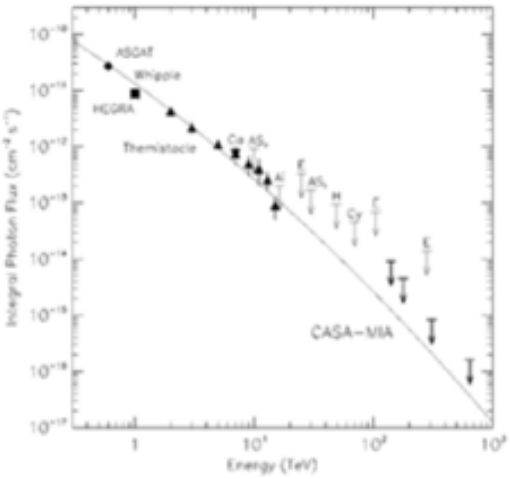

Figure 4.19: Integral fluxes of the Crab Nebula computed by different experiments. Taken from Borione, A., et al. (1997).

4.4.5 Theoretical models for the IC emission from Crab Nebula

Several different models have been proposed to explain the high-energy γ-rays as IC emission on seed photon fields. The main seed photons fields are described in § 4.4.3. The modelization of this high-energy IC component generally requires the definition of the following variables:

- the *spatial distribution of the wind electrons in the nebula*, n_e^W. It is usually assumed to drop off radially following a Gaussian function.
- the *spatial distribution of the radio electrons in the nebula*, n_e^{radio}. Radio electrons are assumed to be homogeneously distributed throughout the nebula.
- the *spatial distribution in the nebula for the seed photon fields*, n_γ. It is commonly approximated to a Gaussian function for the synchrotron, thermal IR and optical emission line photons. Whereas, the CMB photon field is assumed to be constant throughout the nebula.
- the *spectrum of the thermal dust emission.* It is generally represented by a blackbody spectrum where the temperature T is obtained by fitting the observational near-IR/optical data. The reference work for this topic is Temim, T., et al. (2006).
- the *line emission from filaments.*
- the *spectra of the two populations of electrons* (wind and radio electrons § 4.4.3) which can be estimated following different approaches.

The two models which will be discussed in this thesis work, the constant B-field model and the MHD flow model, find their main difference in the definition of the electron spectrum.

- the **constant B-field model** with its simple and robust approach based on the work of Hillas, A. M., et al. (1998). It assumes an entangled magnetic field with a constant field strenght. Under this assumption, it uses the observed synchrotron spectrum to extract the spectrum of the two populations of electrons.

- the application of the **MHD ow model** to the IC component (Atoyan, A. M. & Aharonian, F. A., 1996). The MHD model by Kennel, C. F. & Coroniti, F. V. (1984b) requires few a priori assumptions to describe the evolution of the injected particles, *i.e.* the electron propagation model:
  - spherical symmetry of the nebula. The latter is approximated to a sphere with radius of 1.8 pc.
  - the radius of the *termination shock*, r_S. The canonical value has been for long time 0.10 pc (Rees, M. J. & Gunn, J. E., 1974). Recently, the *termination shock* was identified with the inner ring observed in X-ray by *Chandra* (Weisskopf, M. C., et al., 2000), and estimated at $0\ 14 \pm 0\ 01$ pc.
  - the magnetization parameter, η. Recently, Mori, K., et al. (2004) determined a value of η between 0.01 and 0.03, more likely close to 0.05.
  - the power-law spectrum of the injected electrons.

  By fitting the resulting synchrotron spectrum with the observation data, the free parameters of the electron spectrum can be estimated.

Figure 4.20 illustrates the Crab Nebula SED for the constant B-field and the MHD models as presented in Meyer, M. et al. (2010). These authors revised both models including more recent observational measurements. The best match of the free model parameters (average B-field and magnetization parameter for the constant B-field and the MHD model respectively) to the measured SED were obtained using a rather weak field of $B = (124 \pm 6)\tau$G or a value $\eta = 0\ 0045 \pm 0\ 0003$.

Both the models are in good agreement with the *Fermi* part of the spectrum, even though the shape of the synchrotron cut-off is harder than the measured spectrum for the MHD flow model. At energies beyond the position of the peak in the IC part of the SED, the MHD model does not provide a satisfactory description of the available data: the spectra are considerably harder than the VHE measurements. This discrepancy is directly related to the mismatch visible in the X-ray part of the spectrum. Nevertheless, a re-definition of the standard assumptions might lead to better results. A straight-forward modification is the introduction of an anisotropic wind with variations of η when moving out of the equatorial plane towards the polar regions of the outflow (Volpi, D. et al., 2008). The simpler approach of the constant B-field model yields a better agreement with the VHE observational data.

4.4.6 The Crab Nebula variability

The variability of the Crab Nebula is known almost since its discovery. Scargle, J. D. (1969) claimed the existence of optical features in the nebula, whose brightness varies on different timescales. *Wisps* and *knots* were observed to brighten and fade over weeks and months at different wavelengths (Hester, J. J., et al., 2002; Bietenholz, M. F. et al., 2004). Despite the varying intensity of these compact features, the large-scale integrated emission from the nebula was expected to be steady within a few percent.

In September 2010, for the first time, a flare of the integrated emission from the Crab Nebula at energies above 100 MeV was reported. It lasted few days, between September 18 and 23 (Tavani, M., et al., 2011; Abdo, A. A., et al., 2011). Spectral analysis, as well as the short timescale variability, indicate that this enhanced emission has a synchrotron origin. The integral flux corresponds to an increase by a factor 5.5 ± 0.8 with respect to the average

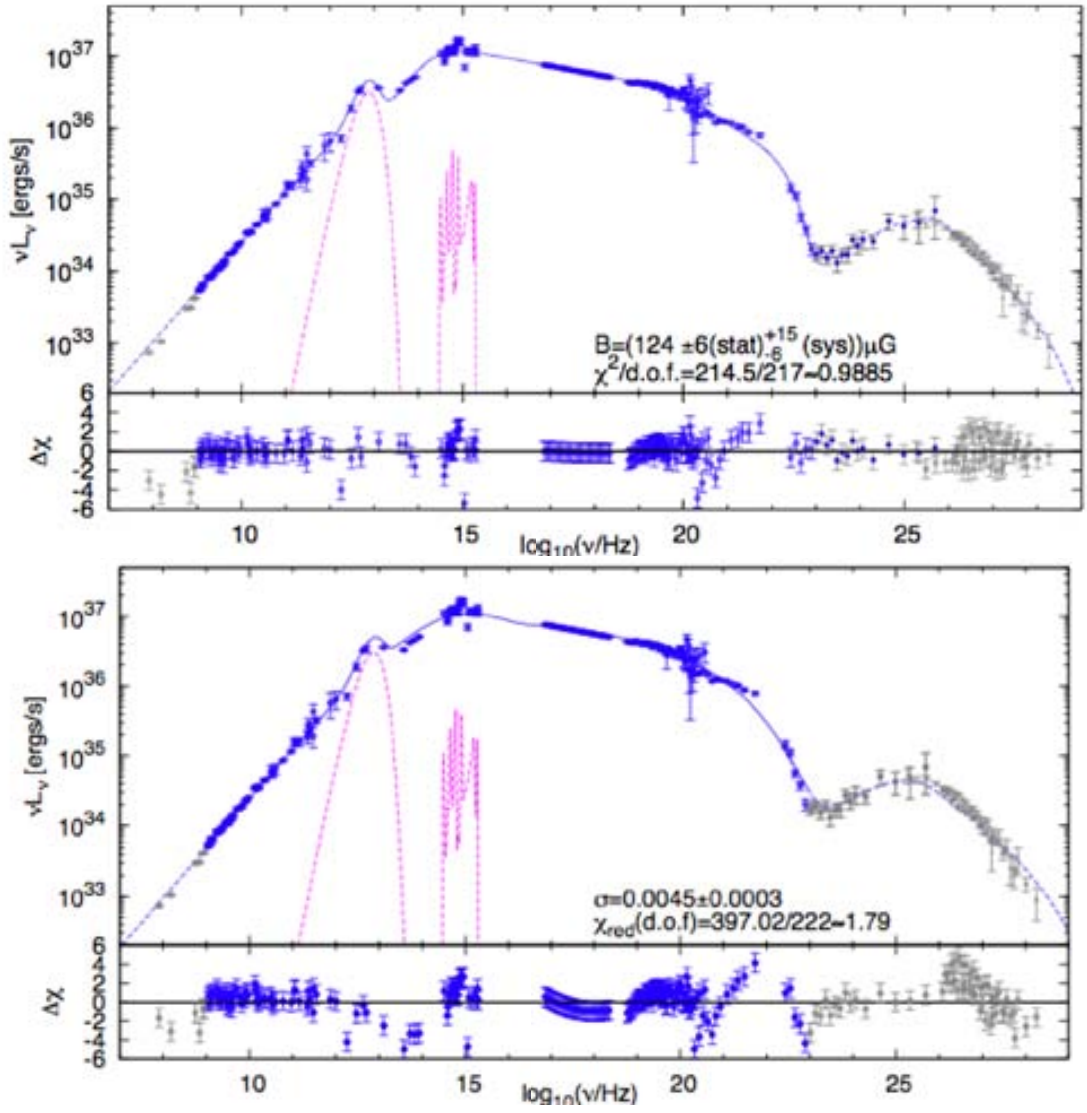

Figure 4.20: SED of the Crab Nebula for the constant B-field and the MHD model.

and has a significance larger than 10 σ in *Fermi*/LAT data. The energy spectrum for the flare is significantly harder, with a photon index of 2.7 $\pm$ 0.2. This serendipitous discovery triggered many observations at different wavelengths: in one month 13 ATels (§ 2.3.2) were published on the topic including follow-up observations at radio, near-IR, optical, X-ray, and VHE γ-ray frequencies (Figure 4.21). No variations in the synchrotron component between infrared and X-ray frequencies were seen above the average nebular flux level. Nevertheless, sub-arc-second resolution images taken in X-rays by *Chandra* and in optical by the HST show some nebular brightened features. One of them is the *anvil* (§ 4.4.2), which is considered a primary site for particle acceleration. Another brightened feature is at larger distance from the pulsar, and appears as an elongated striation. If the peak luminosity of the γ-ray flare suggests that the production region is close to the pulsar, the short flare rising time favors a compact emission region of size smaller than 10^{16} cm. Thus, the *anvil* might be an excellent flare site candidate, and the X-ray brightening might be considered as an afterglow at lower frequencies of the γ-ray flare. However, no conclusions can be drawn on the basis of one event.

At a median energy of 2 TeV, the Astrophysical Radiation with Ground-based Observatory at YangBaJing (ARGO-YBJ) collaboration reported the observation of a flux enhancement by a factor 3–4, which extended up to September 27, *i.e.* it lasted few days longer than the flare detected above 100 MeV (ATel #2921). However the flare at VHE was not confirmed by the IACTs MAGIC (ATel #2967) and VERITAS (ATel #2968).

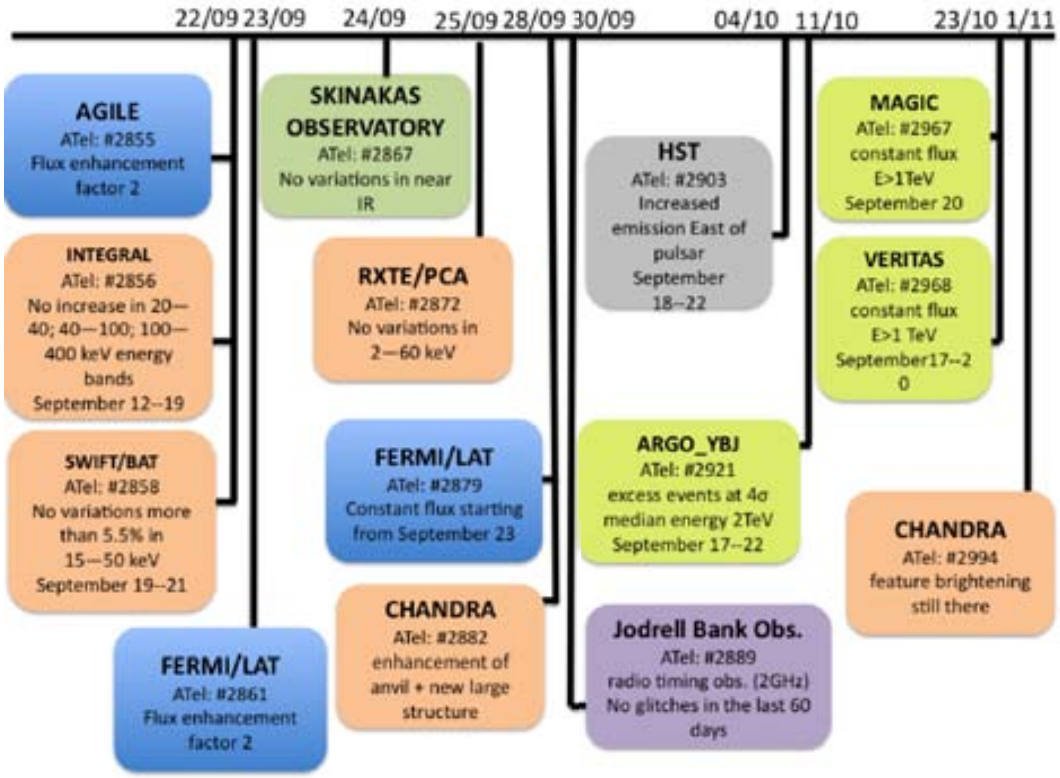

Figure 4.21: Timetable of ATel releases on the Crab Nebula flare in September 2010.

There are other three γ-ray flares from the Crab Nebula reported so far. The *AGILE* team detected a γ-ray flare above 100 MeV in October 2007 (before the launch of the *Fermi* satellite). This flare lasted for two weeks and was almost at the same level of the September 2010 flare (Tavani, M., et al., 2011). *Fermi*/LAT collaboration detected its first γ-ray flare from the Crab Nebula in February 2009. This flare was not observed by *AGILE* because the instrument was pointing at a different part of the sky. It had a duration of 16 days, and an increase in flux by a factor 3.8 ± 0.5. The significance of such an increase was at the level of 8 σ. A study of the spectral variations revealed a softening of the spectrum (Figure 4.22) with a photon index of 4.3 ± 0.3 (Abdo, A. A., et al., 2011).

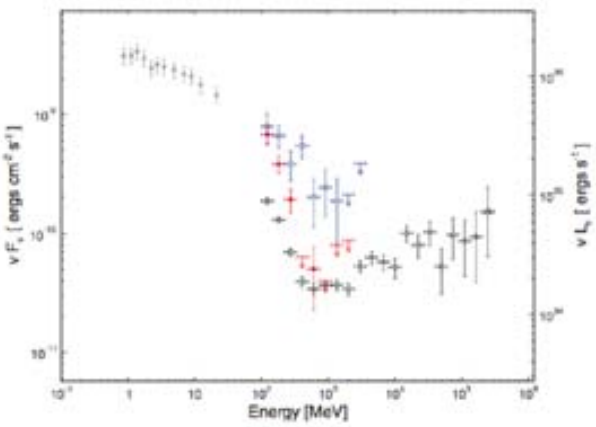

Figure 4.22: SED of the Crab Nebula in the high-energy band measured by *Fermi*/LAT. Black open circles indicate the average spectrum computed over 25 months of observations. Red circles indicate the Crab Nebula spectrum during the February 2009 flare, and blue open squares indicate the spectrum during the flare of September 2010. Taken from Abdo, A. A., et al. (2011).

The last flux enhancement from the Crab Nebula was observed by *AGILE* and *Fermi* in April 2011 (ATels #3279 #3282 #3284 #3286). The integrated flux above 100 MeV started increasing on April 9, 2011, and reached its peak with an increase by a factor 5 on April 14, 2011. *Chandra* followed up observations revealed a new bright *knot*, which is not aligned with the jet (ATel #3283).

Vittorini, V., et al. (2011) explained the γ-ray flares from the Crab Nebula in terms of a fast-rising-synchrotron-cooling model. They assumed a fresh population of impulsively accelerated electrons and positrons which is produced on short timescales (short with respect to the cooling timescales). The acceleration would occur in nebular sites subjected to plasma instabilities and/or substantial pulsar wind particle density enhancements. This assumption follows from the short observed flaring rising time. To fit the synchrotron cooling timescales with the flare observations (for a Lorentz factor $\gamma \sim 5 \times 10^{-9}$ of electrons irradiating in the GeV range) they estimated a local magnetic field as small as 10^{-3} G (5 times larger than the nebular average).

5

Spectrum and flux variability of the Crab Nebula

The MAGIC stereoscopic system observed the Crab Nebula for 50 hours between October 2009 and March 2011. This large data sample allowed to perform a high-precision study on the IC γ-ray emission from the Crab Nebula. It resulted in an unpercented differential energy spectrum which spans eight orders of magnitude in flux and three orders of magnitude in energy between 50 GeV and 45 TeV. The spectrum can be described by a variable power-law f_0 (E/1 TeV)$^{\alpha+bLog(E/1TeV)}$ with $\alpha = 2\ 40 \pm 0\ 01_{stat} \pm 0\ 1_{sys}$, $b = -0\ 15 \pm 0\ 01_{stat} \pm 0\ 05_{syst}$ and $f_0 = 3\ 27 \pm 0\ 03_{stat} \pm 0\ 48_{syst}$. This work presents the most precise estimation of the peak of the IC component of the Crab Nebula spectrum is set at 59 $\pm$ 6 GeV. The integral flux above both 300 and 700 GeV is constant on daily time scales within the systematic uncertainty. No flux enhancement is observed simultaneously to the GeV flares reported by *AGILE* and *Fermi*.

The author is the main responsible of the paper: "The measurement of Crab Nebula spectrum over three orders of magnitude" which is in preparation and will be submitted in Autumn 2011. Part of this work is already published in Zanin, R., et al. (2011).

Measurements of IC γ-ray emission in the region between few GeV and hundred GeV are characterized by large statistical uncertainties. At higher energies, there are some discrepancies between the measurements of the HEGRA and the HESS collaborations. The first claimed a single power-law spectrum from 400 GeV up to 100 TeV, whereas the second reported an exponential cut-off at much lower energies, around 14 TeV. The new MAGIC stereoscopic system with an energy threshold as low as 80 GeV and a flux sensitivity twice better than the previous stand-alone MAGIC I telescope is ideally suited to produce a more precise differential energy spectrum of the Crab Nebula from few tens of GeV up to some tens of TeV. On the other hand, MAGIC has a smaller collection area than the above mentioned experiments at energies above 10 TeV, but this draw-back can be compensated by observing the Crab Nebula longer.

Moreover, the recent discovery of flux variability in the soft-γ-ray band (Tavani, M., et al., 2011; Abdo, A. A., et al., 2011) casts doubts on the notion that the Crab Nebula is a constant

source in the VHE band (§ 4.4.6). Therefore, checking the flux stability in this energy range with precise and more sensitive measurements has become a topic of primary importance. A possible variability of the IC flux component might have the same origin of the soft-γ-ray flares, hence show itself on timescales of days; but it might also have larger variations (months or years) as those detected in the X-rays (Wilson-Hodge, C. A., et al., 2011). In the first case it should be visible at energies above few TeV.

For these reasons, the MAGIC collaboration collected 50 hours of Crab Nebula data since the beginning of its stereoscopic operation. The analysis of these 50 hours is the subject of this chapter which has mainly four goals:

- reconstruction of the IC γ-ray emission spectrum from energies which overlap the satellite measurements up to the VHEs above 10 TeV.
- more precise measurement of the position of IC peak. Right now the most accurate measurement is 77 ± 35 GeV by Albert, J., et al. (2008d).
- disentangling the discrepancies between HESS and HEGRA results above few TeV
- check the flux stability at different energy thresholds

5.1 Data sample

The data sample considered in this analysis includes stereoscopic observations of the Crab Nebula carried out in the last two observation cycles (§ 2.3.1), between October 2009 and March 2011. These observations were performed in *wobble* mode (§ 2.3.3), and at different zenith angles ($4^\circ < \mathrm{ZA} < 50^\circ$). No moonlight was present during the observations. The data set corresponds to about 50 hrs of exposure time.

date [yyyy mm dd]	[MJD]	eff. time [min]	zenith angle [°]
2009 10 15	55119.2	47	6−25
2009 10 20	55124.2	57	9−27
2009 10 21	55125.2	99	8−30
2009 10 22	55126.2	62	6−19
2009 11 11	55146.1	35	15−25
2009 11 13	55148.2	54	7−16
2009 11 14	55149.2	82	9−29
2009 11 15	55150.2	73	6−19
2009 11 16	55151.2	87	6−20
2009 11 19	55154.2	25	14−21
2010 01 05	55200.9	41	14−36
2010 01 08	55204.0	152	8−32
2010 01 11	55207.0	72	5−41
2010 01 12	55208.0	75	8−23
2010 03 13	55267.9	54	20−30
2010 09 17	55456.2	72	19−45
2010 09 20	55459.2	43	14−30
2010 10 05	55474.2	61	6−19
2010 10 06	55475.2	46	15−30
2010 10 09	55478.2	80	7−20
2010 10 10	55479.2	66	10−21
2010 10 13	55482.0	20	39−45
2010 11 08	55508.2	75	14−36
2010 11 09	55509.2	47	20−39
2010 11 10	55510.3	33	30−40
2010 11 12	55512.2	44	15−26
2010 11 13	55513.2	36	16−50
2010 11 14	55514.2	20	21−26
2010 11 16	55516.2	10	8−11
2010 11 17	55517.2	18	21−26
2010 11 18	55518.2	18	30−45
2010 11 19	55519.2	25	34−42
2010 12 14	55544.1	118	6−20
2010 12 28	55558.1	42	11−26
2011 01 01	55562.1	89	20−50
2011 01 02	55563.1	65	25−50
2011 01 03	55564.1	33	34−44
2011 01 04	55565.1	88	5−50
2011 01 05	55566.1	25	22−30
2011 01 06	55567.1	28	21−34
2011 01 28	55589.0	36	9−19
2011 02 06	55598.0	27	21−28
2011 02 07	55599.0	39	20−30
2011 02 08	55600.0	47	19−30
2011 02 27	55618.9	73	5−45
2011 02 28	55619.9	46	28−45
2011 03 02	55621.9	92	30−45
2011 03 27	55646.8	97	30−45
2011 03 31	55650.7	69	35−50

Table 5.1: Log of the Crab Nebula data sample. From left to right: date of the beginning of the observations, also in MJD, effective observation time, and ZA range.

Data affected by hardware problems, bad atmospheric conditions, and unusual analysis rates were rejected in order to ensure a stable performance. The applied data quality checks are those described in § 3.6 with smoother limits on the analysis rate: the latter has to be comprised within the 30% of its mean value (Figure 5.1). This loose quality cut allows to keep the largest amount of statistics which is needed for detecting a signal at above 10 TeV. Removing the "bad data", the sample amounts to 45.4 hrs of effective observation time[1]. Table 5.1 shows the log of the data which survived the data quality selection.

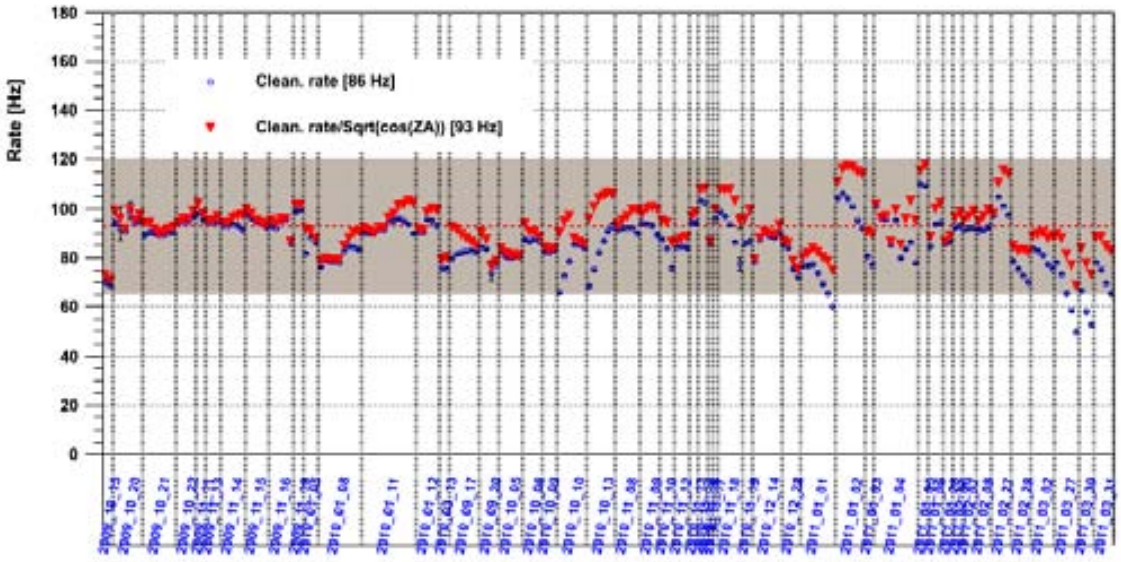

Figure 5.1: Long term evolution of the analysis rate in the Crab Nebula data sample. Open circles correspond to the event rate after image cleaning, whereas filled triangles correspond to the same rate, but corrected for its dependence on zenith angle using the function $\cos^2(\mathrm{ZA})$.

The data sample of the MC simulated γ-ray events used for this analysis consists of the standard stereo MAGIC MC production for point-like sources and a dedicated production which covers the UHEs up to 80 TeV. They are *ringwobble* MC, *i.e.* they have a uniform coverage of the trajectory of the simulated source on the camera plane. Both productions assume that the γ-ray source has a single power-law spectrum with a *photon index* of 1.6[2]. Specific parameters used in the γ-ray event simulation are shown in Table 5.2.

The γ-ray signal from the Crab Nebula is strong enough to make a sample of *off* data dispensable for the training of the γ/hadron separation (§ 3.7). These *off* data were recorded in different regions of the sky around the Crab Nebula position where no γ-ray sources are visible. The sample, taken during dark nights, covers the entire ZA range from 5° up to 50°.

[1]The e ective observation time accounts also for the 10% e ect of the instrument dead time.

[2]The choice of such a at spectrum is a compromise between the CPU time needed for the production of a large amount of events above TeV energies, and a realistic astrophysics spectrum.

	ZA [°]	**min. energy** [TeV]	**max. energy** [TeV]	**MAGIC I PSF** [mm]	**MAGIC II PSF** [mm]	**max. impact par.** [m]	**no. events**
standard	5–35	0.03	50	11.44	12.66	400	1500k
	35–50	0.03	50	11.44	12.66	650	280k
UHE	5–35	1	80	11.44	12.66	700	25k
	35–50	1	80	11.44	12.66	700	34k

Table 5.2: Parameters for the two stereo MC productions of simulated γ-ray events which were used in this analysis. From left to right: zenith angle range, minimum and maximum simulated energy, optical PSF (2.2.3) for MAGIC I , and for MAGIC II , the maximum simulated impact parameter, and, finally, the number of simulated events.

5.2 Description of the analysis

The analysis of the data set was performed with the tools described in Chapter 3. More specifically:

- standard signal reconstruction and calibration was applied to the data set (§ 3.3).
- a clipping of the signals at 750 ph.e. was applied to both data and MC samples.
- the new sum image cleaning algorithm was used instead of the standard timing cleaning (§ 3.4).
- four RFs were used to compute the γ/hadron separation matrices (§ 3.7) in the following four zenith angle ranges:
  - ZA $< 30°$
  - $30° <$ ZA $< 39°$
  - $39° <$ ZA $< 45°$
  - $45° <$ ZA $< 50°$

The distributions of image parameters described in § 3.5 are strongly influenced by the zenith angle of the observation. If the RF training does not properly account for this dependence, the estimation of *hadronness* might be biased. In order to minimize this effect, the training samples were divided into the above-mentioned zenith angle bins.
This choice implied splitting the data set into four subsamples depending on the zenith angle, as illustrated in Figure 5.2. A separate analysis was performed for each of these subsamples, and the obtained results were combined later at the last stage of the analysis (unfolding).

- the event arrival direction was determined through the *stereo Disp* method (§ 3.8). The RFs were trained over the four different above-mentioned zenith angle bins.
- the energy was estimated by using specific LUTs trained on the standard MC sample only (§ 3.11).
- only one *off* position was used to extract the background. This analysis satisfies both conditions which prevent the use of more than one *off* position (§ 3.9).

- a minimum cut in the *size* parameter at 30 ph.e. was applied throughout the entire analysis. Such a low *size* cut aims at keeping the largest possible fraction of low-energy events.

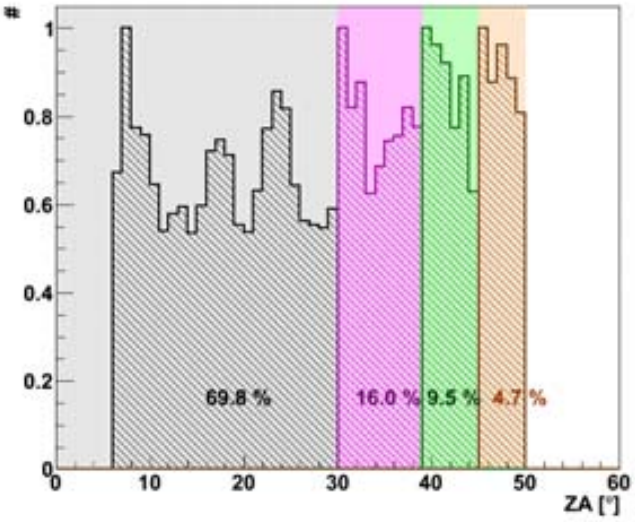

Figure 5.2: ZA distribution of the data set. The colors illustrate the data sample subdivision. A completely independent analysis was applied to each of these data subsamples.

5.2.1 Sum versus standard image cleaning

The performance of the new sum image cleaning algorithm was studied in comparison with the standard cleaning. For this purpose, only data taken at small zenith angles (ZA $< 30°$) were used in order to ensure a uniform low trigger energy threshold ($\equiv$ 34 hrs of observations). Two completely independent analyses were performed on this data sample starting from the image cleaning stage. The analysis with the standard cleaning will be referred to as reference analysis. A common size cut at 30 ph.e. was applied to both of them. Different energy ranges were considered in order to better explore the behaviour of this new cleaning. In the reference analysis, for each energy range the gamma selection cuts were optimized as described in § 3.9.2. On the other hand, in the "new" analysis, the θ^2 cut was fixed at the same value as the one for the reference analysis, and the *hadronness* cuts were chosen such that the same number of excess events was obtained. In this way, the number of background events are comparable and show the different ability in rejecting the background of the two analyses. Results are shown in Table 5.3.

The sum image cleaning shows a significant improvement in rejecting the background at low energies, and consequently in the analysis sensitivity (§ 3.9.1). The improvement is more significant at low energies, below 100 GeV (Table 5.3). The use of this image cleaning allows to find a much clearer hint of signal below 60 GeV (Figure 5.3). Note that the gamma selection cuts used for this analysis had not been optimized. Therefore, the signal could be even stronger. Figure 5.4 shows the comparison of the θ^2 distributions for energies smaller than 70 GeV where the γ-ray signal is detected at more than 5η level. At high energies the background rejection is similar for the two analyses as well as their integral sensitivity. For

energy [GeV]	**analysis**	**had.cut**	**θ^2cut** [°]	**bg**	**exc**	**signif.** [η]	**sens.** [% Crab flux]
> 250	reference	0.20	0.011	309	9607 ± 101	106.8	0.75 ± 0.02
	sum	0.22	0.011	333	9673 ± 102	106.7	0.77 ± 0.02
> 1000	reference	0.22	0.010	35	2354 ± 49	54.7	1.03 ± 0.09
	sum	0.21	0.010	41	2318 ± 49	53.9	1.13 ± 0.09
< 150	reference	0.40	0.032	13243	10109 ± 191	53.2	4.7 ± 0.1
	sum	0.33	0.032	11431	10040 ± 181	55.8	4.37 ± 0.09
< 100	reference	0.50	0.032	11582	4328 ± 166	26.2	10.2 ± 0.4
	sum	0.4	0.032	9687	4337 ± 154	28.2	9.3 ± 0.4
< 80	reference	0.65	0.032	10202	1729 ± 148	11.65	24.0 ± 2.1
	sum	0.41	0.032	5821	1741 ± 116	15.07	18.0 ± 1.3
< 70	reference	0.65	0.032	6477	755 ± 117	6.45	43.9 ± 7.0
	sum	0.41	0.032	3109	771 ± 84	9.23	29.7 ± 3.4
< 60	reference	0.65	0.032	3006	134 ± 78	1.71	168.4 ± 99.6
	sum	0.37	0.032	737	138 ± 41	3.44	80.7 ± 24.5

Table 5.3: Statistics of the θ^2 distributions obtained for different low energy ranges in the case of the two analyses: the reference one using the standard timing image cleaning, and the new one with the sum image cleaning. From left to right: energy range, analysis type, *hadronness* cut, θ^2 cut, number of background events in the signal region, number of excess events, LiMa significance, and corresponding sensitivity.

energies larger than 250 GeV the analysis sensitivity is (0.75 ± 0.02)% of the Crab Nebula flux, in perfect agreement with the value presented in Aleksić J., et al. (2011b).

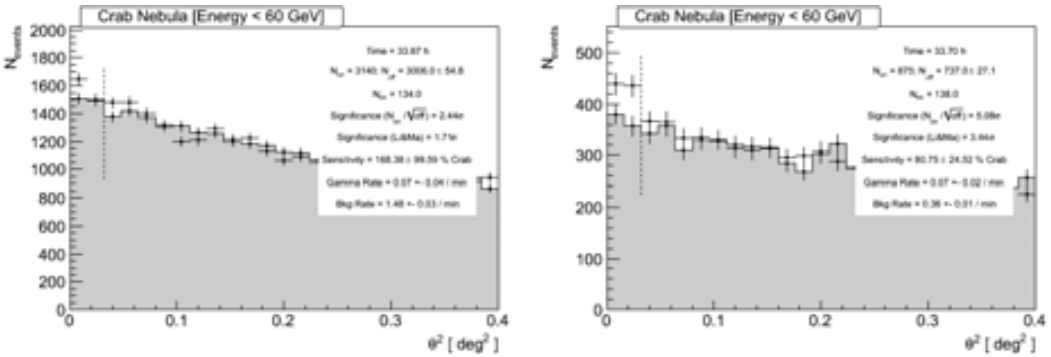

Figure 5.3: θ^2 distribution below 60 GeV. *On the left:* for the standard timing image cleaning analysis. *On the right:* for the sum image cleaning.

In the specific case of this work, the use of the sum image cleaning allowed to reconstruct the first spectral point in the energy bin between 43 and 58 GeV. This effect is illustrated in Figure 5.5: it shows the distributions of the number of excess events and of the significance per spectral point. The significance was computed by using Li & Ma formula 17.

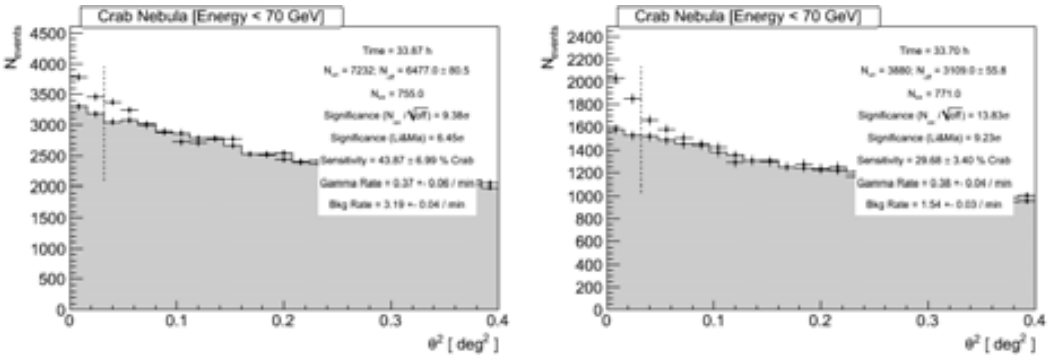

Figure 5.4: θ^2 distribution below 70 GeV. *On the left:* for the standard timing image cleaning analysis. *On the right:* for the sum image cleaning.

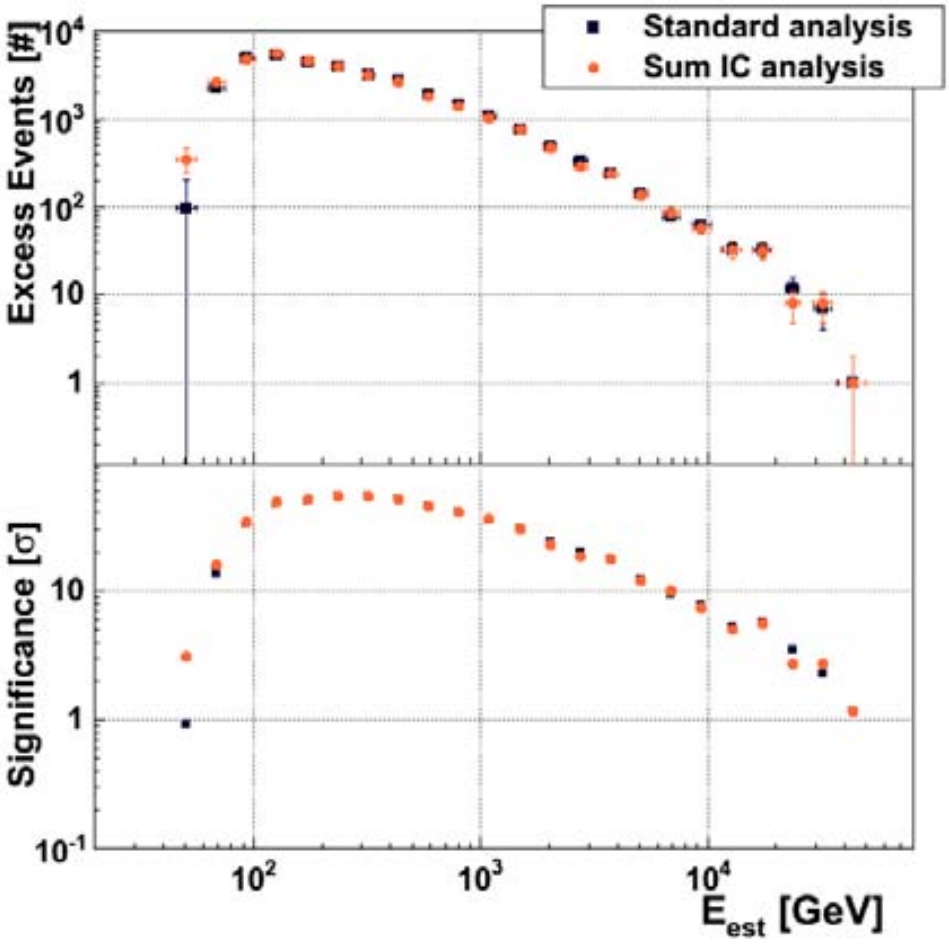

Figure 5.5: Comparison between the analysis with the standard image cleaning and the one with the sum cleaning. Distribution of the number of excess events and of the significance per spectral point.

5.2.2 Energy resolution and bias

The goodness of the energy estimation can be described by the *energy resolution* and the *energy bias*, defined in § 3.11.1. This non-standard analysis requires its own energy charac-

terization up to UHEs.

First of all, a study on the compatibility between the two MC productions (§ 5.1) was performed in the overlapping energy range (between 1 and 30 TeV). It considers only low zenith angle data (ZA $< 30°$).

The *energy resolution* and *bias* of the two MC productions are in perfect agreement for energies smaller than 10–15 TeV (Figure 5.6). Above 10–15 up to 30 TeV the agreement is still acceptable, even though the *energy bias* of UHE MC stretches towards negative values. The energy is underestimated for UHE events because they are not used to construct the energy LUTs (§ 3.11). This choice was meant to improve the performance off the energy estimation in the range 1–15 TeV.

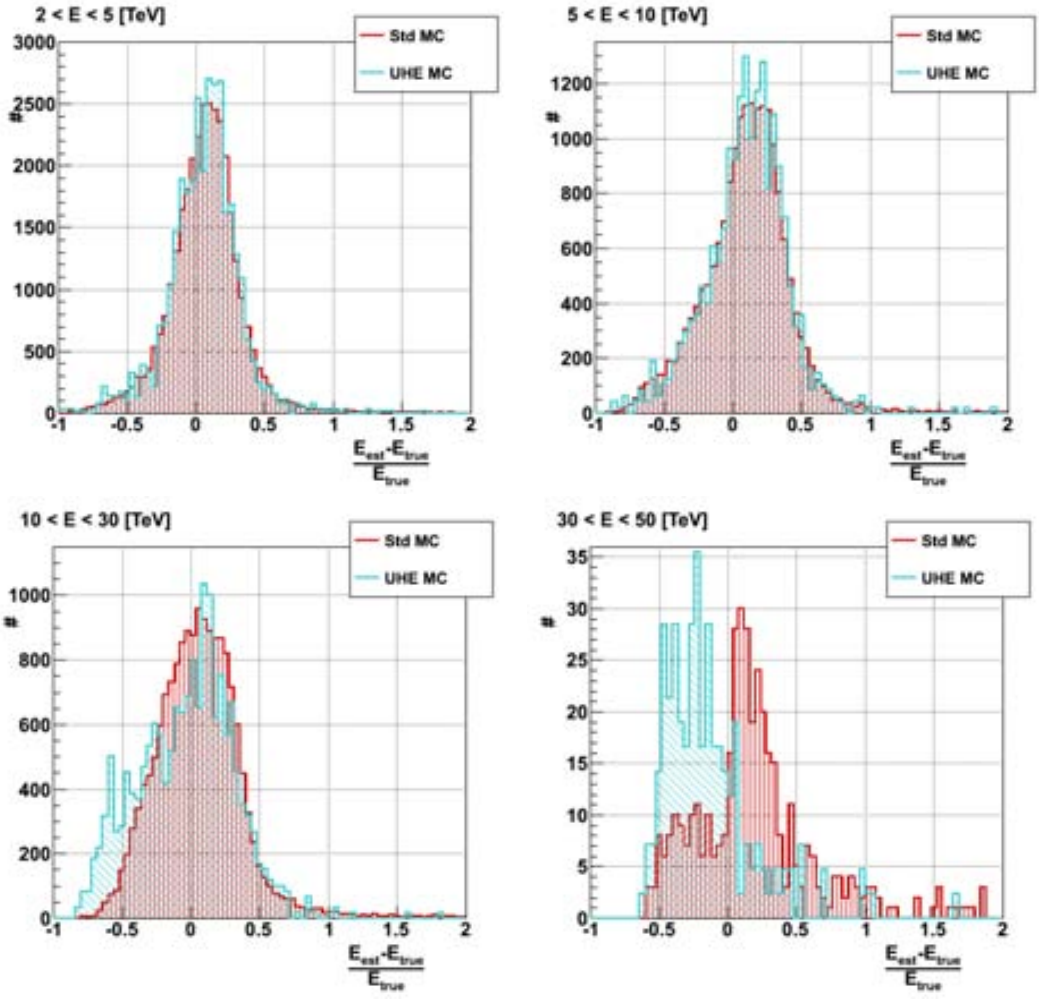

Figure 5.6: Distributions of the *energy bias* for different bins in estimated energy.

At estimated energies larger than 30 TeV, the standard MC production shows a broaden distribution of $(E_{est}\text{-}E_{true})/E_{true}$ due to the fact that it does not contain any event with $E_{true} > 30$ TeV. The large negative *energy bias* of the UHE MC production is due to the above-mentioned effect.

In addition, the energy estimation at different zenith angles was studied. The *energy threshold* (§ 3.11.1) is strongly dependent on the zenith angle, as described in § 3.6 and shown

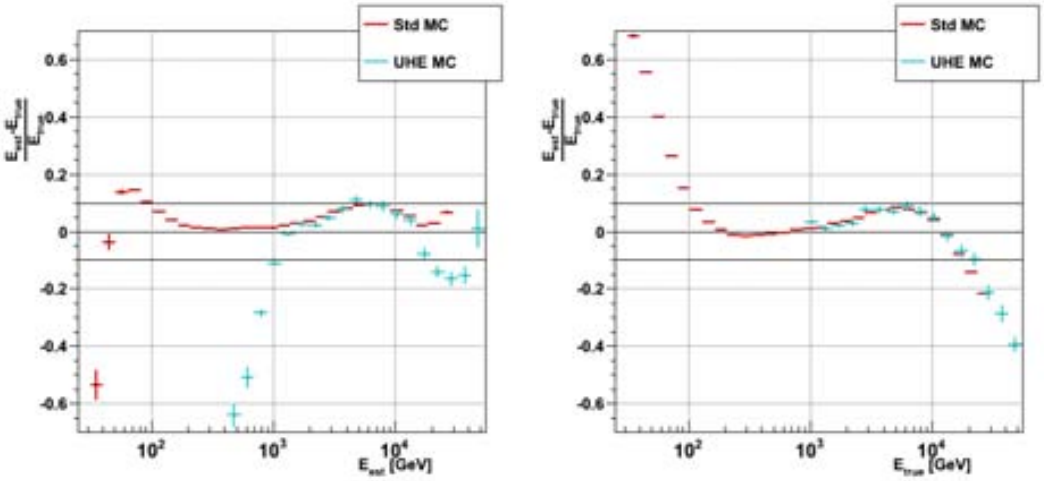

Figure 5.7: *Energy bias* as a function of the energy. *On the left:* : of the estimated energy. *On the right:* : of the true energy.

in Figure 5.8.

This figure illustrates also how the *energy threshold* changes if one applies different set of cuts. In particular, loose cuts indicate cuts which allow 85% of the γ-ray events to survive (spectrum-like selection cuts, § 3.12), while tight cuts keep only 70% of γ-ray events (signal-search-like selection cuts § 3.9.2).

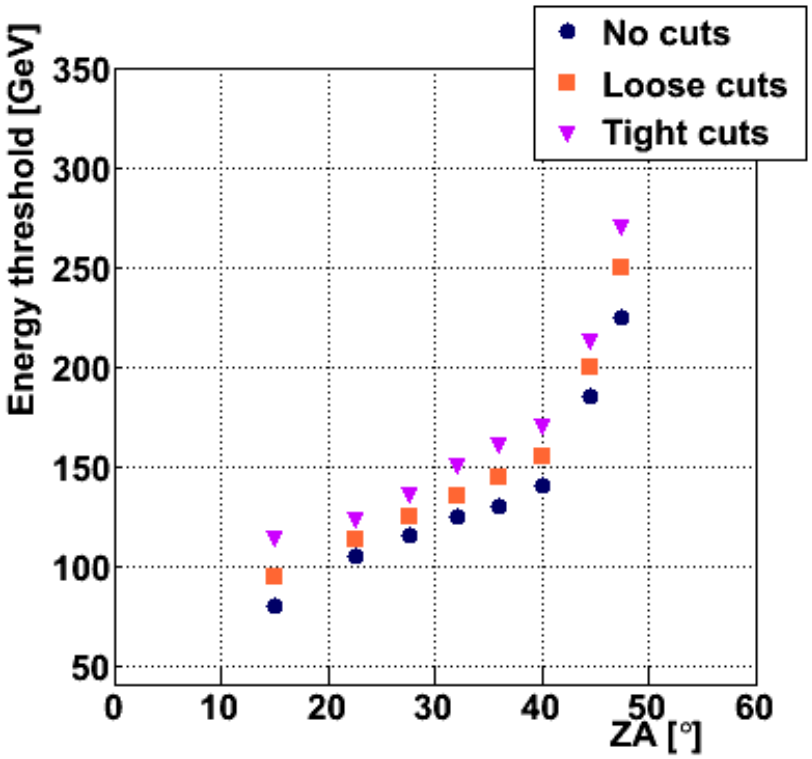

Figure 5.8: *Energy threshold* as a function of the zenith angle for different sets of cuts. Loose cuts guarantee 85% gamma e ciency, tight cuts only 70%.

The *energy resolution* and the *energy bias* were studied for low zenith angles (ZA $< 30°$) and for data in the ZA bin between 39° and 45°(Figure 5.9). The differential *energy resolution* is illustrated in Figure 5.10, and the results obtained for the low zenith angles are in perfect agreement with the values in Aleksić J., et al. (2011b) which are also presented in Figure 3.18. The *energy bias* as a function of both estimated and true energy is displayed in Figure 5.11.

5.2.3 Signal clipping

The current implementation of the pulse saturation in the MC simulation is very simple. The pulses are simply truncated at a given height (900 ph.e.). The saturation in the data is different because the pulses are truncated and broadened. Therefore, there might be some systematic difference between MC and data for the highest energies. This effect can be quantified by applying a truncation on the charge of individual pixels on both data and MC, a so-called "clipping". Two different clipping levels were chosen for this purpose: 750 and 500 ph.e.. The two resulting analyses were compared to the reference analysis (no clipping) in terms of integral sensitivity for energies larger than 1, 5 and 10 TeV. The comparison was performed following the same procedure used for the different image cleaning algorithms (§ 5.2.1), and the results are displayed in Table 5.4. This study proved that the "non optimal"

energy [TeV]	**analysis**	**had.cut**	θ^2**cut** [°]	**bg**	**exc**	**signif.** [η]	**sens.** [% Crab flux]
> 1	reference	0.22	0.010	35	2354 ± 49	54.7	1.03 ± 0.09
	clip 750 ph.e.	0.21	0.010	41	2318 ± 49	53.9	1.13 ± 0.09
	clip 500 ph.e.	0.22	0.010	37	2329 ± 49	54.3	1.08 ± 0.09
> 5	reference	0.22	0.016	4	201 ± 14	15.8	4.1 ± 1.1
	clip 750 ph.e.	0.19	0.016	4	202 ± 15	15.8	4.1 ± 1.1
	clip 500 ph.e.	0.18	0.016	3	202 ± 14	16.0	3.5 ± 1.1
> 10	reference	0.38	0.016	3	72 ± 9	9.1	9.9 ± 3.3
	clip 750 ph.e.	0.32	0.016	3	72 ± 9	9.1	9.9 ± 3.3
	clip 500 ph.e.	0.20	0.016	3	72 ± 9	9.1	9.9 ± 3.3

Table 5.4: Comparison between analyses with different clipping levels.

pulse saturation in our simulations and the consequent mismatch between data and MC does not affect the reconstruction of the high-energy events. The integral sensitivity above 1, 5 and 10 TeV is clipping-independent: all three analyses have the same power in rejecting the background.

Another way to evaluate the impact of the clipping on the analysis is to check for the effect of the larger efficiency in γ-ray selection on the effective collection areas (§ 3.12). As illustrated in Figure 5.12, this is not the case though. The clipping at 750 ph.e. and the reference analyses present collection areas which are comparable within the statistical errors. On the other hand, the clipping at 500 ph.e. analysis shows a 5–10% decrease of the collection area above few TeV.

The forthcoming analysis was performed with a clipping at 750 ph.e., but this choice has no effect on the final results.

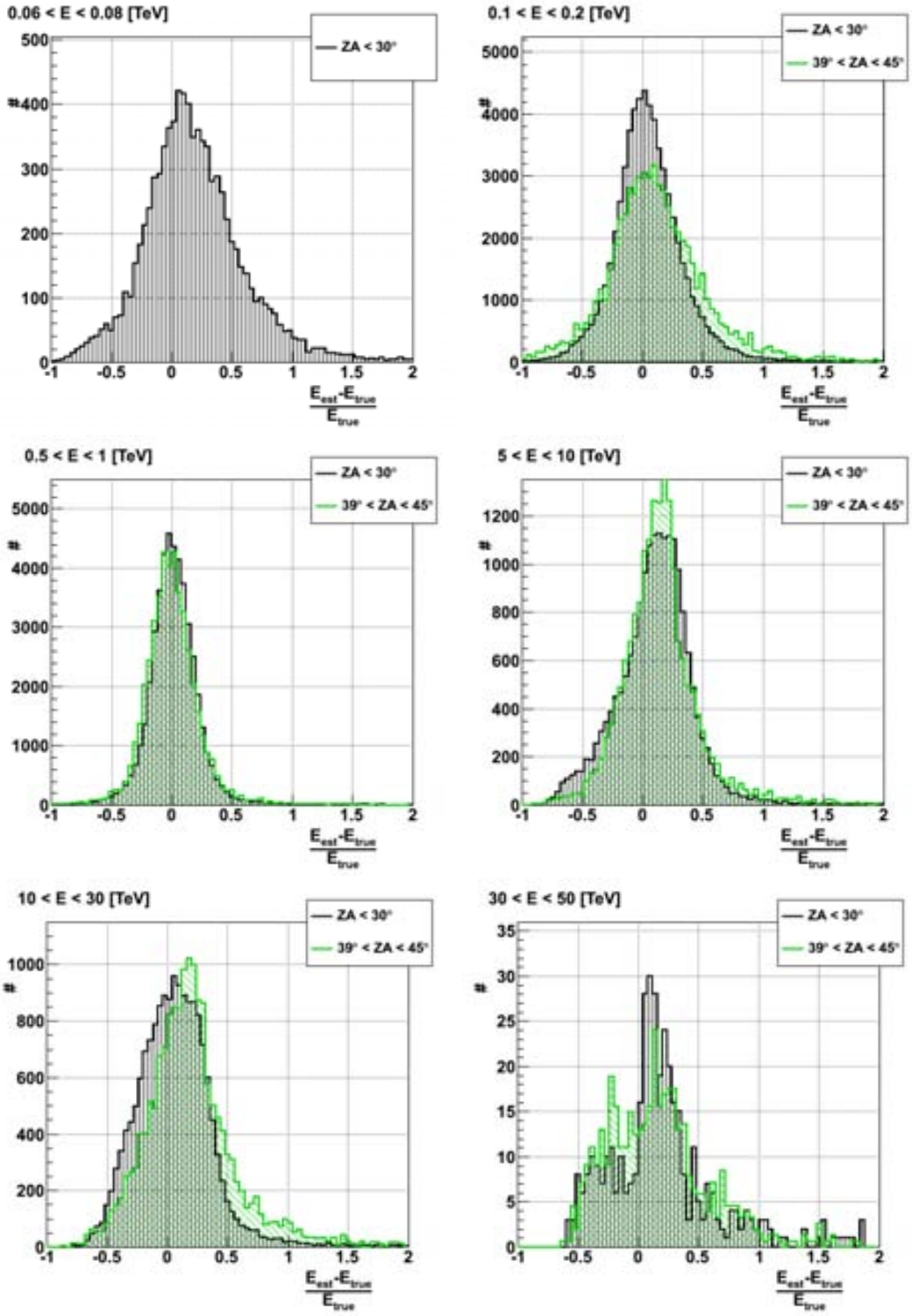

Figure 5.9: Distributions of the *energy bias* for different bins in estimated energy.

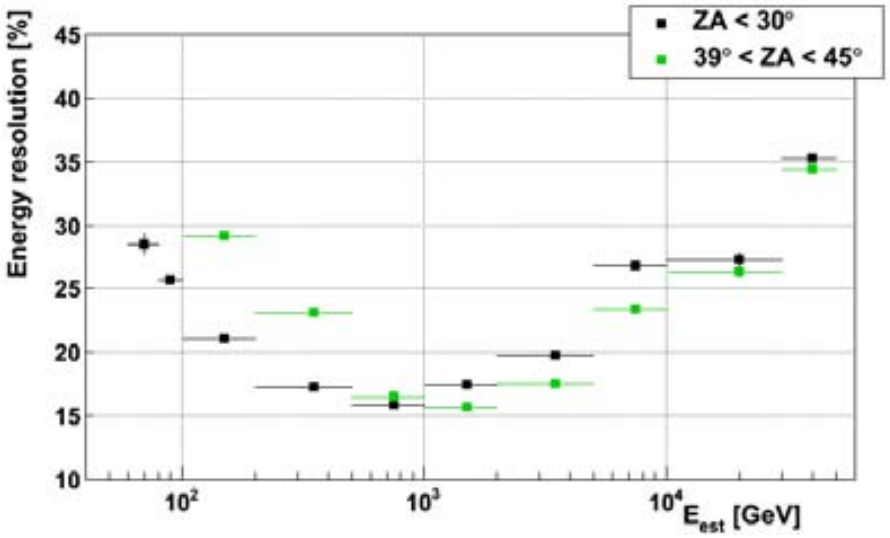

Figure 5.10: ***Energy resolution*** **as a function of estimated energy.**

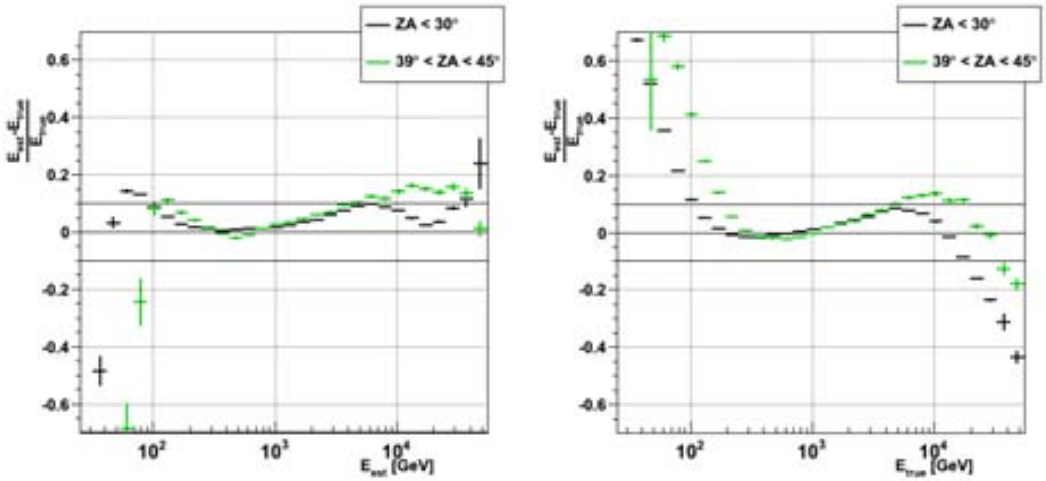

Figure 5.11: ***Energy bias*** **as a function of energy.** *On the left:* : dependence on the estimated energy; *On the right:* : dependence on true energy.

5.3 Di erential energy spectrum

The data sample was divided into four subsamples depending on the zenith angle. An independent analysis was run over each of the subsamples, whose effective observation time amounts to:

- 33.7 hrs for ZA $< 30°$:
- 6.8 hrs for $30° <$ ZA $< 39°$
- 3.5 hrs for $39° <$ ZA $< 45°$
- 1.4 hrs for $45° <$ ZA $< 50°$

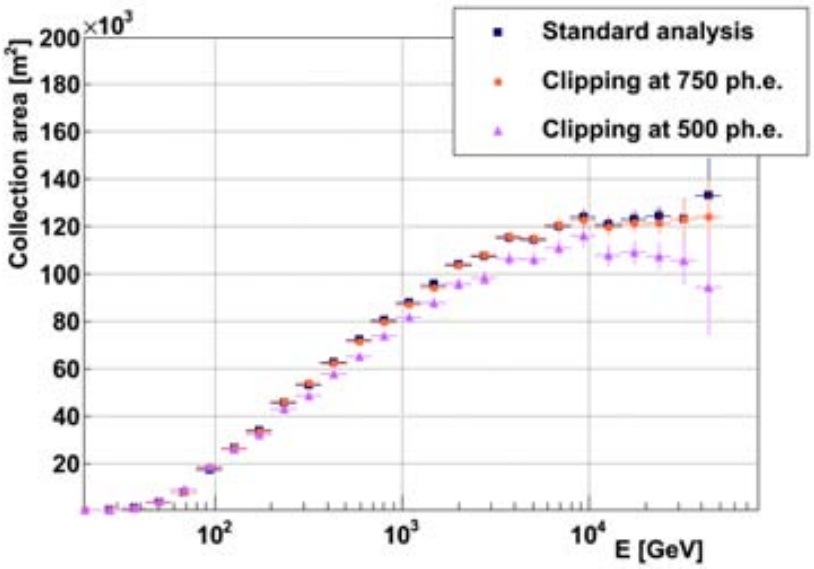

Figure 5.12: Collection area for different clipping levels.

The computation of the differential energy spectrum requires the measurement of the number of excess events in each energy bin (§ 3.12). The gamma selection cuts were optimized on MC to obtain a large gamma efficiency (Equation 3.7). In particular, it was guaranteed that 80% of γ-ray events survived the selection cuts below 5 TeV, and 95% of them at higher energies. At high energies the discrepancies between data and MC are larger than in the other energy range. Keeping such loose cuts reduces systematic effects (§ 3.12).

Results obtained for the data subsamples in the four zenith angle ranges are illustrated below. Figure 5.13 shows the distributions of the effective collection area and the number of excess events as function of the estimated energy. The resulting differential energy spectra are displayed in Figure 5.14 as function of the estimated energy. The correction for the known finite resolution and bias in the energy estimation was applied to these differential energy spectra through the unfolding procedure (§ 3.13). This results in the conversion of the estimated energy in true energy. From now on, unless explicitly stated, "energy", E, will stands for true energy, E_{true}.

5.3.1 Unfolded spectrum

The differential energy spectra obtained for the data subsamples in the four zenith angle ranges were combined at the level of the unfolding (§ 3.13). The result is an unprecedented differential energy spectrum of the Crab Nebula which spans eight orders of magnitude in flux and three orders of magnitude in energy, between 50 GeV and 45 TeV. It is shown in Figure 5.15. The differential flux for each spectral point is quoted in Table 5.5. The differential energy spectrum in Figure 5.15 is unfolded with Bertero's method (Bertero, M., 1989).

This result represents a high-precision measurement with six spectral points per energy decades and statistical errors which are as low as 5% below 100 GeV. This is the first time that such a level of precision has been reached at these energies. Nevertheless, at all energies, the overall uncertainty is dominated by systematic uncertainties rather than statistical ones. The systematic uncertainties, displayed in Figure 5.15 as a yellow-shadowed area, will be discussed

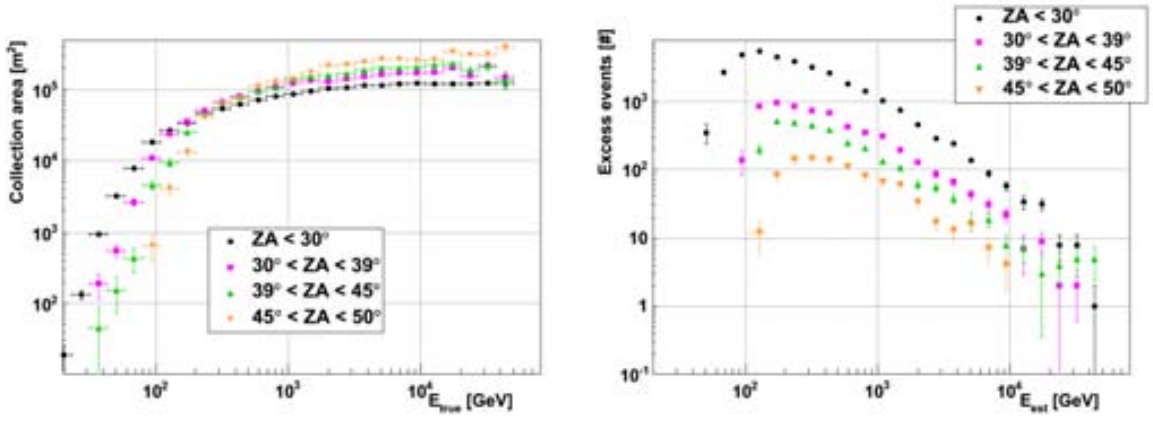

Figure 5.13: Collection area and number of excess events as function of the estimated energy obtained for the data sub-samples in the four zenith angle ranges.

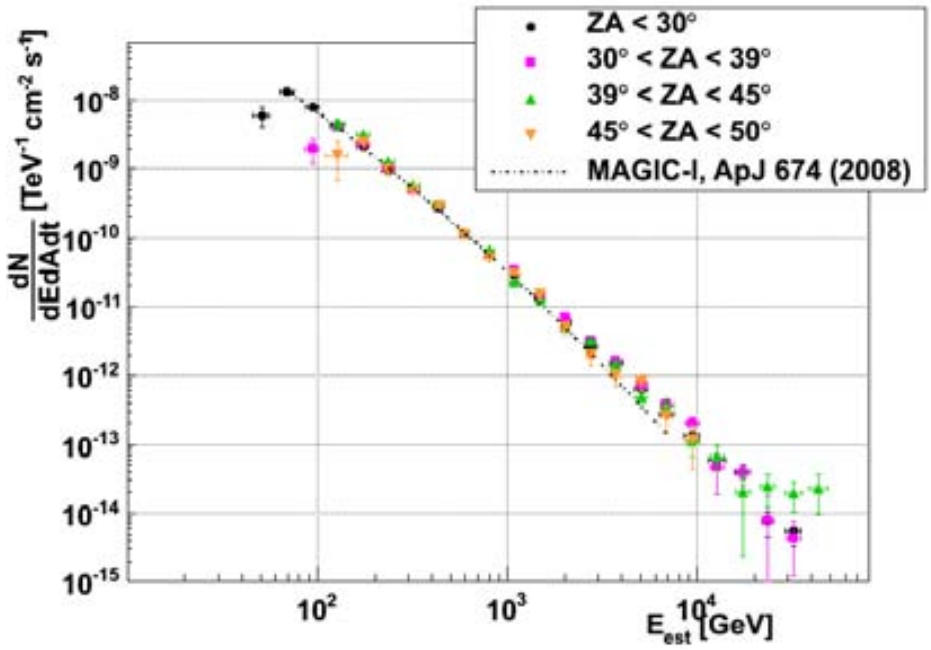

Figure 5.14: Differential energy spectra for the Crab Nebula data in four zenith angle ranges. They are expressed in terms of estimated energy.

in § 5.3.2.

The differential energy spectrum of the Crab Nebula between few tens of GeV and 100 TeV has been parametrized in literature mainly by the following functions (§ 4.4.4):

- a **single power-law**

$$\frac{\mathrm{dN}}{\mathrm{dEdtdA}} = f_0 \cdot \left(\frac{E}{1\mathrm{TeV}}\right)^{-\alpha} \tag{5.1}$$

where f_0 provides the flux normalization, and α the photon index. This is the function used by the HEGRA collaboration (Aharonian, F. A., et al., 2004) and by other

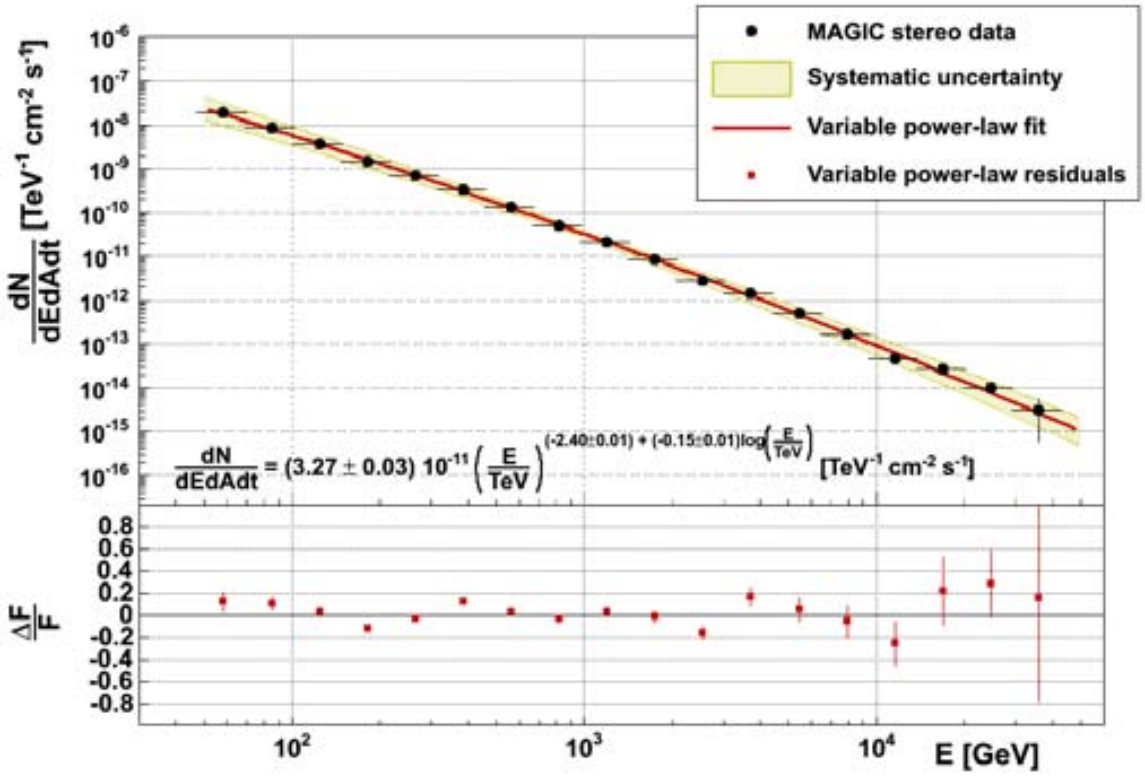

Figure 5.15: Differential energy spectrum for the Crab Nebula between 50 GeV and 45 TeV. It is unfolded with the Bertero's method. The top panel shows in addition to the unfolded data points also results of a variable power-law fit and the systematic uncertainties. The bottom panel shows the relative residuals between the fit results and the data points.

experiments previous to HEGRA.

- a **variable/curved power-law** function

$$\frac{\mathrm{dN}}{\mathrm{dEdtdA}} = f_0 \cdot \left(\frac{E}{1\mathrm{TeV}}\right)^{-\alpha + b\mathrm{Log}_{10}\left(\frac{E}{1\mathrm{TeV}}\right)} \tag{5.2}$$

  where b gives the curvature of the function. The first stand-alone MAGIC telescope showed a hardening of the Crab Nebula spectrum for energies lower than few hundreds GeV (Albert, J., et al., 2008d). A variable power-law fit seems to better describe MAGIC I data.

- a **single power-law with an exponential cut-off**

$$\frac{\mathrm{dN}}{\mathrm{dEdtdA}} = f_0 \cdot \left(\frac{E}{1\mathrm{TeV}}\right)^{-\alpha} \cdot \exp\left(\frac{-E}{E_c}\right) \tag{5.3}$$

  where E_c identifies the energy of the cut-off. This is the fit function suggested by the HESS experiment. They claimed a cut-off energy of (14.3 ± 2.1) TeV (Aharonian, F. A., et al., 2006b).

The obtained differential energy spectrum was fitted to all these three functions. The fit takes into account the correlations between the spectral points, which were introduced by the

mean energy [GeV]	**differential flux** [TeV $cm^{-2}s^{-1}$]
58.4	$(1.95 \pm 0.11)\ 10^{-8}$
85.2	$(8.87 \pm 0.30)\ 10^{-9}$
124.3	$(3.73 \pm 0.10)\ 10^{-9}$
181.4	$(1.41 \pm 0.03)\ 10^{-9}$
264.7	$(6.81 \pm 0.16)\ 10^{-10}$
386.3	$(3.36 \pm 0.07)\ 10^{-10}$
563.6	$(1.30 \pm 0.03)\ 10^{-10}$
822.3	$(5.04 \pm 0.16)\ 10^{-11}$
1199.7	$(2.17 \pm 0.08)\ 10^{-11}$
1750.3	$(8.23 \pm 0.39)\ 10^{-12}$
2553.7	$(2.73 \pm 0.19)\ 10^{-12}$
3727.2	$(1.45 \pm 0.10)\ 10^{-12}$
5437.8	$(4.92 \pm 0.49)\ 10^{-13}$
7933.6	$(1.62 \pm 0.24)\ 10^{-13}$
11574.9	$(4.64 \pm 1.24)\ 10^{-14}$
16887.4	$(2.69 \pm 0.66)\ 10^{-14}$
24647.6	$(9.90 \pm 2.29)\ 10^{-15}$
35960.1	$(3.05 \pm 2.48)\ 10^{-15}$

Table 5.5: Mean energy and differential flux of the spectral points shown in Figure 5.15.

unfolding procedure. No systematic errors were included in the fit. Results are displayed in terms of SED in order to enhance any spectral feature (Figure 5.16). The relative residuals between the spectral points and the fit results are also shown in the bottom panel, same figure.

A correlated fit of a single power-law provides a flux normalization $f_0 = (3.03 \pm 0.03)$ 10^{-11} TeV^{-1} cm^{-2} s^{-1}, and a photon index α=(2.33 $\pm$ 0.01). The γ^2 of the fit is 270 for 16 Degree of Freedom (DoF). The variable power-law fit results in a flux normalization f_0 of (3.27 $\pm$ 0.03) 10^{-11} TeV^{-1} cm^{-2} s^{-1}, a photon index α of 2.40 $\pm$ 0.01 and a curvature b of -0.15 $\pm$ 0.01. This fit has a γ^2 of 72 for 15 DoF. Finally a fit of a single power-law with an exponential cut-off gives a flux normalization of (3.66 $\pm$ 0.08) 10^{-11} TeV^{-1} cm^{-2} s^{-1}, a photon index of -2.22 $\pm$ 0.01, and an exponential cut-off at 9.4 $\pm$ 1.1. It has a γ^2 of 104 for 15 DoF.

All these fits present too high values of the γ^2/DoF. This is due to the fact that the residuals to the fit function shows deviations which are statistically significant, mainly around 200 GeV and 2.5 TeV. These spectral features, so-called *wiggles*, can be explained by systematic effects and will be treated in detail in § 5.3.2. Nevertheless, since the γ^2/DoF for the single power-law fit is 30 larger than the one obtained for the other two fits, this suggests that the power-law behaviour is disfavored. Moreover, at energies above 5 TeV the residuals show a systematic negative trend. On the other hand, the variable power-law and the power-law with cut-off remain equally valid. Note the estimated energy cut-off is compatible with the one reported by HESS (Aharonian, F. A., et al., 2006b). For sake of simplicity from now on, only fits of variable power-laws will be performed.

Three other unfolding methods (Schmelling's, Tikonov's and forward unfoldings) were considered and all of them gave consistent results: both the spectral points and the fit parameters

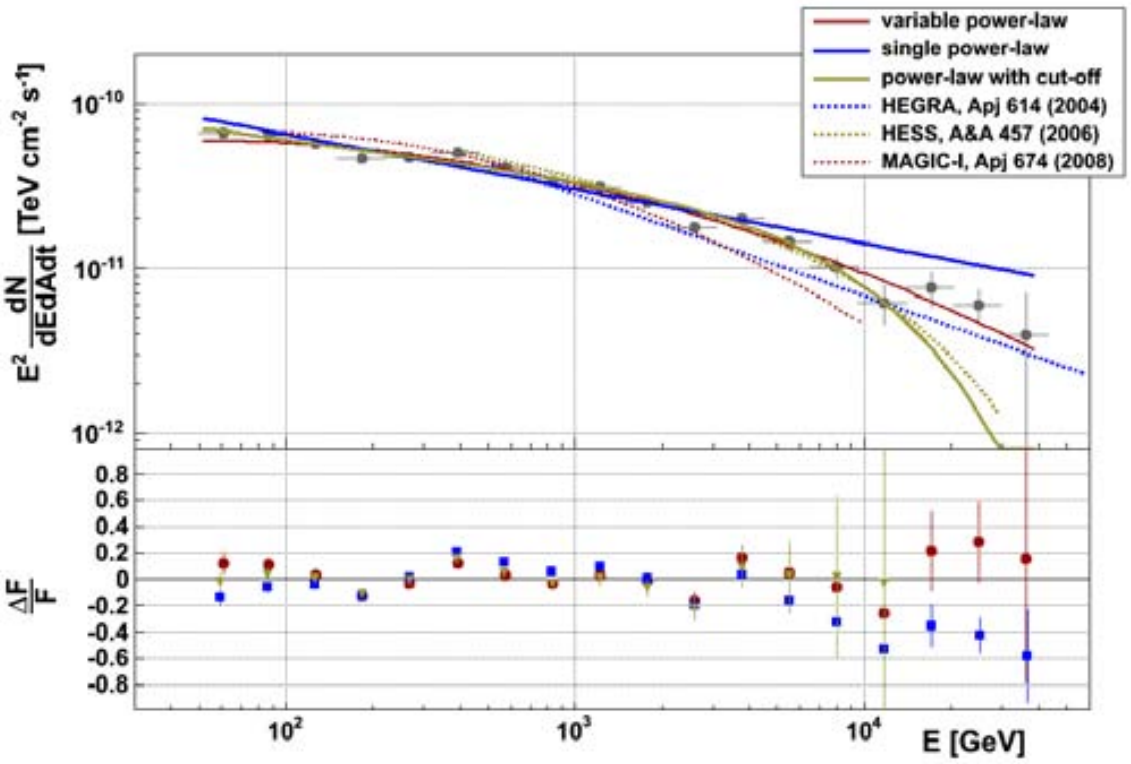

Figure 5.16: SED of the Crab Nebula with different fits of a power-law, a power-law with cut-off and a variable power-law

are compatible within statistical errors. Table 5.6 shows the obtained fit parameters, and Figure 5.17 illustrates the SED of the Crab Nebula for the considered unfolding methods. In addition to the unfolded data points, the top panel of this figure shows the results of a variable power-law fit. The bottom panel shows the relative residuals between the data points and the corresponding fit results. From now on, all the SEDs which will be presented will follow the above-described pattern. Bertero's was favored over the other considered unfolding methods as the one which needs the lowest regularization weight (refer to § 3.13 for the definition of this quantity). Less regularization means that more measured points are used in the unfolding, hence the error bars are smaller and more compatible with the pre-unfolding error-bars.

method	$\mathbf{f_0}$ $[\mathrm{TeV}^{-1}\mathrm{cm}^{-2}\mathrm{s}^{-1}]$	α	**b**
Bertero	$(3.27 \pm 0.03)\times10^{-11}$	2.40 ± 0.01	-0.15 ± 0.01
Schmelling	$(3.29 \pm 0.03)\times10^{-11}$	2.39 ± 0.01	-0.15 ± 0.01
Tikonov	$(3.28 \pm 0.05)\times10^{-11}$	2.40 ± 0.01	-0.16 ± 0.01
Forward	$(3.25 \pm 0.04)\times10^{-11}$	2.40 ± 0.01	-0.14 ± 0.01

Table 5.6: Results of a variable power-law fit (Equation 5.2) of the Crab Nebula differential energy spectrum obtained with different unfolding methods.

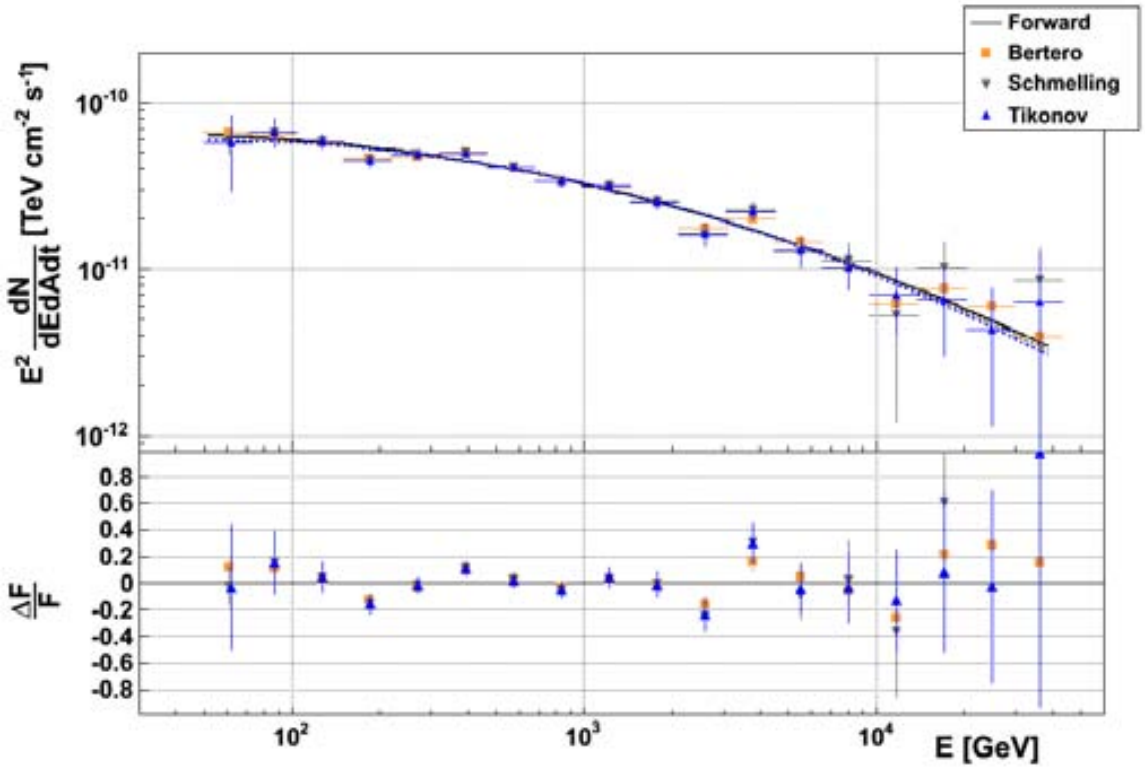

Figure 5.17: SED of the Crab Nebula for different unfolding methods.

5.3.2 Systematic uncertainties

The overall systematic uncertainty affecting the measurement of the differential energy spectrum for the Crab Nebula includes the three different classes of systematic effects described in § 3.16:

- Systematic uncertainty on energy scale.
- Systematic uncertainty on flux normalization.
- Systematic uncertainty on spectral slope.

The estimation of the different uncertainties follows the standard prescription of Aleksić J., et al. (2011b), the procedure adapted to suit the specifics of the present analysis. This section is dedicated to summarize all the different components of the total systematic uncertainty with the corresponding effect on the differential spectrum.

Uncertainty on the energy scale:
The uncertainty on the energy scale is represented by the black arrow in top right corner of Figure 5.18 and is estimated to be at the level of 15–17% (§ 3.16) according to specific studies in Aleksić J., et al. (2011b). Figure 5.19 illustrates the effect of this uncertainty on the SED: the spectral points shift up and down in energy, but the spectral shape does not change.

Uncertainty on the ux normalization:
As described in § 3.16, the sources of systematic effects which affect the flux normalization are four:

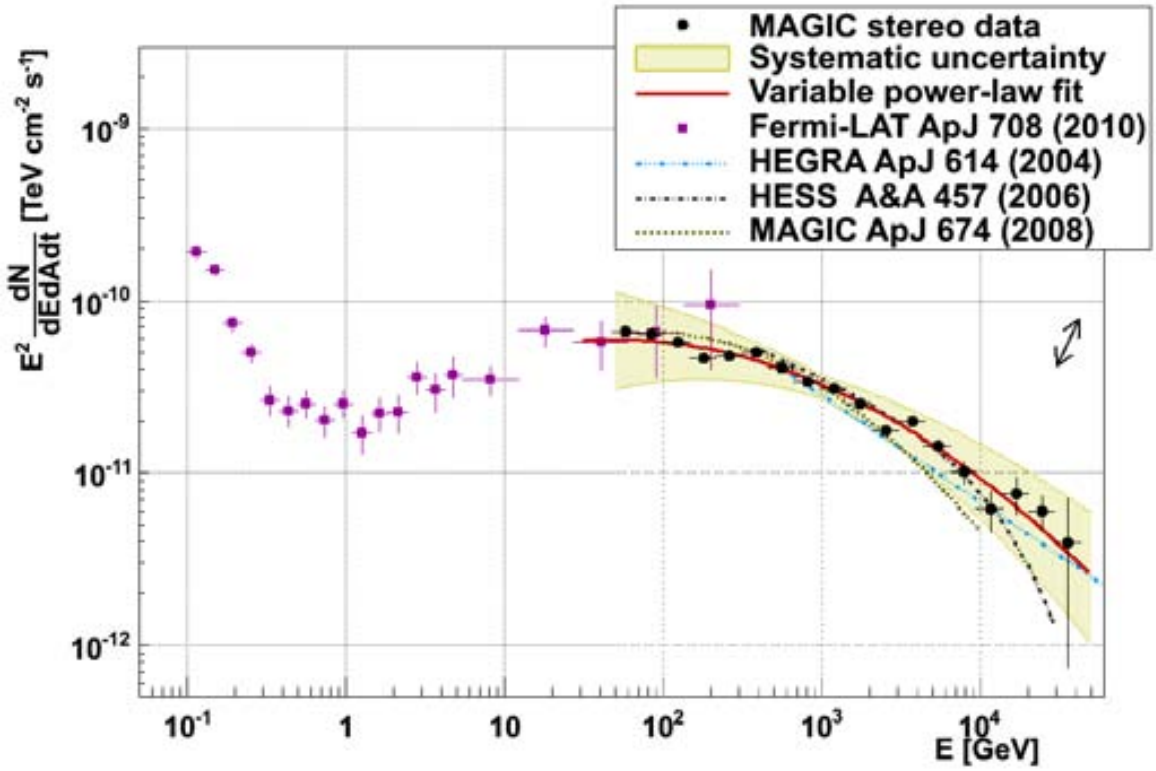

Figure 5.18: SED of the Crab Nebula between 100 MeV and 50 TeV. It includes the MAGIC spectral points presented in this work and the ones by *Fermi*/LAT published in (Abdo, A. A., et al., 2010a). The yellow-shadowed areas represents the systematic uncertainty due to the analysis. The arrow shows the 14% uncertainty on the energy scale.

- the background rejection estimated to produce 1–8% error depending on the energy and the strenght of the source flux. A conservative 8% uncertainty was considered for this analysis given the wide exploited energy range.
- the mispointing can produce a systematic uncertainty of 1–4%. As the mispointing of the overall sample was estimated to be 0.017 ± 0.03, in agreement with the typical values (Aleksić, J., et al., 2010b), a conservative 4% error can be assumed for this source of systematic effects.
- the entire data sample of this analysis was recorded during dark observation time. Nevertheless the level of the NSB in its FoV can because of the presence of bright ζ-Tauri. Therefore a 4% systematic uncertainty was taken into account.
- differences between simulated and real γ-ray events produce a systematic uncertainty at most at the level of 10% . Given the fact that this analysis uses very soft gamma selection cuts to reduce this source of systematic error, just a 5% uncertainty was assumed.

An additional source of systematic uncertainty affects the flux normalization in this analysis. It is given by the zenith angle of the observations which covers a wide range, from 0° up to 50°. From the unfolded differential spectra of the data subsamples for the four zenith angle ranges (Figure 5.20), the uncertainty was estimated to be 8%.
In conclusion, the flux normalization has a systematic uncertainty of 14%.

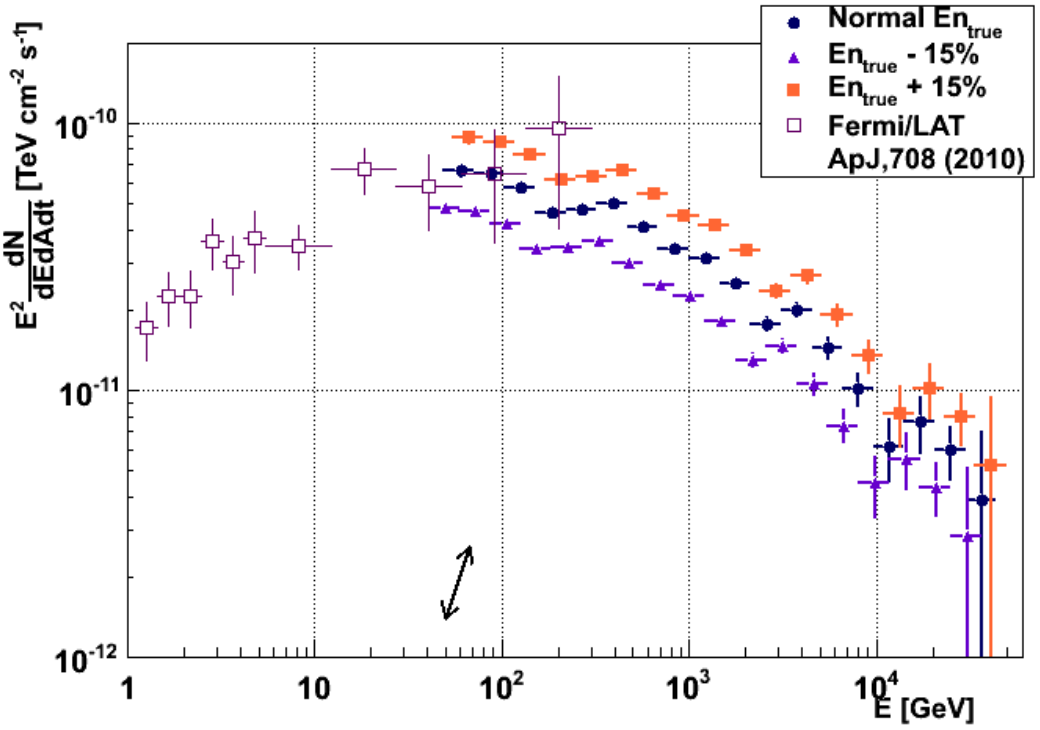

Figure 5.19: The effect on the SED of the Crab Nebula of the 15% uncertainty on the energy estimation.

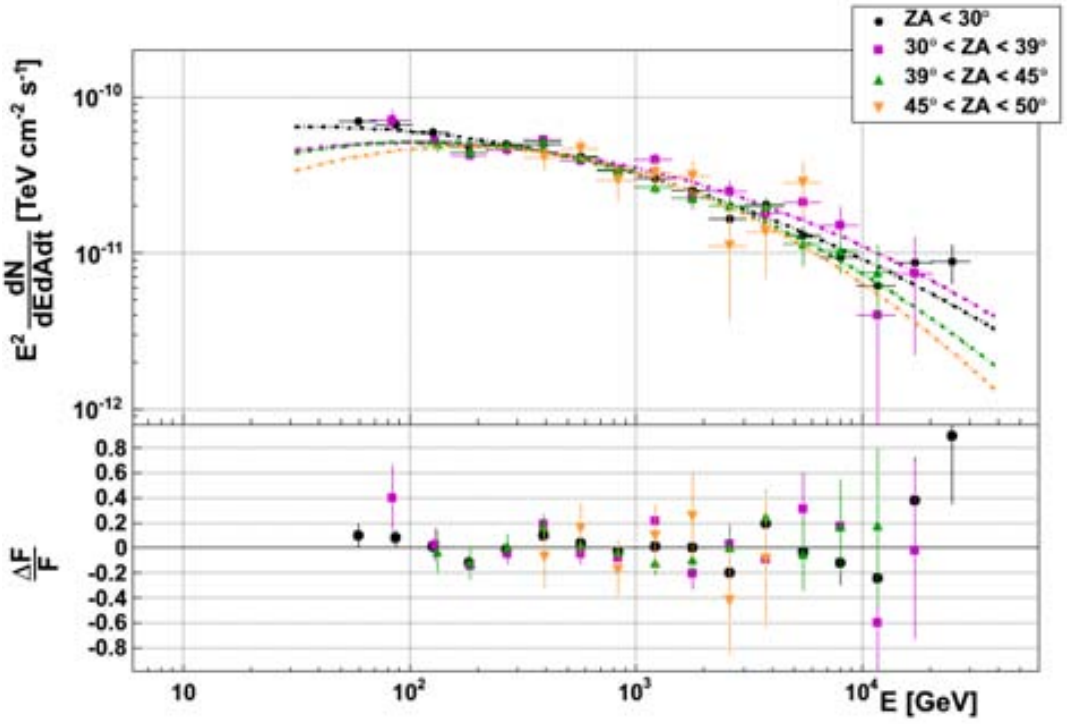

Figure 5.20: Crab Nebula SED for the four zenith angle ranges.

Uncertainty on the spectral slope:
Since the differential energy spectrum is well-fitted by a variable power-law, the systematic uncertainty on the spectral slope is split between the uncertainties of the photon index, α, and the curvature parameter, b. Besides the 0.04 error on the photon index due to the non-linearity of the analog signal chain (§ 3.16), there is another dominant source belonging to this class of systematics: the analysis methods. The latter was evaluated by estimating the effect of the RF, the image cleaning, the zenith angle of the observations, the unfolding methods and the efficiency of the gamma selection cuts (always above the 70% in order to reduce the discrepancy between MC and data). It results in a systematic uncertainty on α of 0.06 and on b of 0.05. The obtained values are in agreement with the overall uncertainty on the spectral slope quoted in Aleksić J., et al. (2011b).

The last two categories of systematics, the uncertainty on the flux normalization and the uncertainty on the spectral slope, are expressed in terms of systematic errors of the fit parameters. The total effect is indicated by the yellow-shadowed bands around the differential spectrum in Figure 5.15 and around the corresponding SED between 100 MeV and 50 TeV in Figure 5.18.

Summarizing the fit parameters are:
$f_0 = (3.27 \pm 0\ 03_{stat} \pm 0\ 46_{syst}) \times 10^{-11}$ photons cm^{-2} s^{-1}.
$\alpha = 2.40 \pm 0\ 01_{stat} \pm 0\ 1_{syst}$
b = -0.15 $\pm$ 0 01$_{stat}$ $\pm$ 0 05$_{syst}$

In the estimation of the systematic uncertainty of the analysis, the effect of the tails in the migration matrix was also checked (Figure 5.21 top left). The original migration matrix was then truncated in such a way that only bins with a relative error of at least 10% survive (Figure 5.21 top right). The bottom panel of Figure 5.21 shows the SEDs obtained with the two different matrices. All the points compatible are within the statistical errors. Therefore, the degradation of the migration matrix does not add any source of systematic uncertainty.

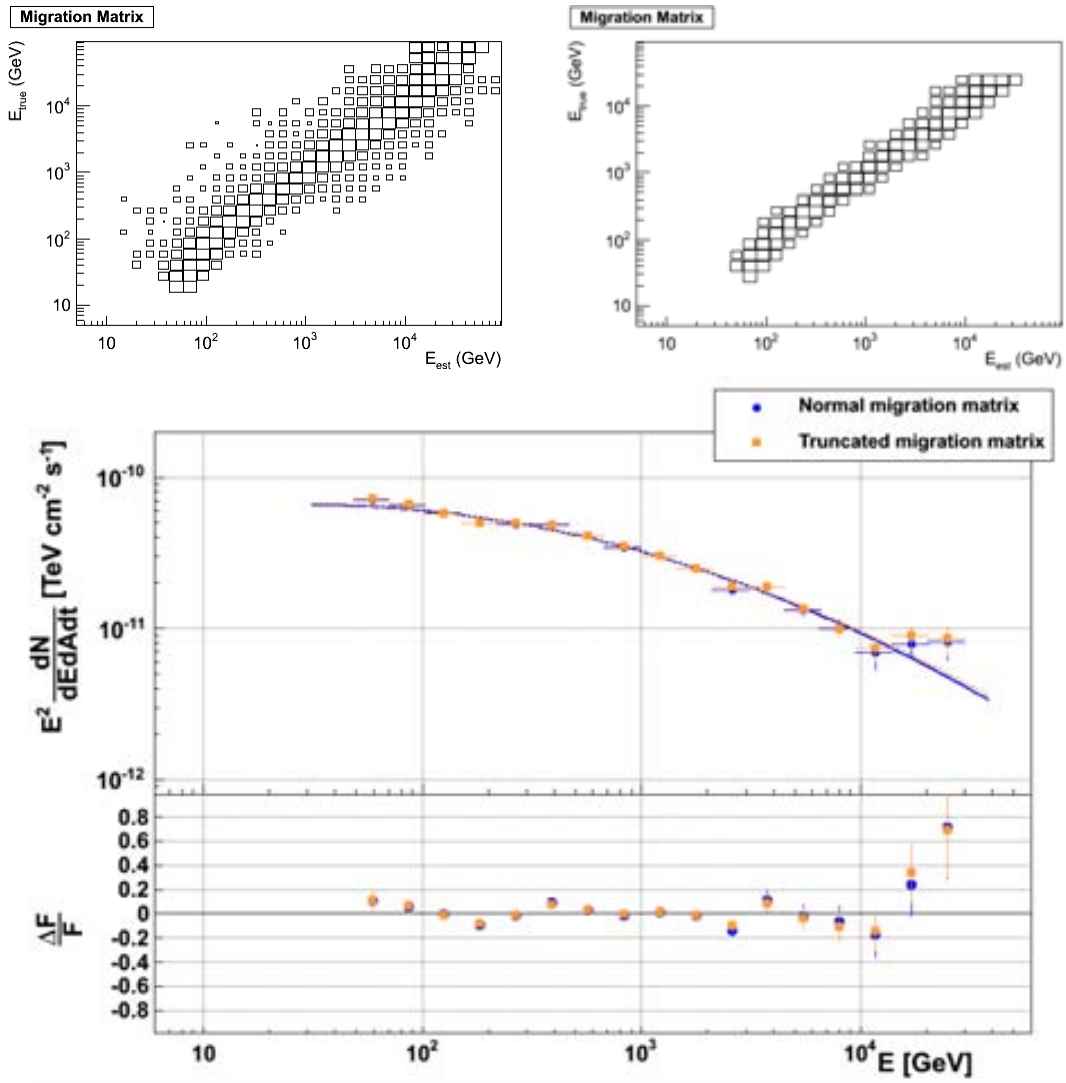

Figure 5.21: Study of the effect of the tails in the migration matrix. *On top left*: the original migration matrix. *On top right*: the truncated migration matrix which considers only bins with at least 10% statistical error. *On bottom*: the SED obtained with the two above-described migration matrices.

Spectral Features

As explained in § 5.3.1, the Crab Nebula differential energy spectrum presents some statistically significant discrepancies from the fitted variable power-law. Though the total systematic uncertainty described in the previous section is wide enough to cover the disagreement, it must be noticed that such uncertainty, influencing the global fit parameters, cannot explain alone the local features of the spectrum. In other words, a strictly energy dependent treatment of the systematics is needed to assign an uncorrelated uncertainty to each energy bin of the unfolded spectrum, and a dedicated effort is ongoing to put into practice this new approach.

The possible source of this energy-dependent effect is under-investigation. It might be related to discrepancy between MC and data, to some hidden features of the atmospheric Cherenkov technique, or even to some yet-to-be-discovered physics effect. In fact, some of these systematic effects maybe only be ruled out by ways of simultaneous observations with

other IACTs. At present, no such measurement is available, and our study is currently focused on MAGIC data only. A first consideration involves the mentioned possible discrepancies between data and MC affecting the definition of the Hillas parameters, hence the γ/hadron separation based on it. In Aleksić J., et al. (2011b) it is shown that the γ-ray efficiency is strongly reduced at around 300 GeV (Figure 5.22).

The effect is due to the transition from the γ/hadron separation based on the maximum of the shower height parameter (§ 3.5.1), to the γ/hadron separation based on Hillas parameters (§ 3.5). This efficiency reduction certainly contributes to the energy dependent systematic uncertainty, even though its effect is less and less significant with softer *hadronness* cuts. Figure 5.22 shows the fraction of surviving gamma events as a function of the *size* and for different *hadronness* cuts. The main discrepancies in the spectrum are at around 200 GeV and 2.5 TeV translate into a *size* of roughly 2.4 and 3.5, respectively, as shown in Figure Figure 3.4. The corresponding *hadronness* cuts for the Crab Nebula analysis are set to 0.3 around 200 GeV and 0.25 around 2.5 TeV. These results seem potentially successful in explaining, at least in part, the origin of the spectral features and careful studies are in progress in the attempt to make them conclusive.

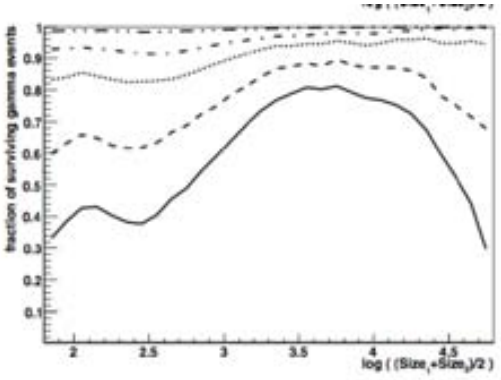

Figure 5.22: γ-ray efficiency as function of size. Different line styles represent different cuts: *hadronness* $<$ 0.1 (solid), $<$ 0.2 (dashed), $<$ 0.4 (dotted), $<$ 0.6 (dot-dashed), and $<$ 0.9 (dot-dot-dashed). Taken from (Aleksić J., et al., 2011b).

In order to ascertain if the wiggles are a systematic effect due to the experimental setup or the analysis method, it is checked if they are present in other sources. If this is the case, one can actually attempt to correct our spectrum. The only available data set with similar statistical precision comes from the observation of the Mrk 421 carried out in January 2010 for a total of 12.3 hours, during a period of enhanced activity with flaring peaks at the level of 2 Crab Nebula flux. The results for Mrk 421 is displayed in Figure 5.23 and compared to the Crab Nebula SED, where the SED representation is favored with respect to the differential energy spectrum itself as it enhances all the spectral features. As it is conventional for this object at VHE, the overall differential energy spectrum of the Mrk 421 can be well described by a power-law with exponential cut-off:

$$\frac{\mathrm{dN}}{\mathrm{dEdtdA}} = (9.18 \pm 0.30) \times 10^{-11} \cdot \left(\frac{E}{1\mathrm{TeV}}\right)^{(-2.05\pm0.02)} \cdot e^{\frac{-E}{(3.5\pm0.3)\mathrm{TeV}}} \ \mathrm{TeV}^{-1}\mathrm{cm}^{-2}\mathrm{s}^{-1} \quad (5.4)$$

It is evident from the comparison in Figure 5.23 that both measurements show analogous statistically significant deviations from the correspondent theoretical functions at comparable energies, although the two data samples are considerably different in the shape of their energy differential spectra. For each bin in energy, a correction factor is calculated as the ratio between the value of the fit function and the measured differential spectrum of the Mrk 421. This factor is then multiplied to the Crab Nebula differential spectrum in the corresponding energy bin. The corrected Crab Nebula SED in the energy range between 80 GeV and 4 TeV is shown in Figure 5.24. The correlated fit[3] to a variable power-law of the new obtained

[3]The covariance matrix of the corrected spectral points was re-computed to account for the propagation of

Crab Nebula spectrum provides a flux normalization of (3.2 ± 0.6) × 10^{-11} TeV^{-1} cm^{-2} s^{-1}, a photon index of (-2.39 ± 0.05) and a curvature parameter of (-0.13 ± 0.08). The γ^2/DoF of the fit to the corrected spectrum is 14/15 with a probability of 52%, and the fit is now statistically acceptable. It must be noticed that such an improvement is partly due to the increasing of the uncertainty on the Crab Nebula data caused by the propagation of the statistical uncertainty of the correcting factors. Nevertheless, the result of this test is a strong indication of the systematic nature of the features in the MAGIC high-precision measurements of the two differential energy spectra.

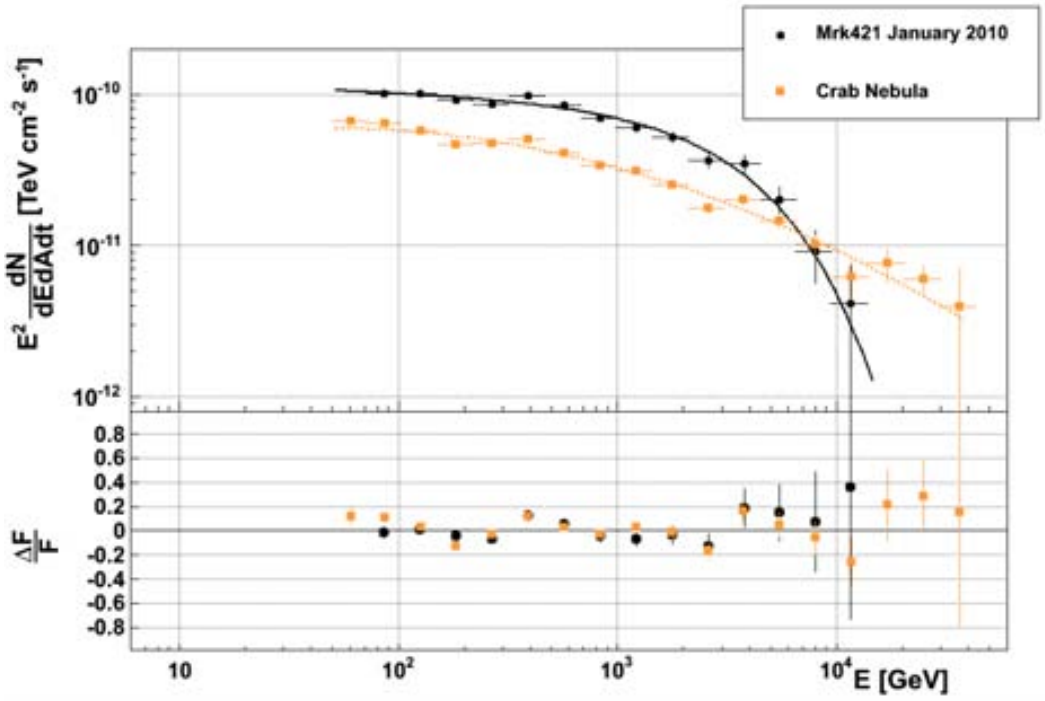

Figure 5.23: SED of the AGN Mrk 421 during its huge flare in January 2010 compared with the Crab Nebula SED.

5.4 Estimation of the Inverse Compton peak

The combination of MAGIC and *Fermi*/LAT data sets can provide a more precise measurement of the position of the peak of the IC component of the Crab Nebula spectrum. Up to now, the only available estimation of this value is 77 ± 35 GeV. It was obtained by the MAGIC collaboration (Albert, J., et al., 2008d) from the results of a variable power-law fit.

Under the assumption that the SED around the peak is described by a variable power-law, *i.e.* a parabola in logarithmic scale, the position of the peak can be estimated by fitting MAGIC and *Fermi* /LAT data together. This γ^2 fit takes into account the correlation between the MAGIC spectral points, whereas no correlation is foreseen between the *Fermi* data (Abdo, A. A., et al., 2010a). Another more generic assumption on the SED distribution around the peak was also considered: an asymmetric parabola with two different slopes for the rising and

the statistical error of the Mrk 421 measurement.

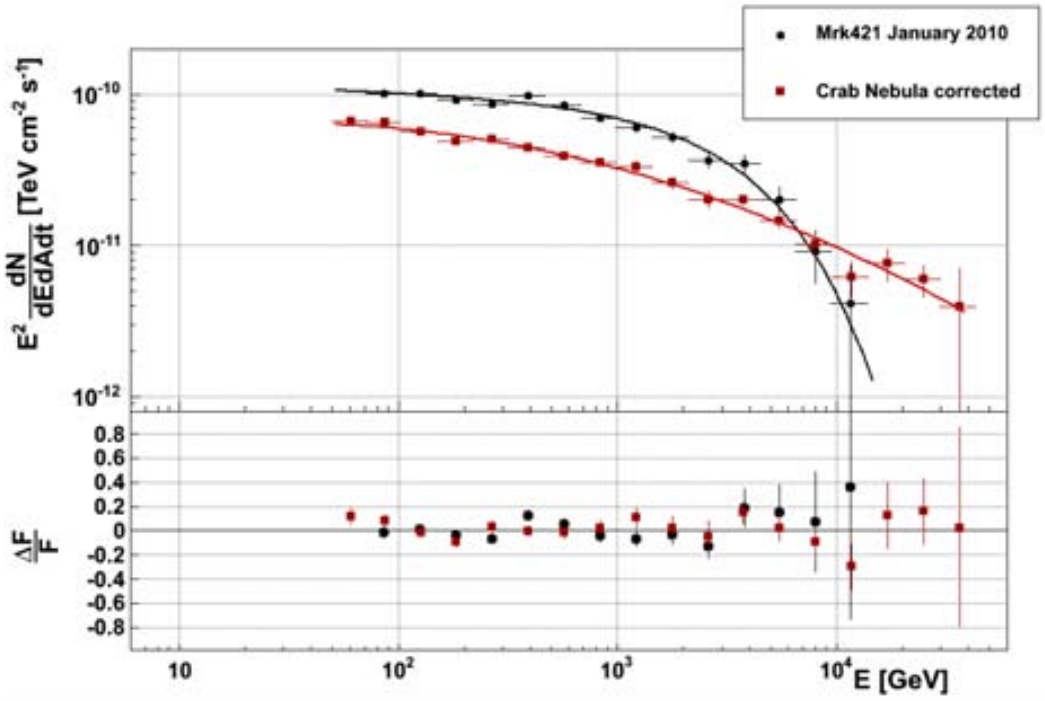

Figure 5.24: The Crab Nebula differential energy spectrum corrected for the Mrk 421 spectrum. Details in the text.

falling edges. Results are summarized in Table 5.7. For completeness, results obtained by fitting only MAGIC data are also reported. Their only aim is to check that the statistical precision improves increasing the considered data set.

Both the fits of a parabola and an asymmetric parabola have $\gamma^2/\mathrm{DoF} \equiv 3$. The high-value of the γ^2 is due to the significant deviations from the fit function in the MAGIC data. What is really relevant in this context is that the two fits have the same probability. In addition, a study of the correlation between fit parameters have been performed. Figure 5.25 illustrates the contours of the γ^2 fit error as a function of the slope and the position of the IC peak. These parameters are strongly correlated: the larger the slope, the higher the energy of the peak. Also the two slopes of the asymmetric parabola are correlated.

fit function	**data**	**slope1**	**peak** [GeV]	**normalization**	**slope2**
parabola	M	$-0.15^{+0\ 01}_{-0\ 01}$	$47.9^{+10\ 2}_{-9\ 6}$	$-10.22^{+0\ 01}_{-0\ 01}$	
parabola	M+F	$0.16^{+0\ 01}_{-0\ 01}$	$58.6^{+6\ 2}_{-5\ 7}$	$-10.24^{+0\ 01}_{-0\ 01}$	
asym. parabola	M+F	$-0.15^{+0\ 01}_{-0\ 01}$	$49.4^{+9\ 6}_{-8\ 7}$	$-10.23^{+0\ 01}_{-0\ 01}$	$-0.21^{+0\ 04}_{-0\ 06}$

Table 5.7: Results for three different fits to the SED around the position of the IC peak. From left to right, the assumed fit function, the considered data set only MAGIC (M) points or MAGIC plus *Fermi*/LAT points (M+F), and the results for the fit parameters.

Depending on the assumption on the spectral shape of the IC component around its peak position, the peak is estimated to be between 50 and 59 GeV with a statistical error at the level of 10–20% . This is a much more precise measurement with respect to the previous one which have a 50% uncertainty.

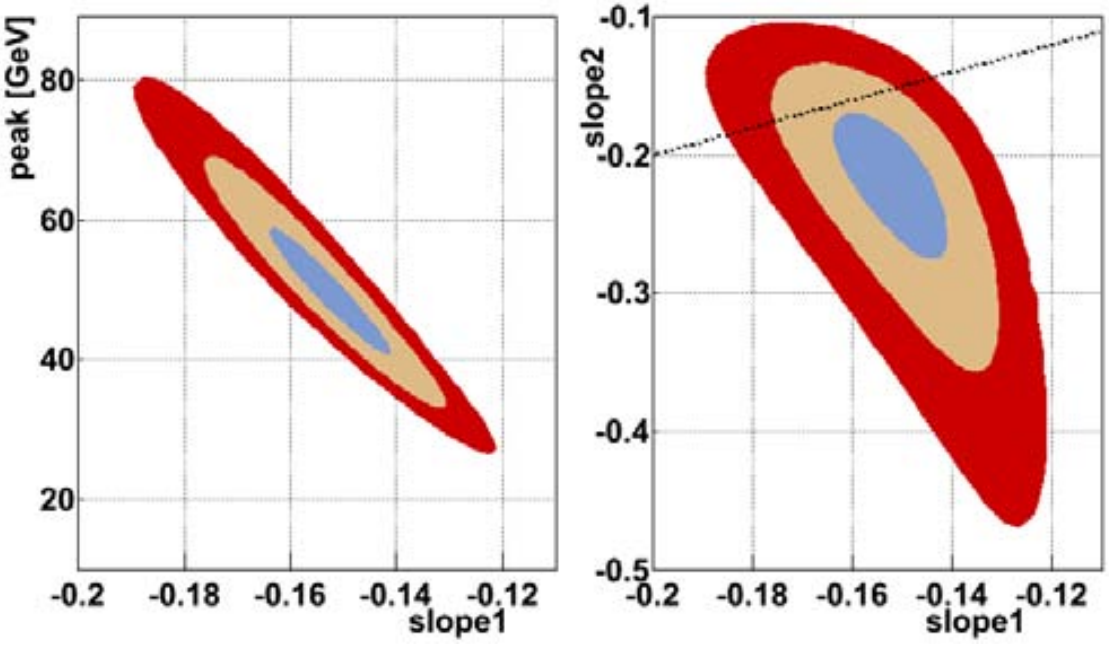

Figure 5.25: Contours of the γ^2 fit error as function of different parameters of the asymmetric parabola fit to the IC peak. *On the left:* the slope and the energy of the IC peak *On the right:* the two slopes. The contours correspond to 1,2 and 3η significances. The dashed line corresponds to an identical value of the slope1 and slope2.

5.5 Theoretical picture

The broad-band SED of the Crab Nebula was matched with two different model calculations that are based on the model first suggested by Hillas, A. M., et al. (1998) assuming a constant B-field as well as a solution of the ideal radial MHD flow (Kennel, C. F. & Coroniti, F. V., 1984b). More specifically the differential energy spectrum has been interpreted using the models in Meyer, M. et al. (2010), described in § 4.4.5. Both model calculations are shown in Figure 5.26 together with the archival data as well as the new measurement presented in this work. The spectral measurement obtained with the MAGIC telescopes covers for the first time the crucial energy range at the peak of the IC component. None of the two models provides a satisfactory match to the data within the statistical errors.

The dip (*i.e. wiggle*) in the differential energy spectrum at 200–300 GeV falls just on top of the expected position of the IC peak. This spectral feature at this specific position is hard to understand: theoreticians may need to postulate the existence of an additional structure in the B-field downstream of the shock. Hence it is of crucial importance to understand the origin of the systematic effect which causes the above-mentioned *wiggle* and, if possible, to correct for it.

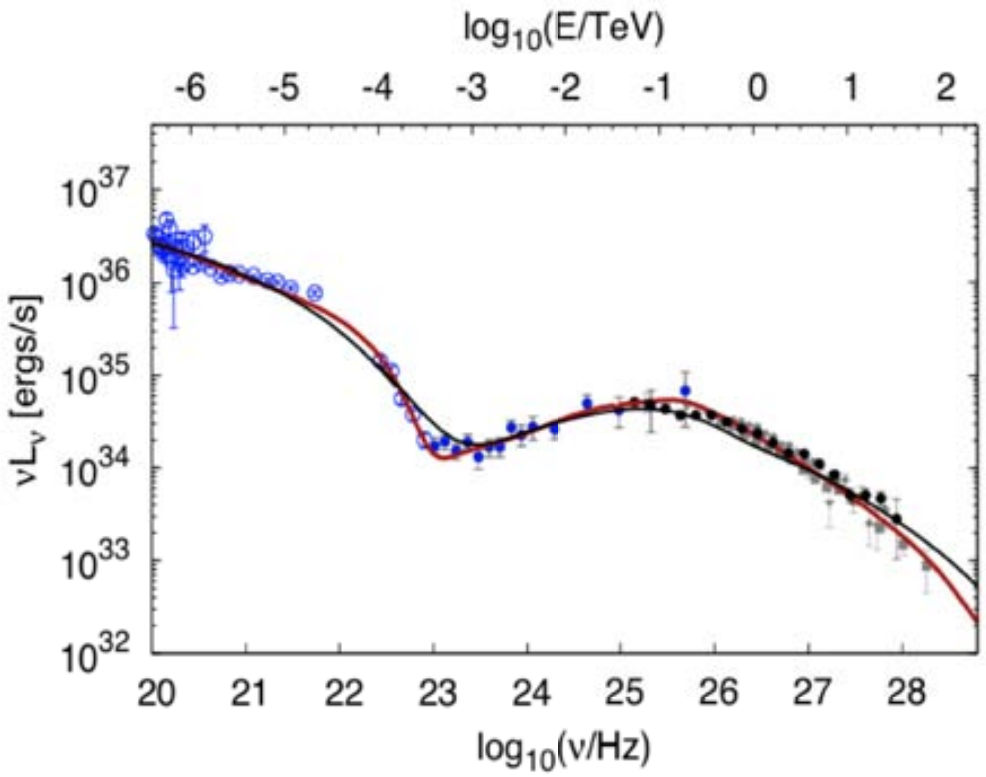

Figure 5.26: The SED of the Crab Nebula superimposed to the two main models. The red line represents the constant B-field model; the black line the MHD one. Filled blue circles are the *Fermi*/LAT measurements, whereas the filled black circles the spectral points presented in this work. All other markers identify historical observations of the Crab Nebula . Credits to D.Horns.

5.6 Flux variability

This section includes time-resolved measurements, *i.e.* light curves (§ 3.14), of the integral γ-ray flux from the Crab Nebula above either 300 or 700 GeV. The threshold at 300 GeV represents a safe lower energy limit which corresponds to the beginning of the collection area plateau (§ 3.14). On the other hand, light curves above 700 GeV are mainly meant to look for fast variations which might have the same origin of the soft-γ-ray flares, as suggested by the claim reported by the ARGO-YBJ collaboration (§ 4.4.6). The threshold is set at 700GeV to guarantee enough statistics with the relatively short duration of the MAGIC daily observation ($\leq$ 2 hours).

The light curves were produced for the four data subsamples separately. Flux points belonging to the same time bin were then averaged and their errors propagated. In addition, a *size* cut at 100 ph.e. was applied to all the analyses in order to reduce possible camera inhomogeneities which may not be cancelled out in case of short time bins.

Searching for flux variability on timescales of days, the light curve above 300 GeV in daily bins was produced, as illustrated in Figure 5.27. The mean flux is $(1.31 \pm 0.01) \times 10^{-10}$ photons cm^{-2} s^{-1}and it is weighted on the observation time. The probability that the light curve is described with a constant flux is $2 \cdot 10^{-7}$. A computation of the systematic uncertainty on the flux integrated in daily bins is needed to establish if the flux variability is

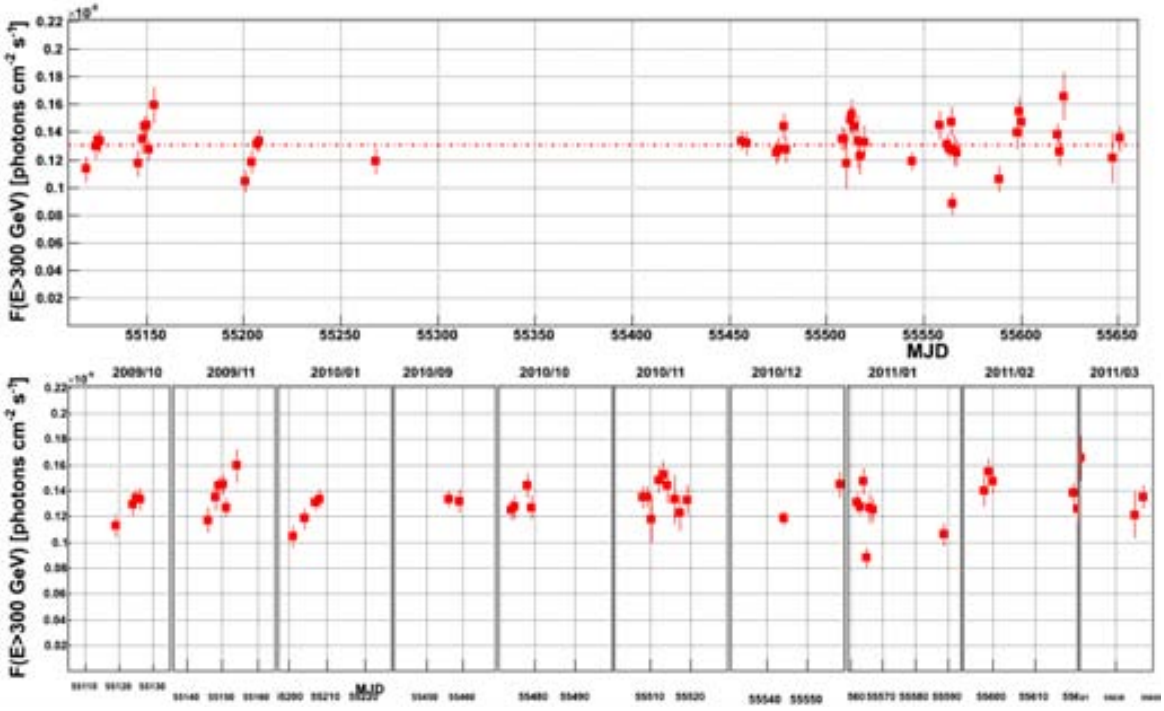

Figure 5.27: Light curve above 300 GeV in bins of days. The upper panel show the daily flux from October 1, 2009 till March 31, 2011. The bottom panels are zoomed per-month portion of the upper panel. Each point of the light curve presents the flux averaged over all the zenith angles ranges.

a real physical effect. Table 3.3 shows the sources of systematic effect which can produce the variations in the flux from night-to-night. Adding them up, the overall systematic uncertainty is estimated to be 13%. The table does not consider the effect of the zenith angle on the flux though and this might constitute a source of systematic uncertainty. In order to check this effect, the mean integral flux above 300 GeV was calculated for each of the four considered zenith angle bins separately. The distribution of the integral mean flux (Figure 5.28) is constant with a probability of 8% between 0° and 50° in zenith angle. More statistics and a wider zenith angle range is needed to determine a possible systematic effect above 45°, but, at the moment, this component can be neglected. Adding the systematic uncertainty of 13% to the statistical error of the flux points, the light curve becomes constant with a probability of 98%. No flux variability on a daily basis can be claimed above 300 GeV.

Some sources of systematic errors, such as the discrepancy between MC and data, are expected to produce correlated variations on the flux of the γ-like background, defined as the number of background events which survive the gamma selection cuts (§ 3.9). Therefore, in the case of an evident correlation between the γ-like background and the source flux, it is possible to employ the background variation respect to the mean flux, to correct the flux points of the signal. With the current data set, no correlation is seen between the γ-like background and the Crab Nebula flux, (Figure 5.29) with a Pearson correlation factor as low as 0.1 . Therefore, the usual correction method cannot be applied and further studies are needed to assess the level of correlation between signal and background implied by the different sources of systematic uncertainty independently.

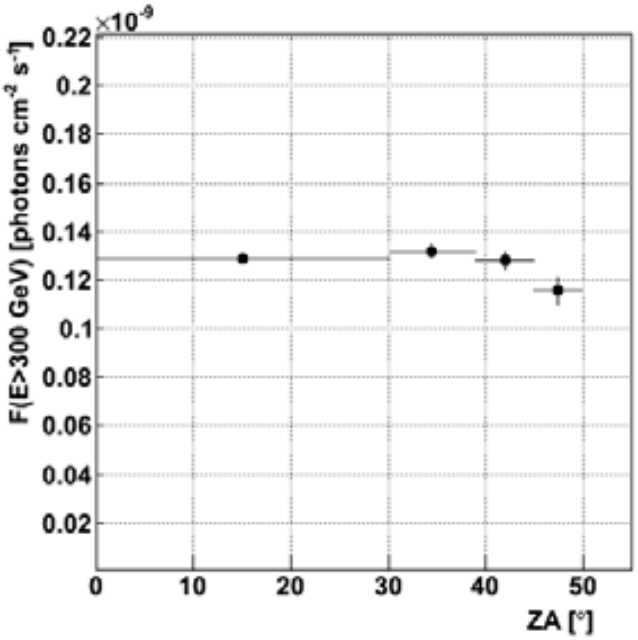

Figure 5.28: Distribution of the mean integral flux above 300 GeV as a function of the zenith angle.

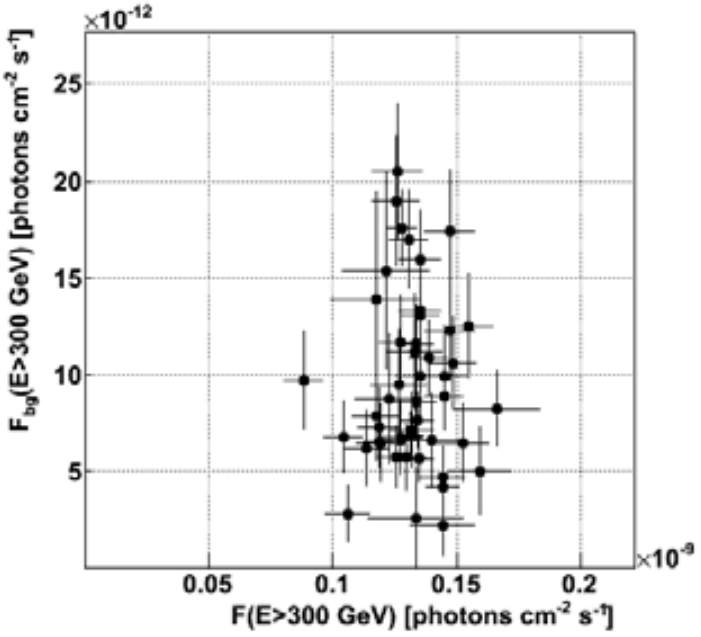

Figure 5.29: Integral flux above 300 GeV of the Crab Nebula versus the integral flux of the γ-like background in the same energy range. The correlation factor is 0.01.

Let us finalize the search for the flux variability at the highest energies, where ARGO-YBJ claimed a flare simultaneous with *Fermi*/LAT. Figure 5.30 shows the light curve above 700

GeV with a time bin of one day. The mean integral flux above 700 GeV is $(4.00 \pm 0.06) \times 10^{-11}$ photons cm^{-2} s^{-1}with a probability of being constant of $3 \cdot 10^{-6}$. Including the above-mentioned 13% systematic uncertainty, the flux is constant with a probability of 52%. The red band in Figure 5.30 shows the 3-days period corresponding to the Crab Nebula flare above 100 MeV detected by both *AGILE* and *Fermi*/LAT in September 2010. MAGIC recorded one hour of data simultaneous to this flare and no flux enhancement is seen either above 300 GeV or above 700 GeV.

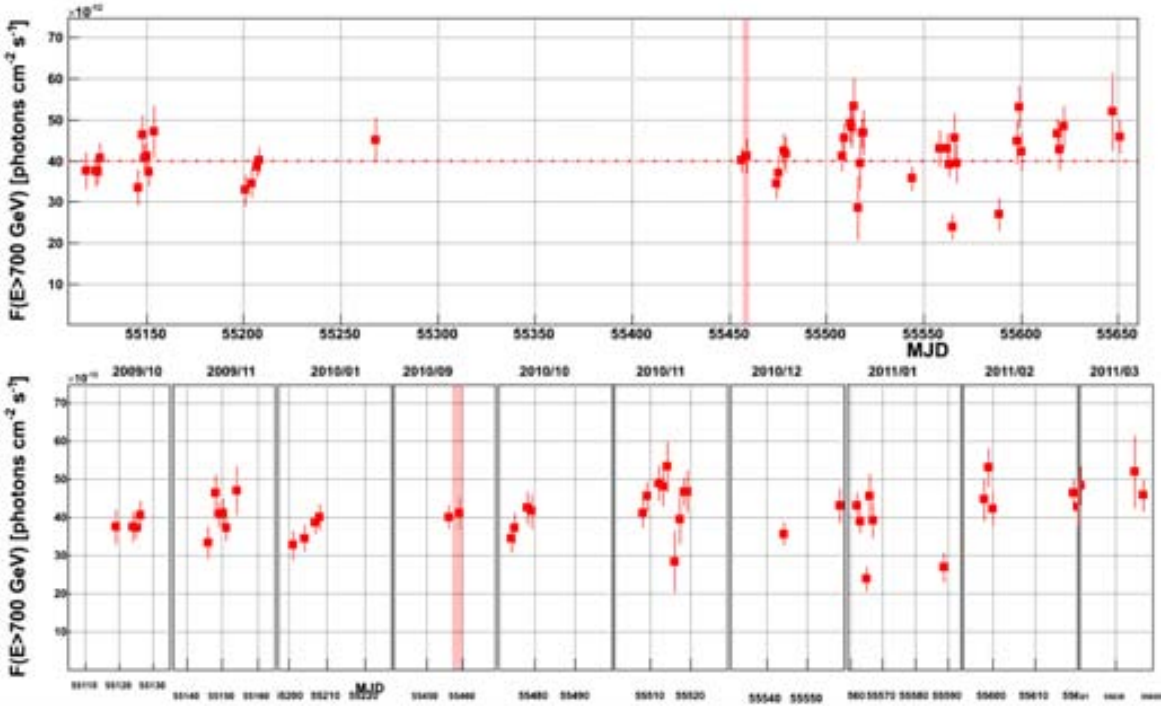

Figure 5.30: Daily light curve above 700 GeV. The upper panel show the daily flux from October 1, 2009 till March 31, 2011. The bottom panels are zoomed per-month portion of the upper panel. Red-shadowed area identifies the period of the flux enhancement in the the soft-γ-ray band.

PART THREE

MICROQUASARS AT VHE

Salvador Dalí - “Swans reflecting elephants”

6 Introduction to microquasars

Microquasars are X-ray binary systems which display relativistic radio jets. As their name suggests, they can be considered a scaled-down version of the quasars due to the morphological and kinematic similarities. This fact increased the interest of the astrophysical community on this kind of sources as they allow to study the physics of jet and accretion on much shorter time scales.
Microquasars were proposed to be VHE emitters: jets contain relativistic particles which can produce VHE radiation via IC scatter with seed photon fields.

This chapter is a summary extracted from literature.

6.1 Binary systems

Most stars are part of binary systems consisting of two stars orbiting around their common center of mass. The brightest star is called primary star, and the weakest one is referred to as companion star. When the primary star approaches its end, it collapses forming a compact object, either a NS or a BH (§ 6.2.1). In most cases the binary system disrupts because of the large mass losses and/or the impulsive kick velocity that the compact object receives at birth. If the binary system survives, the companion star continues its evolution. Some of the binary systems containing a compact object and a companion star can be X-Ray Binaries (XRBs) and others γ-ray binaries.

- **X-ray binaries** are very luminous in X-rays. Due to gravitational attraction, the companion star transfers matter to the compact object creating an accretion disk around the compact object. The accretion disk, heated by viscous dissipation, produces thermal X-rays with a luminosity of 10^{35}–10^{38} erg s^{-1}. In particular, microquasars are a sub-class of the XRBs which exhibits relativistic radio jets (§ 6.1.1).

- **γ-ray binaries** are more luminous in γ-rays than in X-rays. Their nature is not yet understood. There are two credited scenarios which can explain such high-energy emission: the microquasar and the binary pulsar scenarios (Figure 6.1). In the latter, the compact object is a pulsar and orbits around a massive companion star. The pulsar provides energy to the non-thermal relativistic particles in the shocked pulsar wind (§ 4.1.2). The γ-ray emission is produced by IC scattering of the electrons from the pulsar wind on

stellar photons. In the microquasar scenario, the VHE γ-rays are expected to be produced via IC scattering of relativistic electrons accelerated in shocks in the jets with stellar and/or synchrotron photons (§ 6.6).

Three γ-ray binaries have been unambiguously detected so far: LS 5039 (Aharonian, F. A., et al., 2005b), LS I 61° + 303 (Albert, J., et al., 2006b) and PSR 1259–63 (Aharonian, F. A., et al., 2005a). While the latter is known to be a binary pulsar, the first two sources are still a subject of debate. The nature of their compact objects is still unknown. Although it was originally proposed that they were accreting MQs (Paredes, J. M. et al., 2000; Massi, M., et al., 2004), there is growing evidence that they might contain a young non-accreting pulsar (Dubus, G., 2006). A forth candidate γ-ray binary has been only recently identified: HESS J0632+57, a galactic plane point-like source with variable radio, X-ray and TeV emission (Hinton, J. A., et al., 2009).

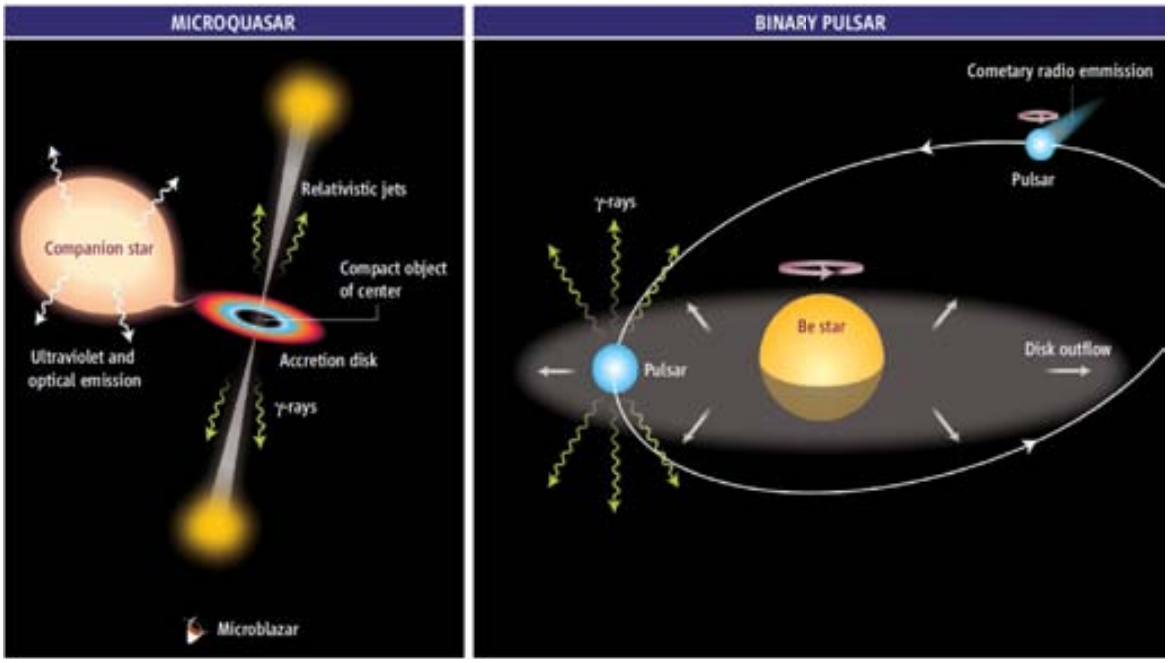

Figure 6.1: Alternative models for γ-ray binaries. *On the left:* jets powered by compact objects via mass accretion from a companion star. VHE particles accelerated in the jet scatter via IC on stellar/synchrotron photons. *On the right:* pulsar wind powered by the rotation of NSs; the wind flows away to large distances to form a comet-shaped tail. IC scattering of relativistic particles in the pulsar winds with the stellar photons might produce VHE emission. Taken from Mirabel, I. F. (2006).

6.1.1 Microquasars

Jet formation and its associated non-thermal emission are the key to identify MQs among the XRBs (Figure 6.5).

The word "microquasar" was proposed by Mirabel, I. F., et al. (1992) to identify the newly discovered Galactic object 1E 1740.7–2942 which showed morphological similarities with the more distant quasars (quasi-stellar radio sources). A microquasar system behaves as a scaled-down version of quasars and AGNs (McHardy et al., 2006). The jets of MQs extend for a few light years instead of several million light years like in AGNs. The thermal temperature

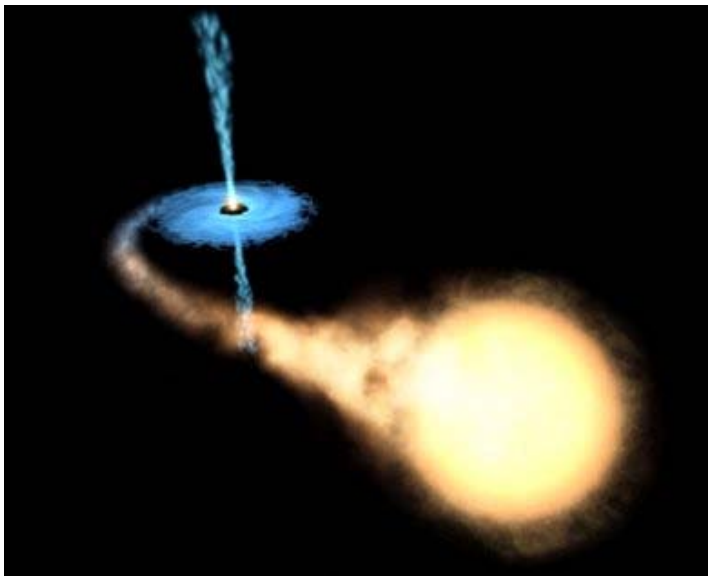

Figure 6.2: Representation of a microquasar.

of the accreting gas in MQs is several million degrees instead of thousand degrees and this explains why the thermal radiation emitted by the galactic objects is observed in the X-ray band instead of in the optical/UV ranges such as for AGNs. The differences in the length- and time-scales between the AGN and MQ phenomena are due to the fact that many physical quantities (lengths, temperatures, luminosities, accretion rates) scale with the mass of the BH, which is, in case of quasars, million/billion times larger. The AGN-MQ analogy was strongly confirmed by the discovery of Galactic superluminal motions[1] (Figure 6.3) at radio frequencies in the jets of GRS 1915+105 (Mirabel, I. F. & Rodríguez, L. F., 1994). Therefore, the study of the MQs, brighter and variable at shorter time scales, helps to understand how distant quasars behave on cosmological scales.

It was suggested that irrespective of their mass there might be a unique universal mechanism for relativistic jets in BHs (Mirabel, I. F. & Rodríguez, L. F., 2002). This mechanism may also be used to understand collapsars. Collapsars are a specific type of SN which is believed to produce long duration GRBs (MacFadyen, A. I. & Woosley, S. E., 1999). Figure 6.4 shows that the three classes of objects share morphological and kinematic properties.

The most updated XRB catalogues count almost 300 XRBs, among which 43 display radio emission of synchrotron origin. Relativistic jets have been detected in 15 of them, hence classified as microquasars. Table 6.1 lists these MQs with their more relevant characteristics. Nevertheless, Grimm, H.-J. et al. (2002) estimated a total number of $\equiv 705$ XRBs brighter than 10^{34} erg s^{-1}. Thus, the existence of MQs in larger number becomes more likely. In fact, some authors sustain that jets are a quite common characteristic of XRBs, suggesting that up to 70% of them might produce jets.

[1]The superluminal motion is a relativistic e ect: the material moves relative to its core at velocities which appear to exceed the speed of light.

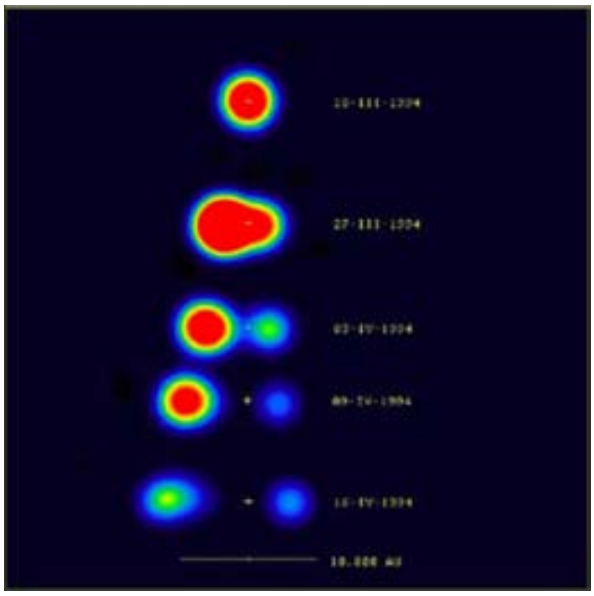

Figure 6.3: Apparent superluminal motion in the jets of GRS 1915+105. The sequence of images shows the temporal evolution in radio waves of a pair of plasma clouds ejected from the surroundings of the BH at a velocity of 98% the speed of light. Taken from Mirabel, I. F. & Rodríguez, L. F. (1994).

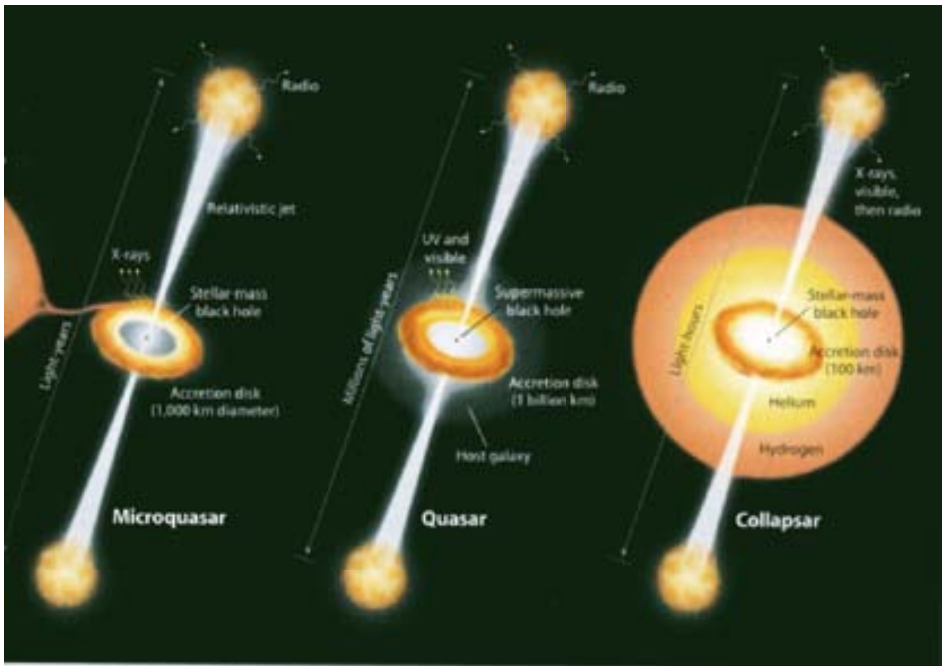

Figure 6.4: A unique universal mechanism responsible for three types of objects: MQs, quasars and collapsars. Each of them contains a BH, and accretion disk and relativistic jets. Taken from Mirabel, I. F. & Rodríguez, L. F. (2002).

source name	compact object	companion star	distance [kpc]	period
High-mass X-ray binaries				
Cygnus X-1	BH	O9.7 Iab	2	5.6d
Cygnus X-3	n.a.	Wolf-Rayet	3.4–9.8	4.8hr
SS 433	BH	A	5.5	13.1d
V4641 Sgr	BH	B	3–8	2.8d
Low-mass X-ray binaries				
Circinus X-1	NS	n.a.	7.8–10.5	16.65 d
GX 339-4	BH	sub-giant	> 6	1.7 d
GRO J1655-40	BH	sub-giant F	<1.7	2.6 d
GRS 1758-258	BH	K	8.5	18.4 d
GRS 1915+105	BH	K,M	11.2	33 d
XTE J1550-564	BH	sub-giant	5.3	37 hr
XTE J1748-288	BH		> 8	
Scorpius X-1	NS	M	2.8	18.9 h
1E 140.7-2942	BH		7	12.73d
4U 0614+091	NS	white dwarf	3.2	0.85 hr
H1743-322	BH	n.a.	n.a.	n.a.

Table 6.1: Established MQ with their main characteristics. From left to right, source name, compact object, type of companion star, distance, and orbital period.

6.2 The main components of microquasars

This section describes the main components of a MQ which are also sketched in the representation in Figure 6.5.

6.2.1 The compact object

A MQ harbors either a NS or a BH. Both of them correspond to the final stages of the star evolution. As described in § 4.1.1, NSs are produced in SN explosions which occur in the collapse of stars with a mass 5–10 $M_\odot$. If the newly created NS is too massive (> 2.9 $M_\odot$) to reach a stable equilibrium, it evolves into a BH. Besides this possible delayed formation, BHs can be formed directly through the collapse of more massive stars with mass ≥ 10 $M_\odot$ (Fryer, C. L., et al., 2002). The question on the explosive or implosive BH formation can be addressed through kinematic studies of BH binaries. They suggest that some stellar BHs form associated with SN explosions: the SN imparts the center of mass of the system with a runaway velocity. In some cases, the kinematic evidence is reinforced by chemical composition of the companion star, when it contains elements produced in the explosion. It was found that the BH microquasar GRO J1665-40 was ejected far from its birth place by an energetic SN (Israelian, G. et al., 1999). Kinematical studies on Cygnus X-1 (Mirabel, I. F. & Rodrigues, I., 2003) and GRS 1915+105(Dhawan, V. et al., 2007) suggest that the BH formation is not related to any SN explosion. Cygnus X-1 moves together with the massive star association Cygnus OB3. Its velocity relative to the association is 9 ± 2 km s^{-1}, which is typical for an expanding association. Since no kick velocity was received by the microquasar, it seems to have formed in situ (Figure 6.6). Another way to understand the BH formation can be provided by observations of nearby GRBs of long duration (§ 1.4). This type of GRBs is

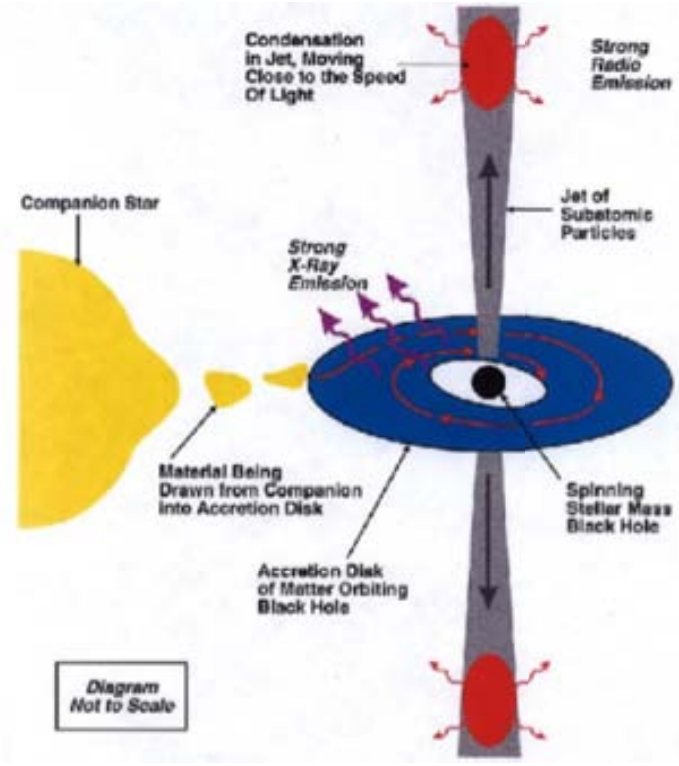

Figure 6.5: Sketch of a microquasar. It consists of a companion star, a compact object which accretes matter from the star, hence the accretion disk and the resulting jets.

believed to take place when a massive star collapses into a stellar BH.

Some signatures are used to identify the nature of the compact object. Dynamical studies allow to infer the mass of the compact object: if it is larger than 3 $M_\odot$, the compact object must be a BH. Furthermore, regular pulsations are a sure proof that the compact object is a NS.

6.2.2 Companion star

XRBs are classified in Low-Mass X-ray Binaries (LMXBs) and High-Mass X-ray Binariess (HMXBs) depending on the mass of the companion star.

- HMXBs host young massive stars of $\sim$ 8–10 $M_\odot$, usually Be stars or O/B supergiants. The majority of the known HMXBs contain Be stars (Liu, Q. Z. et al., 2006). These massive companion stars produce strong stellar winds and are very bright in the optical/UV band. They transfer mass to the compact object either through the stellar wind, or through Roche lobe[2] overflow.
  Generally HMXBs are characterized by orbital periods of several days.

- In LMXBs, the companion star is a low-mass star ($M < 2$ $M_\odot$) which transfers matter only through Roche lobe overflow (Liu, Q. Z. et al., 2007). Among low-mass companion

[2]The Roche lobe indicates a region surrounding a star in a binary system within which the orbiting material is gravitationally bound to the star. If the star expands beyond its Roche lobe, the material outside the lobe falls into the binary companion through an accretion disk.

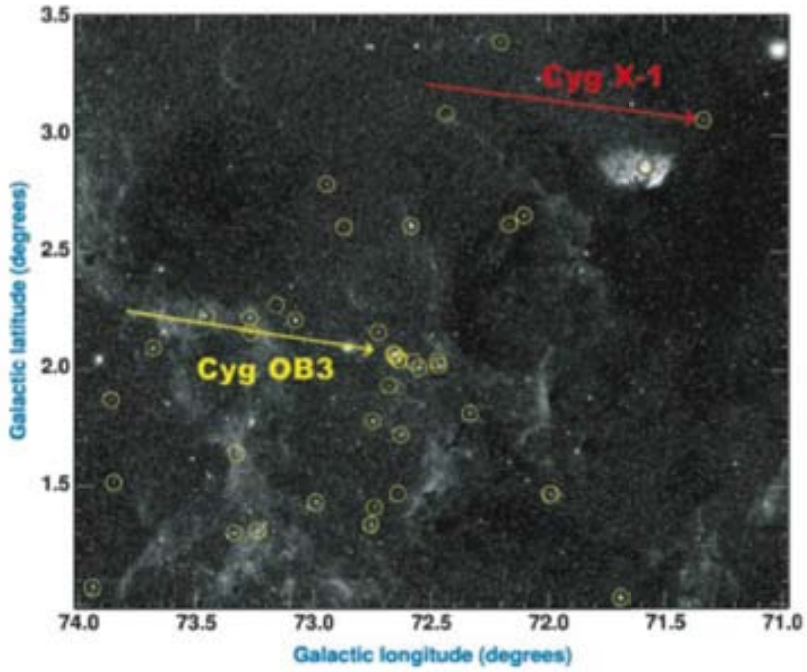

Figure 6.6: Optical image of the sky around the BH microquasar Cygnus X-1 and its association of massive stars Cygnus OB3. The arrows show the motion in the sky of the two objects for the past 0.5 million years. Their velocities in the sky is equivalent. Taken from Mirabel, I. F. & Rodrigues, I. (2003).

stars, there are late-type main sequence stars, white dwarfs and F-G-type subgiants. LMXBs are characterized by orbital periods in the range of 0.2 to 400 hrs.

This classification is relevant for the evolution of the system, but probably not for the physics of the jet formation and disk-jet coupling. In fact, for this purpose, it is more useful to classify the XRBs according to the nature of the compact object. The evolution of the system might play a role in the production of the VHE emission though: the companion star can provide a seed photon field for the IC scattering which produces the HE emission.

6.2.3 Accretion disk

Accretion disks are usually modeled by the Standard Disk Model (SDM). According to this model, the accreting matter has an angular momentum which leads to the formation of a disk. The energy and angular momentum of the orbiting gas are radiated away, and the material drifts towards regions of the accreting disk closer to the compact object. Shakura, N. I. & Sunyaev, R. A. (1973) modeled the rotating gas with hydrodynamic equations for a viscous flow and proposed that the gas loses energy due to viscosity. The amount of energy that can be extracted through viscosity is equal to the binding energy of the innermost stable orbit. For NSs, it corresponds to the compact object surface, whereas for a non-rotating BH it is approximately three times the Schwarzschild radius[3], R_{Sch}. About 10% of the rest mass of the matter can be extracted around a NS and up to 40% around a BH. The effective temperature,

[3]An object of mass M becomes a BH when it is compressed in a sphere whose radius is smaller than the Schwarzschild radius, $R_{Sch} = 2GM\ c^2$, where G is the gravitational constant.

T_{eff}, of the gas depends on the mass, M, of the compact object: $T_{eff} \quad M^{-1\ 4}\ M^{1\ 4}$. The accretion disk of compact objects with a mass of some tens of $M_{\odot}$ radiates X-rays.

Nevertheless, some sources exhibit hard X-rays which are difficult to explain with the SDM. This is the case for Cygnus X-1, for instance, where temperatures as high as 10^9 K are needed to match the observations, which, therefore, can not be fully explained within the SDM. New models have been proposed to explain such emission based on the advection dominated accretion flows (Narayan & Yi, 1994). The Advection Dominated Accretion Flow (ADAF) model assumes a low density accreting gas. This assumption implies that the gas is unable to cool efficiently through viscosity within the accreting time. Most of the released gravitational energy of the gas in the accretion flow is converted into internal energy of the gas. The disk is hot and thick. Only a small fraction of the released energy in ADAFs is radiated away. The radiation efficiency is therefore significantly lower than that for standard thin disks.

6.2.4 The corona

In order to explain the hard X-ray emission, some models have introduced a new component to the SDM, called "corona". In these models, the low density gas is not able to cool efficiently the innermost part of the disk. Consequently, the temperature increases and the disk inflates. This inflated disk is called corona and can explain the hard X-ray emission through the scattering of electrons on seed photons. The transition between the corona (inefficient cooling) and the disk (efficient cooling) takes place at a radius of $\equiv 100\ R_{Sch}$.

6.2.5 Jets

Jets are collimated ejecta with an opening angle $\leq\ 15°$ (Bridle, A. H. & Perley, 1984). They seem to be systematically associated with the presence of an accretion disk around a compact object. Since the main difference between NSs and BHs is the presence of a surface or an event horizon respectively, it seems likely that the formation of the jets does not depend on the nature of the compact object itself, but on the accretion flow process.

The most credited scenario for the explanation of the jet formation is based on MHD. A strong electromagnetic field in the compact object, coupled with differential rotation, converts the rotational energy stored in the disk into the kinetic energy in the ejecta. Plasma trapped in the magnetic field lines is subjected to the Lorentz force which, under conditions of high conductivity (this is the MHD assumption), splits into two vector components: a magnetic pressure gradient and a magnetic tension. The magnetic pressure gradient along the rotation axis accelerates plasma out of the system, whereas the magnetic tension collimates the outflow of material which escapes the gravitational potential well and forms the jet.

Jets in MQs emit non-thermal radiation which has been observed from radio frequencies to optical/UV (Russell, D. M. & Fender, R. P., 2010), and up to X-rays (Corbel, S., et al., 2002) at large scales. This emission is a clear evidence for the presence of relativistic particles inside the jet. It is generally accepted that particle acceleration takes place in shock waves through the Fermi acceleration mechanism (§ A.1). There are different models which explain the creation of shock waves in the microquasar environment:

- **continuous jet and internal shocks**. Jets are considered as a continuous flow and the emission is produced through internal shocks (Kaiser, C. R. et al., 2000). These internal shocks are due to the collision between small regions of the jets characterized by different densities and/or velocities.

- **discrete jets and internal shocks**. Jets consist of discrete material ejected in form of blobs (van der Laan, H., 1966). The collision between blobs with different velocities can mimic internal shocks (Jamil, O. et al., 2010). This mechanism leads to the production of a quasi-steady emission with fluctuations connected to the variation scale of the injected blobs.

- **external shocks**. Aside from the composition of the jets, external shock could be produced as a result of the interaction between the jet and dense material from the stellar wind (Perucho, M. & Bosch-Ramon, V., 2008) or the surrounding medium (Bordas, P. et al., 2009). In such a scenario, the emission may be observable both as a transient and a quasi-stationary phenomenon. Since there is a considerable evidence that the stellar winds are clumpy, these clumps might produce transient emission by interacting with the jets (Araudo, A. T. et al., 2009).

Mirabel, I. F. & Rodríguez, L. F. (1999) proposed that MQs with jet axis that form angles $\leq 10^\circ$ with the line of sight should appear as *microblazars* (analogously to blazars). Due to relativistic beaming, in *microblazars* the brightness of outbursts is enhanced by a factor $8 \times \Gamma^3$, where Γ is the Lorentz factor. In addition, also the time interval of the phenomena is reduced by factors $0.5 \times \Gamma^{-2}$. Then, *microblazars* should appear as intense sources of HE photons with very fast variations of flux. Due to the difficulty to find and follow them and to the relatively low statistical probability of small angles between the jet axis and the line of sight, the most of the so far observed MQs exhibit angles larger than 30°.

6.3 Disk-jet connection

MQs allow to gain an insight into the connection between the accretion disk and the jet. During simultaneous multi-wavelength observations of the frequent outbursts from GRS 1915+105, the X-ray flux was monitored simultaneously with the emission of the jet at different frequencies (Mirabel, I. F., et al., 1998). Figure 6.7 shows the complete temporal sequence of a flare from GRS 1915+105 which lasted less than one hour. A sudden drop in X-ray luminosity was followed by the ejection of jets, first observed in IR, then at radio frequencies. The drop can be interpreted as the disappearance of the warmer inner part of the accretion disk beyond the BH horizon. Few minutes later, fresh matter coming from the companion star feeds again the accretion disk, which has evacuated part of its kinetic energy under the form of bipolar jets. Moving away, the plasma becomes transparent first in IR and then at radio frequencies. The time delay between the IR and the radio peaks is consistent with the model of adiabatically expanding clouds (§ 6.2.5). However, according to this model, the IR emission should be observed 10^{-3} s after the ejection, but it occurred more than 200 s after the drop in X-ray flux. In this observation the ejection of the plasma clouds takes place during the subsequent replenishment of the inner accretion disk, well after the disappearance of the soft component and it can last up to tens minutes.

After this observation of an event involving the accretion disk and the jet of a MQ, a similar event happened for the quasar 3C 120 (Marscher, A. P., et al., 2002), but in scales of years rather than minutes. The ratio of time scales is comparable to the ratio of the masses of the super-massive BH in 3C 120 and the stellar one in GRS 1915+105, as expected in the context of the unified BH model.

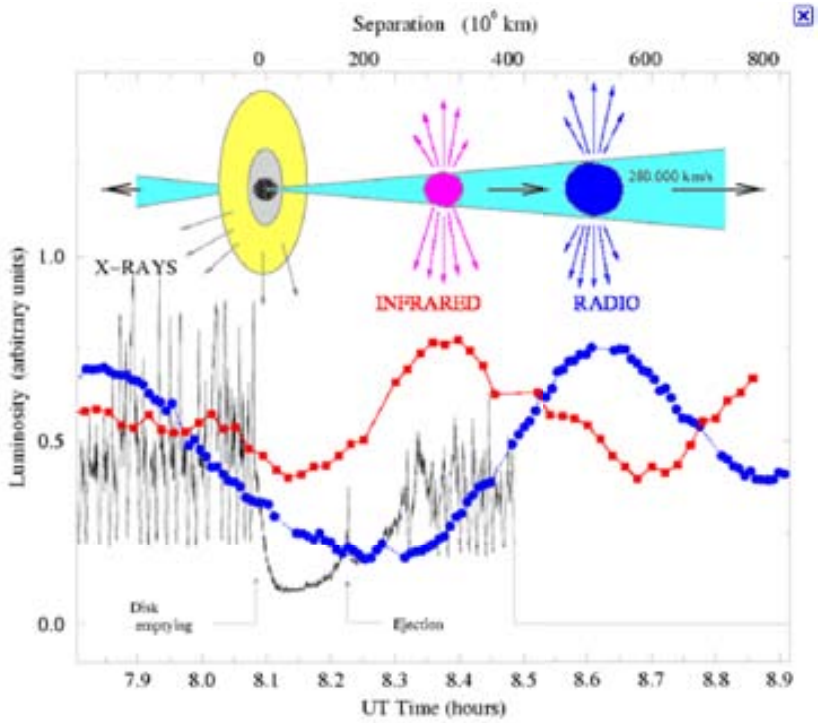

Figure 6.7: Temporal sequence of accretion disk-jet coupling observed during a one-hour outburst from GRS 1915+105. The ejection takes place after the evacuation of matter and energy, at the time of the reconstruction of the inner side of the accretion disk. Taken from Mirabel, I. F., et al. (1998).

6.4 Black hole X-ray binaries

The X-ray emission of BH XRBs presents large flux and spectral variability on time scales of seconds to days. Historically, the classification of the spectral and timing patterns of the 1-100 keV X-ray flux led to the definition of more than twelve different X-ray spectral states (Belloni, T. et al., 2000). Nevertheless, it is widely accepted that the flux and spectral variability can be interpreted as the transition between mainly two separate states:

- ***Hard state***. During the *hard state* the energy spectrum presents a weak thermal component which peaks at a temperature kT $\sim$ 0.1 keV, but it is dominated by a non-thermal component. The latter has a power-law shape with a photon index, Γ, in the range $\sim$1.4-2, and a cut-off above a hundred keV. The total X-ray luminosity in this state, computed for those systems where the distance and the mass are available, is generally a few % of the Eddington luminosity. A steady, powerful, flat-spectrum jet is observable at radio frequencies. The radio and the X-ray luminosities are strongly correlated. They were thought to be related by the universal law $L_{radio} \propto L_X^{0.7}$ (Gallo, E. et al., 2003b). However, very recently, the same group of authors, adding the new results on XRBs, found two different clusters of objects in the plane $L_X - L_{radio}$ (Figure 6.8 a) and the previously estimated law is no longer valid for any of the clusters (Gallo, E., et al., in preparation).

- **Soft state**. The *soft state* is dominated by a component with a near-blackbody spectrum peaking at higher temperatures kT = $\sim$ 1 keV. In addition to this thermal com-

ponent, there is a non-thermal hard X-ray contribution, much less luminous, which can be described by a softer power law ($\Gamma \geq 2.4$). The total X-ray luminosity is larger than 0.01 of the Eddington luminosity. In this state, the radio emission is dramatically suppressed by a factor of ≥ 50.

Figure 6.8 b) shows the SED of Cygnus X-1 for the two X-ray spectral states. Besides the *hard and soft* states, some authors talk also about an *intermediate state* where the source exhibits spectra between the two canonical spectral states and with a strong flaring activity.

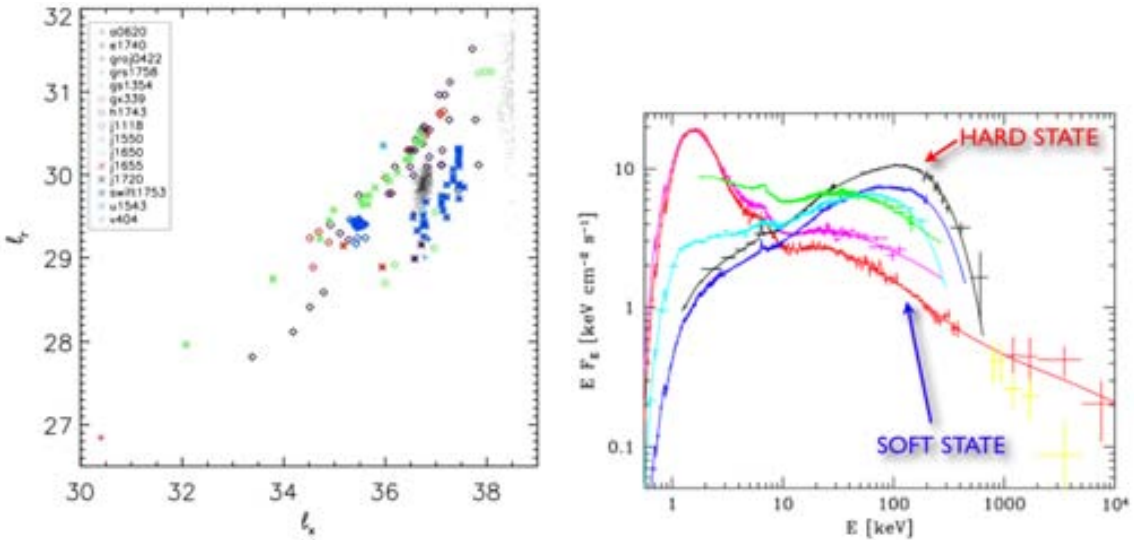

Figure 6.8: *On the left:* **Radio luminosity versus X-ray luminosity for the BH XRBs in the hard state**. Taken from Gallo, E., et al. (in preparation). *On the right:* **SED of Cygnus X-1 in the soft and the hard states.**

Spectral variability is generally attributed to the effect of instabilities of the accretion disk due to changes in the accretion rate. Fender, R. P. et al. (2004) proposed a *unified model for BH XRBs* where the spectral states are interpreted in the context of the disk-jet coupling. This model, sketched in Figure 6.9, foresees four different phases:

- **Phase i:** the source is in the *hard state* with the lowest accretion rate. This phase is characterized by the existence of steady jets which are continuously replenished, and a corona which is responsible for the strong hard X-ray emission. The innermost stable orbit is far away from the compact object.
  The source is radio-loud and the spatially resolved radio emission is associated to synchrotron emission produced in the jets. Radio emission is correlated to X-ray emission in a non-linear fashion: $L_R \propto L_X^b$, where L_R and L_X are the radio and X-ray luminosities respectively and $b \sim 0.7$ (Gallo, E. et al., 2003b).

- **Phase ii:** the source is in *hard intermediate state*. The accretion rate starts to increase. The gas becomes denser, and starts to cool down via synchrotron and Bremsstrahlung. Thus, the thermal emission becomes more and more important and the innermost radius of the disk slides towards the compact object. The corona is still present, even though its temperature reduces due to IC scattering of electrons on the disk photons. This fact explains the progressive softening of the hard X-rays. The jet velocity increases as the

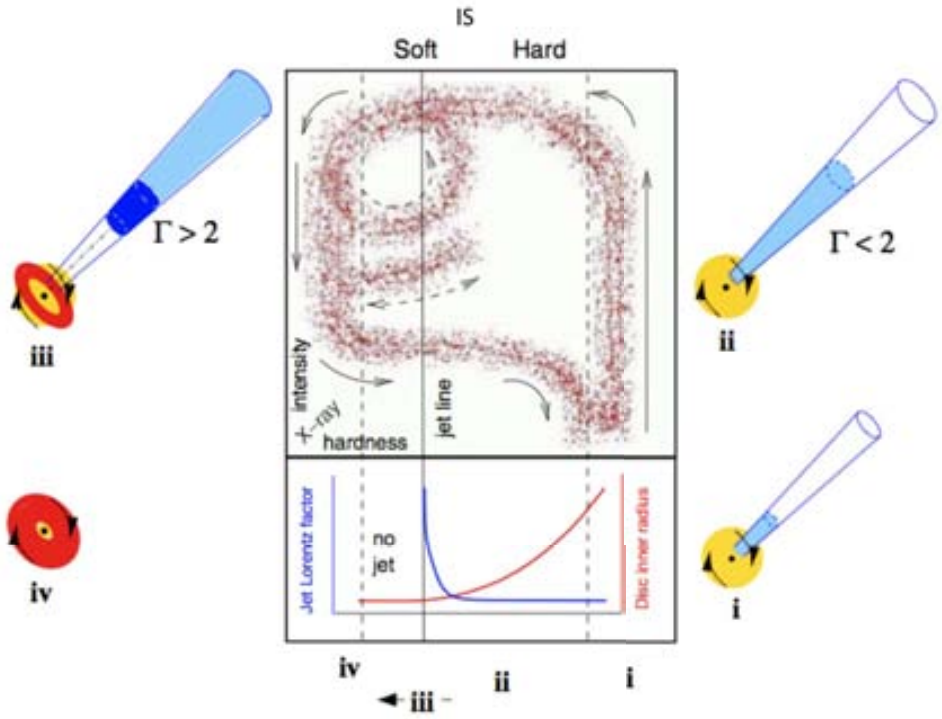

Figure 6.9: A schematic view of the unified model for BH XRBs. It is a hardness-intensity diagram, where the soft, the hard and the hard/soft intermediate states are represented by the corresponding four phases. For each of these phases the accretion disk-jet behaviour is sketched outside the diagram. The lower panel indicates the variation of the inner disk radius and the bulk Lorentz factor of the outflow as function of the hardness. Adapted from Fender, R. P. et al. (2004).

accretion disk moves closer and closer to the compact object. This may be due to the fact that matter needs a higher velocity to escape from the disk.

- **Phase iii:** the source moves to a *soft intermediate state*. The processes explained in the previous phase lead to a maximum softening of the hard X-rays, after which the thermal emission from the disk becomes dominant. Around the time when the source crosses the line between jet-free and jet-producing states, the velocity of the jet increases very rapidly. This increase produces a shock in the pre-existing jet which manifests itself as a flare, seen also at radio frequencies.

- **Phase iv:** the source is in *soft state* when the accretion rate is at its highest. The accretion disk is stable and extends to the last stable orbit. No jet is present; thus the spectrum is dominated by the thermal emission of the accretion disk. When the accretion rate starts to decrease, the corona is produced, new jets are ejected, and the system moves to a *hard state*.
  The origin of the hard X-ray emission in this phase is rather controversial. Some authors propose a residual corona where the magnetic field plays an important role accelerating electrons which produce non-thermal emission. The radio emission is quenched, probably due to physical suppression of the jets (Fender, R. P., et al., 1999).

The loop in the upper left area of the diagram, with the direction indicated by the arrow, is interpreted as radio-IR-X-ray oscillation events. The source can repeatedly enter the jet-producing state then crosses the dividing line to jet-free states. Each transition from right to left is associated with non-thermal emission.

6.5 Neutron star X-ray binaries

NS XRBs have been classified based on their X-ray spectral and timing properties into three main classes: Z-type, atoll-type and X-ray pulsar XRBs (Hasinger, G. & van der Klis, M., 1989). Z-type and atoll-type sources are LMXBs and their name derives from the shape they trace in the X-ray Color-color Diagram (CD). The "color" is defined as the difference of flux in two energy bands.

- **Z-type NS LMXBs** represent a class of six XRBs accreting near or at the Eddington rate. The name of this class of sources derives from the typical "Z" shape traced by the source in the CD (Figure 6.10 right). Along this track the source change between different X-ray spectral states: the Horizontal Branch (HB), the Normal Branch (NB) and the Flaring Branch (FB) from top-left to bottom-right. Nevertheless, in some Z-type sources the tracks in the CDs may be more accurately describes by a double-banana shape, since the upper-left-horizontal branch of the track is missing. In this case the upper banana corresponds to the HB/NB and the lower banana to the NB/FB states (Hasinger, G. & van der Klis, M., 1989).
  Z-sources are rapidly variable in X-rays and trace the entire CD in hours to days. A traditional interpretation of this variability is related to changes in the mass accretion rate, which should increase along the Z-track from the HB to the FB (Hasinger, G. & van der Klis, M., 1989). Recent evidence points towards constant mass accretion rate along the Z-track, whereas different accretion rates would give rise to different subclasses of NS XRBs (Homan, J., et al., 2010).
  All the Z-type sources have been detected in radio. A correlation between X-ray and radio fluxes has been found in most of these sources (Hjellming, R. M., et al., 1990). In fact, qualitatively, the radio emission varies as function of the position in the CD decreasing as increasing the mass accretion rate (strongest radio emission in the HB). Fender, R. P. & Hendry, M. A. (2000) observed a correspondence between the *hard state* of the BH XRBs and the HB state of the Z-type sources.

- **atoll-type NS LMXBs** present low-magnetic-field NSs accreting at relatively low rates (compared to the Z-type sources). They are less luminous in X-rays than Z-type sources. Atoll-type share many X-ray spectral and timing properties of the BH XRBs (§ 6.4). For example, they are characterized mainly by two distinct X-ray states defined by the position in the CD. The "island state" corresponding to the X-ray *hard state* and the "banana state" as the *soft state*.
  Atoll sources are radio-quiet. In fact, just few of them have been detected at radio frequencies so far. Nevertheless, Migliari, S. & Fender, R. P. (2006) observed that generally the X-ray *hard states* present steady radio fluxes, whereas *soft states* are characterized by transient radio outbursts. Given the strict analogy with BH XRBs, the authors conclude that the X-ray/radio correlation seems to be univocally related to the properties of the accretion flow, and not to the nature of the compact object.

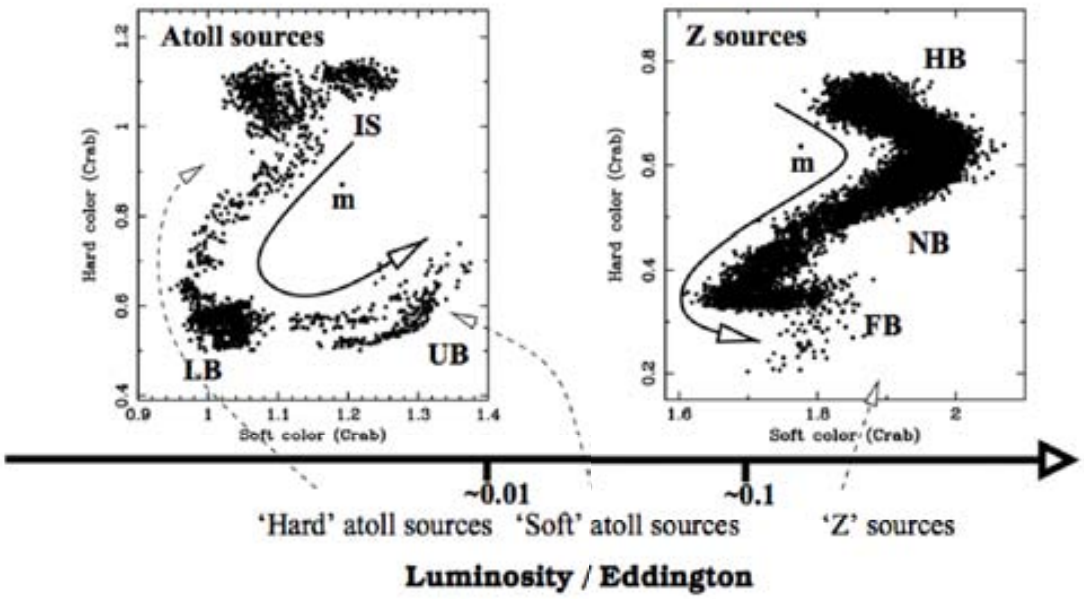

Figure 6.10: Simplified description of the typical CDs of NS XRBs. For both types of sources the expected direction of increasing mass accretion rate, $\dot{m}$, is indicated. For the atoll-type sources the acronyms stand for: IS = island state; LB = lower banana; UB = upper banana. For the Z-type source: HB = horizontal branch; NB = normal branch; FB = flaring branch. Taken from Migliari, S. & Fender, R. P. (2006).

- **Accreting X-ray pulsar binaries** contain high-magnetic field NSs which disrupt the inner accretion disk and channel the accretion material to its magnetic poles (Bildsten, L., et al., 1997). Most of them are HMXBs, suggesting that the NSs are relatively young, but none has been detected at radio frequencies. Fender, R. P., et al. (1997) suggested that the lack of synchrotron radio emission might be related to the disruption of the inner accretion disk which prevents the formation of the jets.

6.6 VHE emission from microquasars

MQs are expected to produce VHE photons based on their analogy with AGNs, some of which have been detected at TeV energies. The mechanisms for the production of VHE photons might be the same in AGNs and in MQs (Levinson & Blandford, 1996). This idea was strengthened by observations showing that the kinetic power of MQ jet may be larger than 10^{39} erg s^{-1}, *i.e.* larger than their radiative power.

Both leptonic and hadronic models for VHE emission have been proposed in the literature. Leptonic models postulate radiative processes involving only leptons, whereas hadronic models rely on acceleration of protons or other nuclei. For a complete review about the mechanisms of the VHE production, the reader is referred to Bosch-Ramon, V. & Khangulyan, D. (2009).

6.6.1 Leptonic models

The leptonic models extend the energy of leptons from synchrotron radio emitting energies up to γ-rays. The most accredited models predict that HE photons come from the IC scattering of relativistic electron with low-energy photons (Atoyan, A. M. & Aharonian, F. A., 1999; Markoff, S. et al., 2001; Georganopoulos, M. et al., 2002; Bosch-Ramon, V. et al., 2006). Figure 6.11 shows the main features considered by the leptonic models listed in their associated regions.

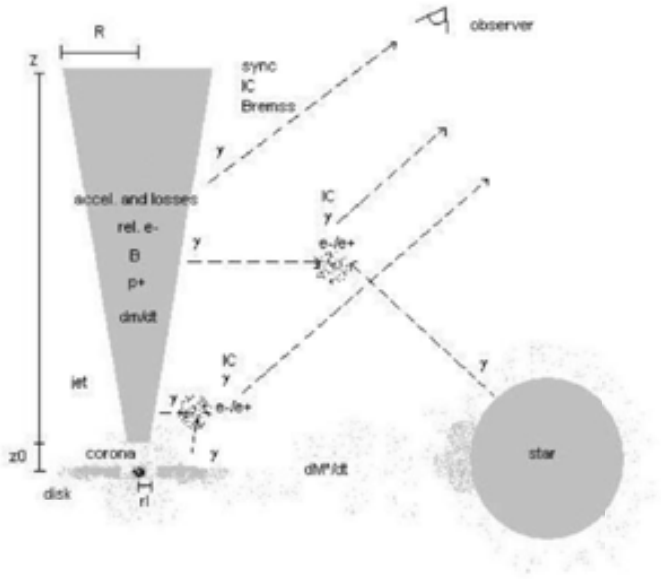

Figure 6.11: Sketch of the microquasar leptonic scenario. The main features considered by the model are listed in their associated regions. The plot, not to scale, is taken from Bosch-Ramon, V. et al. (2006).

Depending on the nature of the seed photons, mainly two scenarios have been proposed: the SSC model where synchrotron photons are IC up-scattered by the same population of electrons which produce them, and the external IC model which foresees that a denser population of photons produced outside the jet (corona/disk photons or from the stellar wind) is the dominant photon field target for the Compton scattering of the electrons. The IC scattering on stellar photons is inefficient in LMXBs, where the stellar luminosity is negligible, as well as in HMXBs at high energies because of the large distance between the companion star and the jet shock. It must be mentioned, however, that recently Bednarek, W. & Pabich, J. (2010) proposed efficient stellar IC scattering also for very compact LMXBs. The low-mass star can be heated by the X-ray source produced to accretion of matter.

As a result, there are parts of the stellar surface which can reach temperature as high as those of the high-mass stars, hence producing enough soft photons to make the IC efficient.

6.6.2 Hadronic models

In hadronic models hadrons are responsible for GeV-TeV γ-rays, whereas electrons are significant emitters at lower energies. The main radiative processes are: the collision of relativistic protons with ions (pp) in the jet or the stellar wind (Romero, G. E. et al., 2003), and the interaction between jet relativistic protons and X-ray photons ($p\gamma$) from the disk, the corona or the jet itself (synchrotron emission) (Romero, G. E., 2008). These proton collisions produce neutral pions (π^0) that decay into γ-rays, and charged pions ($\pi^{\pm}$) that decay into muons and neutrinos, the former decaying then to electron-positron pairs and neutrinos. The leptons originated from the secondary pairs can produce low-energy emission via synchrotron, IC and

Bremsstrahlung (Orellana, M. et al., 2007).

There are other models which take into account the possibility that a significant amount of protons, accelerated in the region where the jet ends, are released and interact further away in a high density region of the ISM (Bosch-Ramon, V. et al., 2005). Proton-proton collisions within the cloud lead to the creation of neutral and charged pions, and consequently to the creation of γ-rays and $e^{\pm}$ pairs. Due to propagation effects, the outcomes of these interactions can differ strongly depending on the age, the nature of the accelerator, and its distance to the cloud.

6.6.3 Microquasar in γ-rays: observations

Although MQs were proposed to emit γ-ray more than one decade ago (Atoyan, A. M. & Aharonian, F. A., 1999), only recently this could be proved thanks to the new generation of γ-ray satellites. The microquasar Cygnus X-3 was detected in 2009 by both *Fermi*/LAT and *AGILE* at energies above 100 MeV (Abdo, A. A., et al., 2009b; Tavani, M., et al., 2009). In addition, *AGILE* reported the detection of several 1-day flares from the well known BH MQ, Cygnus X-1, above 100 MeV (Sabatini, S., et al. 2010; ATels #2512 #2715). This could not be confirmed by *Fermi*/LAT, though.

At higher energies, above few tens of TeV, no emission has been established so far. In the 80's, the first generation of ground-based telescopes reported many claims on the detection of PeV-TeV signals coming from microquasars, mainly Cygnus X-3 (Danaher, S. et al., 1981; Lamb, R. C. et al., 1982; Bhat, C. L. et al., 1986). However, the fact that most sensitive experiments could not confirm such claims, raised many doubts on their validity. Recently, Albert, J., et al. (2007d) published a non-significant evidence of signal, at the post-trial level of 4.1η, from Cygnus X-1 during a short (less than 1 day) flare on September 24, 2006. MAGIC tried to catch a similar flare in the following three cycles of observations (2007–2009), but the subsequent hundred more hours of observations were unsuccessful.

Nowadays, IACTs are making a strong effort to catch a VHE signal from a well-established microquasar. MAGIC pointed towards several interesting candidates; besides Cygnus X-1, MAGIC observed SS 433, GRS 1915+105, Cygnus X-3, and Scorpius X-1. In the third part of this thesis work, the results of the observations of Cygnus X-3 and Scorpius X-1 will be presented.

7
Cygnus X-3

Cygnus X-3 is a peculiar MQ where a compact object orbits around a Wolf-Rayet companion star with a short orbital period of only 4.8 hrs. It has been detected at radio frequencies and up to HE γ-rays. However, many models also predict VHE emission when the source displays relativistic persistent jets or relativistic transient ejections.
The first stand-alone MAGIC telescope observed Cygnus X-3 for 70 hrs between March 2006 and August 2009 in different X-ray/radio spectral states and also during a period of enhanced γ-ray emission. This allows us to search for VHE emission from Cygnus X-3 in the different cases for which this radiation is predicted. MAGIC found no evidence for a VHE signal from the direction of the MQ. An upper limit to the integral flux for energies higher than 250 GeV has been set to 2.2×10^{-12} photons $\mathrm{cm}^{-2}\ \mathrm{s}^{-1}$ (95% CL). This is the best limit so far to the VHE emission from this source.

The results presented in this chapter are published in Aleksić, J., et al. (2010a). The author was the Principal Investigator (PI) of the Cygnus X-3 observations and the main analyzer of the resulting data set.

Cygnus X-3 is a bright and persistent X-ray binary, discovered in 1967 (Giacconi, R. et al., 1967), but the HE processes occurring in the source are still poorly understood. It lies close to the Galactic plane at a distance between 3.4 and 9.8 kpc, probably at 7 kpc depending on different distance estimates to the Cygnus OB2 association (Ling, Z. et al., 2009).

The nature and the mass of the compact object are still a subject of debate. The historical detection in γ-rays of a 12.6 MSP coincident with Cygnus X-3 position (Chadwick, P. M. et al., 1985) would provide an evidence that the compact object is a NS. However, there is no independent confirmation for this pulsar signal. Published results suggest either a NS of 1.4 $\mathrm{M}_\odot$ (Stark & Saia, 2003) or a BH of less than 10 $\mathrm{M}_\odot$ (Hanson, M. M. et al., 2000). The identification of its donor star (§ 6.2.2) as a Wolf-Rayet star (van Kerkwijk, M. H., et al., 1992) makes Cygnus X-3 a rather special XRBs since only two other objects of this class, both extra-galactic, host such a companion star type (Prestwich, A. H., et al., 2007; Carpano, S., et al., 2007). In both cases, there is evidence that the compact object is a BH. The presence of the massive Wolf-Rayet star classifies Cygnus X-3 as a HMXB. Nevertheless, Cygnus X-3 shows a

short orbital period of 4.8 hrs, typical of the LMXBs. This period has been inferred from the modulation of both the X-ray (Parsignault, D. R., et al., 1972) and infrared (Becklin, E. E., et al., 1973) emissions. The orbital phase $\phi = 0$ corresponds to the spectroscopic superior conjunction, *i.e.* when the compact object is behind the star. The orbit of the compact object around the companion star has to be very tight with a semi-major axis of only a few solar radii.

Despite the strong X-ray absorption in this system, which may be caused by the wind of the companion star, the X-ray spectrum has been intensively studied. The source shows two main X-ray spectral states resembling the canonical states of the BH binaries (§ 6.4): the *hard state* and the *soft state* (Zdziarski, A. A. & Gierliński, M., 2004), plus a couple of transitional states which are less understood. The *hard state*, studied in detail by Hjalmarsdotter, L., et al. (2008), displays a HE cut-off at $\approx$ 20 keV, significantly lower than the $\approx$ 100 keV value found for BH binaries. Averaged spectra for different X-ray spectral states are shown in Szostek, A. & Zdziarski, A. A. (2004) which makes use of Proportional Counter Array (PCA) observations in 1996–2000. These data were divided into five groups according to their spectral hardness in the 10–20 keV range. Groups 1–2, 3–4 and 5 correspond to the *hard*, intermediate and *soft* state, respectively.

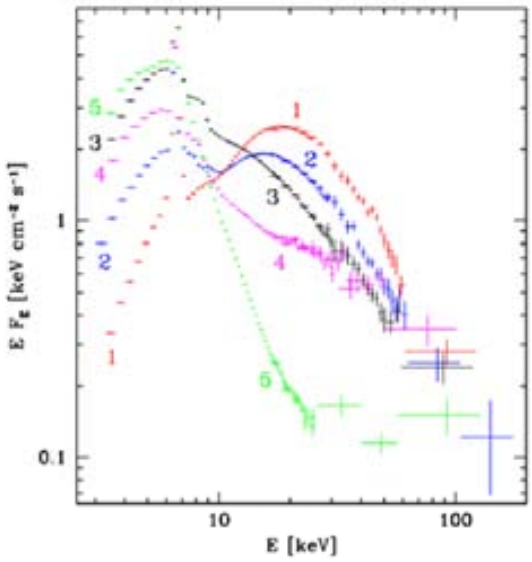

Figure 7.1: Averaged spectra for different X-ray spectral states: 1–2, 3–4 and 5 correspond to the *hard*, intermediate and *soft* state, respectively. Taken from Szostek, A. & Zdziarski, A. A. (2004).

Adding to its peculiarity, Cygnus X-3 is the brightest radio source among the X-ray binaries (McCollough, M. L., et al., 1999). Quite frequently, it exhibits huge radio flares, first seen by Gregory, P. C. & Kronberg, P. P. (1972). They can be as intense as few thousand times the quiescent emission level of $\sim$ 20 mJy at 1.5 GHz (Braes, L. L. E. & Miley, G. K., 1972). During these outbursts, which mainly occur when the source is in the *soft state* and last several days, Cygnus X-3 reveals the presence of collimated relativistic jets (Geldzahler, B. J., et al., 1983; Martí, J. et al., 2001; Mioduszewski, A. J. et al., 2001; Miller-Jones, J. C. A., et al., 2004). Thus, Cygnus X-3 has been classified as a MQ.
Based on 1988–1992 radio observations by the Green Bank Interferometer (GBI) Waltman, E. B., et al. (1994, 1995, 1996) identified four radio states: quiescent (flux densities $\sim$ 50–200 mJy with variations on time scales of months), minor-flaring ($<$ 1 Jy), quenched ($<$ 30 mJy) and major flaring ($>$ 1 Jy). Several studies showed a possible connection between radio and X-ray states (Watanabe, H., et al., 1994; McCollough, M. L., et al., 1999; Gallo, E. et al., 2003a; Hjalmarsdotter, L., et al., 2008), but a complete picture on the subject was drawn only by Szostek, A. et al. (2008). In the latter work, the authors defined six X-ray/radio states which are represented in the so-called *saxophone plot* (Figure 7.2). In the transition from the *hard*/radio quiescent state to the *soft state*, the radio emission is strongly suppressed, and if

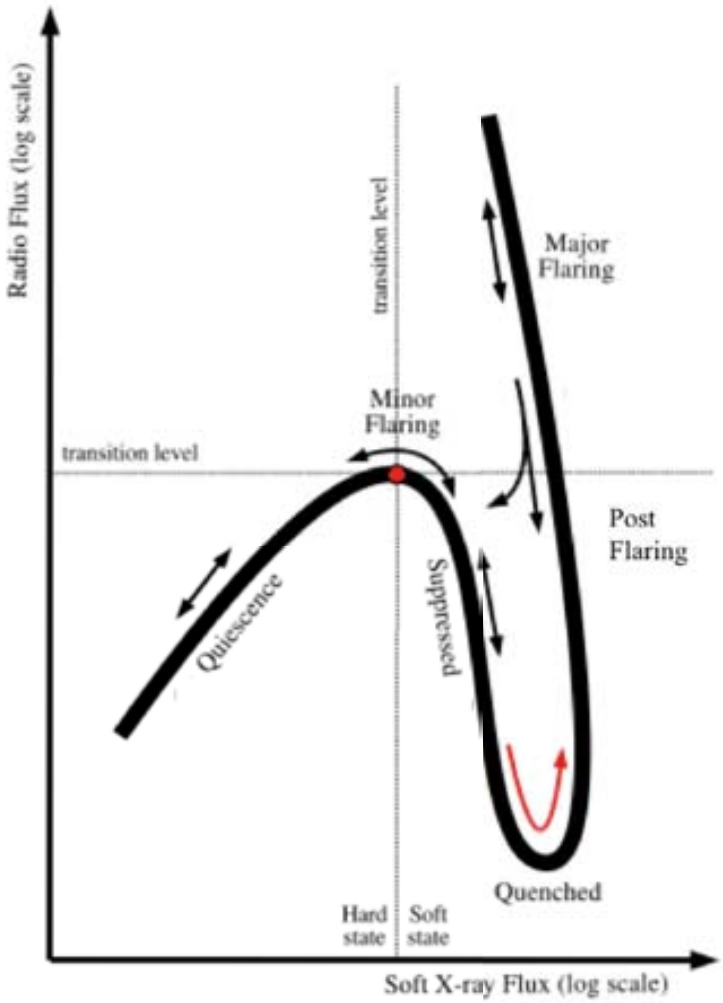

Figure 7.2: ***Saxophone plot***. Schematic representation of the evolution of Cygnus X-3 through its radio and X-ray states. The dotted lines represent the transition levels. Adapted from Szostek, A. et al. (2008).

it reaches the quenched level, the source usually produces a major radio flare.

Cygnus X-3 has also historically drawn a great deal of attention due to numerous claims of detection at TeV and PeV γ-rays, using early detectors in these energy ranges (Vladimirsky, B. M. et al., 1973; Danaher, S. et al., 1981; Lamb, R. C. et al., 1982; Dowthwaite, J. C., et al., 1983; Samorski, M. & Stamm, W., 1983; Cawley, M. F., et al., 1985; Bhat, C. L. et al., 1986). However, a critical analysis of these observations raised doubts about their validity (Chardin, G. & Gerbier, G., 1989), and in recent years more sensitive instruments have not confirmed those claims for energies above 500 GeV (Schilling, M. et al., 2001; Albert, J., et al., 2008a). Nevertheless, MQs are believed to produce VHE emission inside the jets (§ 6.6): high density photon and magnetic fields by the accretion disk and the companion star might create favorable conditions for effective production of γ-rays. This radiation can have:

- an episodic nature due to the ejection of strong radio emitting blobs (Atoyan, A. M. & Aharonian, F. A., 1999), mainly occurring in the *soft state* in the case of BH XRBs

(§ 6.4).

- a quasi-stationary character being originated in the persistent jet (Bosch-Ramon, V. et al., 2006) present during the *hard state* (§ 6.4).

Using data from EGRET, Mori, M., et al. (1997) reported an average flux of $(8.2 \pm 0.9) \times 10^{-7}$ photons cm^{-2} s^{-1} at energies above 100 MeV coming from the direction of Cygnus X-3. However, no orbital modulation was detected in the signal, precluding a solid association. The experimental situation in the HE region changed drastically by the recent results published by *AGILE* (Tavani, M., et al., 2009) and *Fermi*/LAT (Abdo, A. A., et al., 2009b). *AGILE* detected the source above 100 MeV in five different moments, for a couple of days each. Four of them correspond to the peak emissions shown in the detailed *Fermi*/LAT light curve (see below). The last detection, occurred in July 2009, has not been published yet by the *AGILE* collaboration (Bulgarelli, A., et al., in preparation). On the other hand, *Fermi*/LAT detected a clear signal from Cygnus X-3 above 100 MeV during two periods of enhanced activity lasting for several weeks and coinciding with the source being in the *soft state*. The measured flux is variable and shows an orbital modulation, which confirms the origin of the signal from the MQ. The *AGILE* flux level is comparable with the one of the *Fermi*/LAT flux peaks, as high as 2.0×10^{-6} photons cm^{-2} s^{-1} above 100 MeV (Figure 7.3). These recent results made Cygnus X-3 a more and more interesting candidate for the VHE observations.

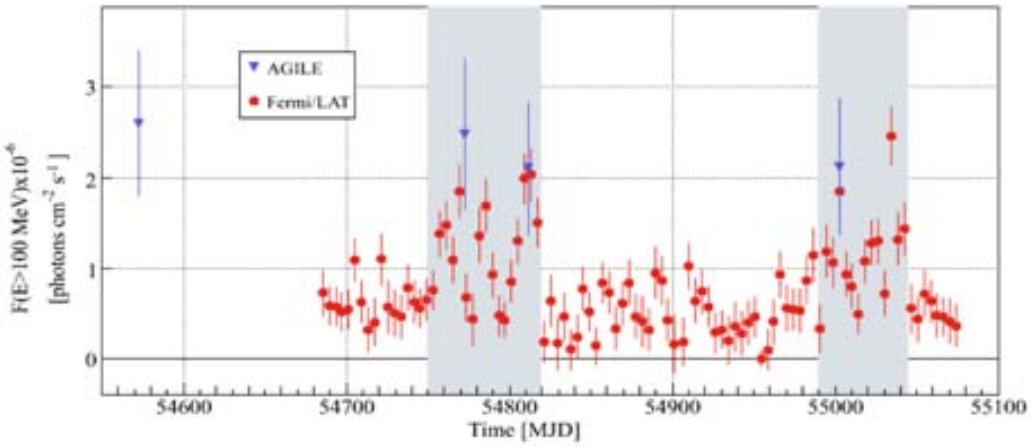

Figure 7.3: Light curve above 100 MeV. The gray areas identifies the two periods of high-activity during which *Fermi*/LAT detected the MQ and the source is in the *soft state*. Results published in Tavani, M., et al. (2009); Abdo, A. A., et al. (2009b).

7.1 MAGIC observations

MAGIC I pointed toward Cygnus X-3 for a total of 69.2 hours between March 2006 and August 2009. Since the source is expected to be variable, its observations were performed as ToO observations (§ 2.3.2), triggered by the source spectral state at other wavelengths. In 2006, observations were prompted by flares at radio frequencies. The MAGIC collaboration received two alerts from the RATAN-600 telescope on March 10, 2006 and on July 26, 2006 (Trushkin, private communication). Both radio flares had a X-ray counterpart: the source was

in the *soft* state according to *Rossi X-ray Timing Explorer (RXTE)*/ASM[1] and *Swift*/BAT[2] measurements. In 2007, the observations were triggered using public *RXTE*/ASM (1.5–12 keV) and *Swift*/BAT (15–50 keV) data, as follows: a) *Swift*/BAT daily flux larger than 0.05 counts cm^{-2} s^{-1} and b) ratio between *RXTE*/ASM and *Swift*/BAT count rates lower than 200. These criteria guarantee the source to be in the *hard state*. During 2008 and 2009, MAGIC observed Cygnus X-3 following HE γ-ray alerts issued by the *AGILE* satellite. The first of these alerts arrived on April 18, 2008, the second one on July 18, 2009 (Tavani, private communication). These last two campaigns occurred when the source was in the *soft state*. All these triggered observations were lasting at most two hours per night depending on the source visibility, its zenith angle and, above all, the competition with other scheduled sources. Nevertheless, if the OA (§ 2.5) had shown a signal larger than 3η, the observation should have been followed up as long as possible with absolute priority with respect to any other scheduled and ToO source.

At La Palma, Cygnus X-3 culminates at a zenith angle of 12°. The observations were carried out with the first stand-alone MAGIC telescope at zenith angles between 12° and 50°. They were performed partially in *on/off* mode (just the first campaign) and in *wobble* mode (§ 2.3.3). The entire Cygnus X-3 data set recorded by MAGIC amounts to 69.2 hours, out of which 12.5 hours[3] were rejected from further analysis because of their anomalous event rates. It led to a total amount of 56.7 hours of useful data distributed in 39 nights of observation. The details of the observations are quoted in Table 7.1.

The recorded Cygnus X-3 data set extends over five different cycles of observation (§ 2.3.1), which are characterized by varying hardware configurations and performances of the telescope:

- during the first campaign (cycle I) MAGIC I was equipped with the old readout system at 300 MSample/s (§ 2.2.6).

- the second campaign (cycle II) was carried out with fiber optic splitters (§ 2.2.6), but still the 300 MHz readout system. The performance of the instrument did not change much with respect to the previous observational cycle, but a new MC production was needed for such analysis.

- from the third campaign on (cycle III, IV, and V), MAGIC I was provided with the upgraded readout system (§ 2.2.6) characterized by a 2 GHz sampling rate. This hardware upgrade together with the development of new analysis methods which make use of the timing parameters of the shower images yielded to an improvement of the instrument performance by a factor 1.4 (Aliu, E., et al., 2009).

- during the third campaign (cycle III) the telescope was characterized by two different performances due to a mirror re-alignment (§ 2.2.3) which led to a significant improvement of the mirror reflectivity. The optical PSF, in fact, passed from 12–14 mm to 9–10 mm. Since the mirror re-alignment was performed on July 30-31, 2007, data from the third campaign were divided into July and August data samples. They were then analyzed separately with two different MC productions accounting for the correct optical PSF of the telescope (§ 3.1).

[1] Based on quick-look results provided by the *RXTE*/ASM team.
[2] *Swift*/BAT transient monitor results provided by the *Swift*/BAT team.
[3] 9.6 hours were rejected due to calima (3.6).

Obs. Cycle	date [yyyy mm dd]	[MJD]	eff. time [h]	ZA [°]	DC [τA]	spectral state
	2006 03 23	53817	0.45	45–50	3.5	
	2006 03 24	53818	0.25	47–50	2.5	
	2006 03 26	53820	0.53	44–50	1.5	
	2006 03 28	53822	0.70	42–50	1.4	
I	2006 03 30	53824	0.80	41–50	1.3	*soft*
	2006 03 31	53825	0.90	40–50	1.4	
	2006 04 01	53826	1.00	38–50	1.8	
	2006 04 02	53827	0.92	40–50	1.2	
	2006 04 03	53828	1.05	38–50	1.2	
	2006 07 27	53943	3.10	12–34	1.2	
	2006 07 28	53944	2.53	12–31	1.1	
II	2006 07 29	53945	1.73	12–20	1.2	*soft*
	2006 07 30	53946	1.36	12–20	1.1	
	2006 08 01	53948	0.92	12–20	1.4	
	2006 08 02	53949	1.88	12–19	1.2	
	2007 07 06	54286	2.16	19–45	2.3	
	2007 07 07	54287	4.53	12–45	2.3	
	2007 07 08	54288	1.07	26–45	1.5	
	2007 07 09	54289	0.38	34–40	1.5	
	2007 07 14	54295	1.82	12–21	1.5	
	2007 07 15	54296	1.93	12–21	1.5	
	2007 07 16	54297	1.93	12–21	1.4	
	2007 07 24	54305	1.75	12–23	1.4	
III	2007 07 26	54307	0.98	19–30	1.4	*hard*
	2007 07 27	54308	0.5	19–30	1.4	
	2007 08 04	54316	0.73	27–35	1.5	
	2007 08 06	54318	2.72	12–30	1.6	
	2007 08 07	54319	1.93	13–31	1.3	
	2007 08 08	54320	1.58	14–31	1.4	
	2007 09 03	54346	1.86	13–37	2.5	
	2008 04 28	54584	0.31	32–40	2.9	
IV	2008 04 29	54585	1.07	24–41	3.2	*soft*
	2008 04 30	54586	1.33	23–40	2.6	
	2009 07 19	55031	3.48	12–36	1.2	
	2009 07 21	55033	2.21	14–42	1.2	
V	2009 07 22	55034	1.63	12–27	1.1	*soft*
	2009 08 01	55044	1.81	17–39	1.5	
	2009 08 02	55045	0.88	27–41	1.6	

Table 7.1: Observation log of Cygnus X-3 . From left to right: MAGIC observational cycle, date of the beginning of the observations in UTC, also in MJD, effective time after quality cuts, zenith angle range, the PMT DCs and the spectral state.

- data from the forth campaign (cycle IV) were recorded under moderate moonlight conditions, as shown by the anode PMT DCs in Table 7.1. Therefore, they required specific image cleaning levels to account for the larger noise, as described in § 3.4.1.
- 0.7 hours of data recorded during cycle I, on March 23–24, 2006 are characterized by moonlight conditions.

7.1.1 Data analysis

Data analysis was carried out using the standard MAGIC calibration and analysis software described in Chapter 3.

- standard calibration (§ 3.3). The signal extractor used in this analysis is the digital filter for the first two observational campaigns (300 MHz FADC) and the cubic-spline extractor for the other data samples.
- standard timing image cleaning (§ 3.4.1) for all campaigns, but the forth for which the image cleaning levels were increased due to the moonlight conditions (§ 3.4.1). The 0.7 hours of moon data in cycle I were analyzed with the standard image cleaning in order to have a uniform sample of cycle I data. This results in $\equiv 20\%$ underestimation of the effective area for those 0.7 hours of observation (Rico, J., et al., 2008).
- use of the timing parameters (§ 3.5) also for data of the first and second campaigns taken with the 300 MHz readout. The use of these parameters became part of the standard analysis only after the upgrade of the MAGIC I readout system (§ 2.2.6). Nevertheless, it has been proved that they lead to an improvement in sensitivity (even if lower in magnitude) for data recorded with the old FADC (§ 3.5).
- low quality data rejected according to the criteria in § 3.6.
- minimum *size* cut at 200 ph.e. in order to homogenize the different data and MC samples and achieve a common stable energy threshold of all the analyses.
- search for VHE signal performed by using the distribution of *alpha* angle (§ 3.5).
- the evaluation of the background depended on the data taking mode (§ 3.9). In particular, for the observations carried out in *wobble* mode, the background was extracted from 3 *off* regions. While, for the *on/off* data, the used *off* data sample included *off* data taken during dark night within March 2006 at zenith angles between 38° and 50°.
- the computation of the ULs to the integral flux at 95% CL was performed by using the Rolke's method assuming a 30% systematic uncertainty (§ 3.15). The source spectrum was assumed to a power-law with a photon index 2.6 which is the one used in the MC production. However, a 30% change in the photon index yields a variation of less than 1% in the ULs.

Given the substantial differences between data from various cycles of observations, each cycle of data was analyzed separately using a matching sample of MC simulated γ-ray events. The gamma selection cuts for each cycle of data were optimized on a corresponding Crab Nebula sample according to the criteria described in § 3.9. The energy threshold common to all the analyses was defined as the highest energy threshold among the single analyses ones. It was set at 250 GeV.

7.2 Results

A search for VHE γ-ray emission from Cygnus X-3 was performed separately for each cycle of observations. None of them yielded a significant excess. The combination of all the data samples yields a 95% CL upper limit to an integral flux of 2.2×10^{-12} photons cm^{-2} s^{-1} for energies greater than 250 GeV. It corresponds to 1.3% of the Crab Nebula flux at these energies. The differential flux upper limits are shown in Table 7.2 and in Figure 7.4.

Energy Range [GeV]	N_{on} **Evts.**	N_{bg} **Evts.**	**Excess Evts.**	**Norm.Fact.**	**Signif.** [σ]	**UL Evts.**	**Flux UL** [TeV^{-1}cm^{-2}s^{-1}]
199–315	4416	4384.5 ± 39.0	31.5 ± 77.0	0.34	0.4	237.8	2.6e−11
315–500	2057	1980.6 ± 28.6	76.4 ± 53.6	0.36	1.5	264.2	1.2e−11
500–792	769	800.8 ± 21.1	−31.8 ± 34.9	0.39	−0.9	51.3	1.1e−12
792–125	289	299.9 ± 12.9	−10.9 ± 21.4	0.38	−0.3	39.2	5.1e−13
1256–1991	102	98.3 ± 6.9	3.7 ± 12.2	0.37	0.5	36.2	3.0e−13
1991–3155	38	32.3 ± 3.5	5.7 ± 7.1	0.35	0.7	27.4	1.3e−13

Table 7.2: Differential flux upper limits for the VHE time-integrated emission at 95% CL.

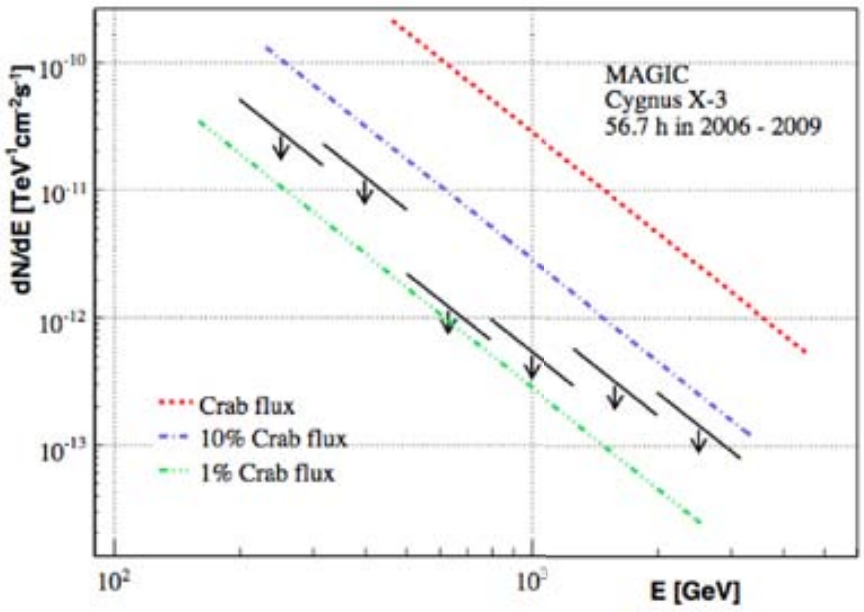

Figure 7.4: Differential flux upper limits at 95% CL for the VHE time-integrated emission. The slope of the arrows indicates the assumed power-law spectrum with a photon index 2.6.

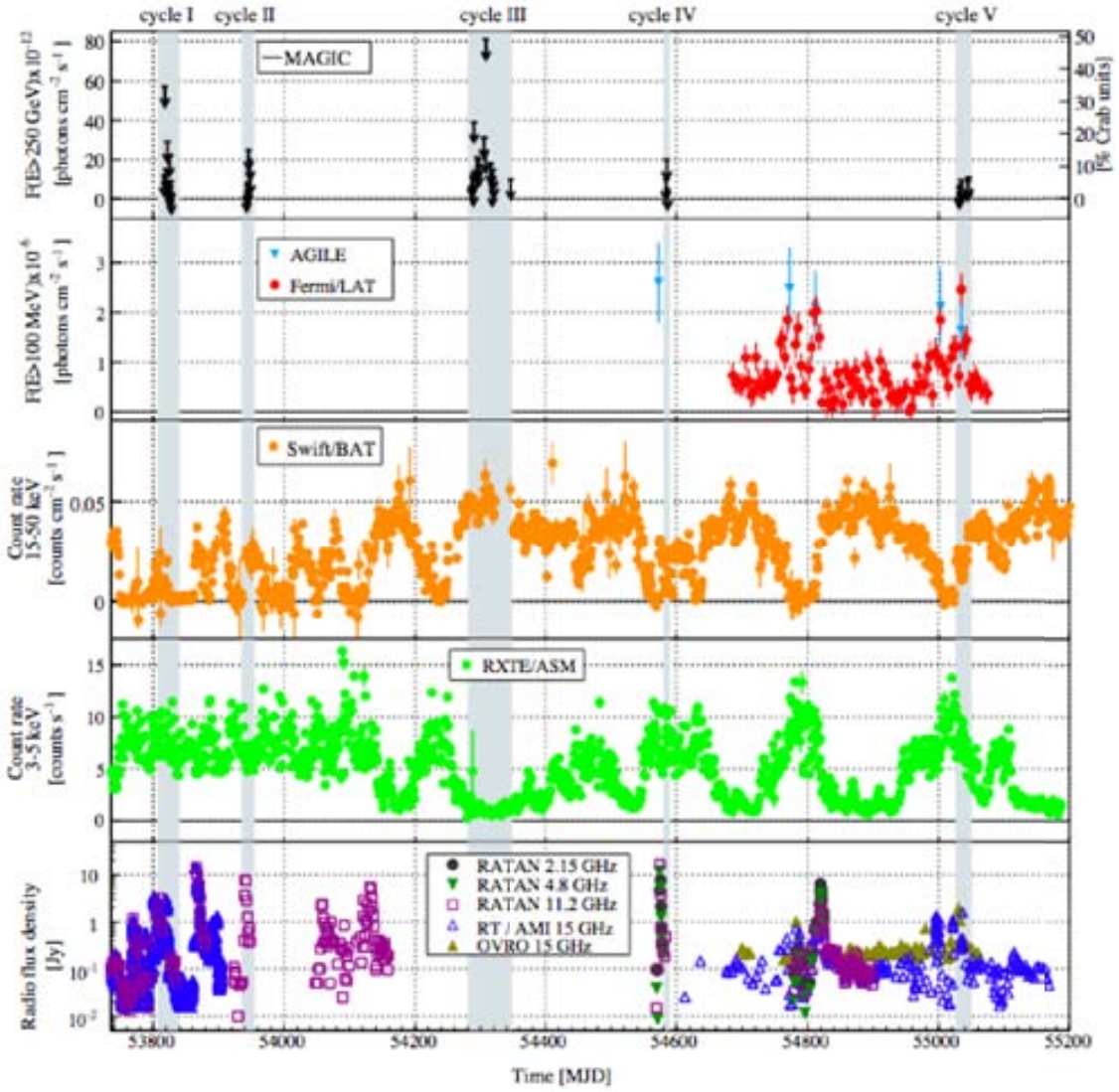

Figure 7.5: From top to bottom: daily MAGIC VHE integral flux ULs for E > 250 GeV, and HE γ-ray (*AGILE* and *Fermi*/LAT), hard X-ray (*Swift*/BAT), soft X-ray (*RXTE*/ASM) and radio fluxes measured for Cygnus X-3 as function of time (from January 1, 2006 until December 15, 2009). The grey bands show the periods corresponding to the MAGIC observations. The OVRO and AMI 15 GHz data generally agree well, except for the offset apparent during steady periods which is due to unrelated extended emission resolved out by AMI.

Given that Cygnus X-3 flux is variable at other energy bands on time scales of days, γ-ray signals were searched for also on a daily basis. No significant excess events were found in any observation night. The integral flux ULs for energies above 250 GeV are shown in Table 7.3 and in the top panel of Figure 7.5.

In Figure 7.5, MAGIC results are presented on a multi-wavelength context where the above-mentioned flux variability at different energy bands is rather clear. In particular, it displays daily MAGIC VHE integral ULs, and HE γ-ray (*AGILE* and *Fermi*/LAT ([0.1–30 GeV]), hard X-ray (*Swift*/BAT [15–50 keV]), soft X-ray (*RXTE*/ASM [3–5 keV]), and radio measured fluxes from January 1, 2006 (MJD 53736) until December 15, 2009 (MJD 55180).

Date [MJD]	Time [h]	N_{on} Evts.	N_{bg} Evts.	Excess Evts.	Norm.Fact.	Signif. [σ]	UL Evts.	Flux UL [$cm^{-2}s^{-1}$]	[% C.U.]
53817	0.46	42	41.4 ± 1.8	0.6 ± 6.7	0.07	0.1	18.7	1.2e−11	7.5
53818	0.26	43	27.0 ± 0.7	16.0 ± 6.6	0.05	2.8	46.7	5.7e−11	34.2
53820	0.54	85	83.8 ± 4.6	1.2 ± 10.2	0.15	0.1	27.4	1.5e−11	9.3
53822	0.70	132	111.4 ± 3.5	20.6 ± 12.0	0.19	1.7	67.9	2.9e−11	17.4
53824	0.80	84	84.8 ± 2.4	−0.8 ± 9.5	0.15	−0.1	24.3	9.1e−12	5.5
53825	0.80	83	64.3 ± 2.1	18.7 ± 9.3	0.15	2.1	58.0	2.2e−11	13.1
53826	1.00	37	34.3 ± 0.6	2.7 ± 6.1	0.06	0.4	20.9	6.1e−12	3.7
53827	0.92	79	76.5 ± 1.9	2.5 ± 9.1	0.13	0.3	28.4	9.1e−12	5.5
53828	1.05	42	49.3 ± 1.1	−7.3 ± 6.6	0.09	−1.0	10.9	3.1e−12	1.8
53943	3.10	257	274.3 ± 9.5	−17.3± 18.6	0.33	−0.9	27.9	4.1e−12	2.5
53944	2.54	232	235.7 ± 8.8	−3.7 ± 17.6	0.33	−0.2	38.6	7.1e−12	4.3
53945	1.73	122	125.7 ± 6.4	−3.7 ± 12.7	0.33	−0.3	27.1	8.4e−12	5.1
53946	1.37	127	108.0 ± 5.9	19.0± 12.7	0.33	1.5	65.0	2.5e−11	15.3
53948	0.90	82	65.7 ± 4.6	16.3 ± 10.2	0.33	1.7	54.3	3.2e−11	19.4
53949	1.79	138	143.3 ± 6.9	5.3 ± 13.6	0.33	0.4	42.1	1.3e−11	7.8
54286	2.16	299	314.0 ± 10.2	−15.0 ± 20.1	0.33	−0.74	62.1	1.1e−11	6.8
54287	4.53	547	547.0 ± 13.4	−0.7 ± 27.0	0.33	−0.03	150.3	1.3e−11	8.1
54288	1.07	176	208.0 ± 8.3	−32.0 ± 15.6	0.33	−1.99	20.3	7.0e−12	4.3
54289	0.38	86	84.3 ± 5.3	1.7 ± 10.7	0.33	0.16	41.3	3.9e−11	23.5
54295	1.82	189	176.3 ± 7.6	12.7 ± 15.7	0.33	0.82	76.4	2.1e−11	13.0
54296	1.93	219	209.0 ± 8.3	10.0 ± 17.0	0.33	0.59	74.9	2.0e−11	11.8
54297	1.93	151	138.7 ± 6.7	12.3 ± 14.0	0.33	0.89	65.9	1.7e−11	10.4
54305	1.75	179	167.7 ± 7.4	11.3 ± 15.3	0.33	0.75	111.6	3.1e−11	19.0
54307	0.98	115	117.0 ± 6.2	−2.0 ± 12.4	0.33	−0.16	52.9	2.4e−11	14.5
54308	0.5	71	59.3 ± 4.4	11.7 ± 9.5	0.33	1.27	100.1	8.1e−11	48.8
54316	0.73	85	88.7 ± 5.4	−3.7 ± 10.7	0.33	−0.34	33.0	1.8e−11	11.0
54318	2.72	262	277.3 ± 9.6	−15.3 ± 18.8	0.33	−0.81	39.2	6.7e−12	4.1
54319	1.93	184	184.0 ± 7.8	0.0 ± 15.6	0.33	0.00	61.8	1.5e−11	8.8
54320	1.58	146	152.3 ± 7.1	−6.3 ± 14.0	0.33	−0.95	38.8	1.1e−11	6.8
54346	1.86	182	200.0 ± 8.1	−18.0 ± 15.7	0.33	−1.12	45.3	1.0e−11	6.3
54584	0.31	17	23.0 ± 2.7	−5.0 ± 5.0	0.33	−1.0	8.0	1.0e−11	6.2
54585	1.07	89	75.3 ± 5.0	13.7 ± 10.7	0.33	1.3	50.2	2.0e−11	11.9
54586	1.33	60	66.7 ± 4.7	−6.7 ± 9.1	0.33	−0.7	15.5	5.1e−11	3.1
55031	3.48	186	183.3 ± 7.8	2.7 ± 15.7	0.33	0.2	43.2	5.7e−12	3.4
55033	2.21	71	63.7 ± 4.6	7.3 ± 9.6	0.33	0.8	36.2	7.2e−12	4.4
55034	1.63	50	43.3 ± 3.8	6.7 ± 8.0	0.33	0.9	31.4	9.7e−12	5.8
55044	1.81	88	80.0 ± 5.1	8.0 ± 10.7	0.33	0.8	40.0	9.4e−12	5.7
55045	0.88	69	69.0 ± 4.8	0.0 ± 9.6	0.33	0.0	24.2	1.1e−11	6.6

Table 7.3: Integral flux upper limits for energies above 250 GeV calculated on a daily basis at 95% CL.

The soft X-ray energy band of *RXTE*/ASM is between 1.5 and 12 keV, out of which only the 3–5 keV band was used, as it yields to the cleanest radio/X-ray correlation (Szostek, A. et al., 2008). The radio measurements, displayed in logarithmic scale, were provided by the RATAN-600 telescope at 2.15, 4.8 and 11.2 GHz, and by the Ryle Telescope (RT), the AMI telescope and the OVRO 40-meter telescope at 15 GHz.
The soft and hard X-ray fluxes shown in Figure 7.5 allow us to derive the X-ray spectral state of Cygnus X-3 during MAGIC observations. Cycle III data are the only ones taken when the source was in the *hard state*, as requested by the observational trigger. All the other observations were carried out when the source was in the *soft state*. The first two MAGIC observational campaigns (cycles I and II) were triggered by flares at radio frequencies, which are expected when the source is in *soft state*. Unfortunately, the conditions on the trigger, together with MAGIC constraints on observation time (moon and weather) did not allow a simultaneous coverage of the flaring states: MAGIC started pointing toward Cygnus X-3 twelve and two days after the strong radio emission, respectively (Figure 7.6). On the other hand, in the last observational cycles (IV and V), MAGIC observed the source during the *soft state*, following two *AGILE* alerts on a high-flux activity in the HE band: the GeV emission occurs only in this X-ray spectral state (Abdo, A. A., et al., 2009b). During the second alert, in July 2009 (MJD 55030), MAGIC recorded some data simultaneous with a GeV peak emission and did not detect any VHE signal. This important result will be discussed in detail in § 7.2.1.

MQs are expected to produce VHE emission inside the jets either when they are compact and persistent, mainly in the *hard state*, or in the presence of strong radio-emitting-blobs, which most likely happen during a *soft state*. Therefore, the results of the MAGIC observations

were divided according to the X-ray spectral state of the source, as described in § 7.2.2 and 7.2.3 for the *soft* and *hard states*, respectively. Besides, in the scenario where the VHE radiation is emitted during powerful synchrotron radio ejections, there might be a correlation between these two wavelengths (Atoyan, A. M. & Aharonian, F. A., 1999). Therefore, in § 7.2.4 the X-ray/radio states during the MAGIC observations are quoted.

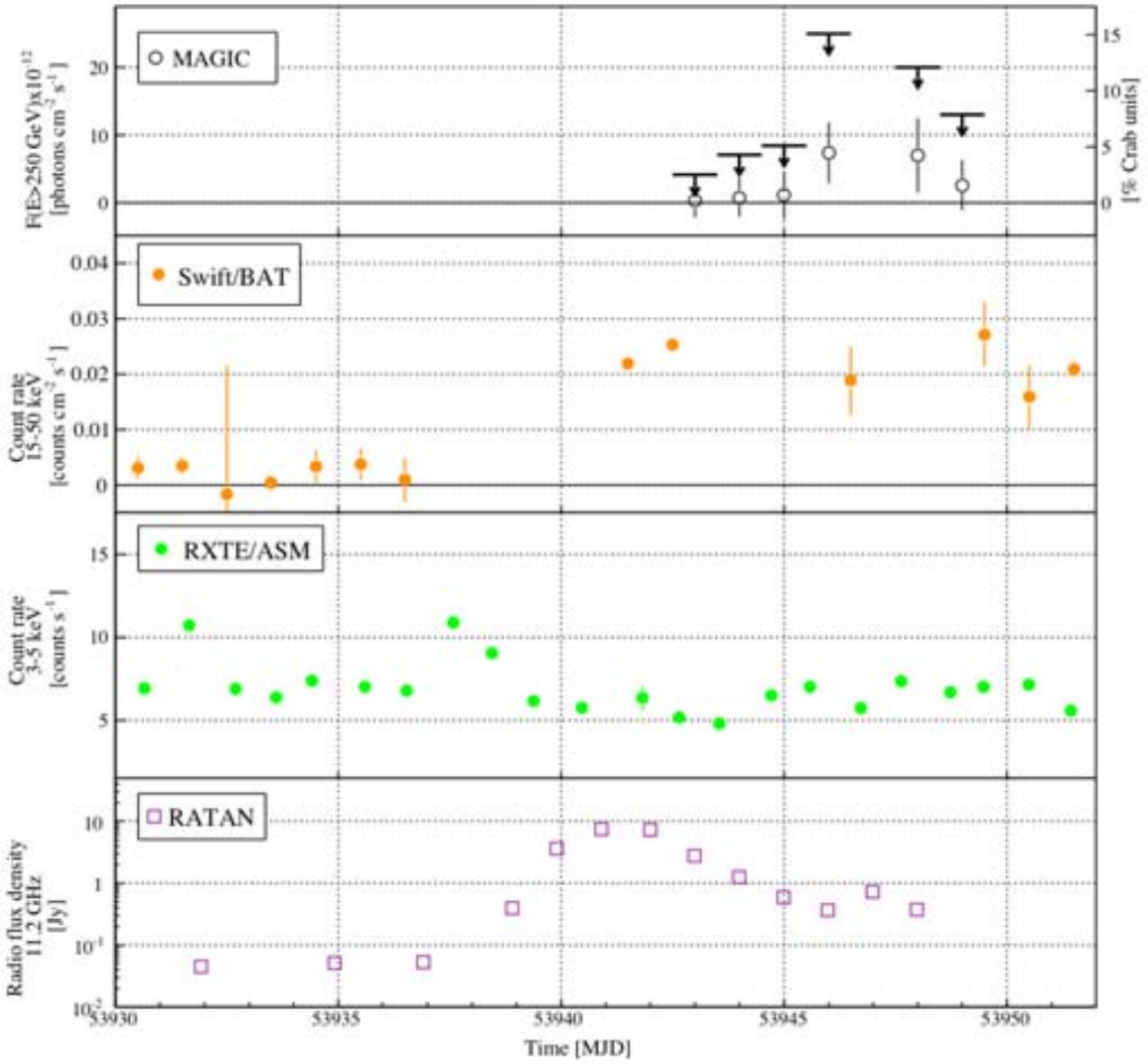

Figure 7.6: Zoom of Figure 7.5 around cycle II campaign between July 14 and August 5, 2006. The open black points in the VHE MAGIC panel show the non-significant measured integral fluxes with their statistical error bars (whereas the upper limits take into account also the systematic errors).

7.2.1 Results during high-energy γ-ray emission

Abdo, A. A., et al. (2009b) presented the *Fermi*/LAT observations of Cygnus X-3 between August 4, 2008 and September 2, 2009. They detected a strong signal above 100 MeV, with an overall significance of more than 29 standard deviations, which is mainly dominated by two active periods (MJD 54750–54820 and 54990–55045). These active periods coincide with

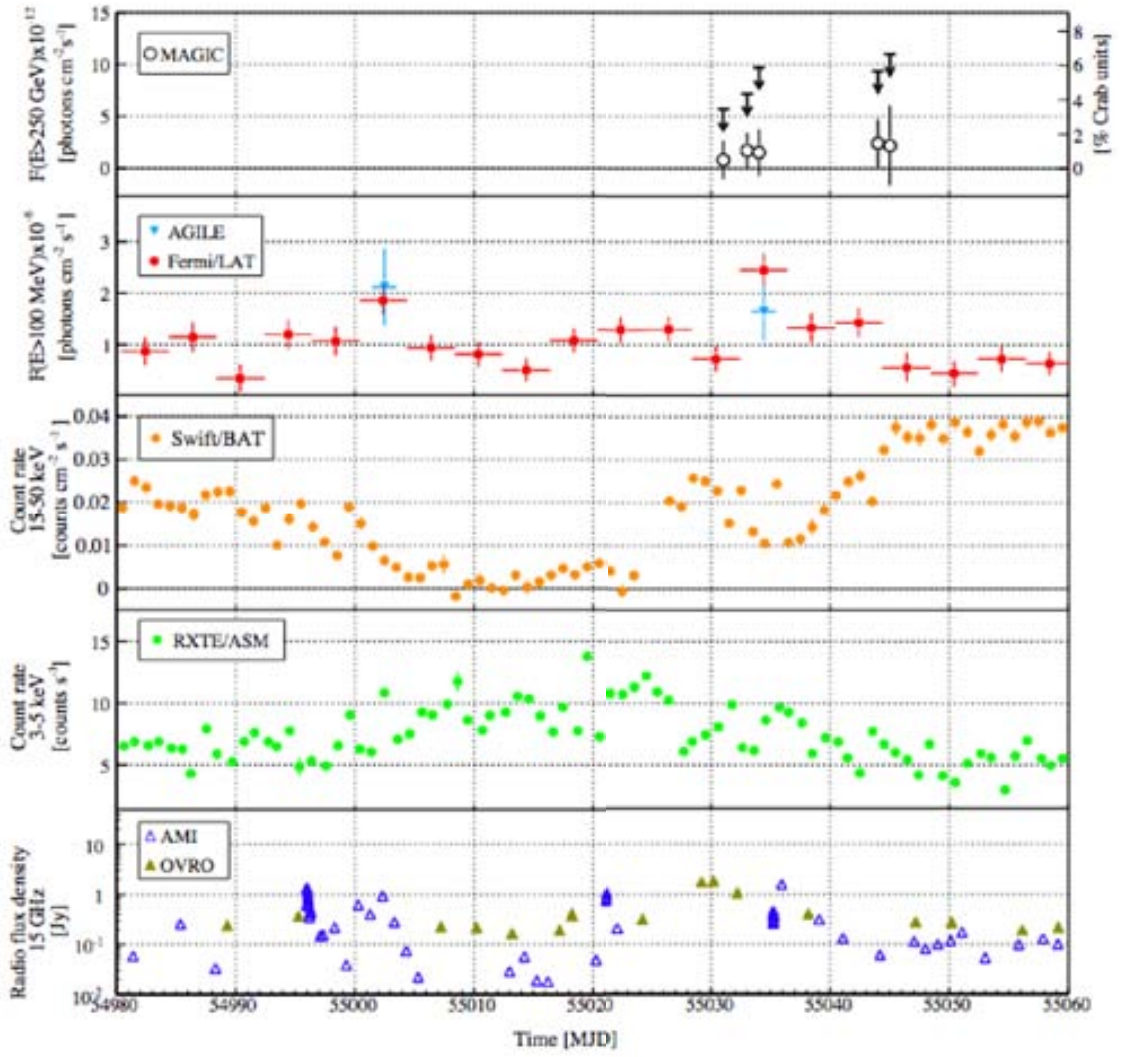

Figure 7.7: Zoom of Figure 7.5 around cycle V campaign between May 29 and August 17, 2009. The open black points in the VHE MAGIC panel show the non-significant measured integral fluxes with their statistical error bars (whereas the ULs take into account also the systematic errors).

the X-ray *soft state* of the source, indicating that Cygnus X-3 emits HE γ-rays during this spectral state, with an average flux of 1.2×10^{-6} photons cm^{-2} s^{-1} and a photon index $2.70 \pm 0.05_{\rm stat} \pm 0.20_{\rm sys}$ (under the assumption of a power-law spectrum). They also estimated that the peak flux can be as high as 2×10^{-6} photons cm^{-2} s^{-1} without providing any photon index.

The five *AGILE* detections between 100 MeV and 3 GeV (Tavani, M., et al., 2009; Bulgarelli, A., et al., in preparation) coincide with the strongest HE outbursts, which can be seen overlapping them with the *Fermi*/LAT light curve. The *AGILE* integral flux averaged over the first four detections is estimated of 1.9×10^{-6} photons cm^{-2} s^{-1} with a corresponding photon index of 1.8 ± 0.2.

In cycle V, MAGIC pointed at Cygnus X-3 during the second period of HE enhanced ac-

tivity detected by *Fermi*/LAT, as shown in the Figure 7.7. In particular, MAGIC carried out observations simultaneous with a GeV emission peak on July 21 and 22, 2009 (MJD 55033–55034), and it did not detect any VHE emission. The corresponding MAGIC integral flux ULs above 250 GeV are lower than 6% of the Crab Nebula flux.

Figure 7.8 shows the SED of Cygnus X-3 between 100 MeV and 5 TeV including MAGIC 95% CL ULs at VHE, and the power-law spectrum in the HE range reported by both *AGILE* and *Fermi*/LAT. The spectra take into account the error on the photon index and the one on the integral flux, which is 30% and 40% for *Fermi*/LAT and *AGILE*, respectively. The SED for the average *soft state* was obtained considering the average *Fermi*/LAT flux and MAGIC results of the *soft state* data set. On the other hand, to obtain the SED during a HE emission peak, the MAGIC measurements simultaneous with the GeV emission peak and both *Fermi*/LAT and *AGILE* spectral power-law fits were used. The *Fermi*/LAT photon index during the peak was assumed to be the same as the one for the *soft state* average flux. Being the latter dominated by the brightest phases of the γ-ray outburst, it can be considered representative also of the flaring activity. Both MAGIC ULs are consistent with the extrapolation of the *Fermi*/LAT spectra up to VHE, but not with the extrapolation of the harder *AGILE* spectrum, which would suggest a cut-off between some tens and 250 GeV.

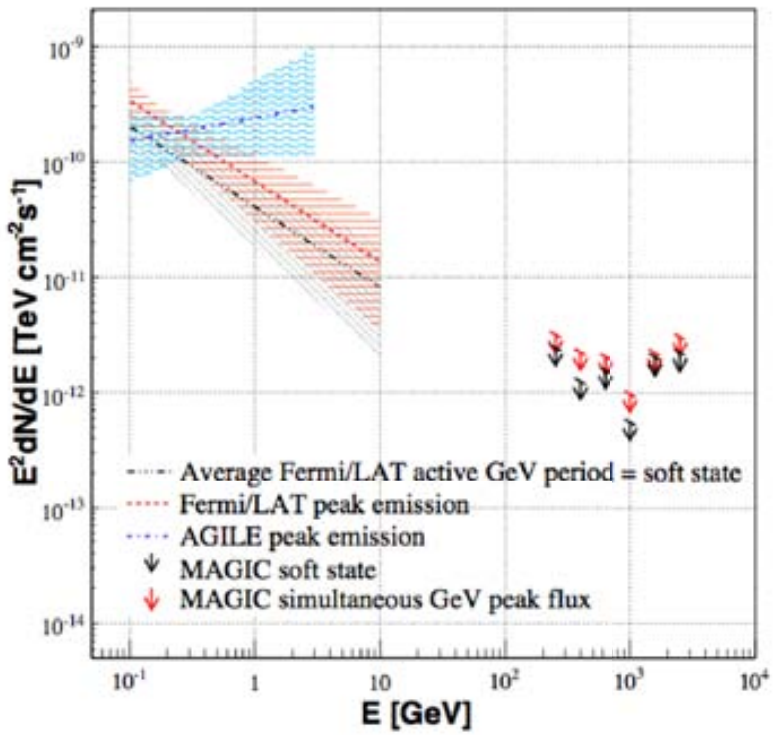

Figure 7.8: Cygnus X-3 spectral energy distribution in the HE and VHE bands. The lines indicate the power-law spectra derived from *Fermi*/LAT and *AGILE* integral fluxes and photon indeces, where the corresponding errors were taken into account and are shown in shadowed areas. The arrows display the 95% CL MAGIC differential flux upper limits and their slope indicates the assumed power-law spectrum with a photon index 2.6. The black indicators show the SED during the period of enhanced GeV activity coinciding with the *soft state*, whereas, the red and blue ones during the HE peak emission (MJD 55031–55034).

7.2.2 Results during the soft state

MAGIC I pointed at Cygnus X-3 when it was in *soft state* during the observational cycles I, II, IV and V, corresponding to a total of 30.8 hours. For these observations, soft X-ray measurements in the 3–5 keV band are always above the transitional level set at 3 counts s^{-1} by Szostek, A. et al. (2008).

After having analyzed each data cycle separately, the data sets were combined in order to obtain a global UL to the integral flux for the *soft state*. The upper limit at 95% CL for energies greater than 250 GeV is 4.1 $\times$ 10^{-12} photons cm^{-2} s^{-1}, i.e. $\sim$ 2.5% of the Crab Nebula flux. The differential flux upper limits for this spectral state are shown in Table 7.4 and in the left panel of Figure 7.9.

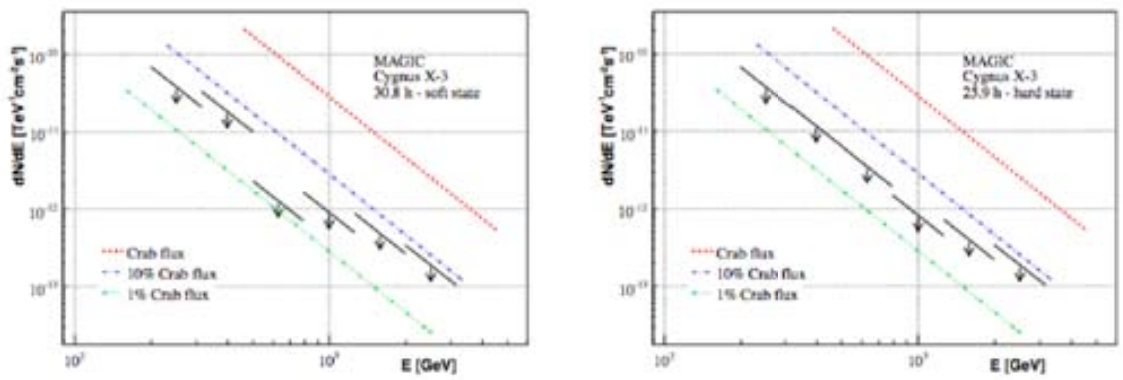

Figure 7.9: 95% CL differential flux upper limits *On the left:* for the *soft state*; *On the right: hard state* observations. The slope of the arrows indicates the assumed power-law spectrum with a photon index 2.6.

Spectral State	Energy [GeV]	N_{on} Evts.	N_{bg} Evts.	Excess Evts.	Norm.Fact.	Signif. [σ]	UL Evts.	Flux UL [$TeV^{-1}cm^{-2}s^{-1}$]
soft	199–315	1709	1677.54 ± 24.6	31.5 ± 48.1	0.36	0.7	169.2	3.5e−11
	315–500	926	858.3 ± 18.5	67.7± 35.6	0.40	1.9	212.3	1.7e−11
	500–792	324	357.5 ± 12.9	−33.5 ± 22.2	0.47	−1.1	30.3	1.2e−12
	792–1256	125	124.9 ± 7.7	0.1 ± 13.6	0.48	0.4	38.0	8.4e−13
	1256–1991	41	33.7 ± 3.9	7.3 ± 7.5	0.46	1.4	32.7	4.5e−13
	1991–3155	14	8.7 ± 1.8	5.3 ± 4.2	0.40	1.3	20.3	1.7e−13
hard	199–315	2707	2707.0 ± 29.9	0.0 ± 60.0	0.33	0.0	146.2	3.4e−11
	315–500	1131	1122.3 ± 19.2	8.7 ± 38.7	0.33	0.2	108.5	1.1e−11
	500–792	445	443.3 ± 12.1	1.7 ± 24.3	0.33	0.1	62.5	3.3e−12
	792–1256	164	175.0 ± 7.5	−11.0 ± 14.9	0.33	−0.7	24.7	7.7e−13
	1256–1991	61	64.7 ± 4.6	−3.7± 9.1	0.33	−0.4	18.4	3.7e−13
	1991–3155	24	23.7 ± 2.7	0.3 ± 5.6	0.33	0.1	15.2	1.7e−13

Table 7.4: Differential flux upper limits for the *soft* and *hard states* observations.

Due to the highly anisotropic radiation from the companion star, the predicted γ-ray emission above 250 GeV would be modulated according to the orbital phase (Bednarek, W., 1997). Absorption might play an important role making the VHE orbital modulation difficult to be detected by the current sensitivity instrumentation (Bednarek, W., 2010). The orbital modulation of the GeV γ-ray emission was detected only when the source was in the *soft state* (Abdo, A. A., et al., 2009b). MAGIC searched for such modulation in this spectral state. A phase-folded analysis was performed assuming the parabolic ephemeris in Singh, N. S., et al. (2002). The results are shown in the left panel of Figure 7.10 and in Table 7.5. No evidence of VHE γ-ray signal was found in any phase bin. The obtained integral flux ULs are smaller than 10% of the Crab Nebula flux for all of them.

7.2.3 Results during the hard state

The 25.9 hours of MAGIC cycle III data sample were obtained when Cygnus X-3 was in *hard state*. *Swift*/BAT count rates during this cycle are rather high, greater than 0.05 counts cm^{-2} s^{-1}, whereas the soft X-ray fluxes in the 3–5 keV band are below 2 counts s^{-1}.

For this spectral state, the integral flux upper limit for energies greater than 250 GeV is 1.1% of the Crab Nebula flux (1.8×10^{-12} photons cm^{-2} s^{-1}). The differential flux ULs are quoted in Table 7.4 and plotted in the right panel of Figure 7.9.

The performed phase-folded analysis for this spectral state did not yield any significant detection. The computed upper limits to the integral flux are, on average, at the level of 5% of the Crab Nebula flux (see right panel in Figure 7.10 and Table 7.5).

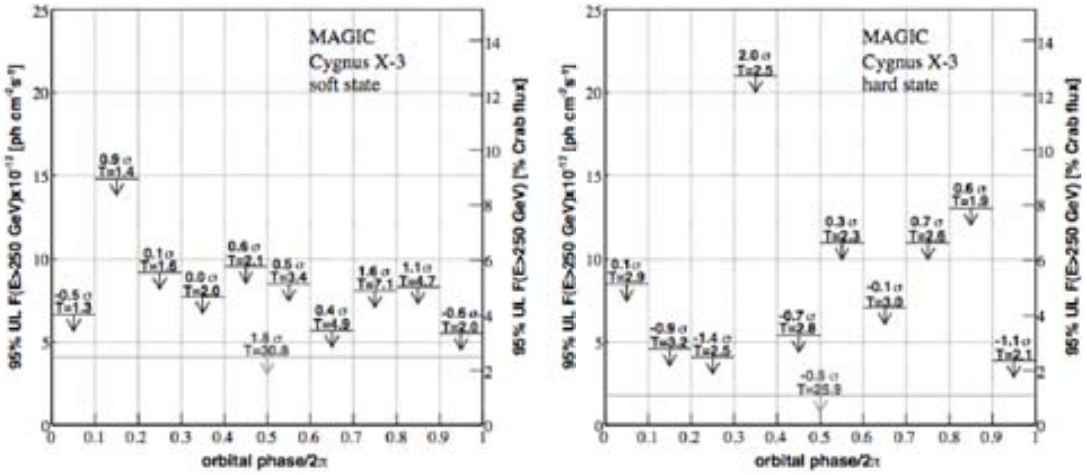

Figure 7.10: Phase-wise integral flux upper limits for E > 250 GeV *On the left:* for the *soft state*; *On the right:* for the *hard state*. The effective observation time (in hours) and the signal significance for each phase bin are written on top of each arrow. The grey arrow indicates the integral flux UL on the VHE time-integrated emission.

X-ray state	Phase	Time [h]	N_{on} Evts.	N_{bg} Evts.	Excess Evts.	Norm. Fact.	Signif. [σ]	UL Evts.	Flux UL [$cm^{-2}s^{-1}$]	Flux UL [% C.U.]
	0.0–0.1	1.34	64	68.0 ± 4.7	−4.3 ± 9.3	0.33	−0.5	18.2	6.7e−12	4.0
	0.1–0.2	1.40	75	67.3 ± 4.7	8.3 ± 9.8	0.33	0.9	38.6	1.5e−11	8.9
	0.2–0.3	1.63	108	107.0 ± 5.9	1.3 ± 12.0	0.33	0.1	32.1	9.2e−12	5.6
	0.3–0.4	2.05	162	162.0 ± 7.3	0.3 ± 14.6	0.33	0.0	37.1	7.7e−12	4.7
	0.4–0.5	2.11	113	106.0 ± 5.9	7.3 ± 12.1	0.33	0.6	42.3	9.6e−12	5.8
soft	0.5–0.6	3.40	231	222.3 ± 8.5	8.7 ± 17.5	0.33	0.5	57.1	8.5e−12	5.1
	0.6–0.7	4.93	370	361.3± 10.2	9.1 ± 21.8	0.29	0.4	68.3	5.7e−12	3.4
	0.7–0.8	7.13	649	600.7 ± 17.1	49.4 ± 30.7	0.49	1.6	163.9	8.1e−12	4.9
	0.8–0.9	4.69	331	310.0 ± 8.4	21.2 ± 20.0	0.23	1.1	86.4	8.3e−12	5.1
	0.9–1.0	2.05	109	116.0 ± 6.2	−7.0 ± 12.1	0.33	−0.6	22.1	5.5e−12	3.3
	0–1	30.78	2216	2120.3 ± 29.5	96.3 ± 55.5	0.41	1.8	311.6	4.1e−12	2.5
	0.0–0.1	2.89	511	509.7 ± 12.9	1.3 ± 26.1	0.33	0.0	102.5	8.6e−12	5.2
	0.1–0.2	3.23	477	501.3 ± 12.8	−24.3 ± 25.3	0.33	−0.9	52.5	4.6e−12	2.7
	0.2–0.3	2.53	281	308.0 ± 10.1	−27.0 ± 19.5	0.33	−1.4	33.6	4.1e−12	2.5
	0.3–0.4	2.53	266	230.0 ± 8.7	36.0 ± 18.5	0.33	2.0	218.1	2.1e−11	12.4
	0.4–0.5	2.79	248	261.0 ± 9.2	−13.0 ± 18.3	0.33	−0.7	43.2	5.4e−12	3.3
hard	0.5–0.6	2.27	210	205.3 ± 8.2	4.7 ± 16.6	0.33	0.3	73.1	1.1e−11	6.8
	0.6–0.7	2.99	242	243.0 ± 8.9	−1.0 ± 17.9	0.33	−0.1	65.8	7.1e−12	4.3
	0.7–0.8	2.63	234	222.7 ± 8.6	11.3 ± 17.5	0.33	0.6	116.3	1.1e−11	6.8
	0.8–0.9	1.95	199	189.7 ± 7.9	9.3 ± 16.2	0.33	0.6	118.5	1.3e−11	7.8
	0.9–1.0	2.13	235	261.3 ± 9.3	−26.3 ± 17.9	0.33	−1.4	33.8	3.9e−12	2.4
	0–1	25.9	2903	2932.0 ± 31.1	−29.0 ± 62.2	0.33	−0.5	191.0	1.8e−12	1.1

Table 7.5: Integral flux upper limits for energies above 250 GeV for the phase-folded analyses of the observations in the *soft* and *hard states*.

7.2.4 Results during X-ray/radio states

MAGIC observed Cygnus X-3 in both X-ray main spectral states (§ 7.2.2 and 7.2.3). However, the state of the source can be further characterized by simultaneous radio flux. Szostek, A. et al. (2008) identified six different X-ray/radio states studying simultaneous observations of the GBI at 8.3 GHz and *RXTE*/ASM in the energy range 3–5 keV. The relation between these two energy bands is shown in the *saxophone plot* (Figure 7.2). It was noted that the use of other radio frequencies yield similar results (Tudose, V., et al., 2010). This gives us the confidence that a direct comparison between their and our results using 15 GHz (RT, AMI and OVRO) and 11.2 GHz (RATAN-600) is reasonable. The OVRO and AMI 15 GHz data generally agree well, but for a ∼0.12 Jy offset apparent during steady periods, probably due to unrelated extended emission resolved out by AMI. Thus, only the AMI 15 GHz were used in this analysis, although our conclusions are not substantially affected by this choice.

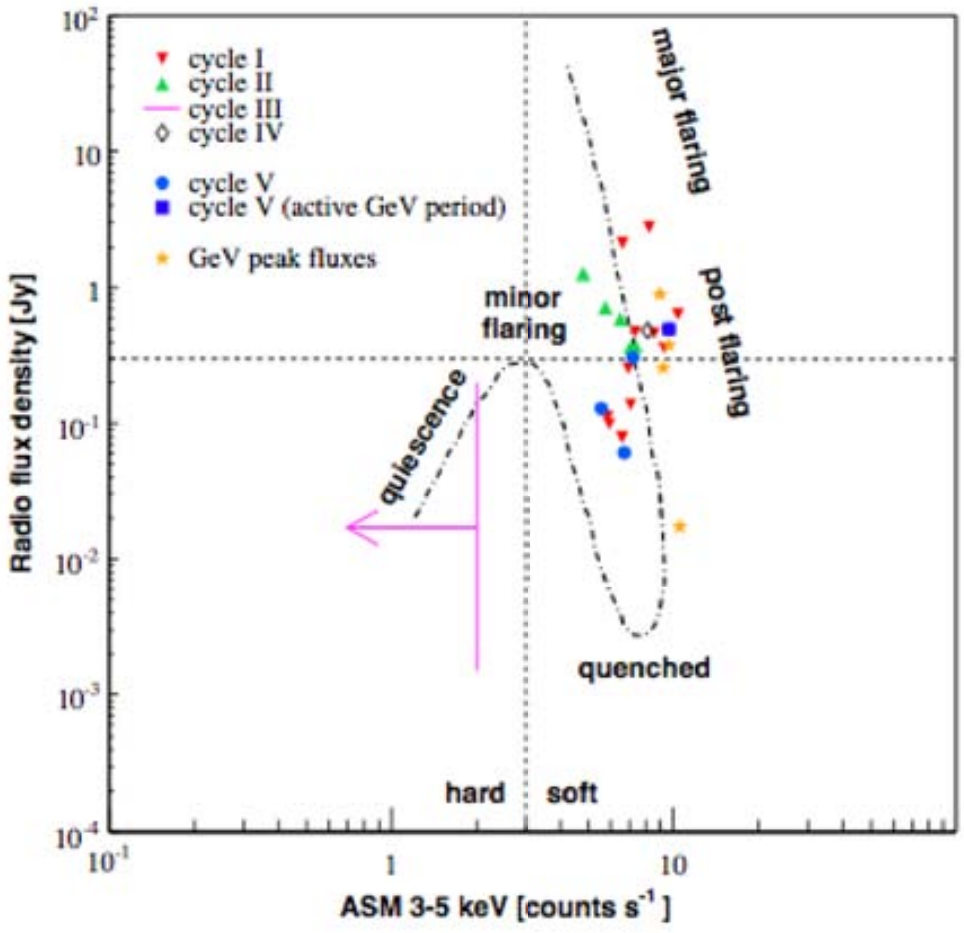

Figure 7.11: Soft X-ray counts versus radio fluxes simultaneous with the GeV peak fluxes (yellow stars) and MAGIC observations, where the different marker colors identify the five MAGIC observational cycles. The pink arrow shows the X-ray flux level during cycle III MAGIC campaign, for which radio data are not available. Radio measurements are at 11.2 GHz from RATAN-600 and at 15 GHz from RT/AMI. The dot-dashed line shows the expected “saxophone" shape (adapted from Szostek, A. et al. (2008)).

Figure 7.11 shows the soft X-ray [3–5 keV] *RXTE*/ASM count rates versus radio flux densities corresponding either to the nights of MAGIC observations for the five observational cycles, or to the *AGILE* flux peaks (only the last four *AGILE* detections were considered, since no simultaneous radio data were available for the first one). Unfortunately, no radio data simultaneous with cycle III and cycle IV MAGIC observations were available. Nevertheless, in case of cycle III data, this does not prevent us from pointing out that Cygnus X-3 was in a quiescent state, just by using the soft X-ray measurements. For cycle IV data, quasi simultaneous radio observations (one day before MAGIC observations) were used. This latter choice does not affect our qualitative result, since the source had already entered a post-flaring state. As shown in Figure 7.12, in April 2008, *AGILE* detected Cygnus X-3 (MJD 54572–54573) one day before a major radio flare (Trushkin, S. A. et al., 2008) lasting a few days, but MAGIC started pointing at the MQ ten days after the peak radio emission.

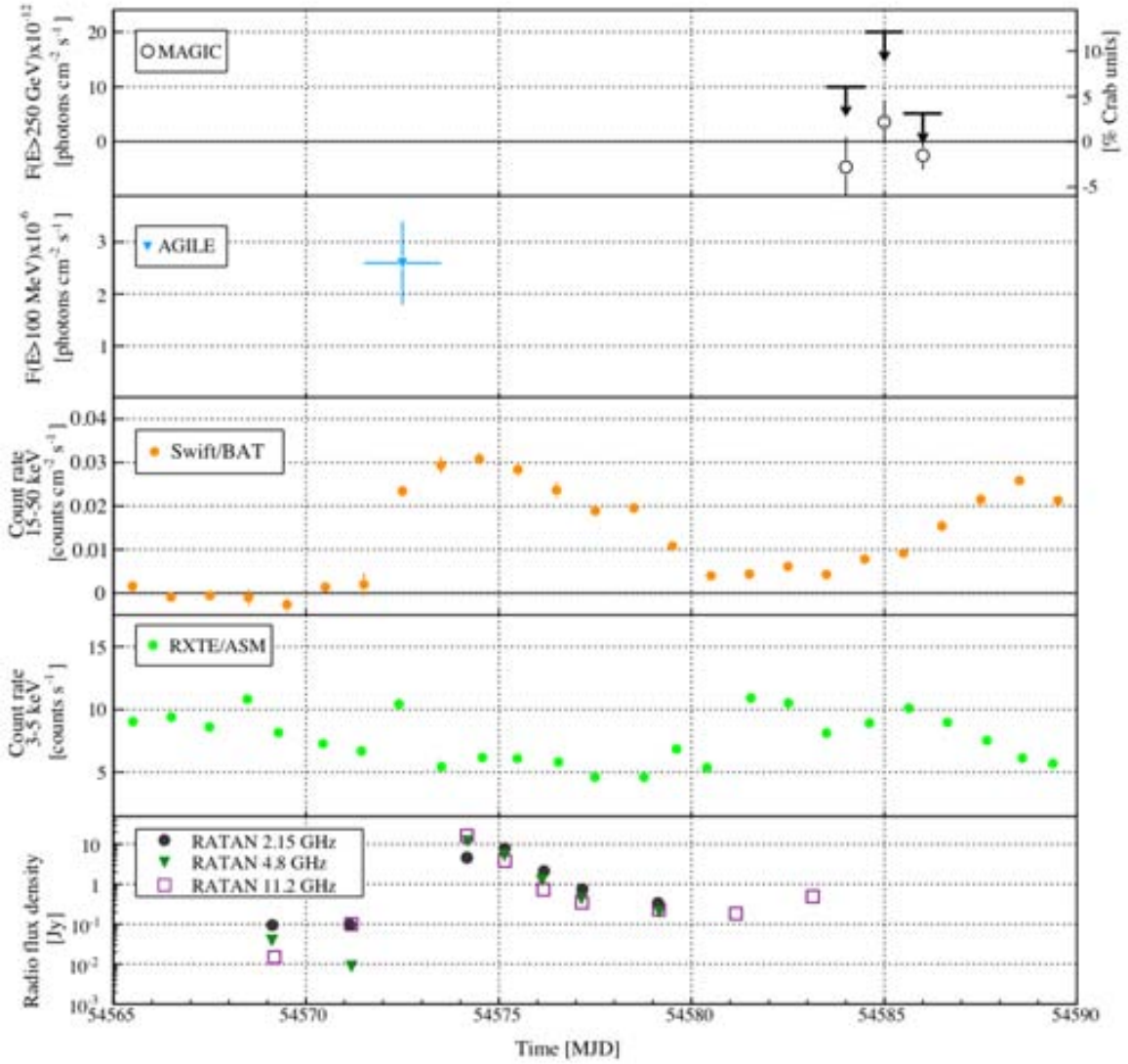

Figure 7.12: Zoom of Figure 7.5 around cycle IV campaign between April 9 and May 2, 2008. The open black points in the VHE MAGIC panel show the non-significant measured integral fluxes with their statistical error bars (whereas the upper limits take into account also the systematic errors).

All the HE flux peaks were detected in the right branch of the *saxophone*, before, after or during a flaring state. Although Abdo, A. A., et al. (2009b) quoted a time lag between the radio and the γ-ray peaks of 5±7 days, the correlation between the two energy bands is not yet clear. On the other hand, MAGIC observed Cygnus X-3 in its *soft state* some days after the radio flare occurred, although for the first nights of cycle V observations, the radio flux densities are rather high and oscillating between two small flares (Figure 7.7).

7.3 Discussion

MAGIC observations of Cygnus X-3 cover all X-ray spectral states of the source in which VHE emission is thought to be likely produced, either from a persistent jet in the *hard state*, or during powerful ejections in the *soft state*. However, no significant excess events were found in any of the inspected samples.

VHE γ-rays have been predicted from microquasar jets (Atoyan, A. M. & Aharonian, F. A., 1999; Romero, G. E. et al., 2003; Bosch-Ramon, V. et al., 2006). A robust prediction of modeling is that photon-photon absorption cannot be neglected if the γ-rays are produced close to a massive star (Bednarek, W., 1997; Orellana, M. et al., 2007). In particular for Cygnus X-3, the presence of a Wolf-Rayet companion, with temperature $T_* \approx 10^5$ K and radius $R_* \approx 10^{11}$ cm, leads to an optical depth $\theta \geq 1$ for VHE γ-rays for an emitter located at several orbital radii from the star (Bednarek, W., 2010). Even under very efficient electromagnetic cascading, i.e. a radiation to magnetic energy density ratio $8\,\nu\,u_*\ B^2 - 1$, the expected VHE fluxes are below the sensitivity of the present instruments (Bednarek, W., 2010). Therefore, in order to detect VHE photons the emitter should be located far from the binary system.

Fermi/LAT detected Cygnus X-3 when it was in the *soft state*, and found orbital modulation for the radiation above 100 MeV with a photon index 2.7 for the periods of enhanced-activity (Abdo, A. A., et al., 2009b). For the epochs outside these high-activity periods, the GeV flux decreases significantly (Figure 7.5 in Abdo, A. A., et al. (2009b)) and no modulation is found. The GeV orbital light curve of Cygnus X-3 in the HE active periods can be explained in the context of anisotropic IC scattering with the stellar photons (Abdo, A. A., et al., 2009b; Bosch-Ramon & Khangulyan, 2009; Dubus et al., 2010), which is also energetically more efficient than hadronic mechanisms such as *pp* interactions or photomeson production. Since very bright X-ray emission is produced in the inner accretion disk or at the base of the jets in Cygnus X-3, the GeV radiation would be absorbed unless it is originated beyond $\equiv 10^{10}$ cm above the compact object. This implies that the GeV radiation is produced in the jet of Cygnus X-3 rather than in the inner accretion disk/corona region. On the other hand, the GeV emitter cannot be too high in the jet, since otherwise there would not be strong orbital modulation (Abdo, A. A., et al., 2009b). Therefore, the observed GeV and the predicted detectable VHE emission cannot be explained by one particular population because the former should be produced in/close to the system and the latter farther from it. The location of a hypothetical VHE emitter could coincide with the innermost region of the radio emitting jet, which, to avoid synchrotron self-absorption, should start relatively far from the binary system. This is consistent with the fact that MAGIC did not detect Cygnus X-3 during the high-activity GeV period, even though the flux upper limits are close to a power-law extrapolation of the *Fermi*/LAT spectrum to energies greater than 100 GeV and well below an extrapolation of the *AGILE* spectrum.

During the periods of GeV high-activity of the source, as by the synchrotron self Compton scenario (Atoyan, A. M. & Aharonian, F. A., 1999), a detectable TeV signal could arise during the first hours of a radio outburst. Unfortunately, MAGIC has never observed the source

during this phase of the flare, but always some days before or after the maximum radio flux. This radiation would not be strongly modulated, due to its origin far from the system. The two times more sensitive MAGIC stereoscopic arrangement may indeed detect Cygnus X-3 if it observes the source for longer time at the very maximum of a GeV flare, which might be even earlier than the onset of the radio outburst (Abdo, A. A., et al., 2009b).

In the *hard state*, the VHE emission is expected to be produced inside the compact and persistent jets, whose total luminosity is estimated to be at least 10^{37} erg s^{-1} (Martí, J. et al., 2005). The MAGIC VHE γ-ray upper limit set at 1.1×10^{-12} erg cm^{-2} s^{-1} is equivalent to a VHE luminosity of 7×10^{33} erg s^{-1} at 7 kpc. Thus, the maximum conversion efficiency of the jet power into VHE γ-rays is 0.07% which is similar to that of Cygnus X-1 for the UL on the VHE steady emission, but one order of magnitude greater than that of GRS 1915+105 (Albert, J., et al., 2007d; Acero, F., et al., 2009b). These ULs are in good agreement with the theoretical expectations which generally predict a VHE steady luminosity of 10^{32} erg s^{-1}. Persistent galactic jets do not seem to be good candidate sources to be detected at VHEs by the current sensitivity instrumentation. Only ten times more sensitive future instruments, such as CTA, may have a chance to detect such VHE emission. This would provide a new handle on the emission mechanisms of compact jets.

8
Scorpius X-1

Scorpius X-1 is a Z-type LMXB which has been classified as microquasar because of the detected discrete radio emission far away from the core source. Its X-ray emission shows a power-law component of non-thermal origin which is more significant when the source is in the X-ray horizontal branch state. These observational results suggest that this NS LMXB might be a VHE γ-ray emitter especially in the horizontal branch state. The MAGIC telescope pointed at Scorpius X-1 in May 2010 in a multi-wavelength campaign which included *RXTE* /PCA observations. The X-ray data were needed to define the X-ray spectral state during the MAGIC observations. MAGIC found no significant VHE signal from Scorpius X-1 and the resulting upper limits to the integral flux above 300 GeV are at the level of 3% of the Crab Nebula flux.

The results of this chapter are published in Aleksić, J., et al. (2011a) where the author contributed in the analysis and interpretation of the MAGIC data.

Scorpius X-1 is a Z-type LMXB (§ 6.5) that contains a low-magnetic-field NS and a M-type star with a mass of 0.4 $M_\odot$ (Steeghs & Casares, 2002). The matter accretion occurs through Roche lobe outflow. Located at a distance of 2.8 ± 0.3 kpc (Bradshaw, C. F. et al., 1999), it has a circular orbit (radius = 1 5×10^{11} cm) with an inclination of 44° ± 6° (Fomalont, E. B. et al., 2001). The orbital period is of 0.787 days (Gottlieb, E. W. et al., 1975).

Scorpius X-1 is the brightest and persistent X-ray source in the sky with an X-ray luminosity $L_X = 4 - 12 \times 10^{37}$ erg s^{-1} (Hasinger, G. & van der Klis, M., 1989). It displays the typical X-ray spectral states of the Z-type sources (§ 6.5) whose definition is based on the source position in double-banana track of the CD (Figure 8.1). Scorpius X-1 covers the whole track of the CD in few hours, but spends most of its time in the HB state. The hard X-ray emission (above 30 keV) from Scorpius X-1 is dominated by a power-law component with a photon index between 2 and 3.4 (Di Salvo, T., et al., 2006; D'Aí, A., et al., 2007). This hard X-ray flux decreases as the source moves toward higher accretion rate (stronger in the HB state) becoming not significantly detectable in the FB state (inset Figure 8.1). The fact that no evidence of high-energy cut-off is observed in this power-law component up to 100–200 keV

suggests a non-thermal origin of this emission.

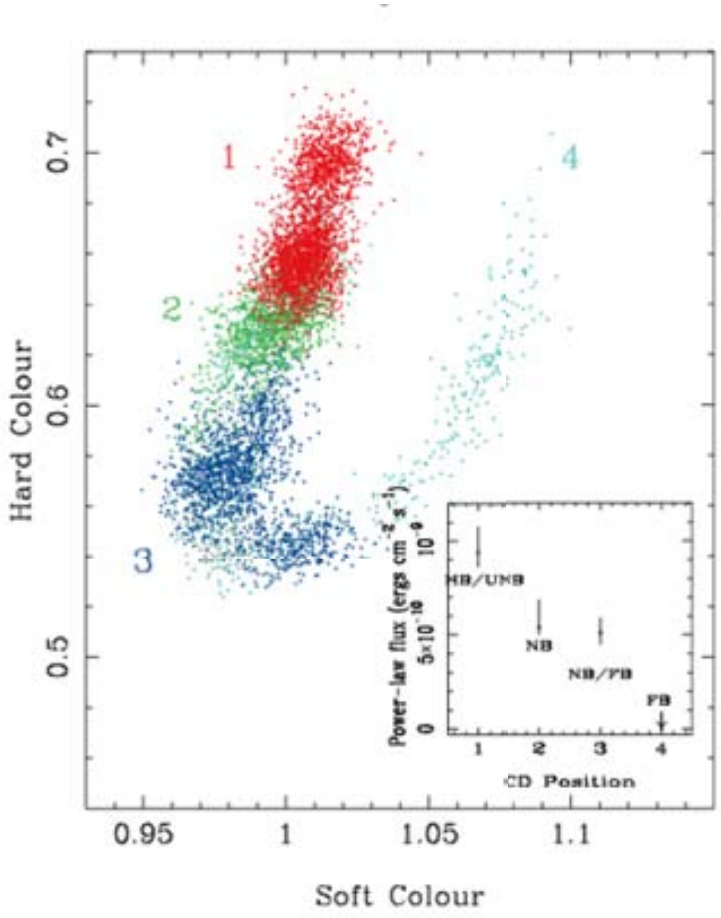

Figure 8.1: CD of Scorpius X-1 obtained from *RXTE* /PCA data (Di Salvo, T., et al., 2006). The "soft color" is defined as the ratio of the count rate in the energy band [3.5–6 keV]/[2–3.5 keV] and the "hard color" as [9.7–16 keV]/[6–9.7 keV]. *Inset:* measured power-law flux in the 20-200 keV range for each X-ray spectral state.

Scorpius X-1 is also the brightest radio source among the NS XRBs with a mean radio flux 10 times higher than that of other Z-type sources (Fender, R. P. & Hendry, M. A., 2000). The radio emission shows variability in morphology and intensity on timescales of hours. In addition discrete components, called radio lobes, are formed in pair near the central source and then move at $\sim 0.5c$ in opposite directions (Fomalont, E. B. et al., 2001). The time-life of the lobe-pairs is almost two days and these pairs are formed near the central source within one day. Flaring episodes related to the lobes appear to be correlated to the central source flares.

This synchrotron discrete and flaring radio emission, together with the significant non-thermal component observed in the hard X-ray during the HB state are clear indications of the presence in the system of relativistic particles up to high energies. This suggests that the IC scattering (likely SSC) might produce VHE emission when the source is in the HB and powerful jets are present.
These experimental considerations were borne out by the work Bednarek, W. & Pabich, J.

(2010) where the authors propose Scorpius X-1 as good target for TeV observations. Given the compactness of the system (the outer radius of its accretion disk is comparable to separation between the NS and the companion star, as stated in Vrtilek, S. D., et al. 1991) the idea of the low-mass star heated by the X-ray source can work well in this source.

Scorpius X-1 was claimed to be a source of TeV/PeV γ-rays in the past (Brazier, K. T., et al., 1990; Tonwar, S. C., et al.., 1991), but the low significance of the results and the lack of later confirmation shed doubt on these results. However, the class of LMXBs has not been intensively monitored by the current generation of Cherenkov telescopes. The only available results concern the microquasar GRS 1915+105 and no significant VHE was found (Acero, F., et al., 2009b; Saito, T. Y., et al., 2009).

8.1 MAGIC observations

In May 2010, the MAGIC collaboration carried out a simultaneous observation campaign with the MAGIC telescopes and the X-ray observatory *RXTE*. In particular the X-ray data were taken with PCA instrument, which is sensitive in the range 2–60 keV. These data are used to produce the CD of the source and consequently select its X-ray spectral states during the MAGIC observations.

MAGIC pointed toward Scorpius X-1 between May 15 and 20, 2010 for a total amount of 7.75 hrs during six consecutive nights. Data were taken in *wobble* mode (§ 2.3.3) and at relatively high zenith angles, between 43° and 50°. Table 8.1 shows the detailed observation log.

Date		**Obs. time**	**ZA**	**Orbital**	**X-ray spectral**
[MJD]	[yyyy/mm/dd]	[hrs]	[°]	**phase**	**state**
55331.09	2010/05/15	1.28	43–48	0.26–0.38	NB/FB
55332.11	2010/05/16	0.48	44–47	0.58–0.64	HB
55333.07	2010/05/17	1.65	44–48	0.77–0.86	NB/FB
55334.06	2010/05/18	1.37	44–49	0.03–0.12	HB
55335.05	2010/05/19	1.73	44–50	0.25–0.39	HB
55336.06	2010/05/20	1.24	44–47	0.52–0.66	NB

Table 8.1: Log of the MAGIC observation of Scorpius X-1. From left to right: the date, the effective observation time, the zenith angle, the orbital phase and the corresponding X-ray spectral state.

These are stereo data which were analyzed by using the standard tools described in Chapter 3. In particular, the data were processed in the following way:

- standard calibration (§ 3.3)
- standard timing image cleaning algorithm (§ 3.4)
- the data quality checked and "bad" data rejection based on the criteria in § 3.6
- a minimum *size* cut at 100 ph.e.
- the energy threshold (§ 3.11.1) of this high-zenith-angle analysis is larger than 250 GeV (Figure 5.8). To be conservative the search for VHE was performed above 300 GeV.

- the gamma selection cuts were optimized on a data sample of Crab Nebula recorded in the same zenith angle range using the criteria described in § 3.9

- the computation of the ULs to the integral flux at 95% CL was performed by using Rolke's method including a 30% systematic uncertainty (§ 3.15). The source spectrum was assumed to be a power-law with a photon index $\Gamma = 3$. This photon index was taken to account for the possibility that the spectrum of Scorpius X-1 is steeper than the Crab Nebula one, as it would be for some plausible scenarios (§ 8.4). However, a 30% change in the photon index yields a variation of less than 1% in the flux ULs at these energies.

The sensitivity (§ 3.9.1) of this high zenith angle analysis is 1.1% of the Crab Nebula flux for energies above 300 GeV in 50 hrs.

8.2 X-ray results

The CD of Scorpius X-1 during the MAGIC observations was obtained by using the definitions of the hard and soft colors in D'Aí, A., et al. (2007). In this way the selection of the different X-ray spectral states can be supported by these historical results. In particular, the "soft color" is defined as the ratio between the count rate in the energy bands [4.08–6.18 keV]/[1.94–4.05 keV], whereas the "hard color" as [8.32–16.26 keV]/[6.18–8.32 keV]. The obtained result is shown in Figure 8.2 (Aleksić, J., et al., 2011a). During the six nights of observations the source covered the full double-banana-shaped track. The top part of the upper-banana was selected as corresponding to the HB (gray box in Figure 8.2). The different symbols and colors of the figure indicate the different observation days. This day-folded analysis shows that the source did not move extensively along the CD track during the single observation nights.

8.3 MAGIC results

The results of the X-ray data show that during three of the six observation nights the source was in the HB state (MJD 55332, 55334, 55335), as indicated also in Table 8.1. Therefore, the source was in the HB during almost half of time (3.58 hrs) that MAGIC pointed at it.

The total Li & Ma significance (Li & Ma, formula 7) of the γ-ray signal coming from Scorpius X-1 for the complete data set of MAGIC observations is 0.52η. The resulting flux UL (§ 3.15) is $2\,4 \times 10^{-12}$ cm^{-2} s^{-1} above 300 GeV. The search for a VHE signal for those periods when the source was in HB state, where such an emission should be expected. No significant signal was found either in this sub-sample. The integral flux UL is $3\,4 \times 10^{-12}$ cm^{-2} s^{-1} above 300 GeV. No γ-ray emission was found either in the complementary sub-sample when the source was in the NB/FB states. A summary of the X-ray-state-selected results is presented in Table 8.2. The differential flux ULs computed for the HB and the whole data sample are shown in Figure 8.3, as a constraint for future theoretical modeling of VHE emission from Scorpius X-1. Differential flux UL can be used to derive also energy flux ULs. Taking $\Gamma = 3$, the energy flux ULs are 3.6, 5.5, and 5.4 $\times 10^{-12}$ erg cm^{-2} s^{-1} above 300 GeV for the whole data set, the HB and the NB/FB respectively.

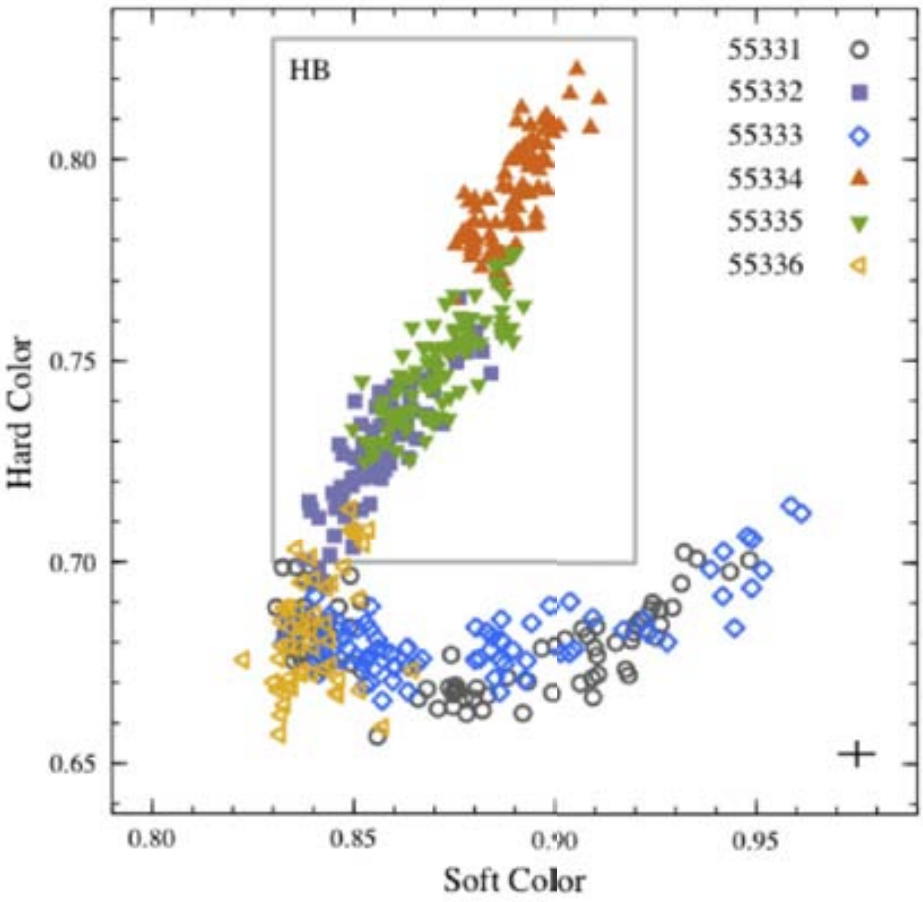

Figure 8.2: CD of Scorpius X-1 during the MAGIC observations. See the text for the definition of the soft and hard colors. The black cross on the bottom-right corner shows the typical relative errors of each measurement ($\sim 0.5\%$). The HB section is identified by the gray box. The different symbols and colors indicate each of the different observation day, labeled in MJD. Taken from Aleksić, J., et al. (2011a).

Additionally, a night-by-night analysis was performed. In none of the six observation nights a significant signal was found. The resulting integral flux ULs are listed in Table 8.3.

X-ray state	**Obs. time**	**Significance**	**UL(E > 300 GeV)**	
	[hr]	[σ]	[cm^{-2} s^{-1}]	[Crab units]
All	7.75	0.52	2.4×10^{-12}	1.9%
HB	3.58	0.72	3.4×10^{-12}	2.7%
NB/FB	4.17	0.08	2.8×10^{-12}	2.3%

Table 8.2: Integral flux upper limits above 300 GeV for selected X-ray spectral states at 95% CL. From left to right, the X-ray spectral state, the effective observation time and the ULs to the integral flux in physical units and in Crab Nebula units (percentage of the Crab Nebula flux).

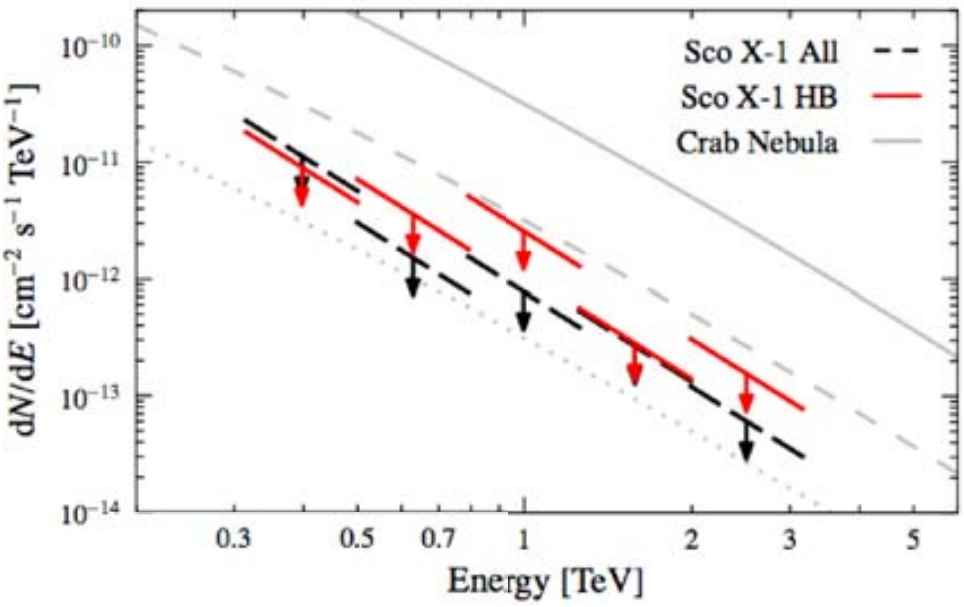

Figure 8.3: Differential flux upper limits above 300 GeV for all the observations (black-dashed) and for the HB state (red). The slope of the bars indicates the power-law photon index assumed in the UL calculation. The Crab Nebula spectrum (Albert, J., et al., 2008d) is shown for comparison, as well as its 10% (dashed) and 1% (dotted) fractions.

Date	**Obs. Time**	**UL(E > 300 GeV)**	
[MJD]	[hrs]	[cm^{-2} s^{-1}]	[Crab units]
55331.09	1.28	7.9×10^{-12}	6.4%
55332.11	0.48	5.2×10^{-12}	4.2%
55333.07	1.65	3.5×10^{-12}	2.8%
55334.06	1.37	5.1×10^{-12}	4.2%
55335.05	1.73	5.3×10^{-12}	4.3%
55336.06	1.24	2.0×10^{-12}	1.6%

Table 8.3: Integral flux upper limits above 300 GeV for day-by-day analysis at 95% CL. From left to right: the date, the corresponding effective observation time, and the ULs to the integral flux in physical and Crab units.

8.4 Discussion

To put in the context the MAGIC results and understand the potentialities of Scorpius X-1 to produce VHE emission, in this section possible emission scenarios are presented. The energy available from the relativistic jet and the processes that could give rise to the VHE emission either as its base or further away from the compact object. Finally, Scorpius X-1 will be compared with other MQs and the detected γ-ray binaries.

The properties of a possible γ-ray emitter will be mostly constrained by the jet power, which dictates the maximum energy budget available, and the emitter size and location. The jet luminosity L_j can be fixed by assuming that the power-law hard X-rays come from the

jet, and assuming an X-ray luminosity to total jet power ratio of 0.01–0.1. Given that the power-law luminosity is $L_{ntX} \equiv 10^{35} - 10^{36}$ erg s^{-1}, a value of $L_j \equiv 10^{39}$ erg s^{-1} seems reasonable, and is also high enough to account for the radio emission of the source (Fomalont, E. B. et al., 2001). The VHE luminosity ULs in the HB show that Scorpius X-1 has a maximum VHE luminosity to jet power ratio of $L_{VHE}\ L_j \leq 10^{-3}$. This value is slightly below the ratio inferred for the Cygnus X-1 flare (Albert, J., et al., 2007d), and similar to the UL of Cygnus X-3 (Aleksić, J., et al., 2010a), but an order of magnitude above the UL of GRS 1915+105 (Acero, F., et al., 2009b). However, given the transient nature of these sources, the orbital coverage and the total length of the observational campaign play a role in their eventual detection. Since the campaign presented here is relatively short and does not provide a complete orbital coverage, it does not rule out the possibility of VHE flares from Scorpius X-1.

Assuming that the jets of Scorpius X-1 can indeed accelerate particles efficiently, there are several possible reasons to explain MAGIC non-detection:

- **If particles were accelerated in the jet base and the power-law hard X-rays were emitted there**, it might be difficult to accelerate particles beyond 100 MeV at this location because of strong radiative cooling. The emitted spectrum is likely to be very soft because of the dominant synchrotron cooling. In addition, the radiation from 10 GeV to 1 TeV would likely to be absorbed through pair creation by the intense radiation field from the accretion disk. At this location even lower energy GeV photons would be absorbed. However, if the magnetic field is low enough and the electromagnetic cascading efficient, absorption at the jet base due to the disk photon field might not be so relevant (Aharonian, F. A. & Vardanian, V. V., 1985). Another source of absorption is the stellar photon field, enhanced through accretion X-ray irradiance of the stellar surface, and could be optically thick to VHE photons in certain orbital phases. Note, however, that MAGIC did not detect the source even for those orbital phases in which this source of γ-ray absorption should be negligible: on MJD 55334 the source was in the HB and the orbital phase range of the observation was σ= 0.03–0.12, for which the expected γ-ray opacity is $\theta \equiv 0.1$ (Bednarek, W. & Pabich, J., 2010). Concluding this scenario, the combined effect of a steep γ-ray spectrum and pair creation absorption would diminish the chances of a VHE detection, particularly for high zenith angle observations and correspondingly high energy threshold as in this study.

- **If the radiation at VHE were produced further from the compact object, at distances larger than 10^8 cm,** it could be eventually detected. The SSC channel, efficient for intermediate values of the magnetic field, would yield a less steep spectrum and may occur in regions where the emitter and the environment are optically thin to VHE photons. IC with the X-ray enhanced stellar photon field could also yield significant and less-steep VHE radiation and would be most efficient for optical depths of order to units. According to the calculations of Bednarek, W. & Pabich, J. (2010), this would take place around orbital phases close to 0.3 and 0.7, but we did not detected such an emission on MJD 55335 at orbital phases 0.25–0.39. At these high altitudes in the jet, GeV photons could easily escape the system and produce detectable high-energy γ-ray emission. The eventual detection of Scorpius X-1 by *Fermi* or *AGILE* , plus a non-detection with low-enough ULs at VHE, would likely favor the scenario where γ-ray radiation is emitted from a location far away from the NS but with a spectrum too steep for a VHE detection. Synchrotron cooling dominance could explain the steep spectrum

and would mean that the power-law hard X-rays have a synchrotron origin.

In a leptonic scenario, such as the SSC and external IC, it can be assumed that X-ray emission has a synchrotron origin and VHE γ-rays have an IC origin. The VHE to non-thermal X-ray luminosity ratio is then a sensitive indicator of the importance of synchrotron cooling and ultimately of the magnetic field of the emitter. Considering only the hard X-ray power-law as non-thermal X-ray emission, this ratio has a maximum value $L_{VHE}\ L_{ntX} \leqq 0\ 02$ for the HB state. This ratio is much higher for the detected gamma-ray binary. For the case of LS I $61°+303$, for example, the VHE to X-ray ratio is between 0.5 and 1 during the X-ray and VHE peak at phases $\sigma = 0\ 6 - 0\ 7$ (Anderhub, H., et al., 2009). However, as mentioned above for the comparison with other MQs, the short total length of the observational campaign presented here prevents us from making absolute comparisons because of the possible transient nature of the source. On the other hand, if there is no such flaring behavior, the difference in the VHE to X-ray luminosity ratios indicates that the underlying physics is significantly different than for LS I $61° + 303$ or LS 5039.

In conclusion, these results place the first ULs on the VHE γ-ray emission from Scorpius X-1 in all of the X-ray spectral states of the source. If Scorpius X-1 is indeed capable of producing TeV emission, either a longer observational campaign, with better coverage (to probe phase-dependent effects such as absorption, cascading..), or an instrument with a significant increase in sensitivity, such as the future CTA, might be required to detect it. These ULs also indicate that the underlying VHE emission physics may be inherently different in the case of Scorpius X-1 and the detected gamma-ray binaries.

9

Conclusions and outlook

The work described in this thesis embraces multiple facets of the VHE γ-ray astrophysics, from the technical aspects of instrument commissioning to the details of data taking and analysis, and the interpretation of physics results.

The author was strongly involved in the commissioning of the second MAGIC telescope as responsible of the central control, and contributed significantly to develop the software for stereo data analysis. With the stereoscopic mode, in operation since 2009, the performance of the instrument improved significantly both in sensitivity (0.8% of the Crab Nebula flux in 50 hours of observation above 250 GeV) and angular resolution (0.06° above 250 GeV). This upgrade constituted a milestone for the MAGIC experiment, and the successful implementation of the central control for the two telescopes was of crucial importance.

From the point of view of the data analysis, this thesis reports on the observations of three galactic sources, the Crab Pulsar Wind Nebula, and two microquasar candidates, Cygnus X-3 and Scorpius X-1. The results of the Crab Nebula observations are based on a total of 50 hours of data collected between October 2009 and March 2011 and take full advantage of the improved sensitivity and the lower energy threshold of the stereoscopic mode. The obtained differential energy spectrum is of unprecedented precision, spans eight orders of magnitude in flux and three orders of magnitude in energy, between 50 GeV and 45 TeV. It represents an extremely accurate measurement, with six spectral points per energy decades and statistical errors as low as 5% below 100 GeV. The spectral data are well described by a variable power-law f_0 (E/1 TeV)$^{\alpha+bLog(E\ 1TeV)}$ with $\alpha = 2\ 40 \pm 0\ 01_{stat} \pm 0\ 1_{sys}$, $b = -0\ 15 \pm 0\ 01_{stat} \pm 0\ 05_{syst}$ and $f_0 = 3\ 27 \pm 0\ 03_{stat} \pm 0\ 48_{syst}$. With this model, the analysis provides the most precise estimation of the peak of the IC component of the Crab Nebula spectrum set at 59 $\pm$ 6 GeV. The differential energy spectrum has been interpreted in the context of both the constant B-field and the MHD model, but none of two models provides a satisfactory match to the data within the statistical errors. Finally, the Crab Nebula flux above 300 GeV calculated on a daily basis across the full data set is found to be constant within the 13% systematic uncertainty. In particular, no enhancement of the flux is observed in correspondence with the September 2010 flare reported by *AGILE* and *Fermi* at energies above 100 MeV. This result does not confirm the claim of a flaring evidence above few TeV by ARGO-YBJ.

In the case of the microquasar candidates to VHE emission, the observations of Scorpius X-

1 are entirely carried out in stereo mode, while the analysis of Cygnus X-3 employs only mono data. Results from the two sources provide the most constraining ULs to date to their integral flux above 250/300 GeV, at the level of 1–3% of the Crab Nebula flux (95% CL). In particular, for Cygnus X-3, the combination of all data samples yields a 95% CL upper limit to the integral flux of 2.2×10^{-12} photons cm^{-2} s^{-1} for energies greater than 250 GeV, corresponding to 1.3% of the Crab Nebula flux at these energies. A γ-ray signal from this source is also searched for on a daily basis and no significant excess events are found in any observation night. Data are then grouped according to the source X-ray spectral state which is related to the corresponding VHE emission model. When the source is an X-ray *soft state* (flaring branch), it is characterized by strong relativistic ejections which might be the source of particle acceleration. On the other hand, the X-ray *hard state* (normal branch) shows persistent relativistic jets which are good candidates for the production of VHE radiation. The upper limits resulting from this study are the first of their kind. For the X-ray *soft state*, an UL of 4.1×10^{-12} photons cm^{-2} s^{-1} is set at 95% CL for energies greater than 250 GeV, corresponding to $\equiv$ 2.5% of the Crab Nebula flux. The upper limit for the hard state at the same energy range is 1.8×10^{-12} photons cm^{-2} s^{-1}, i.e. 1.1% of the Crab Nebula flux. Finally, in July 2009, MAGIC recorded for the first time some data simultaneously with a GeV flare reported by both *AGILE* and *Fermi*. No VHE signal was detected, with corresponding integral flux ULs above 250 GeV lower than 6% of the Crab Nebula flux. In the case of Scorpius X-1, the upper limit on the total flux UL (§ 3.15) is $2\,4 \times 10^{-12}$ cm^{-2} s^{-1} above 300 GeV. Results are also extracted according to their state, with no emission detected in either the HB state or the complementary NB/FB states. In particular for the HB state, where a VHE signal is expected, the upper limit on the integral flux is $3\,4 \times 10^{-12}$ cm^{-2} s^{-1} above 300 GeV. These results place the first ULs on the VHE γ-ray emission from Scorpius X-1 in all of the X-ray spectral states of the source.

The study of the Crab Nebula , as well as the hunt for microquasar TeV emission, will certainly profit form a longer observation campaign with the stereo MAGIC system, especially in the case of Cygnus X-3 whose available data are taken with only one telescope. Furthermore, the advent of CTA will represent a new major step in understanding the mechanisms behind the VHE emission of PWNe and, hopefully, establish microquasars as a new population of VHE emitters.

A

Acceleration mechanisms and photon-matter interactions

This appendix describes the principal mechanisms of CR acceleration and the main processes for the production and absorption of γ-rays.

A.1 Acceleration mechanisms

Acceleration of charged particles can be a direct effect of very large magnetic and electric fields, but it can also occur via statistical diffuse shock acceleration mechanisms. The latter theory was formulated by Enrico Fermi who gave the name to the two main mechanisms. The interested reader can find a copious literature on this topic (Malkov, M. A. & O'C Drury, L., 2001; Kirk, J. G. & Duffy, P., 1999; Aharonian, F. A., 2004b).

A.1.1 Fermi acceleration

The diffuse shock acceleration, also known as Fermi acceleration, can differentiate within *first order* and *second order* depending on the characteristics of the moving plasma.

- The **second order Fermi mechanism** describes the acceleration of a charged particle interacting with a moving, magnetized cloud of material. The mean energy gain of the particle per interaction is $\Delta E \; E \quad \beta^2$, with $\beta = v_{cloud} \; c$. Thus, for typical values of $\beta = 10^{-5}$, the energy gain is $10^{-10} E_1$ per crossing, with E_1 as the energy of the charged particle before being accelerated. The acceleration efficiency is therefore quite low. The resulting energy spectrum is strongly dependent on magnetic cloud properties and is quite unpredictable, which is in contrast with the observed featureless power-law spectrum of the CRs.

- The **first order Fermi mechanism** occurs when the moving material hosts shock waves. A shock identifies a blob of material moving with a velocity which is higher than the speed of the sound in the medium. Every time a particle passes through a shock wave, it is accelerated and its acceleration is proportional to β: $\Delta E \; E \quad \beta \quad V \; c$ where V is the relative velocity between the particle and the cloud. The greater the

relative difference, the larger the energy gain of the particle per shock; the larger the magnetic field strength, the higher the particle crossing frequency.
The *first order* Fermi acceleration is more efficient than the *second order* one and it is believed to be the most diffuse mechanism of acceleration at the TeV, PeV scales.

A.2 Interaction with photon elds

During their travel, CRs and γ-rays interact with dense low-energy photon fields, which are present in many astrophysical environments.

A.2.1 Inverse Compton radiation

IC scattering happens whenever a HE electron interacts with low-energy photons and the photon acquires a large amount of the electron momentum and is re-emitted at much higher energies. This process is one of the main responsible for the acceleration of soft ambient photons to VHE.

The IC scattering process happens in two distinct regimes, defined by the parameter $b = 4Eh\psi_0 \ (m_e c^2)^2$, where E is the electron energy and $h\psi_0$ is the energy of the initial photon.

- in the **Thompson regime**, corresponding to $b \in 1$, the cross-section of the IC scattering is constant. In case of power-law distributed electrons with a photon index Γ_e, the spectra of the up-scattered photons are described by a hard power-law with photon index $\Gamma_\gamma = (\Gamma_e + 1) \ 2$. The efficiency of the IC scattering in the Thompson regime is proportional to the energy density of the target photons.

- in the **Klein-Nishina regime** ($b - 1$) the cross-section decreases with energy ($\ln b \ b$). In case the electrons have a power-law distribution, the up-scattered photons present steep power-law spectra with photon index $\Gamma_\gamma = (\Gamma_e + 1)$. The efficiency of the IC scattering process in the Klein-Nishina regime is proportional to the number density of target photons. This implies that low-frequencies photons can contribute significantly to the production of VHE γ-rays.

A.2.2 Pair production

Pair production is the mechanism which leads to the production of an electron/positron pair through the annihilation of a high-energy photon with a low-energy photon.
The pair production can be divided into two families of processes:

- *Classical pair production.* A high-energy γ-ray interacts with the electric field of an atomic nucleus and produces the pair. The second photon is a virtual photon of the electric field.

$$\gamma(\gamma) \quad e^+ + e^- \tag{A.1}$$

- *Photon-photon pair production.* In this case the soft photons are available in the environment, as stellar of inter-stellar radiation:

$$\gamma\gamma \quad e^+ + e^- \tag{A.2}$$

The reaction is allowed provided there is enough energy to create the pair, at least the total rest-mass-energy of the two particles. The cross-section for this process peaks when:

$$E_{\gamma_1} E_{\gamma_2} (1 - \cos\theta) \equiv 2(m_e c^2)^2 \tag{A.3}$$

where θ is the collision angle. Thus, for photons of energy near 100 MeV, the highest cross-section occurs for the head-on collision with X-ray photons of $\equiv 5$ keV.

The former process prevents high-energy γ-rays to cross the Earth atmosphere, whereas the second one is responsible for the absorption of γ-rays during their travel through ISM and IGM.

A.3 Interaction in matter

While propagating, CRs interact with ambient gas or dust. These interactions produce γ-rays.

A.3.1 Bremsstrahlung

Bremsstrahlung is a process involving charge particles, mainly electrons, when crossing a medium. They can be accelerated by the electric field produced by nuclei of heavy atoms, hence produce radiation. The energy loss as function of the path length follows the Bethe & Heither formula:

$$\left(\frac{\mathrm{d}E}{\mathrm{d}x}\right)_{rad} = -\frac{E}{X_0} \tag{A.4}$$

$$\frac{1}{X_0} \qquad \frac{Z^2}{A}\alpha\,\mathrm{cm}^{-1} \tag{A.5}$$

where X_0 is the radiation length which corresponds to the path length that gives an energy fraction loss of $1/e$. It depends on the material atomic number, Z, and its density, α. Therefore, low density materials have a larger radiation length, hence CRs are more penetrating.

Bremsstrahlung becomes dominant with respect to ionization when the energy of the incoming particle is larger than a *critical energy*, E_0. The *critical energy* identifies the energy at which the energy loss by ionization equals the energy loss for Bremsstrahlung. It depends mainly on the atomic number of the medium:

$$E_c \qquad \frac{1600 \cdot m_e c^2}{Z} \tag{A.6}$$

Since the energy loss through Bremsstrahlung is proportional to the particle energy, the emitted photons follow the same spectral distribution of the ch-raged particles. All charged particles can emit Bremsstrahlung radiation, but electrons by far the most efficient ones. In fact, the total radiate powers goes as m^{-4}.

A.3.2 π_0 decay

Relativistic protons and nuclei interact with ambient gas through inelastic collisions. The interactions with larger cross-section are those ones which involve the production of pions,

such as:

$$pp \qquad pp\nu^{+}\nu^{-}\nu^{0} \tag{A.7}$$

Positive, negative and neutral charged pions are produced with equal probability. The decay of charged pions is accompanied by the production of neutrinos ψ_e ψ_μ:

$$\nu^{+} \qquad \tau^{+}\psi_\mu; \quad \tau^{+} \qquad e^{+}\psi_\mu\bar{\psi}_e \tag{A.8}$$

$$\nu^{-} \qquad \tau^{-}\bar{\psi}_\mu; \quad \tau^{-} \qquad e^{-}\psi_e\bar{\psi}_e \tag{A.9}$$

These neutrinos have a spectral shape which resembles the one for accelerated particles.

Neutral pions annihilate into two energetic photons ($\nu^0 \qquad \gamma\gamma$). The energy of the emitted photons by a ν_0 at rest is half of the ν_0 mass: $E_\gamma = m_0c^2 \ \ 2 \equiv 67\ 5$ MeV. If the ν_0 is moving with a velocity $v = \beta c$, the energy of the photon in the laboratory frame is:

$$E_\gamma = \gamma \cdot m_\pi(1 + \beta\cos\theta_\gamma) \equiv \gamma \cdot m_\pi \tag{A.10}$$

where θ_γ is the angle between the photon direction with respect to the pion one. The spectrum of such emission is well-fitted by a power-law with a photon index of sim 2.5.

γ-ray produced by pions are the so-called γ-rays of hadronic origin. They are distinguishable from those of electromagnetic origin because of their spectral features, lack of correlation with other wavelengths (like X-rays in the SSC scenario), and presence of molecular clouds. In addition, their emission coexists with a neutrino flux coming from the charged pion decays.

A.3.3 Electron-positron annihilation

High-energy electrons interact with positrons and annihilate into two energetic photons:

$$e^{+}e^{-} \qquad \gamma\gamma \tag{A.11}$$

Seed positrons are found as secondary products of spallation of CRs with matter. Conversely, positrons can interact with cold thermal electrons in ambient gas or plasma. The γ-ray spectrum is steeper than the positron spectrum: $\Gamma_\gamma = \Gamma_p - 1$, at least if the electrons are not too much relativistic.

A.4 Interaction with magnetic elds

A.4.1 Synchrotron radiation

Charged particles in magnetic fields emit radiation. In the classical approximation, due to the effect of the Lorentz force, the charged particle spirals around the magnetic field lines with a frequency $w_L = qB \ \ 2m$, called Larmor frequency, where m and q are the mass and the charge of the particle, and B the magnetic field component perpendicular to the plane of the particles' trajectory. The radiation has the shape of a dipole radiation with frequency w_L.

In case of relativistic charged particles, the emitted radiation is beamed in a cone centered on the particle and with an angular spread inversely proportional to velocity. In addition, it is a broad-band emission.
The spectrum of synchrotron radiation of mono-energetic electrons is a continuum that peaks

at:

$$E_\gamma \quad 1\ 5 \cdot 10^{-5} \cdot \left(\frac{B}{\mathrm{G}}\right)\left(\frac{E_e}{\mathrm{TeV}}\right)^2 \tag{A.12}$$

where E_e is the energy of the electron population.

The lifetime of a relativistic electron with respect to the synchrotron energy losses, *i.e.* the synchrotron cooling time is:

$$\theta_{synch} \approx 1\ 2 \times 10^3 \left(\frac{B}{10^{-4}\mathrm{G}}\right)^{-2} \times \left(\frac{E_e}{\mathrm{TeV}}\right)^{-1} \mathrm{yr} \tag{A.13}$$

The characteristic frequency of synchrotron radiation is about $\psi_{synch} \equiv \psi_B \times \gamma^2$ where $\psi_B = w_L \sin \quad 2\nu$ is the cyclotron frequency of a electron moving at a pitch angle to the magnetic field. For isotropic pitching angles:

$$\psi_{synch} \approx 1\ 8 \times 10^{15} \left(\frac{B}{3 \times 10^{-4}\mathrm{G}}\right)\left(\frac{E_e}{\mathrm{TeV}}\right)^2 \mathrm{Hz} \tag{A.14}$$

B

Astrophysical detectors

This appendix provides a list of the principal detectors which were developed for astrophysical studies in the last decades. In particular, the chapter is divided into air shower particle detectors, mainly focus on the observation of charged CRs, atmospheric Cherenkov telescopes which study the VHE γ-ray sky, and, finally neutrino telescopes.

B.1 Air shower arrays

- **AGASA** is an air shower particle array placed near Tokyo, Japan at 900 m asl. Its construction started in 1990 and it stopped its operations in 2004. It was instrumented with 110 5-cm-thick scintillators, on a grid with 1 km spacing, covering an area of of $\equiv 100$ km^2 (Chiba, N., et al., 1992). It provided the first results on the CR spectrum after the *knee* (§ 1.1).

- **ARGO-YBJ** is an air shower particle array built in Tibet at 4300 m asl covering an area of 10000 m^2. The detector is divided in 154 clusters, each made by 12 resistive plate chambers. The meadian energy it is sensitive to is 2 TeV (Aielli, G., et al., 2007).

- **CELESTE** is an air Cherenkov array which used the de-commissioned THEMIS electric solar plant in French Pyrenees (Paré, E., et al., 2002). It consists of a large mirror surface area (2000 m^2) from 40 independent heliostats.

- **EAS-TOP** is an air shower particle array located at Campo Imperatore, near the Gran Sasso Laboratory, Italy, at 2000 m asl. It was equipped with 35 scintillators and muon-hadron calorimeters (Aglietta, M., et al., 1986). The energy range it was sensitive to is $10^{13} - 10^{16}$ eV. In addition it was equipped with 8 IACTs (Aglietta, M., et al., 1992).

- **HiRES** is an array of air fluorescence detectors located in the West Desert of Utah, USA. It observes CRs above 10^{19} eV. The detector comprises 67 modules, each containing a spherical mirror of 1.6 m diameter wit 12–14 PMTs mounted at the focal surface (Cassiday, L. G., et al., 1990). It was operative between 1981 and 1993.

- **KASCADE** is an array of detectors containing a iron-sampling calorimeter and multiwire-proportional-chambers. It is located in Karlsruhe, Germany. Its extension called KASCADE-Grande covers an area of 0.5 km^2 with 253 detectors spaced by 13 m each (Antoni, T., et al., 2003).

- **Milagro** is a large pool (like a football field) of water covered with a light-tight barrier and it is instrumented with 723 PMTs (Figure **??**) (McEnery, J. E., et al., 2001). It is located in Los Alamos National Laboratory, New Mexico (USA).

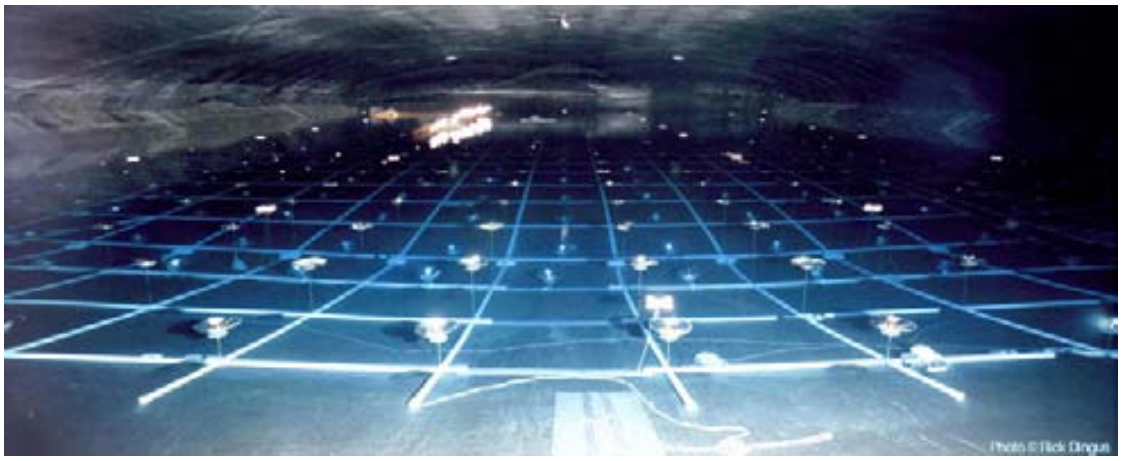

Figure B.1: Photo of the Milagro experiment

- **Pierre Auger Observatory** is a huge array of water Cherenkov detectors built in two different sites. The southern site is located in the state of Mendoza, Argentina (Figure B.2) and the Northern is under construction in Colorado. This instrument is designed to study CRs above 10^{19} eV. It has two independent detector systems: the surface detector, consisting of 1600 Cherenkov water tanks spaced by 1.5 km and covering an area of 3000 km^2 (Abraham, J., et al., 2004) and the fluorescence detector (Abraham, J., et al., 2010).

- **THEMISTOCLE** is an air array of Cherenkov counters. It was the first to apply the air Cherenkov technique using a relatively large amount of mirrors (Baillon, P., et al., 1993b). It was operating in the 90s.

- **Tibet ASγ** is an air shower particle detector located in Tibet, China at 4300 m asl. It consist of 697 scintillation counters which are placed at a lattice with 7.5 m spacing, plus 36 more scintillation counters in a larger spacing (15 m) lattice. each counter has a plate of plastic scintillator, 0.5 m^2 and 3 cm thickness equipped with a PMT (Amenomori, M., et al., 1991). It has a median energy at $\equiv$ 10 TeV.

- **TUNKA** is an air Cherenkov array located in Siberia (50 km from Lake Baikal) which cover an area of 1 km^2. It consists of 133 PMTs grouped in 19 clusters. In a cluster one detector is located in the center, and six at a distance of 85m from the center in the vertexes of a regular hexagon. Such an array allows the investigation of CRs in the energy range $10^{15} - 10^{18}$ eV (Antokhonov, B. V., et al., 2011).

Figure B.2: Map of the Pierre Auger Southern Observatory, in the state of Mendoza, Argentina.

B.2 Imaging Atmospheric Cherenkov telescopes

- **CANGAROO**: an array of four 10 m telescopes. The full operation started in 2004. It is located in Woomera, Australia.

- **CAT**: an single IACT, located at the site of the former solar plant THEMIS, started its operation in 1996. It was equipped with a 546 PMTs camera.

- **HEGRA**: an array of 5 Cherenkov telescopes, each having a 8.5 m^2 mirror surface and a camera with 271 PMTs. It was located in the Canary island of La Palma, where nowadays is the MAGIC site. It stopped its operation in 2003.

- **HESS**: an array of four identical telescopes of 13 m diameter. Right now the commissioning of another larger telescope is ongoing. It will the largest IACT with a reflector surface of 23 m diameter. It is located in Namibia.

- **MAGIC**: an array of two IACTs with a parabolic reflector of 17 m diameter. Detailed explanation in Chapter 2.

- **VERITAS**: an array of four 12 m diameter Cherenkov telescopes, located in Tucson, Arizona (US).

B.3 Neutrino telescopes

- **Antarctic Muon And Neutrino Detector Array (AMANDA)**: an array of 677 PMTs in 19 strings located under the ice in the South Pole. Its construction started in 1996 and ends in 2000. It effective area of 20000 m^2 was one order of magnitude below the size suggested by the theoretical models. It looks for high-energy neutrino from the Northern sky.
- **Astronomy with a Neutrino Telescope and Abyss environmental RESarch (ANTARES)**: located in the Mediterranean sea close to Toulouse, France, it consists of 12 strings, with 75 PMTs each, anchored at the sea bed at 2.5 km. The full detector is in operation since 2007. It observes the Southern sky.
- **IceCube**: 1 km^3 array of ice Cherenkov detectors built as extension of the AMANDA detector in the South Pole. Its construction was completed at the beginning of 2011. It consists of 4800 PMTs arranged in 80 strings.
- **IceTop**: 1 km array of ice Cherenkov detectors at the surface.
- **NEutrino Mediterranean Observatory (NEMO)**: located in the Mediterranean sea at 3.3 km depth near the East coast of Sicily. It consists of a mechanical structure, consisting of 20 m long rigid arms connected by each other by ropes. Inside the arms the PMTs are set. It observes the Southern sky.
- **Neutrino Extended Submarine Telescope with Oceanographic Research (NESTOR)**: located near the West Coast of the Peloponnese at 4 km depth. Its design is based on rigid hexagonal structures with 32 m diameter, each of them carrying 6 pairs of PMTs. These rigid structures are the basic blocks of the "towers" of 300 m height. It observes the Southern sky.
- **Neutrino Telescope-200 (NT-200)**: the pioneering neutrino detector built in the Lake Baikal, Russia in 1993. It consists of $\equiv$ 200 PMTs at 8 strings. It was expanded in 2005, nut now it is dismissed.

Bibliography

Abbasi, R. U., et al. (2008). First observation of the Greisen-Zatsepin-Kuzmin suppression. *Physical Review Letters*, *100*(10), 101101–101105.

Abbasi, R. U., et al. (2010). Measurement of the anisotropy of cosmic-ray arrival directions with IceCube. *Astrophys. Journal Letters*, *718*, L194–198.

Abdo, A. A., et al. (2007). TeV gamma-ray sources from a survey of the galactic plane with MILAGRO. *Astrophys. Journal Letters*, *664*, L91–94.

Abdo, A. A., et al. (2009a). A population of γ-ray millisecond pulsars seen with the *Fermi* Large Area Telescope. *Science*, *325*, 848–852.

Abdo, A. A., et al. (2009b). Modulated high-energy γ-ray emission from the microquasar Cygnus X-3. *Science*, *326*, 1512–1516.

Abdo, A. A., et al. (2010a). *Fermi* Large Area Telescope observations of the Crab Pulsar and Nebula. *Astrophys. Journal*, *708*, 1254–1267.

Abdo, A. A., et al. (2010b). The First Fermi Large Area Telescope catalog of gamma-ray pulsars. *Boh*, *187*, 460–494.

Abdo, A. A., et al. (2011). γ-ray flares from the Crab Nebula. *Science*, *331*, 739–742.

Abraham, J., et al. (2004). Properties and performance of the prototype instrument for the Pierre Auger Observatory. *Nuclear Instruments and Methods in Physics Research A*, *523*, 50–95.

Abraham, J., et al. (2008). Observation of the suppression of the flux of cosmic rays above 4×10^{19}eV. *Physical Review Letters*, *101*(6), 061101–061105.

Abraham, J., et al. (2010). The fluorescence detector of the Pierre Auger Observatory. *Nuclear Instruments and Methods in Physics Research A*, *620*, 227–251.

Acciari, V. A., et al. (2009). A connection between star formation activity and cosmic rays in the starburst galaxy M82. *Nature*, *462*, 770–772.

Acero, F., et al. (2009a). Detection of gamma rays from a starburst galaxy. *Science*, *326*, 1080–1082.

Acero, F., et al. (2009b). HESS upper limits on very high energy γ-ray emission from the microquasar GRS 1915+105. *Astronomy & Astrophysics*, *508*, 1135–1140.

Aglietta, M., et al. (1986). High-energy cosmic-ray physics with an EAS array on the top of the Gran Sasso Laboratory. *Nuovo Cimento C Geophysics Space Physics C*, *9*, 262–270.

Aglietta, M., et al. (1992). Imaging of atmospheric EAS Cherenkov light at EAS-TOP. *Nuovo Cimento C Geophysics Space Physics C*, *15*, 357–363.

Aharonian, F. A. (2004a). *Very high energy cosmic gamma radiation*. World Scientific Printers.

Aharonian, F. A. (2004b). *Very high energy cosmic gamma radiation : a crucial window on the extreme Universe*.

Aharonian, F. A., Buckley, J., Kifune, T., & Sinnis, G. (2008). High energy astrophysics with ground-based gamma ray detectors. *Reports on Progress in Physics*, *71*(9), 56pp.

Aharonian, F. A., & Vardanian, V. V. (1985). On the origin of soft gamma-rays from Cygnus X-1. *Astrophysics and space science*, *115*, 31–37.

Aharonian, F. A., et al. (2000). The energy spectrum of TeV γ-rays from the Crab Nebula as measured by the HEGRA system of Imaging Air Cerenkov Telescopes. *Astrophys. Journal*, *539*, 317–324.

Aharonian, F. A., et al. (2001). Evidence for TeV gamma ray emission from Cassiopeia A. *Astronomy & Astrophysics*, *370*, 112–120.

Aharonian, F. A., et al. (2004). The Crab Nebula and pulsar between 500 GeV and 80 TeV: observations with the HEGRA stereoscopic air Cerenkov telescopes. *Astrophys. Journal*, *614*, 897–913.

Aharonian, F. A., et al. (2005a). Discovery of the binary pulsar PSR B1259-63 in very-high-energy gamma rays around periastron with HESS. *Astronomy & Astrophysics*, *442*, 1–10.

Aharonian, F. A., et al. (2005b). Discovery of very high energy γ-rays associated with an X-ray binary. *Science*, *309*, 746–749.

Aharonian, F. A., et al. (2006a). Discovery of very-high-energy γ-rays from the Galactic Centre ridge. *Nature*, *439*, 695–698.

Aharonian, F. A., et al. (2006b). Observations of the Crab Nebula with HESS. *Astronomy & Astrophysics*, *457*, 899–915.

Aharonian, F. A., et al. (2006c). A detailed spectral and morphological study of the gamma-ray supernova remnant RX J1713.7-3946 with HESS. *Astronomy & Astrophysics*, *449*, 223–242.

Aharonian, F. A., et al. (2006d). First detection of a VHE gamma-ray spectral maximum from a cosmic source: HESS discovery of the Vela X nebula. *Astronomy & Astrophysics*, *448*, L43–47.

Ahlers, M., Ringwald, A., & Tu, H. (2005). Strongly interacting neutrinos as the highest energy cosmic rays: a quantitative analysis. *ArXiv Astrophysics e-prints*.

Aielli, G., et al. (2007). The status of the ARGO experiment at YBJ. *Nuclear Physics B Proceedings Supplements*, *166*, 96–102.

Akerlof, C., et al. (1989). Detection of very high energy gamma-rays from the Crab nebula. *Proceedings of the at the Gamma Ray Observatory Science Workshop*, (pp. 10–12).

Albert, J., et al. (2006a). Observation of gamma rays from the Galactic Center with the MAGIC Telescope. *Astrophys. Journal Letters*, *638*, L101–104.

Albert, J., et al. (2006b). Variable very-high-energy γ-ray emission from the microquasar LS I $61^\circ + 303$. *Science*, *312*, 1771–1773.

Albert, J., et al. (2007a). Discovery of very high energy gamma radiation from IC 443 with the MAGIC telescope. *Astrophys. Journal Letters*, *664*, L87–90.

Albert, J., et al. (2007b). Observation of VHE γ-rays from Cassiopeia A with the MAGIC telescope. *Astronomy & Astrophysics*, *474*, 937–940.

Albert, J., et al. (2007c). Unfolding of differential energy spectra in the MAGIC experiment. *Nuclear Instruments and Methods in Physics Research A*, *583*, 494–506.

Albert, J., et al. (2007d). Very high energy γ-ray radiation from the stellar mass black hole binary Cygnus X-1. *Astrophys. Journal Letters*, *665*, L51–54.

Albert, J., et al. (2008a). MAGIC observations of the unidentified γ-ray source TeV J2032+4130. *Astrophys. Journal Letters*, *675*, L25–28.

Albert, J., et al. (2008b). FADC signal reconstruction for the MAGIC telescope. *Nuclear Instruments and Methods in Physics Research A*, *594*, 407–419.

Albert, J., et al. (2008c). Implementation of the Random Forest method for the imaging atmospheric Cherenkov telescope MAGIC. *Nuclear Instruments and Methods in Physics Research A*, *588*, 424–432.

Albert, J., et al. (2008d). VHE γ-ray observation of the Crab Nebula and its pulsar with the MAGIC Telescope. *Astrophys. Journal*, *674*, 1037–1055.

Albert, J., et al. (2008e). Very-high-energy γ-rays from a distant quasar: how transparent is the universe? *Science*, *320*, 1752–.

Aleksić, J. (2009). Characterization of the MAGIC II data acquisition read-out system. *Master Thesis at Institut de Fisica d Altes Energies. Available at http://wwwmagic.mppmu.mpg.de/pubblications/theses/index.html*.

Aleksić, J., et al. (2010a). MAGIC constraints on γ-ray emission from Cygnus X-3. *Astrophys. Journal*, *721*, 843–855.

Aleksić, J., et al. (2010b). Search for an extended VHE γ-ray emission from Mrk 421 and Mrk 501 with the MAGIC Telescope. *Astronomy & Astrophysics*, *524*, A77(9pp).

Aleksić, J., et al. (2011a). A search for very high energy γ-ray emission from Scorpius X-1 with the MAGIC Telescopes. *Astrophys. Journal Letters*, *735*, L5–11.

Aleksić J., et al. (2011b). Performance of the MAGIC stereo system obtained with the Crab Nebula data. *submitted to Asptroparticle Physics*.

Aliu, E., et al. (2008). Observation of pulsed γ-rays above 25 GeV from the Crab pulsar with MAGIC. *Science*, *322*, 1221–1224.

Aliu, E., et al. (2009). Improving the performance of the single-dish Cherenkov telescope MAGIC through the use of signal timing. *Astroparticle Physics*, *30*, 293–305.

Amenomori, M., et al. (1991). Status and performance of the AS array of the Tibet AS experiment. In J. Matthews (Ed.) *High Energy Gamma Ray Astronomy*, vol. 220 of *American Institute of Physics Conference Series*, (pp. 257–264).

Anderhub, H., et al. (2009). Correlated X-ray and very high energy emission in the γ-ray binary LS I $61^\circ + 303$. *Astrophys. Journal Letters*, *706*, L27–32.

Antokhonov, B. V., et al. (2011). The new Tunka-133 EAS Cherenkov array: status of 2009. *Nuclear Instruments and Methods in Physics Research A*, *628*, 124–127.

Antoni, T., et al. (2003). The cosmic-ray experiment KASCADE. *Nuclear Instruments and Methods in Physics Research A*, *513*, 490–510.

Antoni, T., et al. (2005). KASCADE measurements of energy spectra for elemental groups of cosmic rays: Results and open problems. *Astroparticle Physics*, *24*, 1–25.

Anykeyev, V. B., Spiridonov, A. A., & Zhigunov, V. P. (1991). Comparative investigation of unfolding methods. *Nuclear Instruments and Methods in Physics Research A*, *303*, 350–369.

Araudo, A. T., Bosch-Ramon, V., & Romero, G. E. (2009). High-energy emission from jet-clump interactions in microquasars. *Astronomy & Astrophysics*, *503*, 673–681.

Arons, J. (1979). Some problems of pulsar physics. *Space Science Review*, *24*, 437–510.

Arons, J. (1983). Pair creation above pulsar polar caps - Geometrical structure and energetics of slot gaps. *Astrophys. Journal*, *266*, 215–241.

Arons, J., & Scharlemann, E. T. (1979). Pair formation above pulsar polar caps - Structure of the low altitude acceleration zone. *Astrophys. Journal*, *231*, 854–879.

Aschenbach, B., & Brinkmann, W. (1975). A model of the X-ray structure of the Crab Nebula. *Astronomy & Astrophysics*, *41*, 147–151.

Atoyan, A. M. (1999). Radio spectrum of the Crab Nebula as an evidence for fast initial spin of its pulsar. *Astronomy & Astrophysics*, *346*, L49–52.

Atoyan, A. M., & Aharonian, F. A. (1996). On the mechanisms of gamma radiation in the Crab Nebula. *Monthly Notices of the Royal Astronomical Society*, *278*, 525–541.

Atoyan, A. M., & Aharonian, F. A. (1999). Modelling of the non-thermal flares in the Galactic microquasar GRS 1915+105. *Monthly Notices of the Royal Astronomical Society*, *302*, 253–276.

Atwood, W. B., et al. (2009). The Large Area Telescope on the Fermi gamma-ray space telescope mission. *Astrophys. Journal*, *697*, 1071–1102.

Baade, W., & Zwicky, F. (1934). Cosmic rays from super-novae. *Proceedings of the National Academy of Science*, *20*, 259–263.

Baillon, P., et al. (1993a). Energy spectrum of the Crab Nebula in the multi-TeV region. *International Cosmic Ray Conference*, *1*, 271–273.

Baillon, P., et al. (1993b). Status report on THEMISTOCLE experiment. In R. C. Lamb (Ed.) *Towards a Major Atmospheric Cherenkov Detector II for TeV Astro/Particle Physics*, (pp. 121–125).

Barrau, A., et al. (1997). Performances of the CAT imaging telescope and some preliminary results on Mkn 180 and the Crab. *ArXiv Astrophysics e-prints*.

Bauleo, P. M., & Rodríguez Martino, J. (2009). The dawn of the particle astronomy era in ultra-high-energy cosmic rays. *Nature*, *458*, 847–851.

Becker, W., & Truemper, J. (1997). The X-ray luminosity of rotation-powered neutron stars. *Astronomy & Astrophysics*, *326*, 682–691.

Becklin, E. E., et al. (1973). Infrared and X-ray variability of Cygnus X-3. *Nature*, *245*, 302–304.

Bednarek, W. (1997). Cascade initiated by VHE γ-rays in the radiation field of a close massive companion. *Astronomy & Astrophysics*, *322*, 523–532.

Bednarek, W. (2010). On the possibility of sub-TeV-ray emission from Cygnus X-3. *Monthly Notices of the Royal Astronomical Society*, *406*, 689–700.

Bednarek, W., & Bartosik, M. (2003). Gamma-rays from the pulsar wind nebulae. *Astronomy & Astrophysics*, *405*, 689–702.

Bednarek, W., & Pabich, J. (2010). Optical depths for gamma-rays in the radiation field of a star heated by an external X-ray source in LMXBs. Application to Hercules X-1 and Scorpius X-1. *Astronomy & Astrophysics*, *514*, A61–71.

Belloni, T., Klein-Wolt, M., Méndez, M., van der Klis, M., & van Paradijs, J. (2000). A model-independent analysis of the variability of GRS 1915+105. *Astronomy & Astrophysics*, *355*, 271–290.

Berezinsky, V., Kachelrieß, M., & Vilenkin, A. (1997). Ultrahigh energy cosmic rays without Greisen-Zatsepin-Kuzmin cutoff. *Physical Review Letters*, *79*, 4302–4305.

Bernlohr, K. (2000). Impact of atmospheric parameters on the atmospheric Cherenkov technique. *Astroparticle Physics*, *12*, 255–268.

Bertero, M. (1989). Linear inverse and ill-posed problems. *Advances in eectronics and electron physics*, (pp. 1–120).

Bhat, C. L., Sapru, M. L., & Razdan, H. (1986). Estimate from Gulmarg of PeV photon flux from Cygnus X-3 and its relevance. *Astrophys. Journal*, *306*, 587–598.

Bietenholz, M. F., Hester, J. J., Frail, D. A., & Bartel, N. (2004). The Crab Nebula's wisps in radio and optical. *Astrophys. Journal*, *615*, 794–804.

Biland, A., et al. (2008). The active mirror control of the MAGIC telescopes. *Proceedings of the 30th International Cosmic Ray Conference*, *3*, 1353–1356.

Bildsten, L., et al. (1997). Thermonuclear burning on the accreting X-ray pulsar GRO J1744-28. *Astrophys. Journal*, *113*, 367–408.

Bitossi, M. (2009). Ultra-fast sampling and readout for the MAGIC II telescope data acquisition system. *PhD Thesis at the Universita degli Studi di Pisa, Italy. Available at http://wwwmagic.mppmu.mpg.de/pubblications/theses/index.html*.

Blumer, J., Engel, R., & Horandel, J. R. (2009). Cosmic rays from the knee to the highest energies. *Progress in Particle and Nuclear Physics*, *63*, 293–338.

Bock, R. K., et al. (2004). Methods for multidimensional event classification: a case study using images from a Cherenkov gamma-ray telescope. *Nuclear Instruments and Methods in Physics Research A*, *516*, 511–528.

Bogovalov, S. V., & Aharonian, F. A. (2000). Very-high-energy gamma radiation associated with the unshocked wind of the Crab pulsar. *Monthly Notices of the Royal Astronomical Society*, *313*, 504–514.

Bordas, P., Bosch-Ramon, V., Paredes, J. M., & Perucho, M. (2009). Non-thermal emission from microquasar/ISM interaction. *Astronomy & Astrophysics*, *497*, 325–334.

Borione, A., et al. (1997). A search for ultra-high-energy γ-ray emission from the Crab Nebula and Pulsar. *Astrophys. Journal*, *481*, 313–326.

Borla Tridon, D., et al. (2009). Performance of the camera of the MAGIC II telescope. *Proceedings of the 31st International Cosmic Ray Conference*.

Bosch-Ramon, V., & Khangulyan, D. (2009). Understanding the very-high emission from microquasars. *International Journal of Modern Physics D*, *18*, 347–387.

Bosch-Ramon, V., Aharonian, F. A., & Paredes, J. M. (2005). Electromagnetic radiation initiated by hadronic jets from microquasars in the ISM. *Astronomy & Astrophysics*, *432*, 609–618.

Bosch-Ramon, V., & Khangulyan, D. (2009). Understanding the very-high emission from microquasars. *International Journal of Modern Physics D*, *18*, 347–387.

Bosch-Ramon, V., Romero, G. E., & Paredes, J. M. (2006). A broadband leptonic model for γ-ray emitting microquasars. *Astronomy & Astrophysics*, *447*, 263–276.

Bradshaw, C. F., Fomalont, E. B., & Geldzahler, B. J. (1999). High-resolution parallax measurements of Scorpius X-1. *Astrophys. Journal Letters*, *512*, L121–124.

Braes, L. L. E., & Miley, G. K. (1972). Radio detection of Cygnus X-3. *Nature*, *237*, 506.

Brazier, K. T., et al. (1990). Scorpius X-1: a source of 300 GeV γ-rays. *Nuclear Physics B Proceedings Supplements*, *14*, 191–195.

Bretz, T., Dorner, D., Wagner, R. M., & Sawallisch, P. (2009). The drive system of the major atmospheric γ-ray imaging Cherenkov telescope. *Astroparticle Physics*, *31*, 92–101.

Bridle, A. H., & Perley, R. A. (1984). Extragalactic radio jets. *Annual Review of Astronomy and Astrophysics*, *22*, 319–358.

Brinkmann, W., Aschenbach, B., & Langmeier, A. (1985). X-ray morphology of the Crab nebula. *Nature*, *313*, 662–664.

Britzger, D., et al. (2009). Studies of the influence of moonlight on observations with the MAGIC telescope. *Proceedings of the of 29th International Cosmic Ray Conference*.

Bucciantini, N. (2008). Theory of pulsar wind nebulae. *Proceedings of the of the "40 Years of Pulsars: Millisecond Pulsars, Magnetars and More" conference*, *983*, 186–194.

Bucciantini, N., Amato, E., Bandiera, R., Blondin, J. M., & Del Zanna, L. (2004). Magnetic Rayleigh-Taylor instability for pulsar wind nebulae in expanding supernova remnants. *Astronomy & Astrophysics*, *423*, 253–265.

Bucciantini, N., Thompson, T. A., Arons, J., Quataert, E., & Del Zanna, L. (2006). Relativistic magnetohydrodynamics winds from rotating neutron stars. *Monthly Notices of the Royal Astronomical Society*, *368*, 1717–1734.

Bulgarelli, A., et al. (in preparation).

Carmona, E., et al. (2011). Performance of the MAGIC stero system. *Proceedings of the of the 33th International Cosmic Ray Conference*.

Carpano, S., et al. (2007). A 33 hour period for the Wolf-Rayet/black hole X-ray binary candidate NGC 300 X-1. *Astronomy & Astrophysics*, *466*, L17–20.

Cassiday, L. G., et al. (1990). The HIRES fly's eye project. *Proceedings of the of the International Cosmic Ray Conference*, *10*, 244–246.

Cawley, M. F., et al. (1985). Variability in the light curve of very high energy gamma rays from Cygnus X-3. *Astrophys. Journal*, *296*, 185–189.

Chadwick, P. M., Dipper, N. A., Dowthwaite, J. C., Gibson, A. I., & Harrison, A. B. (1985). A 12.6-ms pulsar in Cygnus X-3. *Nature*, *318*, 642–644.

Chandrasekhar, S. (1931). The maximum mass of ideal white dwarfs. *Astrophys. Journal*, *74*, 81–82.

Chardin, G., & Gerbier, G. (1989). Cygnus X-3 at high energies - A critical analysis of observational results. *Astronomy & Astrophysics*, *210*, 52–65.

Cheng, K. S., Ho, C., & Ruderman, M. (1986a). Energetic radiation from rapidly spinning pulsars. I - Outer magnetosphere gaps. II - VELA and Crab. *Astrophys. Journal*, *300*, 500–539.

Cheng, K. S., Ho, C., & Ruderman, M. (1986b). Energetic radiation from rapidly spinning pulsars. II. VELA and Crab. *Astrophys. Journal*, *300*, 522–539.

Chevalier, R.A. (1977). In supernovae. *66*, 202.

Chiba, N., et al. (1992). Akeno Giant Air Shower Array (AGASA) covering 100 km^2 area. *Nuclear Instruments and Methods in Physics Research A*, *311*, 338–349.

Clear, J., et al. (1987). A detailed analysis of the high energy γ-ray emission from the Crab pulsar and nebula. *Astronomy & Astrophysics*, *174*, 85–94.

Cocke, W. J., Disney, M. J., & Taylor, D. J. (1969). Discovery of optical signals from pulsar NP 0532. *Nature*, *221*, 525–527.

Comella, J. M., Craft, H. D., Lovelace, R. V. E., & Sutton, J. M. (1969). Crab Nebula pulsar NP 0532. *Nature*, *221*, 453–454.

Contopoulos, I., Kazanas, D., & Fendt, C. (1999). The axisymmetric pulsar magnetosphere. *Astrophys. Journal*, *511*, 351–358.

Contopoulos, I., & Kazanas, D. (2002). Toward resolving the Crab η-problem: a linear accelerator? *Astrophys. Journal*, *566*, 336–342.

Corbel, S., et al. (2002). Large-scale, decelerating, relativistic X-ray jets from the microquasar XTE J1550-564. *Science*, *298*, 196–199.

Cortina, J., & Zanin, R. (2011). Data operational manual for the magic telescopes. *MAGIC-TDAS. Private use at http://www.magic.mppmu.mpg.de*.

Cortina, J., et al. (2003). Camera and central control of the magic telescope. *Proceedings of the 28th International Cosmic Ray Conference*.

Cortina, J., et al. (2010). The control system of the magic telescopes. *MAGIC-TDAS. Private use at http://www.magic.mppmu.mpg.de*.

CTA Consortium (2010). Design Concepts for the Cherenkov Telescope Array. *ArXiv e-prints*.

D'Aí, A., et al. (2007). Broadband spectral evolution of Scorpius X-1 along its color-color diagram. *Astrophys. Journal*, *667*, 411–426.

Danaher, S., Fegan, D. J., Porter, N. A., & Weekes, T. C. (1981). Gamma-ray observations of Cygnus X-3 at energies of 10 to the 12th eV. *Nature*, *289*, 568–569.

Daugherty, J. K., & Harding, A. K. (1982). Electromagnetic cascades in pulsars. *Astrophys. Journal*, *252*, 337–347.

Davies, J., & Cotton, E. (1957). *Journal Solar Energy Sci. and Eng.*, (pp. 1–16).

de Jager, O. C., & Harding, A. K. (1992). The expected high-energy to ultra-high-energy γ-ray spectrum of the Crab Nebula. *Astrophys. Journal*, *396*, 161–172.

de Jager, O. C., et al. (1996). γ-ray observations of the Crab Nebula: a study of the synchro-Compton spectrum. *Astrophys. Journal*, *457*, 253–266.

Dean, A. J., et al. (2008). Polarized γ-ray emission from the Crab. *Science*, *321*, 1183–1185.

Dhawan, V., Mirabel, I. F., Ribó, M., & Rodrigues, I. (2007). Kinematics of black hole X-ray binary GRS 1915+105. *Astrophys. Journal*, *668*, 430–434.

Di Salvo, T., et al. (2006). A hard X-ray view of Scorpius X-1 with INTEGRAL: nonthermal emission? *Astrophys. Journal Letters*, *649*, L91–94.

Domingo-Santamaria, E., Flix, J., Rico, J., Scalzotto, V., & Wittek, W. (2005). The DISP analysis method for point-like or extended gamma source searches/studies with the MAGIC Telescope. *Proceedings of the 29th International Cosmic Ray Conference*, *5*, 363–+.

Doro, M. (2009). Novel reflective elements and indirect dark matter searches for MAGIC II and future IACTs. *PhD Thesis at Universita degli Studi di Padova, Italy. Available at http://wwwmagic.mppmu.mpg.de/pubblications/theses/index.html*.

Doro, M., et al. (2008). The reflective surface of the MAGIC telescope. *Nuclear Instruments and Methods in Physics Research A*, *595*, 200–203.

Doro, M., et al. (2011). The reflector of the imagining cherenkov telescopes MAGIC I and MAGIC II . *Journal of instrumentation*.

Dowthwaite, J. C., et al. (1983). Ultra high energy gamma rays from Cygnus X3. *Astronomy & Astrophysics*, *126*, 1–6.

Dubus, G., Cerutti, B., & Henri, G. (2010). The relativistic jet of Cygnus X-3 in gamma rays. *Monthly Notices of the Royal Astronomical Society*, *404*, L55–59.

Dubus, G. (2006). Gamma-ray binaries: pulsars in disguise? *Astronomy & Astrophysics*, *456*, 801–817.

Elterman, L. (1964). Parameters for attenuation in the atmospheric windows for fifteen wavelengths. *Applied Optics IP*, *3*, 745.

Errando, M. (2009). Discovery of very high energy gamma-ray emission from 3c 279 and 3c 66 a/b with the magic telescope. *PhD Thesis at Institut de Fisica d Altes Energies, Barcelona, Spain. Available at http://wwwmagic.mppmu.mpg.de/pubblications/theses/index.html*.

Feldman, G. J., & Cousins, R. D. (1998). Unified approach to the classical statistical analysis of small signals. *Phyicasl Review D*, *57*, 3873–3889.

Fender, R. P., Belloni, T. M., & Gallo, E. (2004). Towards a unified model for black hole X-ray binary jets. *Monthly Notices of the Royal Astronomical Society*, *355*, 1105–1118.

Fender, R. P., & Hendry, M. A. (2000). The radio luminosity of persistent X-ray binaries. *Monthly Notices of the Royal Astronomical Society*, *317*, 1–8.

Fender, R. P., et al. (1997). A deep search for radio emission from three X-ray pulsars: are radio emission and X-ray pulsations anti-correlated? In C. Winkler, T. J.-L. Courvoisier, & P. Durouchoux (Ed.) *"The Transparent Universe" conference*, vol. 382 of *ESA Special Publication*, (pp. 303–306).

Fender, R. P., et al. (1999). Quenching of the radio jet during the X-ray high state of GX 339-4. *Astrophys. Journal Letters*, *519*, L165–168.

Fierro, J. M., Michelson, P. F., Nolan, P. L., & Thompson, D. J. (1998). Phase-resolved studies of the high-energy γ-ray emission from the Crab, Geminga, and VELA pulsars. *Astrophys. Journal*, *494*, 734–746.

Fomalont, E. B., Geldzahler, B. J., & Bradshaw, C. F. (2001). Scorpius X-1: the evolution and nature of the twin compact radio lobes. *Astrophys. Journal*, *558*, 283–301.

Fomin, V. P., et al. (1994). New methods of atmospheric Cherenkov imaging for gamma-ray astronomy. I. The false source method. *Astroparticle Physics*, *2*, 137–150.

Frail, D. A., & Scharringhausen, B. R. (1997). A radio survey for pulsar wind nebulae. *Astrophys. Journal*, *480*, 364–370.

Fryer, C. L., et al. (2002). The limiting stellar initial mass for black hole formation in close binary systems. *Astrophys. Journal*, *578*, 335–347.

Gaensler, B. M., & Slane, P. O. (2006). The evolution and structure of pulsar wind nebulae. *Annual Review of Astronomy and Astrophysics*, *44*, 17–47.

Gallo, E., Fender, R. P., & Pooley, G. G. (2003a). A universal radio-X-ray correlation in low/hard state black hole binaries. *Monthly Notices of the Royal Astronomical Society*, *344*, 60–72.

Gallo, E., Fender, R. P., & Pooley, G. G. (2003b). A universal radio-X-ray correlation in low/hard state black hole binaries. *Monthly Notices of the Royal Astronomical Society*, *344*, 60–72.

Gallo, E., et al. (in preparation).

Garczarczyk, M. (2007). First observations of the grb prompt and early afterglow emission phase at ≡ 100 gev energy regime with the 17 m diameter magic telescope. *PhD Thesis at Max-Planck Institute fuer Physik, Muenchen, Germany. Available at http://wwwmagic.mppmu.mpg.de/pubblications/theses/index.html*.

Garczarczyk, M., et al. (2003). The active mirror control of the magic telescope. *Proceedings of the 28th International Cosmic Ray Conference*.

Gaug, M. (2008). Calibration of the magic telescope and observation of gamma-ray bursts. *PhD Thesis at Institut de Fisica d Altes Energies, Barcelona, Spain. Available at http://wwwmagic.mppmu.mpg.de/pubblications/theses/index.html*.

Geldzahler, B. J., et al. (1983). The 1982 September radio outburst of Cygnus X-3 - evidence for jetlike emission expanding at not less than about 0.35 C. *Astrophys. Journal Letters*, *273*, L65–69.

Georganopoulos, M., Aharonian, F. A., & Kirk, J. G. (2002). External Compton emission from relativistic jets in Galactic black hole candidates and ultraluminous X-ray sources. *Astronomy & Astrophysics*, *388*, L25–28.

Ghia, P. L., & Navarra, G. (2005). The experimental data on the high energy Galactic cosmic rays from Eas-Top. *International Journal of Modern Physics A*, *20*, 6817–6820.

Giacconi, R., Gorenstein, P., Gursky, H., & Waters, J. R. (1967). An X-ray survey of the Cygnus region. *Astrophys. Journal Letters*, *148*, L119.

Giacconi, R., Gursky, H., Paolini, F. R., & Rossi, B. B. (1962). Evidence for X-rays from sources outside the solar system. *Physical Review Letters*, *9*, 439–443.

Gini, C. (1921). Measurement of inequality of income. *Economic Journal*, *31*, 22–43.

Goebel, F., et al. (2003). The data acquisition of the MAGIC telescope. *Proceedings of the 28th International Cosmic Ray Conference*.

Goebel, F., et al. (2008). Upgrade of the MAGIC telescope with a multiplexed fiber-optic 2GSamples/s FADC data acquisition system. *Proceedings of the 30th International Cosmic Ray Conference*, *3*, 1481–1484.

Gold, T. (1968). Rotating neutron stars as the origin of the pulsating radio sources. *Nature*, *218*, 731–732.

Goldreich, P., & Julian, W. H. (1969). Pulsar electrodynamics. *Astrophys. Journal*, *157*, 869–880.

Gonzalez-Garcia, M. C., Halzen, F., & Mohapatra, S. (2009). Identifying Galactic PeVatrons with neutrinos. *Astroparticle Physics*, *31*, 437–444.

Gottlieb, E. W., Wright, E. L., & Liller, W. (1975). Optical studies of UHURU sources. XI. A probable period for Scorpius X-1 = V818 Scorpii. *Astrophys. Journal Letters*, *195*, L33–35.

Gould, R. J. (1965). High-energy photons from the Compton-synchrotron process in the Crab Nebula . *Physical Review Letters*, *15*, 577–579.

Gregory, P. C., & Kronberg, P. P. (1972). Discovery of giant radio outburst from Cygnus X-3. *Nature*, *239*, 440–443.

Greisen, K. (1966). End to the cosmic-ray spectrum? *Physical Review Letters*, *16*, 748–750.

Grimm, H.-J., Gilfanov, M., & Sunyaev, R. (2002). The Milky Way in X-rays for an outside observer. Log(N)-Log(S) and luminosity function of X-ray binaries from *RXTE*/ASM data. *Astronomy & Astrophysics*, *391*, 923–944.

Halzen, F. (2010). The search for the sources of the cosmic rays one century after their discovery. *Proceedings of the of the XVI International Symposium on Very High Energy Cosmic Ray Interactions*.

Hanson, M. M., Still, M. D., & Fender, R. P. (2000). Orbital dynamics of Cygnus X-3. *Astrophys. Journal*, *541*, 308–318.

Harding, A., & Muslimov, A. (2005). Pulsar slot gaps and unidentified Egret sources. *Astrophysics and Space Science*, *297*, 63–70.

Harding, A. K., Baring, M. G., & Gonthier, P. L. (1997). Photon-splitting cascades in γ-ray pulsars and the spectrum of PSR 1509-58. *Astrophys. Journal*, *476*, 246–261.

Hasinger, G., & van der Klis, M. (1989). Two patterns of correlated X-ray timing and spectral behaviour in low-mass X-ray binaries. *Astronomy & Astrophysics*, *225*, 79–96.

Heck, D., Knapp, J., Capdevielle, J. N., Schatz, G., & Thouw, T. (1998). *CORSIKA: a Monte Carlo code to simulate extensive air showers.*.

Helene, O. (1983). Upper limit of peak area. *Nuclear Instruments and Methods in Physics Research*, *212*, 319–322.

Hester, J. J. (2008). The Crab Nebula: an astrophysical chimera. *Annual Review of Astronomy and Astrophysics*, *46*, 127–155.

Hester, J. J., et al. (1996). WFPC2 Studies of the Crab Nebula. III. Magnetic Rayleigh-Taylor Instabilities and the Origin of the Filaments. *Astrophys. Journal*, *456*, 225–233.

Hester, J. J., et al. (2002). Hubble space telescope and *Chandra* monitoring of the Crab synchrotron Nebula. *Astrophys. Journal Letters*, *577*, L49–52.

Hewish, A., Bell, S. J., Pilkington, J. D. H., Scott, P. F., & Collins, R. A. (1968). Observation of a rapidly pulsating radio source. *Nature*, *217*, 709–713.

Hillas, A. M. (1985). Cerenkov light images of EAS produced by primary gamma. *International Cosmic Ray Conference*, *3*, 445–448.

Hillas, A. M., et al. (1998). The spectrum of TeV γ-rays from the Crab Nebula. *Astrophys. Journal*, *503*, 744–759.

Hinton, J. A., et al. (2009). HESS J0632+057: a new γ-ray binary? *Astrophys. Journal Letters*, *690*, L101–104.

Hirata, K., Kajita, T., Koshiba, M., Nakahata, M., & Oyama, Y. (1987). Observation of a neutrino burst from the supernova SN1987A. *Physical Review Letters*, *58*, 1490–1493.

Hirotani, K. (2008). High-energy emission from rotation-powered pulsars: outer-gap vs. slot-gap models. *ArXiv e-prints*.

Hirotani, K. (2006). Particle accelerator in pulsar magnetospheres: super-Goldreich-Julian current with ion emission from the neutron star surface. *Astrophys. Journal*, *652*, 1475–1493.

Hjalmarsdotter, L., et al. (2008). The nature of the hard state of Cygnus X-3. *Monthly Notices of the Royal Astronomical Society*, *384*, 278–290.

Hjellming, R. M., et al. (1990). Radio observations of the X-ray binary Cygnus X-2. *Astronomy & Astrophysics*, *235*, 147–155.

Homan, J., et al. (2010). XTE J1701-462 and its implications for the nature of subclasses in low-magnetic-field neutron star low-mass X-ray binaries. *Astrophys. Journal*, *719*, 201–212.

Israelian, G., Rebolo, R., Basri, G., Casares, J., & Martín, E. L. (1999). Evidence of a supernova origin for the black hole in the system GRO J1655 - 40. *Nature*, *401*, 142–144.

Jamil, O., Fender, R. P., & Kaiser, C. R. (2010). Shocks: X-ray binary jets with an internal shocks model. *Monthly Notices of the Royal Astronomical Society*, *401*, 394–404.

Kaiser, C. R., Sunyaev, R., & Spruit, H. C. (2000). Internal shock model for microquasars. *Astronomy & Astrophysics*, *356*, 975–988.

Kalogera, V., & Baym, G. (1996). The maximum mass of a neutron star. *Astrophys. JournalLetter*, *470*, L61+.

Kennel, C. F., & Coroniti, F. V. (1984a). Confinement of the Crab pulsar's wind by its supernova remnant. *Astrophys. Journal*, *283*, 694–709.

Kennel, C. F., & Coroniti, F. V. (1984b). Magnetohydrodynamic model of Crab Nebula radiation. *Astrophys. Journal*, *283*, 710–730.

Khangoulian, D. V., & Bogovalov, S. V. (2003). The role of a magnetic field in the formation of jet-like features in the Crab nebula. *Astronomy Letters*, *29*, 495–501.

Kirk, J. G., & Duffy, P. (1999). Particle acceleration and relativistic shocks. *Journal of Physics G Nuclear Physics*, *25*, 163–206.

Kitaura, F. S., Janka, H.-T., & Hillebrandt, W. (2006). Explosions of O-Ne-Mg cores, the Crab supernova, and subluminous type II-P supernovae. *Astronomy & Astrophysics*, *450*, 345–350.

Kohnle, A., et al. (1996). Stereoscopic imaging of air showers with the first two HEGRA Cherenkov telescopes. *Astroparticle Physics*, *5*, 119–131.

Kranich, D., & Stark, L. S. (2003). An new method to determine the arrival direction of individual air showers with a single air Cherenkov telescope. *Proceedings of the of the 28thInternational Cosmic Ray Conference*, *5*, 3023–+.

Lamb, R. C., Godfrey, C. P., Wheaton, W. A., & Tumer, T. (1982). Cygnus X-3 observed at photon energies above 500 GeV. *Nature*, *296*, 543–544.

Lessard, R. W., Buckley, J. H., Connaughton, V., & Le Bohec, S. (2001). A new analysis method for reconstructing the arrival direction of TeV gamma rays using a single imaging atmospheric Cherenkov telescope. *Astroparticle Physics*, *15*, 1–18.

Levinson, A., & Blandford, R. (1996). On the jets associated with Galactic superluminal sources. *Astrophys. Journal Letters*, *456*, L29–32.

Lewis, D. (1990). Optical characteristics of the whipple observatory tev γ-ray imaging telescope. *Experimental Astronomy*, *1*.

Li, T.P., & Ma, Y.Q. (1983). Analysis methods for results in γ-ray astronomy. *Astrophys. Journal*, *271*.

Ling, Z., Zhang, S. N., & Tang, S. (2009). Determining the distance of Cygnus X-3 with its X-Ray dust scattering halo. *Astrophys. Journal*, *695*, 1111–1120.

Liu, Q. Z., van Paradijs, J., & van den Heuvel, E. P. J. (2006). Catalogue of high-mass X-ray binaries in the Galaxy (4th edition). *Astronomy & Astrophysics*, *455*, 1165–1168.

Liu, Q. Z., van Paradijs, J., & van den Heuvel, E. P. J. (2007). A catalogue of low-mass X-ray binaries in the Galaxy, LMC, and SMC (Fourth edition). *Astronomy & Astrophysics*, *469*, 807–810.

Lorimer, D. R. (2010). Radio pulsar populations. *ArXiv e-prints*.

Lorimer, D. R. (2005). Binary and millisecond pulsars. *Living Reviews in Relativity*, *8*, 7–77.

Lundmark, K. (1921). Suspected new stars recorded in old chronicles and among recent meridian observations. *Publ.Astronom.Soc.Pac.*, *33*, 225–238.

MacFadyen, A. I., & Woosley, S. E. (1999). Collapsars: gamma-ray bursts and explosions in "failed supernovae". *Astrophys. Journal*, *524*, 262–289.

Majumdar, P., Moralejo, A., Bigongiari, C., Blanch, O., & Sobczynska, D. (2005). Monte Carlo simulation for the MAGIC telescope. *Proceedings of the of the 29th International Cosmic Ray Conference*, *5*, 203–+.

Malkov, M. A., & O'C Drury, L. (2001). Nonlinear theory of diffusive acceleration of particles by shock waves. *Reports on Progress in Physics*, *64*, 429–481.

Markoff, S., Falcke, H., & Fender, R. (2001). A jet model for the broadband spectrum of XTE J1118+480. Synchrotron emission from radio to X-rays in the Low/Hard spectral state. *Astronomy & Astrophysics*, *372*, L25–28.

Marscher, A. P., et al. (2002). Observational evidence for the accretion-disk origin for a radio jet in an active galaxy. *Nature*, *417*, 625–627.

Marsden, P. L., et al. (1984). Far-infrared observations of the Crab Nebula. *Astrophys. Journal Letters*, *278*, L29–32.

Martí, J., Paredes, J. M., & Peracaula, M. (2001). Development of a two-sided relativistic jet in Cygnus X-3. *Astronomy & Astrophysics*, *375*, 476–484.

Martí, J., Pérez-Ramírez, D., Garrido, J. L., Luque-Escamilla, P., & Paredes, J. M. (2005). Possible hot spots excited by the relativistic jets of Cygnus X-3. *Astronomy & Astrophysics*, *439*, 279–285.

Massi, M., et al. (2004). Hints for a fast precessing relativistic radio jet in LS I $61° + 303$. *Astronomy & Astrophysics*, *414*, L1–4.

Mazin, D. (2007). A study of very high energy γ-ray emission from AGNs and contraints on the extragalactic background light. *PhD Thesis at the Max-Planck Institute fuer Physik, Muenchen, Germany. Available at http://wwwmagic.mppmu.mpg.de/pubblications/theses/index.html*.

McCollough, M. L., et al. (1999). Discovery of correlated behavior between the hard X-ray and the radio bands in Cygnus X-3. *Astrophys. Journal*, *517*, 951–955.

McEnery, J. E., et al. (2001). The Milagro gamma-ray observatory. In F. A. Aharonian & H. J. Volk (Ed.) *American Institute of Physics Conference Series*, vol. 558 of *American Institute of Physics Conference Series*, (pp. 549–552).

McHardy, I. M., Koerding, E., Knigge, C., Uttley, P., & Fender, R. P. (2006). Active galactic nuclei as scaled-up Galactic black holes. *Nature*, *444*, 730–732.

Meyer, M., Horns, D., & Zechlin, H.-S. (2010). The Crab Nebula as a standard candle in very high-energy astrophysics. *Astronomy & Astrophysics*, *523*, A2.

Michel, F. C. (1982). Theory of pulsar magnetospheres. *Reviews of Modern Physics*, *54*, 1–66.

Migliari, S., & Fender, R. P. (2006). Jets in neutron star X-ray binaries: a comparison with black holes. *Monthly Notices of the Royal Astronomical Society*, *366*, 79–91.

Miller-Jones, J. C. A., et al. (2004). Time-sequenced Multi-Radio Frequency Observations of Cygnus X-3 in Flare. *Astrophys. Journal*, *600*, 368–389.

Mioduszewski, A. J., Rupen, M. P., Hjellming, R. M., Pooley, G. G., & Waltman, E. B. (2001). A one-sided highly relativistic jet from Cygnus X-3. *Astrophys. Journal*, *553*, 766–775.

Mirabel, I. F. (2006). Very energetic gamma-rays from microquasars and binary pulsars. *Science*, *312*, 1759–1760.

Mirabel, I. F., & Rodrigues, I. (2003). Formation of a black hole in the dark. *Science*, *300*, 1119–1121.

Mirabel, I. F., & Rodríguez, L. F. (1994). A superluminal source in the galaxy. *Nature*, *371*, 46–48.

Mirabel, I. F., & Rodríguez, L. F. (1999). Sources of relativistic jets in the Galaxy. *Annual Review of Astronomy and Astrophysics*, *37*, 409–443.

Mirabel, I. F., & Rodríguez, L. F. (2002). Microquasars in the Milky Way. *Sky & Telescope*, *103*(5), 32.

Mirabel, I. F., et al. (1992). A double-sided radio jet from the compact galactic center annihilator 1E1740.7-2942. *Nature*, *204*, 981–982.

Mirabel, I. F., et al. (1998). Accretion instabilities and jet formation in GRS 1915+105. *Astronomy & Astrophysics*, *330*, L9–12.

Mirzoyan, R. (1997). On the calibration accuracy of light sensors in atmospheric Cherenkov fluorescence and neutrino experiments. *Proceedings of the of the 25th International Cosmic Ray Conference*, *7*, 265–+.

Moralejo, A., et al. (2009). MARS, the MAGIC Analysis and Reconstruction Software. *ArXiv e-prints*.

Mori, K., et al. (2004). Spatial variation of the X-ray spectrum of the Crab Nebula. *Astrophys. Journal*, *609*, 186–193.

Mori, M., et al. (1997). Cygnus X-3 and EGRET gamma-ray observations. *Astrophys. Journal*, *476*, 842–846.

Narayan, R., & Yi, I. (1994). Advection-dominated accretion: a self-similar solution. *Astrophys. Journal Letters*, *428*, L13–16.

Neyman, J (1937). *Phil. Trans. Royal Socienty London*, *236*.

Ng, C.-Y., & Romani, R. W. (2006). Proper motion of the Crab Pulsar revisited. *Astrophys. Journal*, *644*, 445–450.

Nolan, P. L., et al. (1993). Observations of the Crab pulsar and nebula by the EGRET telescope on the Compton Gamma-Ray Observatory. *Astrophys. Journal*, *409*, 697–704.

Orellana, M., Bordas, P., Bosch-Ramon, V., Romero, G. E., & Paredes, J. M. (2007). Leptonic secondary emission in a hadronic microquasar model. *Astronomy & Astrophysics*, *476*, 9–15.

Ostriker, J. P., & Gunn, J. E. (1969). On the nature of pulsars. I. Theory. *Astrophys. Journal*, *157*, 1395–1417.

Otte, N. (2011). . *Proceedings of the of the Third Fermi Symposium*.

Paciesas, W. S., et al. (1999). The fourth BATSE gamma-ray burst catalog (Revised). *Astrophys. Journal*, *122*, 465–495.

Pacini, F. (1967). Energy emission from a neutron star. *Nature*, *216*, 567–568.

Pacini, F. (1968). Rotating neutron stars, pulsars and supernova remnants. *Nature*, *219*, 145–146.

Paneque, D., Gebauer, H. J., Lorenz, E., & Mirzoyan, R. (2004). A method to enhance the sensitivity of photomultipliers for Air Cherenkov Telescopes by applying a lacquer that scatters light. *Nuclear Instruments and Methods in Physics Research A*, *518*, 619–621.

Paoletti, R., et al. (2007). The trigger system of the MAGIC Telescope. *IEEE Transactions on Nuclear Science*, *54*, 404–409.

Paré, E., et al. (2002). CELESTE: an atmospheric Cherenkov telescope for high energy gamma astrophysics. *Nuclear Instruments and Methods in Physics Research A*, *490*, 71–89.

Paredes, J. M., Martí, J., Ribó, M., & Massi, M. (2000). Discovery of a high-energy γ-ray-emitting persistent microquasar. *Science*, *288*, 2340–2342.

Parsignault, D. R., et al. (1972). No X-ray flare seen by Uhuru. *Nature*, *239*, 123–126.

Pelling, R. M., et al. (1987). A scanning modulation collimator observation of the high-energy X-ray source in the Crab Nebula. *Astrophys. Journal*, *319*, 416–425.

Pellizzoni, A., et al. (2009). Discovery of new γ-ray pulsars with AGILE. *Astrophys. Journal Letters*, *695*, L115–119.

Perucho, M., & Bosch-Ramon, V. (2008). On the interaction of microquasar jets with stellar winds. *Astronomy & Astrophysics*, *482*, 917–927.

Piron, F., et al. (2003). CELESTE observations of the Crab Nebula and Mkn 421 in 1999-2000 and 2000-2001. *International Cosmic Ray Conference*, *5*, 2607–2610.

Prestwich, A. H., et al. (2007). The orbital period of the Wolf-Rayet binary IC 10 X-1: dynamic evidence that the compact object is a black hole. *Astrophys. Journal Letters*, *669*, L21–24.

Ptuskin, V. S., et al. (1993). Diffusion and drift of very high energy cosmic rays in galactic magnetic fields. *Astronomy & Astrophysics*, *268*, 726–735.

Rees, M. J., & Gunn, J. E. (1974). The origin of the magnetic field and relativistic particles in the Crab Nebula. *Monthly Notices of the Royal Astronomical Society*, *167*, 1–12.

Reynolds, S. P. (2008). Supernova remnants at high energy. *Annual Review of Astronomy and Astrophysics*, *46*, 89–126.

Richards, D. W., & Comella, J. M. (1969). The period of pulsar NP 0532. *Nature*, *222*, 551–552.

Rico, J., et al. (2008). Observations of very high energy gamma-rays during moonlight and twilight with the MAGIC telescope. In *International Cosmic Ray Conference*, vol. 3 of *International Cosmic Ray Conference*, (pp. 1365–1368).

Rissi, M., Otte, N., Schweizer, T., & Shayduk, M. (2009). A new sum trigger to provide a lower energy threshold for the MAGIC telescope. *IEEE Transactions on Nuclear Science*, *56*, 3840–3843.

Rissi, M. (2009). Detection of pulsed very-high-energy γ rays from the crab pulsar with the magic telescope using an analog sum trigger. *PhD Thesis at Swiss Federal Institute of Technology Zurigh. Available at http://wwwmagic.mppmu.mpg.de/pubblications/theses/index.html*.

Rolke, W. A., López, A. M., & Conrad, J. (2005). Limits and confidence intervals in the presence of nuisance parameters. *Nuclear Instruments and Methods in Physics Research A*, *551*, 493–503.

Rolke, W. A., & López, A. M. (2001). Confidence intervals and upper bounds for small signals in the presence of background noise. *Nuclear Instruments and Methods in Physics Research A*, *458*, 745–758.

Romero, G. E. (2008). Hadronic models of high-energy radiation from microquasars: recent developments. In *Microquasars and Beyond*.

Romero, G. E., Torres, D. F., Kaufman Bernadó, M. M., & Mirabel, I. F. (2003). Hadronic gamma-ray emission from windy microquasars. *Astronomy & Astrophysics*, *410*, L1–4.

Russell, D. M., & Fender, R. P. (2010). Powerful jets from accreting black holes: evidence from the optical and infrared. *ArXiv e-prints*.

Sabatini, S., et al. (2010). Episodic transient gamma-ray emission from the microquasar Cygnus X-1 . *Astrophys. Journal*, *712*, L10–15.

Saito, T. Y., et al. (2009). Microquasar observations with the MAGIC telescope. *ArXiv e-prints*.

Samorski, M., & Stamm, W. (1983). Detection of 2 X 10 to the 15th to 2 X 10 to the 16th eV gamma-rays from Cygnus X-3. *Astrophys. Journal Letters*, *268*, L17–21.

Sankrit, R., & Hester, J. J. (1997). The shock and extended remnant around the Crab Nebula. *Astrophys. Journal*, *491*, 796–807.

Scargle, J. D. (1969). Activity in the Crab Nebula. *Astrophys. Journal*, *156*, 401–426.

Scharlemann, E. T., Arons, J., & Fawley, W. M. (1978). Potential drops above pulsar polar caps - Ultrarelativistic particle acceleration along the curved magnetic field. *Astrophys. Journal*, *222*, 297–316.

Schilling, M., Mang, O., & Siems, M. (2001). Recent HEGRA observations of Cygnus X-3. In *International Cosmic Ray Conference*, vol. 6 of *International Cosmic Ray Conference*, (pp. 2521–2525).

Schmelling, M. (1998). Numerische methoden der datenanalyses. *MPI K, Heidelberg*.

Shakura, N. I., & Sunyaev, R. A. (1973). Black holes in binary systems. Observational appearance. *Astronomy & Astrophysics*, *24*, 337–355.

Shayduk, M., Hengstebeck, T., Kalekin, O., Pavel, N. A., & Schweizer, T. (2005). A new image cleaning method for the MAGIC Telescope. *Proceedings of the of the 29th International Cosmic Ray Conference*, *5*, 223–+.

Shibanov, Y. A., Lundqvist, N., Lundqvist, P., Sollerman, J., & Zyuzin, D. (2008). Optical identification of the 3C 58 pulsar wind nebula. *Astronomy & Astrophysics*, *486*, 273–282.

Singh, N. S., et al. (2002). New measurements of orbital period change in Cygnus X-3. *Astronomy & Astrophysics*, *392*, 161–167.

Sollerman, J., et al. (2000). Observations of the Crab Nebula and its Pulsar in the far-ultraviolet and in the optical. *Astrophys. Journal*, *537*, 861–874.

Spitkovsky, A. (2006). Time-dependent force-free pulsar magnetospheres: axisymmetric and oblique Rotators. *Astrophys. Journal Letters*, *648*, L51–54.

Staelin, D. H., & Reifenstein, III, E. C. (1968). Pulsating radio sources near the Crab Nebula. *Science*, *162*, 1481–1483.

Stanev, T., Biermann, P. L., & Gaisser, T. K. (1993). Cosmic rays. IV. The spectrum and chemical composition above 10' GeV. *Astronomy & Astrophysics*, *274*, 902–908.

Stark, M. J., & Saia, M. (2003). Doppler modulation of X-ray lines in Cygnus X-3. *Astrophys. Journal Letters*, *587*, L101–104.

Steeghs, D., & Casares, J. (2002). The mass donor of Scorpius X-1 revealed. *Astrophys. Journal*, *568*, 273–278.

Steinke, B., et al. (2009). MAGIC-II camera slow control software. *Proceedings of the 31st International Cosmic Ray Conference*.

Stephenson, F. R., & Green, D. A. (2002). Historical supernovae and their remnants. *Historical supernovae and their remnants, by F. Richard Stephenson and David A. Green. International series in astronomy and astrophysics, vol. 5. Oxford: Clarendon Press, 2002, ISBN 0198507666*, *5*.

Sturrock, P. A. (1971). A model of pulsars. *Astrophys. Journal*, *164*, 529–556.

Szostek, A., & Zdziarski, A. A. (2004). A study of RXTE and BeppoSAX observations of Cygnus X-3. *ArXiv Astrophysics e-prints*.

Szostek, A., Zdziarski, A. A., & McCollough, M. L. (2008). A classification of the X-ray and radio states of Cygnus X-3 and their long-term correlations. *Monthly Notices of the Royal Astronomical Society*, *388*, 1001–1010.

Tanimori, T., et al. (1998). Detection of γ-rays of up to 50 TeV from the Crab Nebula. *Astrophys. Journal Letters*, *492*, L33–36.

Tavani, M., et al. (2009). Extreme particle acceleration in the microquasar CygnusX-3. *Nature*, *462*, 620–623.

Tavani, M., et al. (2011). Discovery of powerful γ-ray flares from the Crab Nebula. *Science*, *331*, 736–739.

Temim, T., et al. (2006). Spitzer Space Telescope Infrared Imaging and Spectroscopy of the Crab Nebula. *Astronomical Journal*, *132*, 1610–1623.

Tescaro, D. (2010). Tev γ-ray observations of nearby active galactic nuclei with the magic telescope: exploring the high energy region of the multiwavelength picture. *PhD Thesis at Institut de Fisica d Altes Energies. Available at http://wwwmagic.mppmu.mpg.de/pubblications/theses/index.html*.

Tescaro, D., et al. (2009). The readout system of the MAGIC II Cherenkov Telescope. *Proceedings of the 31st International Cosmic Ray Conference*.

Tikonov, A.N., & Arsenin, V.J. (1979). Methods of solution of ill-posed problems.

Tonwar, S. C., et al.. (1991). Detection of ultrahigh-energy radiation from Scorpius X-1: Ooty observations during 1984 - 1987. *Phys. Rev. Lett.*, *67*, 2248–2251.

Trimble, V. (1968). Motions and structure of the filamentary envelope of the Crab Nebula . *Astronomical Journal*, *73*, 535–547.

Trushkin, S. A., Nizhelskij, N. A., & Bursov, N. N. (2008). Longterm multi-frequency monitoring of microquasars. *Proceedings of the of Microquasars and Beyond*.

Tudose, V., et al. (2010). Probing the behaviour of the X-ray binary Cygnus X-3 with very long baseline radio interferometry. *Monthly Notices of the Royal Astronomical Society*, *401*, 890–900.

Urry, C. M., & Padovani, P. (1995). Unified schemes for radio-loud active galactic nuclei. *Publ. of the Astronomical Society of the Pacific*, *107*, 803–845.

Vacanti, G., et al. (1991). Gamma-ray observations of the Crab Nebula at TeV energies. *Astrophys. Journal*, *377*, 467–479.

van der Laan, H. (1966). A model for variable extragalactic radio sources. *Nature*, *211*, 1131–1133.

van Kerkwijk, M. H., et al. (1992). Infrared helium emission lines from Cygnus X-3 suggesting a Wolf-Rayet star companion. *Nature*, *355*, 703–705.

Vittorini, V., et al. (2011). Spectral evolution of the 2010 September γ-ray flare from the Crab Nebula. *Astrophys. Journal Letters*, *732*, L22(5pp).

Vladimirsky, B. M., Stepanian, A. A., & Fomin, V. P. (1973). High-energy gamma-ray outburst in the direction of the X-ray source Cygnus X-3. In *International Cosmic Ray Conference*, vol. 1 of *International Cosmic Ray Conference*, (pp. 456–460).

Volpi, D., Del Zanna, L., Amato, E., & Bucciantini, N. (2008). Non-thermal emission from relativistic MHD simulations of pulsar wind nebulae: from synchrotron to inverse Compton. *Astronomy & Astrophysics*, *485*, 337–349.

Vrtilek, S. D., et al. (1991). Observations of Scorpius X-1 with IUE - Ultraviolet results from a multiwavelength campaign. *Astrophys. Journal*, *376*, 278–288.

Wagner, R. (2006). Measurement of vhe γ-ray emission from four blazars using the magic telescope and a comparative blazar study. *PhD Thesis at the Max-Planck Institute fuer Physik, Muenchen, Germany. Available at http://wwwmagic.mppmu.mpg.de/pubblications/theses/index.html*.

Waltman, E. B., et al. (1994). The quiescent level of Cygnus X-3 at 2.25 and 8.3 GHz: 1988-1992. *The Astronomical Journal*, *108*, 179–187.

Waltman, E. B., et al. (1995). The evolution of outbursts in Cygnus X-3 at 2.25 and 8.3 GHz. *The Astronomical Journal*, *110*, 290–299.

Waltman, E. B., et al. (1996). Quenched radio emission in Cygnus X-3. *The Astronomical Journal*, *112*, 2690–2698.

Watanabe, H., et al. (1994). Correlation between X-ray intensity and radio outbursts of Cygnus X-3. *Astrophys. Journal*, *433*, 350–356.

Waxman, E. (1995). Cosmological gamma-ray bursts and the highest energy cosmic rays. *Physical Review Letters*, *75*, 386–389.

Weber, F. (2005). Strange quark matter and compact stars. *Progress in Particle and Nuclear Physics*, *54*, 193–288.

Weekes, T. C., et al. (1989). Observation of TeV γ-rays from the Crab Nebula using the atmospheric Cerenkov imaging technique. *Astrophys. Journal*, *342*, 379–395.

Weiler, K. W., & Panagia, N. (1978). Are Crab-type supernova remnants (Plerions) short-lived? *Astronomy & Astrophysics*, *70*, 419–422.

Weisskopf, M. C., et al. (2000). Discovery of spatial and spectral structure in the X-ray emission from the Crab Nebula. *Astrophys. Journal Letters*, *536*, L81–84.

Wilson-Hodge, C. A., et al. (2011). When a standard candle flickers. *Astrophys. Journal Letters*, *727*, L40(6pp).

Wittek W. (2002). Determination of the effective observation time. *MAGIC-TDAS. Private use at http://www.magic.mppmu.mpg.de*.

Zanin, R., & Cortina, J. (2009). The central control of the MAGIC telescopes. *Proceedings of the 31st International Cosmic Ray Conference*.

Zanin, R., Moralejo, A., & Hsu, C. C. (2008). Online analysis. *MAGIC-TDAS. Private use at http://www.magic.mppmu.mpg.de*.

Zanin, R., et al. (2011). Measurement of the Crab Nebula spectrum over three orders of magnitude. *Proceedings of the of 32th International Cosmic Ray Conference*.

Zdziarski, A. A., & Gierliński, M. (2004). Radiative Processes, Spectral States and Variability of Black-Hole Binaries. *Progress of Theoretical Physics Supplement*, *155*, 99–119.

List of Figures

List of Tables

Acknowledgments

This PhD gave me the opportunity to meet, share ideas, and work with many beautiful people in the VHE γ-ray community. With some, I also developed a long lasting friendship in the numerous weeks spent together up there, at the Roque de los Muchachos observatory: I will always be thankful to all these friends of mine for teaching me what doing physics is all about.

Among them, my first thought goes to Florian Goebel. All his courage, his enthusiasm, his optimism are with me now, together with the indelible memory of his smile, and the grim reality of my tears for not having him within us anymore.

I am particularly grateful to five more people who strongly contributed to the work of my PhD and my scientific formation in general. Juan Cortina, my supervisor, a tough and direct boss, who has always supported my projects and from whom I always managed to steal a smile, even in the most difficult moments. Daniel Mazin, invaluable guide in the Crab Nebula analysis and great colleague when it comes the moment of taking key decisions. He has always encouraged me to broaden my horizons and seek collaboration. Oscar Blanch, who has unfailingly found the time to give me his priceless advices for any problem I faced, and whose only fault was to arrive in our group too late to start a project together. Abelardo Moralejo, the guru of the MAGIC analysis, the man you know you can count on when you need to unravel the knottiest problem. Nepomuk Otte, ex-magician and now successful member of the VERITAS collaboration. We met at the University of California Santa Cruz where we laid the foundation of a three years long collaboration that is now coming to a fruitful conclusion. It is hard to overestimate the importance for my work and my career of those three months spent with him and his team.

Many other people played an important role in the making of this thesis. A special thanks goes to all the students and ex-students I met at Institut de Física d'Altes Energies (IFAE). Diego Tescaro, the third "compagno" of the adventures in La Palma, who shared with me and Florian all the happy and sad moments of those days. And then Manel Errando, Gianluca Giavitto, Ignasi Reichardt, Jelena Aleksić, Alicia Lopez: with all of them I have, soon or later, shared office, laugh, and drinks. A warm thank you to Roger Firpo, once my officemate and now the administrator of our computing farm, for the patience and the time he dedicated to the thousands of technical problems we faced. How not to mention the IFAE engineers, with whom I shared many days and nights in La Palma for the commissioning of the second telescope: Miquel, Pepe, Alex, thanks for what you taught me, and even more so for the food and the fun. A word of acknowledgement for Manel Martínez, Enrique Fernández and Matteo Cavalli-Sforza who gave me the opportunity to be an IFAE member, and take my PhD in this prestigious research center.

I would like to acknowledge the team of the Universitat de Barcelona, Josep Maria Paredes, Marc Ribó, Víctor Zabalza, Valentí Bosch-Ramon, and Pol Bordas who helped me in the interpretation and analysis of the microquasar observations. Emiliano Carmona, Stefan Klepser and Julian Sitarek as valuable collaborators in the problem-solving of the analysis, Elisa Bernardini and Javier Rico for their precious advices in the refereeing processes.

Let me also thank the other people who worked with me during the commissioning:

Riccardo Paoletti, Thomas Schweizer, Markus Garczarczyk, Markus Gaug, Tobias Jogler, Francesco Dazzi and the team of the mirror installation: Michele Doro, Mosé Mariotti, Luigi Lessio, Massimo Rebeschini, Cornelia Schultz, and Marco Scarcioffolo.

Finally, the honour of the last huge grazie to my mum and dad, Margherita and Pino, and to Gianluca, who shared with me every single moment of this PhD: without your love and support, I know I could not have made it through.